# Classification and repeatability studies of transient electromagnetic measurements with respect to the development of $CO_2$-monitoring techniques

By the Faculty of Geosciences, Geoengineering and Mining
of the Technische Universität Bergakademie Freiberg

approved

**Thesis**

to attain the academic degree of

Doktor der Naturwissenschaften
(Dr. rer. nat.)

submitted by **M. Sc. Matthias Bär**

born on the 9th June 1985 in Greifswald

**Assessor: Prof. Dr. rer. nat. Klaus Spitzer, Freiberg**
**Prof. i.R. Dr. rer. nat. Helmut Schaeben, Freiberg**
**Prof. Dr. rer. nat. Bülent Tezkan, Köln**

**Date of the award: Freiberg, 16.12.2020**

**To**
**Dr. Gordon Freeman and Dr. Angela Ziegler**

**Acknowledgements**

First and foremost, I want to thank Prof. Dr. Klaus Spitzer for supervising my thesis, his encouraging words and fruitful discussions throughout the preparation of this thesis. Furthermore, I thank Prof. i.R. Dr. Helmut Schaeben and Prof. Dr. Bülent Tezkan for their willingness to review my thesis. I thank Prof. Dr. Hans-Jörg Starkloff for the numerous consultations and his hints regarding time series models and functional data analysis.

I further thank the German Research Foundation (DFG) for founding parts of the field measurements in Canada and the European Social Fund for financial support.

Special thank goes to Tino Beyer and Udo Böhme for their enormous efforts in realizing the construction of the transmitter output current measurement system and the multiple field deployments throughout this thesis.

Great thanks go to all my colleagues for their supportive role and advice during the thesis. Especially Dr. Jana Börner for her kindness and suggestions in countless discussions regarding geophysical problems. Furthermore, Dr. Ralph-Uwe Börner for providing his 1D- and 3D-codes to calculate transient electromagnetic fields.

Many thanks to my family and friends for supporting me throughout this thesis, especially in bad times or circumstances.

# Abstract

The mitigation of greenhouse gases, like $CO_2$, is a challenging aspect for our society with a constantly growing population that has a high demand for energetic raw resources. A strategy to hamper the constant emission of $CO_2$ is utilizing carbon capture and storage technologies. Thereby, the $CO_2$ is sequestrated in suitable subsurface reservoirs. However, these reservoirs harbor the risk of leakage and therefore appropriate geophysical monitoring methods are needed to initiate early countermeasures. A crucial aspect of monitoring is the assignment of measured data to certain events occurring (leakage, migration, etc.). Especially if the changes in the measured data are small due to e.g. small amounts of injected $CO_2$, suitable statistical methods are needed to distinguish between certain events.

In this thesis, classification and repeatability studies of transient electromagnetic measurements with respect to the development of $CO_2$-monitoring techniques are investigated. Since there does not seem to be a standardized workflow of detecting similar transient electromagnetic responses from successive repeat measurements, a new statistical workflow based on cluster analysis is proposed. Thereby, the time series distance metrics dynamic time warping, the autoregressive distance based on integrated autoregressive moving average time series models, and the normalized root-mean-square serve as similarity criterion in the clustering process. These time series distance metrics are compared and evaluated with respect to the classic Euclidean norm. The pairwise distances between the normalized transient electromagnetic signals are then clustered using an agglomerative hierarchical clustering method and the optimal number of clusters is determined using the gap statistic. For better visualization of the underlying dependency structure between the time series, the multidimensional scaling method is used as a dimensional reduction technique. To validate the clustering results, silhouette values and average silhouette widths are used.

The statistical workflow is applied to a synthetic data set and a long-term monitoring data set at Tharandter Wald, Saxony, to test its capabilities of detecting similar transient electromagnetic measurements. Furthermore, the workflow is applied to repeat measurements at a pilot $CO_2$-sequestration site in Brooks, Alberta.

# Contents

# 1. Introduction and motivation

Our society is highly dependent on making use of existing energy and raw material resources. The worldwide demand for mineral and energy raw materials is increasing and is subject to strong price volatility due to economic and political fluctuations. Mineral and energy resources are the foundation for social life, ranging from information and communication technology to consumer goods, pharmaceuticals, and medical technology. The continuous methodological development of mining and localization methods is the basis for the current utilization of the limited resources available. As a consequence of a steadily growing world population, the annual energy demand and therefore the consumption of natural energy sources such as coal and gas are increasing as well. This leads to constant global warming as a result of greenhouse gas emissions like carbon dioxide ($CO_2$), methane ($CH_4$) or nitrous oxide ($N_2O$). In an effort to mitigate greenhouse gases, the European Parliament committed the Community to reduce the total amount of greenhouse gas emissions by 30 % by 2020 and by 50 % by 2050. Besides massive funding for renewable energy technologies, the European Parliament further established the directive on the geological storage of $CO_2$ (CSS-Directive) in 2009 as a bridging technology to achieve the goal by 2050 (European Union, 2009).

The concept of carbon capture and storage (CCS) was born in the 1970s. It was intended to maximize the oil production of large oil fields by injecting $CO_2$ into the reservoir. Injected $CO_2$ has the capability to swell the oil, reducing its viscosity and interfacial tension resulting in an enhanced flow. This process is called enhanced oil recovery (EOR) and was first established at the SACROC Unit in Scurry County, Texas in 1972. The ultimate oil recovery was maximized to 50 % instead of the conventional 18 % (Crameik and Massey, 1972). However, the oil price dropped in the mid-1980s and the production cost of the $CO_2$ capture process were too high for EOR operations (Herzog, 1999). Instead, CCS is nowadays used as a bridging technology to mitigate greenhouse gases by sequestrating and trapping $CO_2$ into geological formations such as depleted gas or oil reservoirs, and deep saline aquifers. Other $CO_2$ storage types such as ocean storage and mineral carbonation exist but are not considered economically feasible yet (see Figure 1.1). Table 1.1 summarizes the current status of $CO_2$ storage types (IPCC, 2005).

The storage of $CO_2$ in geological formations harbors the risk that the low-permeable sealing layer is damaged due to the increased reservoir pressure during injection, causing a leakage (EASAC, 2013). As a consequence, the sequestered $CO_2$ could migrate to critical geological units, e.g. domestically and agriculturally used groundwater aquifers. Current research topics focus on the detection of $CO_2$ leakages at the surface utilizing chemical analysis of soil air (Pak et al., 2016). The oxygen and carbon dioxide concentration at the surface before and after $CO_2$ injection is measured and compared. The ratio provides information about the leakage rate of the injected $CO_2$ in the storage formation. However, these methods are only effective if leakages are already occurring and are also influenced by changes to soil air in the vadose zone or at the Earth‘s surface (Romanak et al., 2012). This results in considerable forecast

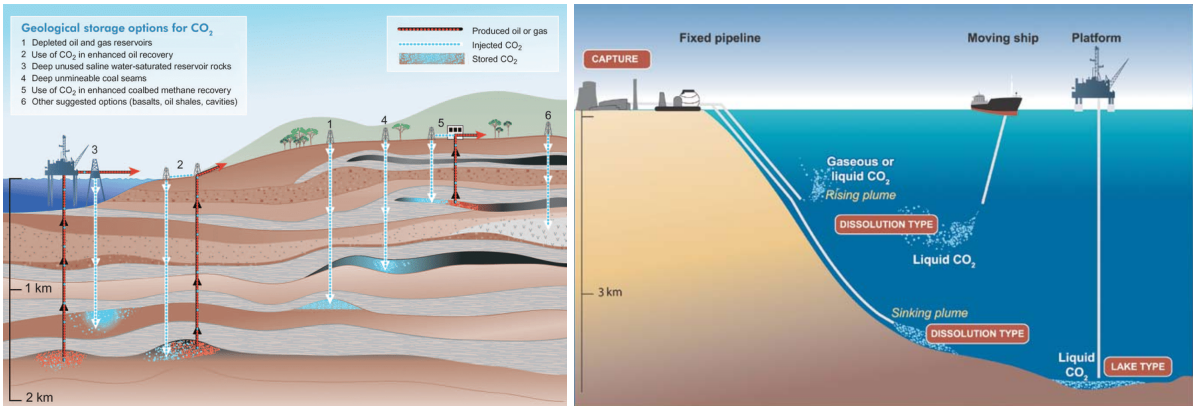


(a) geological storage (b) ocean storage

**Fig. 1.1.:** Overview of the geological (a) and the ocean (b) $CO_2$ storage type. (IPCC, 2005)

**Tab. 1.1.:** Current status of $CO_2$ storage types (after IPCC (2005))

| $CO_2$ **storage type** | **Storage technology** | **Research phase** | **Demonstration phase** | **Economically feasible** | **Mature market** |
|---|---|---|---|---|---|
| Geological storage | Enhanced Oil Recovery (EOR) | | | | X |
| | Gas or oil fields | | | X | |
| | Saline formations | | | X | |
| | Enhanced Coal Bed Methane recovery (ECBM) | | X | | |
| Ocean storage | Direct injection (dissolution type) | X | | | |
| | Direct injection (lake type) | X | | | |
| Mineral carbonation | Natural silicate minerals | X | | | |
| | Waste materials | | X | | |

uncertainties and shortens the time needed to initiate necessary countermeasures and to warn or evacuate the adjacent population.

For this reason, the monitoring of sequestrated $CO_2$ at depth is of particular importance. Storage formations often only have a thickness of a few tens of meters and, due to the supercritical properties of $CO_2$, can usually only be used effectively at greater depths. This poses a particular challenge for monitoring methods, especially if they are carried out from the earth's surface. 3D time-lapse seismics and seismic tomography are currently the most frequently used methods for monitoring sequestered $CO_2$. It causes weak changes in the seismic P and S-wave velocity of the geological unit, which allows for delineating the $CO_2$ reservoir and possibly its propagation in the storage formation (Lumley et al., 2008; Lumley, 2010). However, this method may be inappropriate since their sensitivity is sensitive to the degree of $CO_2$ saturation (JafarGandomi and Curtis, 2011).

Here electric and electromagnetic methods come into play. They are particularly sensitive to changes in the conductivity, making them well-suited for monitoring the migration of poorly conductive $CO_2$ in well-conducting brine. This thesis work has been conducted in the context of a collaborative project between the Institute of Geophysics and Geoinformatics at the Technical University Bergakademie Freiberg and the Carbon Management Canada Research Institutes (CMC). The aim of this project was to investigate a new approach to quantitative $CO_2$ injec-

tion monitoring using borehole electromagnetic measurements (CMC Project C394) in order to investigate if electromagnetic monitoring is feasible and possibly advantageous to seismic monitoring with regard to the aspects addressed above. Especially borehole configurations are well suited to increase the sensitivity of electromagnetic methods at depth.

A pilot CCS site was established by CMC including a Field Research Station (FRS) near Brooks, Canada, providing an experimental environment for a multitude of different experiments. The FRS is operated by the Containment and Monitoring Institutes (CaMI), a subdivision of CMC. Originally, it was planned to sequestrate 600 t gaseous $CO_2$ into a saline aquifer at a depth of around 300 m. The shallow target was particularly chosen to test trapping mechanisms of gaseous $CO_2$ and to initiate a controlled leakage to investigate migration patterns. In order to detect changes in the conductivity due to sequestrated $CO_2$, a surface-to-borehole variant of the transient electromagnetic (TEM) method was applied. Transient measurements are obtained by abruptly switching off the transmitter current (usually a square horizontal wire loop), which induces eddy currents in the subsurface, resulting in a secondary field whose rate of change is measured over time by an induction coil in terms of the time derivative of the magnetic flux density $\dot{\vec{b}}$. At the FRS, two observation wells for geophysical equipment and multiple water wells were provided for monitoring the sequestration process and to perform chemical analyses of the groundwater. They were used to carrying out TEM measurements downhole in close vicinity of the reservoir which increases the sensitivity on TEM responses with respect to injected $CO_2$.

A crucial aspect of reservoir monitoring is to predict resistivity changes in the target formation once $CO_2$ is injected. Our calculations of the reservoir resistivity under presence of 600 t gaseous $CO_2$ yield an increased resistivity of 100 Ω m compared to the initial 10 Ω m prior to $CO_2$ injection (Börner et al., 2013). Based on these resistivity calculations, we performed 3D-forward TEM simulations for two scenarios. The first scenario covers the baseline state where no $CO_2$ is injected whereas the second scenario covers the case of a $CO_2$ filled reservoir. The baseline response ($\dot{\vec{b}}_{\text{base}}$) is the transient response of a homogeneous 10 Ω m half-space whereas for the post-injection response ($\dot{\vec{b}}_{\text{inj}}$) a $CO_2$-plume of cylindrical shape ($r = 80\,\text{m}, h = 6\,\text{m}$) is additionally included in the homogeneous half-space. Figure 1.2 shows relative changes $\delta\dot{\vec{b}}^{\text{inj}}_{\text{base}}$ in % between the baseline and the post-injection state for the vertical and radial component of the transient response along the observation well as a function of time. After $CO_2$ sequestration, relative changes of about 10 % in the vertical and about ±20 % in the radial component are expected close to the reservoir.

Since the relative changes are rather small and only occur at certain time windows, the question arose of how accurate TEM signals can be measured and how repeat measurements can be identified as similar using statistical methods. Furthermore, how "stable" can transient measurements be conducted with the PROTEM system by the manufacturer Geonics Limited available at the institute. To answer those questions, continuous measurements at a fixed test site were made over more than one year at Tharandter Wald (Saxony/ Germany). Since there does not seem to be a standardized workflow of detecting similar transient electromagnetic responses from successive repeat measurements, we propose a new statistical workflow to detect similar transient responses based on cluster analysis. The baseline measurements at the FRS were obtained from June to July 2016 before $CO_2$ injection. Due to a failure of the main output stage of the TEM57-MK2 power transmitter, only a rather small part of the originally planned baseline data set could be obtained during the 2016 field survey. However, the baseline measurements could be repeated in 2018, as only an insignificant amount of $CO_2$ (∼4 t) had been injected into

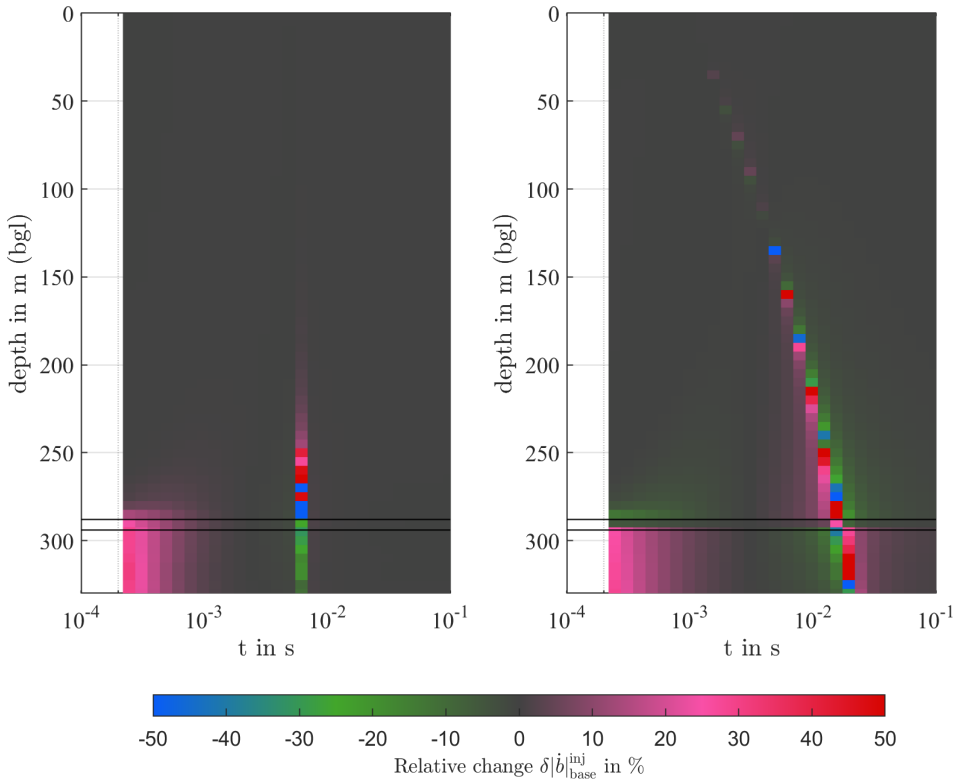


**Fig. 1.2.:** Simulated relative difference $\delta\vec{\dot{b}}^{\text{inj}}_{\text{base}}$ in % between the baseline $\vec{\dot{b}}_{\text{base}}$ and the injected $CO_2$ state $\vec{\dot{b}}_{\text{inj}}$ for the vertical (left) and radial (right) component of the transient response as a function of depth below ground level (bgl) and time. The baseline state is the transient response of a homogeneous 10 Ω m half-space. For the injected state a $CO_2$-plume of cylindrical shape ($r = 80$ m, $h = 6$ m) is additionally included in the homogeneous half-space. Black lines indicate depth limits of the identified reservoir at the FRS.

the reservoir due to technical problems at the well site. As a consequence, a comprehensive high-quality TEM baseline data set for the undisturbed reservoir is now available. At the time of writing, a post-injection repeat survey is still lacking but would be highly desirable as $CO_2$ is being continuously injected since March 2020.

The thesis is divided into four main chapters. The essential geophysical theory of electromagnetics and the governing equations are described in Chapter 2. Chapter 3 provides the reader with the basic concepts of time series analysis. This includes a detailed explanation of the most common distance metrics like dynamic time warping, the autoregressive distance metric for time series models, and the normalized root-mean-square distance metric. Furthermore, the reader is provided with a detailed introduction to cluster analysis with respect to partitioning and hierarchical clustering methods as well as multidimensional scaling which is used as a dimensional reduction technique. Chapter 4 is in the context of applying these time series distance metrics and clustering methods to both synthetic data and the Tharander Wald long-term monitoring data, based on a developed statistical workflow to identify similar transient responses. A complete description and comparison in terms of repeatability of the field surveys of 2016 and 2018 as well as the resistivity calculation of the reservoir under the presence of $CO_2$ can be found in Chapter 5 and Appendix C. At the end of this thesis, a summary and outlook is provided in Chapter 6. Additional in-depth explanations of statistical tests and concepts can be found in Appendix A. A description of the PROTEM system and investigations with respect to time stability of the transient response and the current turn-off function are given in Appendix B.

# 2. Principles of the transient electromagnetic method

Intentionally designed for mineral exploration, the transient electromagnetic method quickly developed as state-of-the-art technique for hydrogeological and landfill monitoring. First attempts to transmit and receive transient signals in the subsurface where made by Statham (1936) and Hawley (1938) in the 1930s. However, feasible applications firstly developed in the mid-60s in the USSR as electronics and computer capabilities significantly improved (Barringer, 1962). Thus, transient electromagnetics is a relative young geophysical method compared to frequency domain and geoelectrical methods. Due to its properties in the time domain, which result in large dynamic frequency ranges compared to other geophysical techniques, it has an enormous versatility in its application (Christiansen et al., 2006).

The transient electromagnetic method is characterized by transmitting timed electromagnetic pulses into the subsurface, usually by quickly switching off a constant current in a horizontal wire loop at the Earth's surface (Figure 2.1). The primary magnetic field interacts with conductive matter in the subsurface resulting in a secondary field as a consequence of induced eddy currents. The secondary magnetic fields are then measured at Earth surface or in a borehole in the absence of the primary magnetic field.

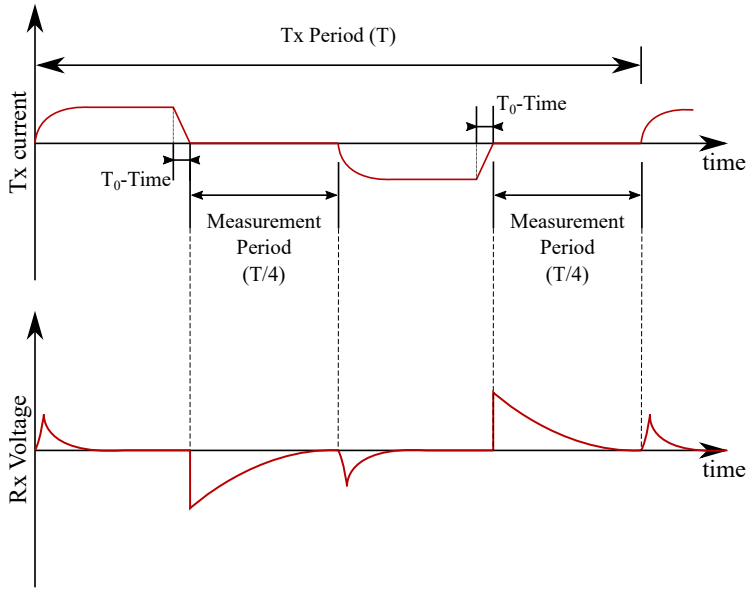


**Fig. 2.1.:** Schematic diagram of the working cycle for a typical TEM transmitter system. Transmitter output current function (top) vs. induced receiver voltage (middle) over time (after Levy and McNeil (1984)).

## 2.1. Governing equations

Electromagnetic fields can be described by the four fundamental vector functions (Ward and Hohmann, 1988), which are

$\vec{e}$ - the electric field density in [V/m],

$\vec{b}$ - the magnetic field flux density in [T =V s/m$^2$],

$\vec{d}$ - the dielectric displacement in [A s/m$^2$], and

$\vec{h}$ - the magnetic field intensity in [A/m].

Based on these fundamental vector functions, any electromagnetic phenomena can be described by introducing Maxwell's equations which are coupled first order linear differential equations. In time domain they read as follows (Note: in this Chapter, capital letters describe quantities in the frequency-domain and lower-case letters describe quantities in the time domain. The operator $\partial_t$ is a short notation of the partial differentiation with respect to time $\frac{\partial}{\partial t}$):

$$\nabla \times \vec{e} = -\partial_t \vec{b} - \vec{j}^s_m, \tag{2.1}$$

$$\nabla \times \vec{h} = \vec{j} + \partial_t \vec{d} + \vec{j}^s_e, \tag{2.2}$$

$$\nabla \cdot \vec{d} = \rho_e, \tag{2.3}$$

$$\nabla \cdot \vec{b} = 0, \tag{2.4}$$

where $\rho_e$ is the electric charge density in [A s/m$^3$],and $\vec{j}$ the current density in [A/m$^2$]. The terms $\vec{j}^s_m$ in [V/m$^2$] and $\vec{j}^s_e$ in [A/m$^2$] are the specific source current densities for magnetic and electric sources. Equation 2.1, also known as Faraday's law, describes the phenomenon that a time varying magnetic field causes eddy currents of opposite sign in an electrical conductor. Ampère's circuital law (Equation 2.2) describes the phenomenon that an electrical line segment produces a circular magnetic field $\vec{h}$. The source of the electric field is the electric charge density $\rho_e$, described by Gauss's law (Equation 2.3). From Gauss law for magnetic fields (Equation 2.4) follows, that the magnetic field is source free and hence no magnetic monopoles exist. The constitutive relations

$$\vec{d} = \varepsilon \vec{e} = \varepsilon_0 \varepsilon_r \vec{e}, \tag{2.5}$$

$$\vec{b} = \mu \vec{h} = \mu_0 \mu_r \vec{h}, \tag{2.6}$$

and Ohm's law

$$\vec{j} = \sigma \vec{e}, \tag{2.7}$$

thereby describe the coupling between Maxwell's equations through matter, where $\mu_0$ and $\mu_r$ in [V s/(A m)] are the vacuum respectively the relative magnetic permeability, $\varepsilon_0$ and $\varepsilon_r$ in [A s/(V m)] the vacuum respectively the relative electrical permittivity, and $\sigma$ is the electrical conductivity in [S/m]. The quantities $\varepsilon, \mu$ and $\sigma$ are in general tensors which depend on frequency, time, space, temperature, and pressure. However, for isotropic media, the quantities become scalar and since for most earth materials $\mu_r$ and $\varepsilon_r$ are close to one for low frequencies, $\mu$ and $\varepsilon$ are set to the vacuum permeability $\mu_0 = 4\pi \cdot 10^{-7}$ V s/(A m) and permittivity $\varepsilon_0 \approx 8.854 \cdot 10^{-12}$ A s/(V m).

By introducing the Fourier transformation pair for the field quantities

$$G(\omega) = \int_{-\infty}^{\infty} g(t) e^{-i\omega t} dt \,, \tag{2.8}$$

$$g(t) = \frac{1}{2\pi} \int_{-\infty}^{\infty} G(\omega) e^{i\omega t} d\omega \,, \tag{2.9}$$

and by applying the constitutive relations (Equation 2.5 to 2.7) and the approximation $\mu = \mu_0$ and $\varepsilon = \varepsilon_0$, Maxwell's equations can be expressed in the frequency domain as

$$\nabla \times \vec{E} = -i\omega\mu_0 \vec{H} - \vec{J}_m^s \,, \tag{2.10}$$

$$\nabla \times \vec{H} = (\sigma + i\omega\varepsilon_0)\vec{E} + \vec{J}_e^s \,, \tag{2.11}$$

$$\nabla \cdot \vec{D} = \rho_e \,, \tag{2.12}$$

$$\nabla \cdot \vec{B} = 0 \,, \tag{2.13}$$

where $i$ denotes the imaginary unit for complex numbers and $\omega$ the angular frequency in $[1/\mathrm{s}]$. In general, the fields $\vec{E}$ and $\vec{H}$ can be expressed as a superposition of electric and magnetic sources (Ward and Hohmann, 1988) where,

$$\vec{E} = \vec{E}_m + \vec{E}_e \,, \tag{2.14}$$

$$\vec{H} = \vec{H}_m + \vec{H}_e \,. \tag{2.15}$$

In the following, fields will only be seen as the result of magnetic sources, since the most frequently used source types of TEM are of inductive nature (horizontal wire loops). Therefore, a separate set of equations

$$\nabla \times \vec{E}_m = -i\omega\mu_0 \vec{H}_m - \vec{J}_m^s \,, \tag{2.16}$$

$$\nabla \times \vec{H}_m = (\sigma + i\omega\varepsilon_0)\vec{E}_m \,, \tag{2.17}$$

for Faraday's and Ampere's Law exists for the magnetic source type, assuming that the source term $\vec{J}_e^s$ is zero for $[\vec{E}_m, \vec{H}_m]$. Taking the divergence of Equation 2.16 and 2.17 leads to

$$\nabla \cdot \vec{H}_m = -\frac{\nabla \cdot \vec{J}_m^s}{i\omega\mu_0} \,, \tag{2.18}$$

$$\nabla \cdot \vec{E}_m = 0 \,. \tag{2.19}$$

From Equation 2.19 it follows, that $\vec{E}_m$ can be calculated by using the ansatz

$$\vec{E}_m = -\nabla \times \vec{F} \,, \tag{2.20}$$

since any divergence of the curl of a vector field is zero ($\nabla \cdot (\nabla \times \vec{F}) = 0$). Here, $\vec{F}$ is called the electric vector potential. Substituting Equation 2.20 in 2.17 yields,

$$\vec{H}_m = -(\sigma + i\omega\varepsilon_0)\vec{F} - \nabla\phi \,, \tag{2.21}$$

where $\phi$ is an arbitrary scalar potential as a result of the successive integration (constant of integration). Since the scalar potential $\phi$ vanishes by forming the curl ($\nabla \times \nabla\phi = 0$), it can be arbitrary selected. Ward and Hohmann (1988) define the scalar potential as

$$\phi = \frac{1}{i\omega\mu_0} \nabla \cdot \vec{F} \,, \tag{2.22}$$

also known as “Lorenz-gauge”. For convenience, the index $m$ as indicator for a magnetic source is dropped from now on. Substituting $E$ and $H$ in Equation 2.10 with the expressions derived in Equation 2.20 to 2.22 and by utilizing the vector identity,

$$\nabla \times \nabla \times \vec{A} = \nabla\nabla \cdot \vec{A} - \nabla^2 \vec{A}\,, \tag{2.23}$$

yields the inhomogeneous Helmholtz equation

$$\nabla^2 \vec{F} - (i\omega\mu_0\sigma - \omega^2\mu_0\varepsilon_0)\vec{F} = -\vec{J}^s\,. \tag{2.24}$$

## 2.2. Quasi-static approximation

The Helmholtz equations may be further reduced by taking advantage of the quasi-static approximation. In general, the current density

$$J = J_c + J_d\,, \tag{2.25}$$

is a superposition of conductive currents $J_c$ and displacement currents $J_d$ (Knödel and Krummel, 2005), with

$$J_c = \sigma\vec{E} \tag{2.26}$$

and

$$J_d = \omega\varepsilon\vec{E}\,. \tag{2.27}$$

Since most of the applied frequencies in geophysical prospecting methods are below 100 kHz (Tezkan, 1999), and the conductivity for earth materials, is usually larger than $0.1\ \mathrm{mS/m}$ (Ward and Hohmann, 1988), the ratio between the displacement and conduction currents is smaller one;

$$\frac{J_d}{J_c} = \frac{\omega\varepsilon_0}{\sigma} \approx 5.56 \cdot 10^{-2} \ll 1\,. \tag{2.28}$$

This indicates, that the displacement currents are much smaller than the conduction currents and can therefore be neglected. Figure 2.2 shows the spectrogram of the measured current output over time of the PROTEM TEM57-MK2 transmitter. High frequencies with a significant amplitude can be observed during the current turn-off processes at 10 ms and 30 ms. Thereby, the frequencies do not exceed 100 kHz. However, harmonic instrument noise in a high frequency band of ∼250 kHz to 1000 kHz can be observed. The noise originates from switching power supplies (Peikert et al., 2014) of the oscilloscope and the laptop which is induced into the partially unshielded measurement cables of the measurement setup.

By taking advantage of the quasi-static approximation, Equation 2.24 further reduce to

$$\nabla^2 \vec{F} + k^2 \vec{F} = -\vec{J}^s\,, \tag{2.29}$$

where $k^2 = -i\omega\mu_0\sigma$.

## 2.3. 1D solution

In the following section, 1D analytical solutions for a homogeneous half-space and a layered half-space conductivity distribution is presented. If not stated explicitly otherwise, the basic solution approach emanate from Ward and Hohmann (1988) and Zhdanov (2009).

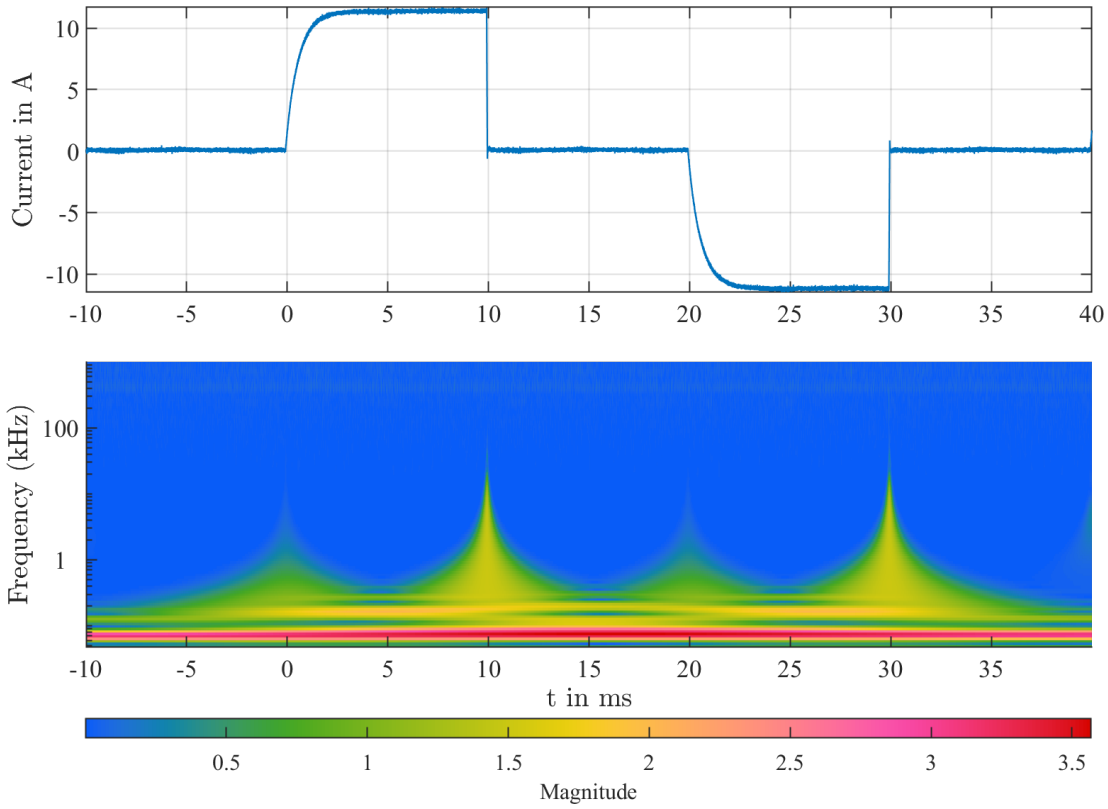


**Fig. 2.2.:** Spectrogram of the measured current output function of an 100m × 100m transmitter loop and the PROTEM TEM57-MK2 transmitter at 11 A output current.

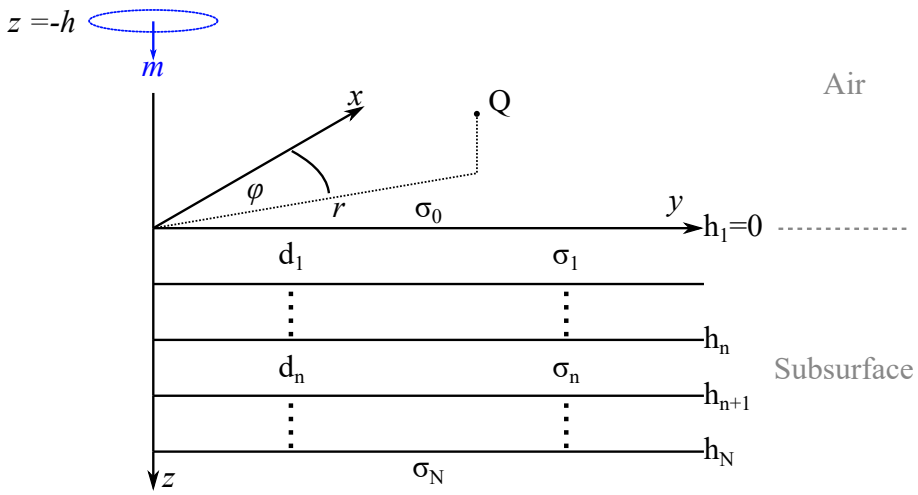


**Fig. 2.3.:** Schematic overview of the N-layered half-space conductivity model. The VMD is positioned at $[0,0,-h]^\top$ above the Earths surface. The conductivity $\sigma_i$ of each layer with layer thickness $d_i$ is assumed to be constant.

## 2.3.1. Solution approach

Considering a magnetic dipole source above Earths surface at $\vec{p}_0 = [0,0,-h]^\top$, the right-hand side source term $J_s$ in Equation 2.29 is then defined as a point source in the form of a vertical

magnetic dipole (VMD) (Ward and Hohmann, 1988)

$$\nabla^2\vec{F} + k^2\vec{F} = -i\omega\mu_0\vec{m}\delta(x)\delta(y)\delta(z+h)\,, \tag{2.30}$$

where $\vec{m} = [0,0,m_z]^\top$ denotes the magnetic dipole moment. Since the dipole moment only features a vertical component, it follows that the vector potential $\vec{F} = [0,0,F_z]^\top$ also features only a vertical component ($F = F_z$). Due to the symmetry of the problem, it is convenient to choose cylindrical coordinates with

$$x = r\cos(\varphi) \qquad y = r\sin(\varphi) \qquad z = z\,, \tag{2.31}$$

where $r = \sqrt{x^2+y^2}$ (c.f. Figure 2.3).

The general approach of solving Equation 2.30 with respect to the vector potential $F$ is by assuming that the total potential is a superposition of a source related potential in a non-conductive full-space ($F^*$) and a secondary potential ($F^0$, $F^1$, $F^j$) of induced currents in the conductive half-space;

$$F := \begin{cases} F^0_{\text{total}} = F^* + F^0 & \text{for } z \le 0 & \text{(Air half-space)} \\ F^1 & \text{for } z \ge 0 & \text{(Homogeneus half-space)} \\ F^j & \text{for } z \ge 0,\ j \ne 0 & \text{(Layered half-space).} \end{cases} \tag{2.32}$$

### 2.3.2. Continuity conditions

Since the vector potential is a superposition of the primary and secondary potential, each potential has to satisfy Maxwell's equations. Thus, two appropriate conditions have to be applied at the boundaries between adjacent layers, for instance the air-earth interface. Firstly, the vector potential has to vanish at an infinite distance of the source due to the damping characteristic of the electromagnetic fields

$$\lim_{R\to\infty} F_{\text{total}} \to 0\,, \tag{2.33}$$

for $R = \sqrt{r^2+(z+h)^2}$. Secondly, the tangential components

$$E^0_\phi = \partial_r F^0_{\text{total}} = \partial_r F^1_{\text{total}} = E^1_\phi \tag{2.34}$$

$$\beta H^0_r = \partial^2_{rz} F^0_{\text{total}} = \partial^2_{rz} F^1_{\text{total}} = \beta H^1_r \quad \text{for } \beta = i\omega\mu_0 \tag{2.35}$$

of $E_\phi$ and $H_r$ have to be continuous at the interface between adjacent layers. Since this continuity conditions have to be full-filled across the whole layer interface, the continuity conditions for the potential $F$ can be obtained by integrating Equation 2.34 and 2.35 with respect to $r$,

$$F^0 = F^1 \tag{2.36}$$

$$\partial^2_z F^0 = \partial^2_z F^1\,. \tag{2.37}$$

### 2.3.3. The primary potential in the air half-space ($z \le 0$)

The primary potential $F(r,z)$ can be calculated as the solution of a point source in the homogeneous full-space. Thus, for a VMD source the solution is given as a weighted scalar Green's function in cylindrical coordinates

$$F(r,z) = \frac{i\omega\mu_0 m}{4\pi R} e^{-ikR}\,, \tag{2.38}$$

with the magnetic dipole moment $m$ and $R = \sqrt{r^2 + (z+h)^2}$. Assuming an air conductivity $\sigma_0 \approx 0\,\mathrm{S/m}$, the primary potential in the air half-space is

$$F^*(r,z) = \frac{i\omega\mu_0 m}{4\pi R}\,. \tag{2.39}$$

### 2.3.4. The secondary potential in the air half-space ($z \leq 0$)

Since the primary potential $F^*$ accounts for the source related part of the total potential, the secondary potentials ($F^0$, $F^1$, $F^j$) satisfy the homogeneous Helmholtz equation in cylindrical coordinates

$$\partial_{rr}^2 F + \frac{1}{r}\partial_r F + \partial_{zz}^2 F + k^2 F = 0\,. \tag{2.40}$$

Equation 2.40 can be solved by applying the method of "separation of variables". This allows to express the potential $F(r,z)$, which depends on the two variables $r$ and $z$, as a product of two functions $U$ and $V$

$$F(r,z) = U(r)V(z)\,, \tag{2.41}$$

which only depend on $r$ respectively $z$. This leads to two ordinary differential equations with the particular solution

$$U(r,\lambda) = \hat{\alpha}(\lambda)J_0(\lambda r) + \hat{\beta}(\lambda)Y_0(\lambda r) \tag{2.42}$$

$$V(z,\lambda) = \hat{\gamma}^-(\lambda)e^{-\sqrt{\lambda^2-k^2}z} + \hat{\gamma}^+(\lambda)e^{+\sqrt{\lambda^2-k^2}z}\,, \tag{2.43}$$

where $\hat{\gamma}^-$ and $\hat{\gamma}^+$ are the amplitudes of the downward and upward traveling waves, $J_0(\lambda r)$ is the zeroth-order Bessel function of the first kind, and $Y_0(\lambda r)$ is the zeroth-order Bessel function of the second kind. Since $Y_0(\lambda r)$ is singular for $r = 0$, which does not yield a reasonable physical interpretation, $\hat{\beta}(\lambda)$ is set to zero.

The general solution is then found as a superposition of all particular solution by integrating over $\lambda$ and by enforcing the vanishing of the potential at an infinite distance to the source ($F \to 0$, for $z \to -\infty$). This yields the secondary potential in the air as

$$F^0(r,z) = \frac{i\omega\mu_0 m}{4\pi}\int_0^\infty \gamma^+(\lambda)e^{+\lambda z}J_0(\lambda r)\mathrm{d}\lambda\,, \tag{2.44}$$

with

$$\hat{\alpha} = \frac{i\omega\mu_0 m}{4\pi} \tag{2.45}$$

and the total potential

$$\begin{aligned} F^0_{\text{total}}(r,z) &= F^*(r,z) + F^0(r,z) \\ &= \frac{i\omega\mu_0 m}{4\pi}\int_0^\infty \left[e^{-\lambda|z+h|} + \gamma^+(\lambda)e^{+\lambda z}\right]J_0(\lambda r)\mathrm{d}\lambda\,, \quad \text{for } k_0^2 = 0\,. \end{aligned} \tag{2.46}$$

### 2.3.5. The potential in the homogeneous half-space ($z \geq 0$)

In the same manner as the secondary potential in the air half-space was derived, the total potential in the homogeneous half-space is derived;

$$F^1(r,z) = \frac{i\omega\mu_0 m}{4\pi} \int_0^\infty \left( \gamma^-(\lambda) e^{-\sqrt{\lambda^2 - k_1^2} z} + \gamma^+(\lambda) e^{+\sqrt{\lambda^2 - k_1^2} z} \right) J_0(\lambda r) \mathrm{d}\lambda \,. \tag{2.47}$$

By enforcing the vanishing of the potential at an infinite distance ($F \to 0$, for $z \to +\infty$), Equation 2.47 further reduce to

$$F^1(r,z) = \frac{i\omega\mu_0 m}{4\pi} \int_0^\infty \gamma^-(\lambda) e^{-\lambda_1 z} J_0(\lambda r) \mathrm{d}\lambda \,, \tag{2.48}$$

with $\lambda_1 = \sqrt{\lambda^2 - k_1^2} = \sqrt{\lambda^2 + i\omega\mu_0\sigma_1}$.

The coefficients $\gamma^+$ and $\gamma^-$ can be determined by applying the continuity conditions given in Equation 2.36 and 2.37 at the air-earth interface ($z = 0$). Evaluating the resulting linear system of equations, the coefficients are

$$\gamma^+(\lambda) = \frac{\lambda - \lambda_1}{\lambda + \lambda_1} e^{-\lambda h} \quad \text{, and} \tag{2.49}$$

$$\gamma^-(\lambda) = \frac{2\lambda}{\lambda + \lambda_1} e^{-\lambda h} . \tag{2.50}$$

The resulting electromagnetic fields can then be determined by partial differntiation of the total potential $F$

$$E_\varphi = \frac{\partial F}{\partial r} \tag{2.51}$$

$$H_r = \frac{1}{i\omega\mu_0} \frac{\partial^2 F}{\partial r \partial_z} \tag{2.52}$$

$$H_z = -\frac{1}{i\omega\mu_0} \frac{1}{r} \frac{\partial}{\partial r} \left( r \frac{\partial F}{\partial r} \right) \tag{2.53}$$

$$\tag{2.54}$$

for each half-space separately.

### 2.3.6. The potential in the N-layered half-space ($z \geq 0$)

The transition from a homogeneous half-space to a N-layered half-space can be found by calculating the vector potential for each layer separately and applying the continuity conditions at each layer interface. Since there is only a vertical dependence of the conductivity, only $V(z,\lambda)$ of Equation 2.43 needs to be adapted. In each layer

$$V(z,\lambda) = \gamma_n^- \left[ e^{-\lambda_n (z - h_n)} + r_n e^{+\lambda_n (z - h_n)} \right] , \tag{2.55}$$

with

$$\lambda_n = \sqrt{\lambda^2 + i\omega\mu_0\sigma_n} \quad \text{for } h_n \leq z \leq h_{n+1},\ 1 \leq n \leq N \,. \tag{2.56}$$

Thereby, $r_n := \frac{\gamma_n^+}{\gamma_n^-}$ is the amplitude ratio of the downward and upward wave in the layer interface at $z = h_n$.

Defining the admittance

$$B(z,\lambda) = -\frac{\partial_z V(z,\lambda)}{V(z,\lambda)} \tag{2.57}$$

and evaluating Equation 2.57 at the layer boundaries $z = h_n$ and $z = h_{n+1}$ leads to recursive formulation of the admittance for each layer

$$B_n = \lambda_n \frac{B_{n+1} + \lambda_n \tanh(\lambda_n d_n)}{\lambda_n + B_{n+1} \tanh(\lambda_n d_n}, \quad \text{for } n = N-1, \ldots, 1\,,\ B_N = \lambda_N\,. \tag{2.58}$$

For a VMD source on the surface ($h = 0$) the frequency response for the vertical component of the magnetic flux for an N-layered half-space is then (Börner, 2019)

$$B_z(r,z) = \frac{\mu_0 m}{2\pi} \int_0^\infty \frac{\lambda^3}{\lambda + B_1} e^{-B_1 z} J_0(\lambda r) \mathrm{d}\lambda, \quad z \geq 0\,, \tag{2.59}$$

where $B_1$ is the surface admittance. The frequency response can then be back transformed into the time domain by applying the inverse Fourier transform. The corresponding time derivative of the magnetic flux density is then (Börner, 2019)

$$\frac{\partial b_z(r,z)}{\partial t} = \sqrt{\frac{2}{\pi t}} \int_0^\infty \mathrm{Re}(B_z(r,z)) \sqrt{\omega} J_{-1/2}(\omega t) \mathrm{d}\omega \tag{2.60}$$

and can be evaluated using a Fast Hankel Transform (Christensen, 1990).

The electromagnetic fields for realistic transmitter loop setups can be obtained by either applying a Gauß-Legendre quadrature approach (Malecki, 2017) or as a superposition of individual solutions of horizontal electric dipoles (HED) of finite length, which reconstruct the transmitter loop wire exactly (Yogeshwar, 2014).

# 3. Basic concepts of time series analysis

The following chapter provides the reader with the basic concepts of time series analysis with respect to time series distance metrics and cluster analysis. In the first section, an overview of the most common distance metrics for time series is presented, especially dynamic time warping, the autoregressive distance metric based on autoregressive integrated moving average time series models, and the normalized root-mean-square. The second section deals with the basic concepts of cluster analysis using partitioning and hierarchical clustering methods as well as concepts for identifying the optimal number of clusters based on the gap statistic respectively silhouette values. In order to visualize high dimensional data structures, the multidimensional scaling method is applied to reduce the degree of data dimensions.

## 3.1. Time series distance metrics

Repeated measurements taken of the same quantity on the same object will not be the same in general. One reason for this could be variations of the studied object over time, changes to the initial conditions of the surroundings of the studied object, variation of the applied measurement setup or alterations of the measuring device due to technical reasons. In the worst case one has to face all of that at once. Following the terminology of the National Institute of Standards and Technology (Taylor and Kuyatt, 2001);

**Repeatability** is the quantification of the degree of similarity between successive measurements on the same object under identical conditions. An essential precondition for this is the use of the same method, device and observer. The measurements also have to be made over a "short" period at the same location in which the conditions of the subject can considered to be constant. These conditions are called "*repeatability conditions*".

Since similarity is a widely ranged term, there does not seem to be a standard metric to quantify the degree of repeatability. A similarity measure is the relation between time series objects and a scalar number, which represents the degree of similarity between two objects. In general, repeatability can be defined as the maximum similarity between successive measurements. In clinical studies the *Bland-Altman-Method* (Bland and Altman, 1986) is used to quantify the degree of repeatability of medical instruments via evaluating the differences of repeated measurements in dependence of the mean value followed by a regression analysis (e.g. Nelson et al., 2015; Tello et al., 2010). However, the Bland-Altman-Method can only be applied to time series exhibiting a constant mean and only allows conclusions of similarity based on the mean value of two time series. *Dynamic time warping* (DTW) on the other hand is a commonly used technique in various research areas for comparing similarity of time series with different shapes and temporal behavior (Myers et al., 1980). As part of speech recognition techniques, it quickly gained popularity in time series clustering, gesture recognition and signal processing. DTW minimizes effects of time shifting and bias (noise, amplitude shifts) by

aligning time series through elastic transformations between data points (Oates et al., 2001). This allows to detect similar shapes and patterns in time series and can even be applied if the investigated time series have a different amount of data points. A common method to investigate repeatability or similarity in economics is to employ *autoregressive moving average* (ARMA) or *autoregressive integrated moving average* (ARIMA) time series models. The main idea behind time series models is to identify a set of model parameters which represents a data point of the time series by its previous values. A similarity measurement is then applied by evaluating the *autoregressive distance metric* (AR-metric) by comparing the time series model parameters (Maharaj, 1996; Corduas, 2000; Corduas and Piccolo, 2008). With increasing sampling rates and accuracy of measurement equipment in the last years, their outputs can rather be seen as samples of functions or curves. *Functional data analysis* (FDA) (Ramsay and Silverman, 1997) adapts standard statistical methods like the analysis of variance (ANOVA) to a functional approach like the functional analysis of variance (FANOVA) in order to describe and model sets of functional data or curves (Cuevas et al., 2004). In seismics, repeatability between seismic traces is often expressed as a percentage value calculated with the *normalized root-mean-square* (NRMS) (Kragh and Christie, 2002) which is the root-mean-square (RMS) of the differences of the traces divided by the RMS of the input traces.

The method of choice for calculating repeatability, or similarity, depends strongly on the properties of the observed time series. For instance, the Bland-Altman-Method and ARMA time series models can only be used for time series with stationary behavior (constant variation of data points around a mean value), whereas the NRMS distance metric can only be applied to time series exhibiting the same length. In this thesis the Euclidean, dynamic time warping, the autoregressive and normalized root-mean-square distance metrics are investigated, since they seem to be the best promising candidates based on the time series properties of transient electromagnetics as well as software implementation.

### 3.1.1. Dynamic time warping

Classic similarity measures are distance metrics in the Euclidean space. Considering the time series $\vec{X} = \{x_1, x_2, \ldots, x_n\}$ and $\vec{Y} = \{y_1, y_2, \ldots, y_m\}$, the common distance metrics are defined as follows (Merziger and Wirth, 2006):

1. **Euclidean distance**

$$d(\vec{X}, \vec{Y}) = \sqrt{\sum_{i=1}^{k} (x_i - y_i)^2} \tag{3.1}$$

2. **Manhattan distance**

$$d(\vec{X}, \vec{Y}) = \sum_{i=1}^{k} |x_i - y_i| \tag{3.2}$$

3. **Mahalanobis distance**

$$d(\vec{X}, \vec{Y}) = \sqrt{(\vec{X} - \vec{Y})\mathrm{Cov}(\vec{X}, \vec{Y})^{-1}(\vec{X} - \vec{Y})^T}, \tag{3.3}$$

for $k = \min(n, m)$ and $\mathrm{Cov}(\vec{X}, \vec{Y})$ the covariance matrix of $\vec{X}$ and $\vec{Y}$.

Although the distance metrics, defined in the Euclidean space, are very robust and numerically fast, compared to more advanced similarity measures, they exhibit drawbacks and are inappropriate in certain circumstances for similarity determination. These are (Cassisi et al., 2012):

- only time series of the same length can be compared
- no outlier or noise handling
- very sensitive to signal transformation (e.g. shifting, uniform and non-uniform amplitude scaling, uniform time scaling, uniform bi-scaling)

Instead of applying a point-to-point comparison like the classic distance metrics, the DTW method applies a many-to-point respectively a point-to-many comparison to achieve a more robust similarity computation. This mapping technique allows for a better recognition of similar shapes, even if the signals are transformed by shifting or scaling (either in time or amplitude, or both).

Following the formal definition by Müller (2007), the DTW distance $d_{\mathrm{DTW}}(\vec{X},\vec{Y})$ is calculated by first calculating the $n \times m$ local cost matrix $\mathbf{C}$ (Figure 3.1 left) with

$$\mathbf{C}(i,j) = d(x_i, y_j) \quad \text{for } i = 1,\ldots,n\,, j = 1,\ldots,m \tag{3.4}$$

Usually the local cost function $d(x_i, y_j)$ is defined as the squared difference $(x_i - y_j)^2$ or the absolute value of the difference $|x_i - y_j|$. However, other metrics are possible as well and depend on the specifications of the problem (Berndt and Clifford, 1994). The mapping between $\vec{X}$ and $\vec{Y}$ is called the warping path

$$\vec{W} = \{w_1, w_2, \ldots, w_L\} \quad \max(n,m) \leq L \leq m+n-1. \tag{3.5}$$

It is a contiguous set of matrix elements where the $\ell$'th element of $\vec{W}$ is defined as $w_\ell = (i,j)$ and corresponds to an alignment between $x_i$ and $y_j$. The warping path $\vec{W}$ is subject to the following restrictions given the elements $w_\ell = (i,j)$ and $w_{\ell-1} = (i',j')$ (Keogh and Ratanamahatana, 2005).

- **Boundary conditions:** $w_1 = (1,1)$ and $w_L = (n,m)$
- **Monotonicity condition:** $i - i' \geq 0$ and $j - j' \geq 0$
- **Continuity condition:** $i - i' \leq 1$ and $j - j' \leq 1$

The boundary condition ensures that the start, respectively end of the warping path is defined by the first and last data point of $\vec{X}$ and $\vec{Y}$. The continuity condition prohibits jumps along the warping path and thus, ensures every data point is taken into account in the calculation. Furthermore, the monotonicity ensures that each data point is mapped to either the present or a future data point (we cannot go back in time). The DTW problem is then defined by finding a warping path $\vec{W}$ in the local cost matrix $\mathbf{C}$ so that the alignment costs are minimal. That is,

$$\mathrm{DTW}(\vec{X},\vec{Y}) = \min\left(\sqrt{\sum_{\ell=1}^{L} w_\ell}\right) \tag{3.6}$$

This can be recursively obtained by calculating the accumulated cost matrix (Figure 3.1 right)

$$\mathbf{D}(i,j) = d(x_i, y_j) + \min(\mathbf{D}(i-1, j-1), \mathbf{D}(i-1, j), \mathbf{D}(i, j-1)) \tag{3.7}$$

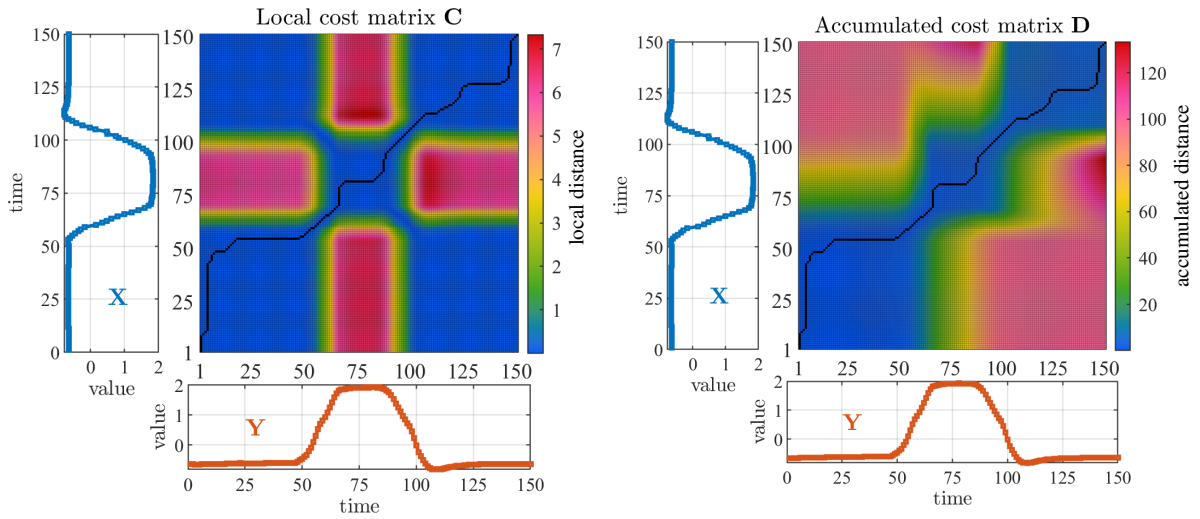


**Fig. 3.1.:** Calculated local cost matrix **C** (left) with squared differences as local cost function and unconstrained accumulated cost matrix **D** (right) for time series $\vec{X}$ and $\vec{Y}$. Blue colors indicate regions with low costs, whereas red colors mark regions with high costs. The warping path $\vec{W}$ is marked as black cells (cf. Figure 3.3(b)).

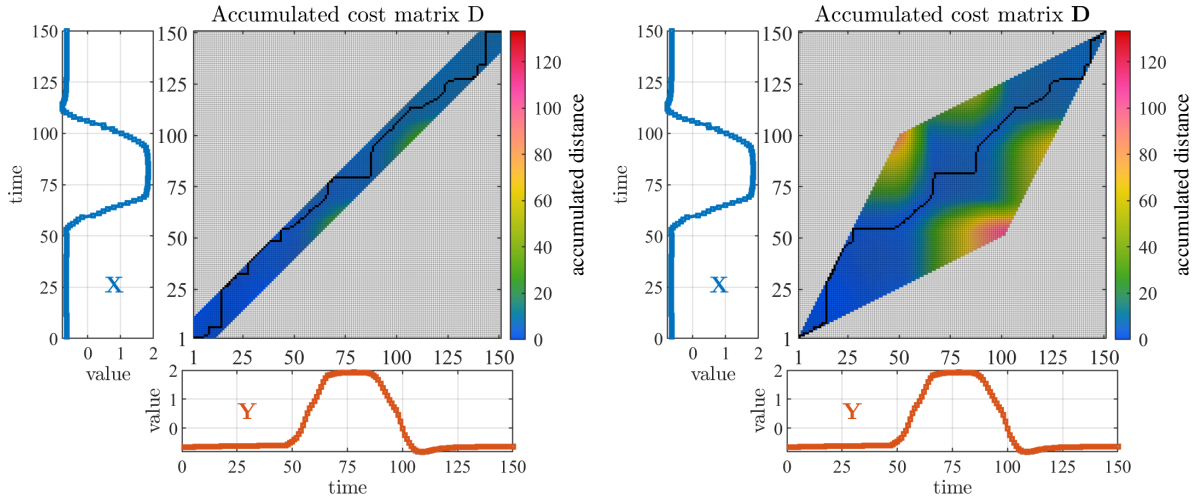


**Fig. 3.2.:** Sakoe-Chiba band restricted (left) and Itakarua restricted (right) accumulated cost matrix **D** and warping path $\vec{W}$ marked as black cells (cf. Figure 3.3(c) and 3.3(d)).

for $i = 1,\ldots,n$ and $j = 1,\ldots,m$. **D** is initialized as an $n \times m$ matrix with $\mathbf{D}(i,j) = \infty$ and $\mathbf{D}(0,0) = 0$. The DTW distance is then defined by

$$d_{\mathrm{DTW}}(\vec{X},\vec{Y}) = \mathbf{D}(n,m)\,. \tag{3.8}$$

The optimal warping path can then be found by backtracking through the accumulated cost matrix starting with $w_L = (n,m)$. The corresponding elements of the warping path are then defined as

$$w_{\ell-1} := \begin{cases} (1, j-1), & \text{if } n = 1 \\ (i-1, 1), & \text{if } m = 1 \\ \operatorname{argmin} \begin{cases} \mathbf{D}(i-1, j-1) \\ \mathbf{D}(i-1, j) \\ \mathbf{D}(i, j-1)) \end{cases} & \text{otherwise.} \end{cases} \tag{3.9}$$

By applying global constraints to the warping path $\vec{W}$ of the DTW, the computational time and required storage space can be reduced drastically. Global constraints limit the possible warping path to a limited window, called the warping window. The most common applied global constraints are the Sakoe-Chiba band constraint (Sakoe and Chiba, 1978) and the Itakaru (Itakura, 1975) parallelogram (Figure 3.2). For example, the Sakoe-Chiba band constraint applies a symmetric warping window in **D** of width $T$ reducing the overall computational cost. The warping window also prevents distorted mapping, where small sections of one sequence are mapped to a large section of the other (Figure 3.3(b))(Keogh and Ratanamahatana, 2005). However, the *optimal* warping path $\vec{W}$ can still lie outside of the warping window. Therefore, applying global constraints is a trade-off between the DTW calculation speed and the accuracy of similarity detection.

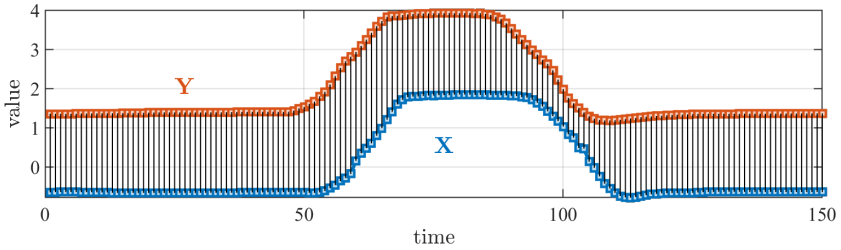


(a) Euclidean distance

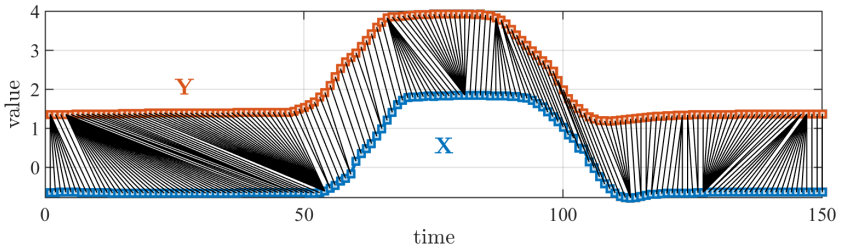


(b) Dynamic time warping - classic

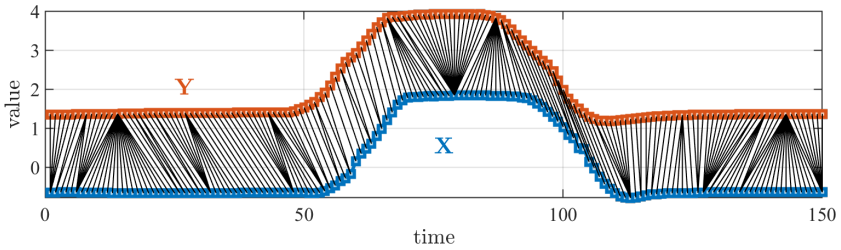


(c) Dynamic time warping - Sakoe-Chiba restricted

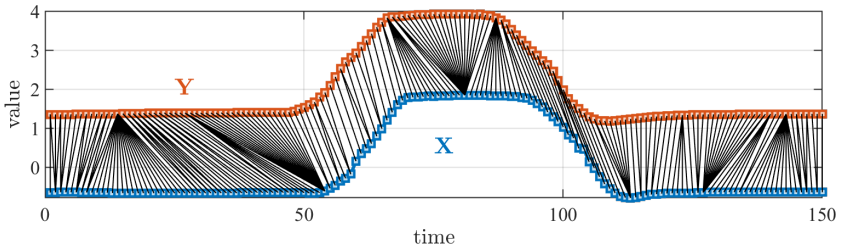


(d) Dynamic time warping - Itakura restricted

**Fig. 3.3.:** Comparison of Euclidean distance mapping (a), unrestricted (b), Sakoe-Chiba restricted (c) and Itakura restricted (d) dynamic time warping mapping technique. For illustration purposes, a constant amplitude offset of 2 was added to the time series $\vec{Y}$ after calculation.

### 3.1.2. ARIMA time series models

While DTW measures the similarity of time series by detecting similar shapes through elastic transformations, ARIMA time series models are used to investigate the dependent structure of time series by applying stochastic and dynamic models in order to model the behavior of time series without knowing the underlying dependency. These models can be used to forecast future values of a certain quantity based on current and past data points or to investigate seasonal effects of time series (e.g., market prices, airline passenger count). The similarity between two time series can then be found by comparing the model parameters of the estimated time series models using the autoregressive distance metric (AR-metric).

For univariate time series (i.e., dependency on only one variable) an extensive variety of linear time series models exists. For instance,

- Autoregressive Models (AR)
- Moving Average Models (MA)
- Autoregressive Moving Average Models (ARMA)
- Autoregressive Integrated Moving Average Models (ARIMA)
- Seasonal Autoregressive Integrated Moving Average Models (SARIMA)
- Autoregressive Fractionally Integrated Moving Average Models (ARFIMA)

This thesis focuses exclusively on AR, MA, ARMA and ARIMA models, since transient electromagnetic responses neither exhibit seasonal nor fractional patterns.

Following the formal notation of Box and Jenkins (Box et al., 2008), let $\vec{X} = \{x_1, x_2, x_3, \ldots, x_n\}$ be a discrete series of length $n$ equally spaced in time. For later use, the following concepts are introduced.

1. **The backshift (alias Lag) operator** is defined as

$$Bx_t = x_{t-1} \tag{3.10}$$

and maps the value of $\vec{X}$ at time index $t$ to the value of $\vec{X}$ at time index $t-1$, and in general, the m'th power of $B$ maps the value of $\vec{X}$ at time index $t$ to the value of $\vec{X}$ at time index $t-m$

$$B^m x_t = x_{t-m}\,.$$

2. **The difference operator** is defined as

$$\nabla x_t = (1-B)x_t = x_t - Bx_t = x_t - x_{t-1} \tag{3.11}$$

and yields the first order difference of the time series $\vec{X}$. In general, $\nabla^d$ yields the d'th difference of $\vec{X}$

$$\nabla^d x_t = (1-B)^d x_t\,. \tag{3.12}$$

For example, the second order difference is then,

$$\nabla^2 x_t = (1-B)^2 x_t = (1-2B+B^2)x_t = x_t - 2x_{t-1} + x_{t-2}\,. \tag{3.13}$$

3. **Stationarity**:
   A time series is *strictly* stationary if the joint distribution

$$F_{\vec{X}_t,\vec{X}_{t+k}} = F_{\vec{X}_t,\vec{X}_{t+k+r}} \; \forall\, k > 0, r > 0 \text{ and } k, r \in \mathbb{N}, \tag{3.14}$$

   where $\vec{X}_t = \vec{X}$ and $\vec{X}_{t+k}$ is the lagged version of $\vec{X}$. That is, the joint distribution $F$ of $(\vec{X}_t, \vec{X}_{t+k})$ is identical to $(\vec{X}_t, \vec{X}_{t+r})$ and therefore time independent.
   A time series is *weakly* stationary if the mean of $\vec{X}$

$$E(\vec{X}) = \bar{X} = \mu$$

   is time independent and the covariance

$$\mathrm{Cov}(\vec{X}_t, \vec{X}_{t+k}) = \gamma_k$$

   is identical for each time interval $k$. In other words, the values of $\vec{X}$ scatter around a constant mean $\mu$ with variance $\mathrm{Var}(\vec{X}) = \sigma^2$.

4. **The Autocorrelation function (ACF)** is a measure for "non-randomness" of a time series (NIST/SEMATECH, 2003). It is a correlation between a time series $\vec{X}$ and it's lagged version $\vec{X}_{t+k}$. If autocorrelation is present, the values of the time series can be expressed by the lagged values and hence a dependent structure is present. The autocorrelation coefficients $\rho_k$ can be calculated by

$$\rho_k = \frac{\mathrm{Cov}(\vec{X}_t, \vec{X}_{t+k})}{\mathrm{Var}(\vec{X}_t)} = \frac{\sum_{i=1}^{N-k}(x_i - \bar{X})(x_{i+k} - \bar{X})}{\sum_{i=1}^{N-k}(x_i - \bar{X})} \quad -1 \leq \rho \leq 1\,, \tag{3.15}$$

   with $\rho_0 = 1$ since the time series is perfectly correlated with itself at lag $k = 0$. If $\rho_k = -1$, the time series is perfectly negatively correlated at lag $k$. The standard deviation of the ACF coefficients is given by

$$\mathrm{std}(\rho_k) = \sqrt{\frac{1}{N}\left(1 + 2\sum_{i=1}^{j}\rho_i^2\right)} \qquad \text{for } k > j \tag{3.16}$$

   and is used for calculating the confidence intervals of the ACF. For a non-stationary time series, the ACF coefficients are slowly decaying, indicating a trend or a seasonal component. In the Box-Jenkins approach for ARIMA modeling, the ACF is a commonly used tool for identifying the degree of the underlying MA operator of a stationary time series (Box et al., 2008).

5. **The partial autocorrelation function (PACF)** describes the correlation between the time series $\vec{X}_t$ and its lagged version $\vec{X}_{t+k}$ where the correlation of in-between values $\vec{X}_{t+1}$ to $\vec{X}_{t+k-1}$ is removed. The partial autocorrelation coefficients are obtained by the Durbin recursion formula (Durbin, 1960)

$$\phi_{kk} = \frac{\rho_k - \sum_{j=1}^{k-1}\phi_{k-1,j}\rho_{k-1}}{1 - \sum_{j=1}^{k-1}\phi_{k-1,j}\rho_j}, \tag{3.17}$$

   with $\phi_{00} = 1$ and $\phi_{11} = \rho_1$. In analogy to the ACF, the PACF is a commonly used tool for identifying the degree of the underlying AR operator of a stationary time series (Box et al., 2008). Hence, applying the PACF to a non-stationary time series yields no meaningful information.

### The generalized ARIMA time series model

An autoregressive integrated moving average time series model combines the autoregressive model and the moving average model for non-stationary time series. Based on the previous definitions of the operator, an ARIMA process of order (p,d,q) is defined as

$$\varphi(B)x_t = \phi(B)\nabla^d x_t = \theta(B)a_t \tag{3.18}$$

with

$$\phi(B) = 1 - \phi_1 B - \phi_2 B^2 - \cdots - \phi_p B^p,$$
$$\theta(B) = 1 - \theta_1 B - \theta_2 B^2 - \cdots - \theta_q B^q.$$

$\phi(B)$ is called the *autoregressive* operator of order $p$ which describes the current value of $\vec{X}$ as a finite, linear weighted sum of previous values of $\vec{X}$ so that

$$x_t = \phi_1 x_{t-1} + \phi_2 x_{t-2} + \cdots + \phi_p x_{t-p} + a_t. \tag{3.19}$$

Furthermore, $\theta(B)$ is called the *moving average* operator of order $q$ and adequately to Equation 3.19, the current value of $\vec{X}$ can be expressed as a finite weighted sum of random "shocks" $a$ so that

$$x_t = a_t - \theta_1 a_{t-1} - \theta_2 a_{t-2} - \cdots - \theta_q a_{t-q}. \tag{3.20}$$

A "shock" is a random drawing from a fixed distribution, usually a white noise process. $\varphi(B)$ is called the generalized autoregressive operator. By applying the *backward difference* operator $\nabla^d$ to the time series $\vec{X}$, the stationarity, by differencing the time series $d$ times, is ensured. If $d = 0$ the ARIMA model becomes the autoregressive moving average model (ARMA).

### The Box-Jenkins approach for ARIMA modelling

The Box-Jenkins approach is a well-established process for ARIMA modeling in order to identify ARIMA time series model parameters (Figure 3.4). It is a three stage process consisting of *model identification*, *model estimation* and *model verification*.

**Model identification:**
The first stage of model identification is the determination of the degree $d$ of the backward difference operator $\nabla^d$ in order to achieve a stationary time series. Box et al. (2008) state, that stationarity can be achieved by differencing a non-stationary time series $d$ times. A visual inspection of the ACF-plot helps to identify if a time series is stationary. The time series is non-stationary if the ACF-coefficients die out slowly with a linear or exponential trend. However, if the ACF-coefficients die out quickly and are close to zero after a certain lag $k$, the time series is considered to be stationary. A more sophisticated approach are statistical tests for *unit-roots* like the Dickey-Fuller test (Dickey and Fuller, 1979) or the Kwiatkowski, Phillips, Schmidt, Shin test (Kwiatkowski et al., 1992). If a unit-root exists, the time series is non-stationary (see Appendix A.1).

Once stationarity is assured, the second step of the Box-Jenkins approach is to validate the model parameters of the resulting stationary ARMA(p,q) process. Therefore, the autocorrelation function and the partial autocrorrelation function are used to identify the degree $p$ of the

autoregressive operator and the degree $q$ of the moving average operator. The degree $q$ is chosen if the autocorrelation function cuts off at lag $q+1$ and the degree $p$ is chosen if the partial autocorrelation function cuts off at lag $p+1$ (Box et al., 2008). However, these techniques are only suitable for pure autoregressive or moving average models. For mixed models, the ACF and PACF are harder to interpret and do not necessarily help in the identification process (Brockwell and Davis, 1991). Instead, a direct search approach for $p$ and $q$ is used so that the Akaike-Information-Criterion (AIC)

$$AIC_{p,q} = -2\log(L) + 2r \tag{3.21}$$

or the Bayesian-Information-Criterion (BIC)

$$BIC_{p,q} = -2\log(L) + r \cdot \log(n)\,, \tag{3.22}$$

where $r = p+q+1$, $L$ is the maximum likelihood and $n$ the length of the time series, is minimal. The second term in Equation 3.21 and 3.22 penalizes the estimated maximum likelihood with the number of chosen model parameters in order to avoid overfitting. In contrast to the AIC, the BIC also takes the length of the time series into account. Hence, the time series model with the smallest of either criterion is preferred.

**Model estimation:**
If all three parameters are defined, the ARIMA model is estimated by a least squares or maximum likelihood estimator. A detailed explanation about the estimation process will not be discussed in this thesis since it is beyond the scope. However, a very brief explanation of the maximum likelihood estimation is given in appendix A.4. Detailed explanations are given in several books on time series theory like Tsay (2010), Brockwell and Davis (1991), Box et al. (2008) or Neusser (2016). A variety of software packages exists to estimate ARIMA model parameters, by minimizing the AIC or BIC, like R, Matlab®, Python or SPSS.

**Model verification:**
The third step of the Box-Jenkins approach is model verification. The residuals between the fitted model and the actual time series should be uncorrelated. If the residuals are correlated, the model does not represent the time series accurately. This can be tested by utilizing the Ljung-Box test (see Apendix A.2). If the residuals are correlated (not looking like white noise) an adaptation to the parameters $p$ and $q$ has to be made and the model needs to be estimated again. Especially for mixed models (ARMA) the initial estimation process for $p$ and $q$ can be very difficult. In order to avoid over-fitting it is recommended to use an information-based criteria like the AIC or BIC (Equation 3.21, 3.22).

### The Autoregressive Distance Metric

In order to measure the distance or similarity between two time series or their corresponding ARIMA(p,d,q) processes, Piccolo (1990) provided the Euclidean distance metric

$$d_{\mathrm{AR}}(\vec{X},\vec{Y}) = \sqrt{\sum_{i=1}^{k} (\pi_{x_i} - \pi_{y_i})^2} \tag{3.23}$$

based on the $k$ truncated $\pi$ weights of the AR($\infty$) representation. Any ARIMA(p,d,q) model (Equation 3.18) can be transformed to an infinite autoregressive process AR($\infty$) (see Appendix A.3)

$$\pi(B)x_t = a_t\,, \tag{3.24}$$

where

$$\pi(B) = \varphi(B)\theta^{-1}(B) = \phi(B)\nabla^d\theta^{-1}(B)\,. \tag{3.25}$$

Since the classical properties of a distance metric, i.e non-negativity, symmetry and triangularity, are satisfied, $d_{\mathrm{AR}}(\vec{X},\vec{Y})$ always exists between two ARIMA processes. The $\pi$-weights can be calculated after Box et al. (2008) recursively through

$$\pi_j = \theta_1\pi_{j-1} + \theta_2\pi_{j-2} + \cdots + \theta_q\pi_{j-q} + \varphi_j \quad j > 0, \tag{3.26}$$

where $\pi_0 = -1$, $\pi_j = 0$ for $j < 0$ and $\varphi_j = 0$ for $j > p+d$.

The AR-metric is widely used for clustering time series, especially in economics. For further examples see Corduas and Piccolo (2008), Kardiyen and Güney (2015) or Umberto (2004).

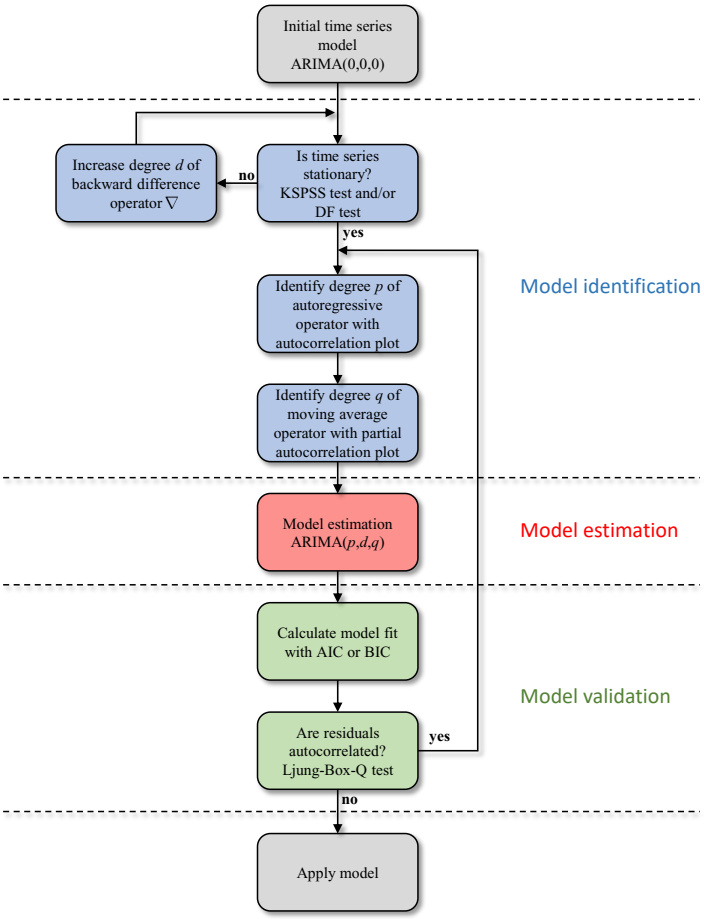


**Fig. 3.4.:** Overview of Box-Jenkins approach for model identification (blue), model estimation (red) and model validation (green) for non-stationary time series.

### 3.1.3. Normalized root-mean-square

Another non-model based approach for identifying similarity between time series is the normalized root-mean-square metric (NRMS), which is extensively used in seismic monitoring experiments (Kragh and Christie, 2002). The NRMS metric between two time series (seismic traces) $\vec{X}$ and $\vec{Y}$ is defined as the root-mean-square (RMS) of the difference between $\vec{X}$ and $\vec{Y}$ divided by the sum of the RMS of $\vec{X}$ and $\vec{Y}$,

$$\mathrm{NRMS} = \frac{200 \cdot \mathrm{RMS}(\vec{X} - \vec{Y})}{\mathrm{RMS}(\vec{X}) + \mathrm{RMS}(\vec{Y})}, \tag{3.27}$$

where RMS is the root-mean-square operator defined as

$$\mathrm{RMS}(\vec{X}) = \sqrt{\frac{\sum_{i=1}^{n} x_i^2}{n}}, \tag{3.28}$$

and $n$ the sample length. The values of the NRMS are expressed as a percentage value, ranging from 0% to 200%. Lower values thereby indicate higher similarity between two time series.

Typical values of the NRMS in marine seismic measurements range from 18 % to 30 % (Kragh and Christie, 2002) whereas Ziolkowski et al. (2010) achieved averaged NRMS values of 3.9 % to 11.9 % for a marine multi-transient electromagnetic survey.

## 3.2. Cluster analysis

The main goal of monitoring studies is to identify those groups or clusters of objects under investigation that exhibits a certain degree of similarity (or dissimilarity). These clusters can then be related to certain events occurring during a monitoring. Cluster analysis is a common tool to identify those groups based on the similarity measurements provided to the algorithm. The definition of similarity is thereby subject to technical points of view and depends on the object to be examined.

### 3.2.1. Clustering methods and algorithms

A wide variety of clustering types exists, including *partitioning clustering* and *hierarchical clustering*.

Let $\mathbf{X}$ be a data matrix,

$$\mathbf{X} = \{\vec{x}_1, \vec{x}_2, \ldots, \vec{x}_n\} \tag{3.29}$$

where $\vec{x}_i$ represents the data vector of the i-th observation. Then the pairwise Euclidean distance matrix $\mathbf{D}$ is defined as

$$\mathbf{D}_{ij} = d_{ij} = ||\vec{x}_i - \vec{x}_j||^2 \quad i, j = 1, \ldots, n\,. \tag{3.30}$$

The distance matrix $\mathbf{D}$ serves as an input for most of the clustering algorithms (Maharaj et al., 2019). Depending on the clustering algorithm, the pairwise distance function $d_{ij}$ can be any metric (e.g., DTW, AR-metric) and hence, the observations $\vec{x}_i$ and $\vec{x}_j$ do not necessarily have to be of same length.

**Partitioning clustering** methods split a data set into $k$ clusters were the number of clusters is predefined by the user. Popular candidates are the k-means and the k-medoid algorithm, which are both centroid (cluster center) based methods. An overview of the algorithms is given in Table 3.1. The first step is to decide the number of clusters into which the data should be partitioned. This can be done by visual inspection of the data set or on any other predefined criterion. In the next step, the $k$ centroids of the clusters are initialized (randomly if necessary). The observations are assigned to a cluster, based on the minimal distance between the observations and the centroids. The centroids are then recalculated by the mean of the observations, representing the cluster. In an iterative process, the observations are reassigned to a cluster with respect to the new defined centroids in the previous step (Figure 3.5). The main difference between the k-means and the k-medoids algorithm is the definition of the centroids. Since the k-means algorithm is based on the Euclidean distance, the centroids are defined by the mean of the observations in the clusters. Instead, a centroid in the k-medoid algorithm is a "representative observation", which is the object for which the average distance to all other observations is minimal, and is called medoid (Kaufmann and Rousseeuw, 1987). The k-means and k-medoid algorithm are easy to implement and an object can be reassigned to a different cluster once the centroids/medoids are recomputed. However, both algorithms have a huge disadvantage. The result is highly dependent on the initial seed of the centroids/medoids. Babu and Murty (1993) address this issue by using generic algorithms in order to find the optimal initial seed values.

**Tab. 3.1.:** Outline of the k-means/ k-medoid clustering algorithm.

**K-means/K-medoid clustering algorithm**

1. Decide on a value for $k$.
2. Initialize the $k$ cluster centroid/medoid (randomly, if necessary).
3. Decide the class memberships $C$ of the $n$ objects by assigning them to the nearest cluster centroid $\vec{m}_j, j = 1,\ldots,k$ by

$$\begin{aligned} C(i) &= \underset{1\le j\le k}{\operatorname{argmin}} ||\vec{x}_i - \vec{m}_j||_2, \\ \text{where } \vec{m}_j &= \frac{1}{n_{C_j}} \sum_{\ell=1}^{n_{C_j}} \vec{x}_\ell \end{aligned} \tag{3.31}$$

   respectively closest medoid by

$$\begin{aligned} C(i) &= \underset{1\le j\le k}{\operatorname{argmin}}\, \mathbf{D}(\vec{x}_i, \vec{m}_j), \\ \text{where } \vec{m}_j = \vec{x}_{i_j^\star} \text{ and } i_j^\star &= \operatorname{argmin} \sum_{\ell\in C(j)} \mathbf{D}(\vec{x}_i, \vec{x}_\ell) \end{aligned} \tag{3.32}$$

4. Reestimate the $k$ cluster centroids/medoids by assuming the memberships found above are correct.
5. If none of the objects changed membership in the last iteration, exit. Otherwise, repeat step three and four.

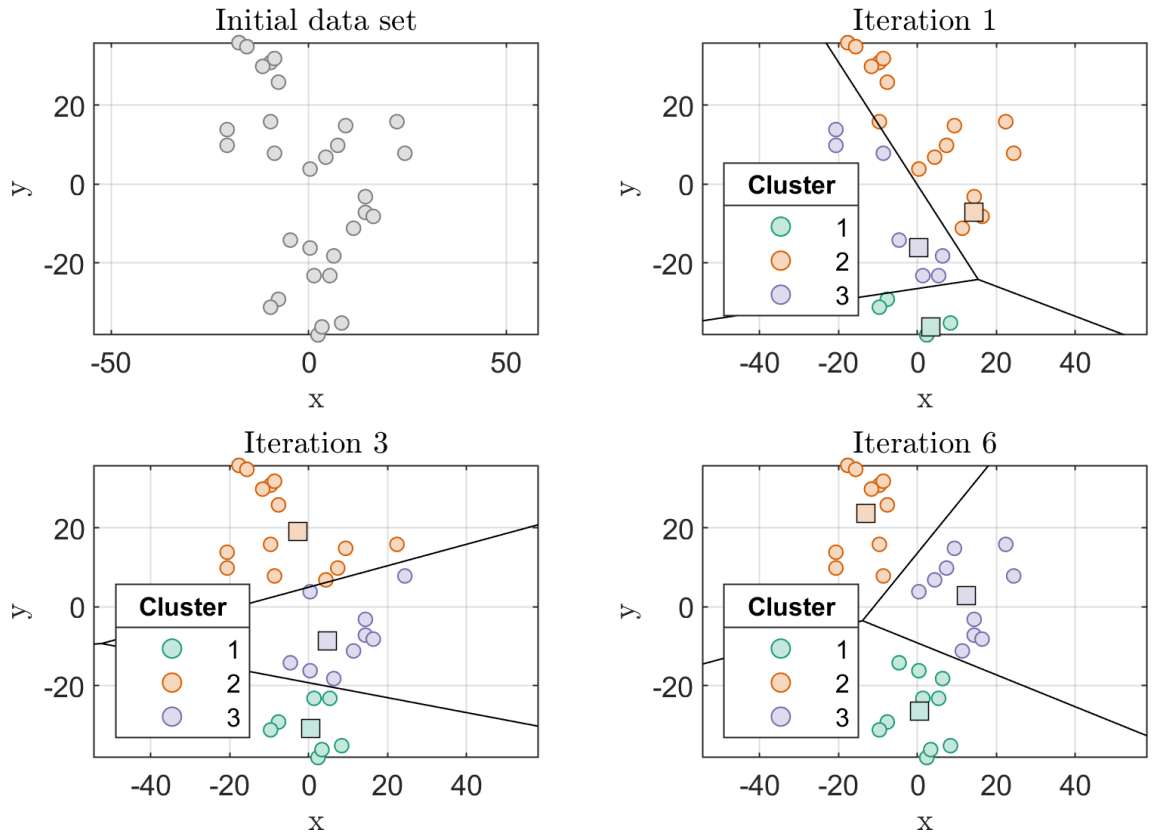


**Fig. 3.5.:** Iterative cluster forming by the k-means algorithm for the initial data set in gray (top left). Circles mark data points, squares mark centroids of the color-coded clusters.

Since the centroids of the k-means algorithm are based on the average of the observations assigned to each cluster, the k-means algorithm is strictly applicable for the Euclidean distance metric and cannot be used with other arbitrary distance metrics like DTW or the AR-metric. For illustration purposes, let $\vec{X}$ and $\vec{Y}$ be two identical time series (e.g. sine waves). Furthermore, let time series $\vec{Y}$ be shifted in time by $\pi$. The DTW algorithm would align both perfectly and hence classifying both as similar (independently of the amount of time shift), resulting in a DTW distance of 0. The recalculated centroid of this cluster would yield a null vector since both time series cancel each other out. Therefore, a medoid based algorithm or hierarchical clustering method would be recommended since these methods are more flexible with respect to arbitrary distance metrics.

**Hierarchical clustering** methods, in contrast to partitioning clustering methods, do not depend on the initial choice of the number of clusters. Instead, a hierarchical data representation is constructed in which each cluster at each level is represented by the closest clusters at the previous lower level. Hierarchical clustering methods can be split into the agglomerative and divisive scheme. In the divisive approach (top-down) all observations are assigned to one cluster during the initialization step. This cluster is then split into separate clusters in each iteration according to a similarity criterion until no change in cluster separation is observed (Figure 3.6(b)). In opposite to the divisive approach, the agglomerative approach (bottom-up) assigns each observation into a separate cluster in the initialization step and combines similar clusters in each iteration according to a similarity criterion until all observations are represented by a single cluster (Figure 3.6(a) and Table 3.2). Both approaches result in a tree-like structure with $n-1$ hierarchical levels where the leave nodes represent single observations and branches forming

**Tab. 3.2.:** Outline of the agglomerative hierarchical clustering algorithm.

| **Agglomerative hierarchical clustering algorithm** |
|---|
| **1.** Calculate the distance between all objects. Store the results in a distance matrix. |
| **2.** Assign each observation to a single random cluster |
| **3.** Search through distance matrix and find the two most similar clusters/objects based on minimum distance. |
| **4.** Join the two clusters/objects to produce a cluster that now has at least two objects. |
| **5.** Update the matrix by calculating the distances between the newly formed cluster and the remaining clusters/objects. |
| **6.** Repeat step two until all instances form one cluster. |
| **7.** Choose number of clusters by visual inspection of the dendrogram |

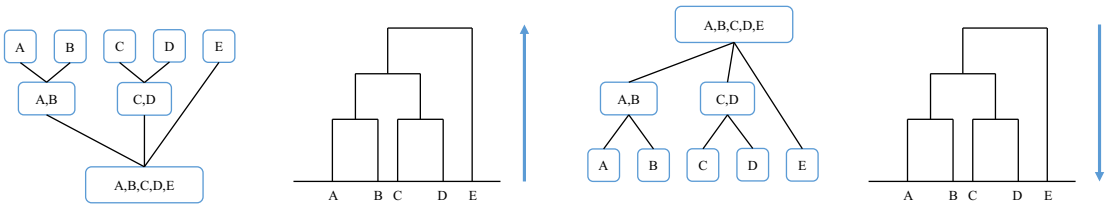


(a) Agglomerative hierarichal clustering scheme (b) Divisive hierarichal clustering scheme

**Fig. 3.6.:** Illustration of the agglomerative (left) and divisive (right) hierarchical clustering scheme for five observation from A to E (after Sembiring et al., 2011).

the clusters. This hierarchical tree $L$ can effectively be visualized with dendrogram plots (Figure 3.6(a), right). The main disadvantage of hierarchical clustering methods are the irreversible assignment process. If an object is assigned to a group, it cannot be reassigned. According to Hastie et al. (2009), the divisive clustering approach has not been studied as extensively as the agglomerative approach and due to the shorter time complexity, better accuracy (Camargos et al., 2016) and due to the wide availability in software packages, the agglomerative clustering method will be used in this thesis. As illustrated in Figure 3.6(a), the first step of the agglomerative clustering method is to assign each observation to a single cluster. In the second step, the closest two clusters are merged into a single cluster, reducing the number of clusters by one in each iteration. To combine the individual clusters, a distance criterion has to be chosen. The three most common criteria are (Hastie et al., 2009):

1. **Single linkage**: The single linkage criterion combines the clusters A and B by the minimal intergroup distance (nearest neighbor),

$$d_{SL}(A,B) = \min_{\substack{\vec{x}_i \in A \\ \vec{x}_j \in B}} d(\vec{x}_i, \vec{x}_j)\,. \tag{3.33}$$

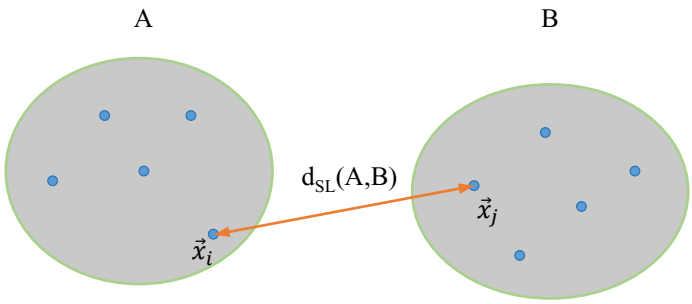


2. **Complete linkage**: The complete linkage criterion combines the clusters A and B by the maximal intergroup distance (farthest neighbor),

$$d_{CL}(A,B) = \max_{\substack{\vec{x}_i \in A \\ \vec{x}_j \in B}} d(\vec{x}_i, \vec{x}_j)\,. \tag{3.34}$$

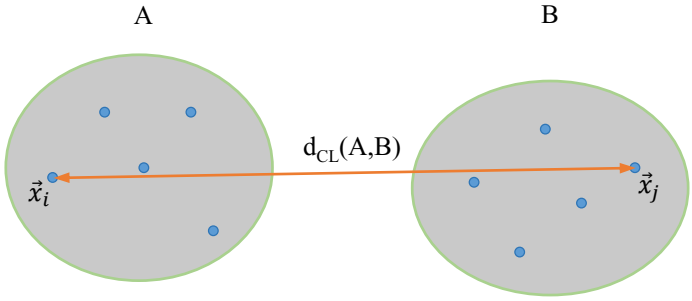


3. **Group Average linkage**: The group average linkage criterion combines the clusters A and B by the average intergroup distance,

$$d_{GAL}(A,B) = \frac{1}{N_A N_B} \sum_{\substack{\vec{x}_i \in A \\ \vec{x}_j \in B}} d(\vec{x}_i, \vec{x}_j)\,. \tag{3.35}$$

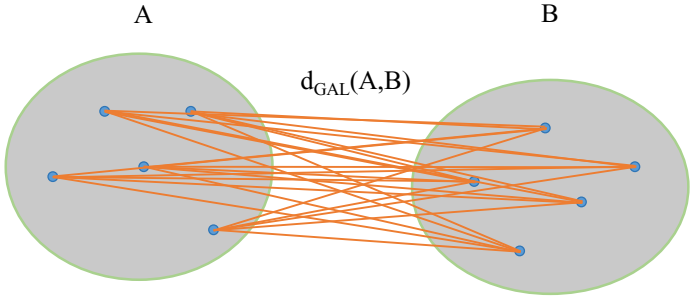

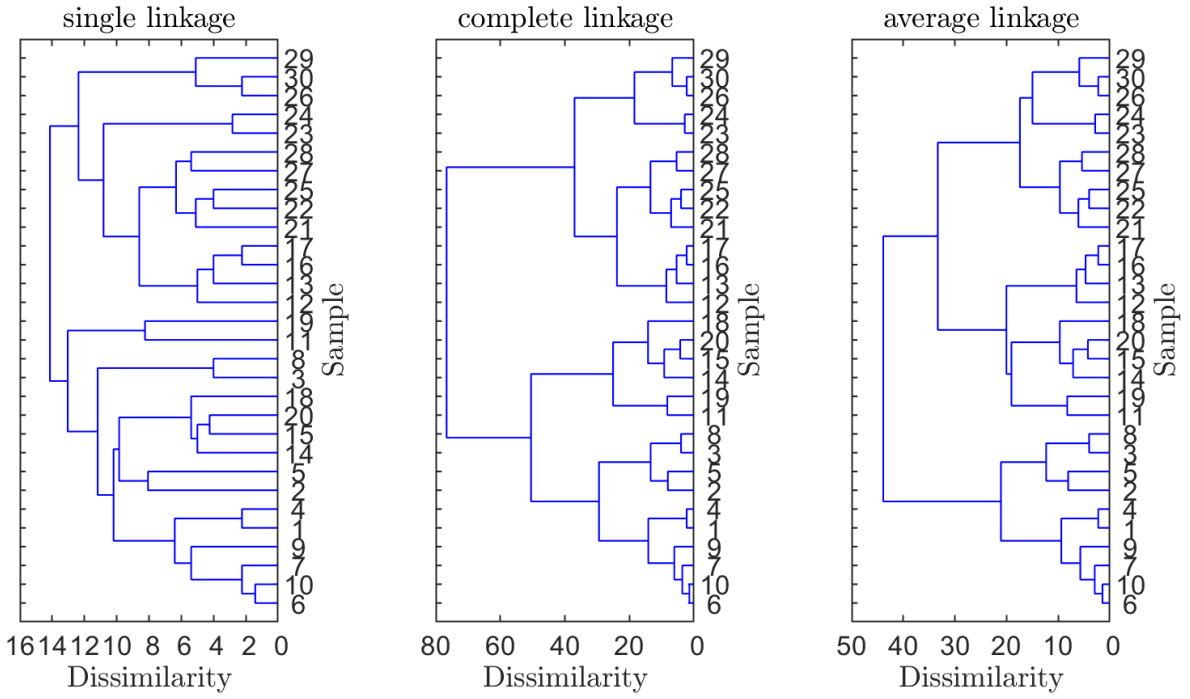


**Fig. 3.7.:** Illustration of different hierarchical clustering trees, represented by dendrogram plots, as result of the single (left), complete (middle) and average (right) linkage criterion for the example data set shown in Figure 3.5.

Figure 3.7 shows different hierarchical clustering trees as a result of different linkage criteria. In this thesis, the complete linkage criterion is used since it does not introduce an assumed similarity based on the shortest distance and therefore it is a far more conservative approach compared to the single and average group linkage criterion. Furthermore, the resulting clusters are much more compact compared to the single linkage criterion. A detailed example of the agglomerative clustering method is provided in Appendix A.5.1.

### 3.2.2. Multidimensional Scaling

Since dendrograms are used to illustrate the hierarchical dependency of cluster trees as an outcome of hierarchical cluster algorithms, it can be very difficult to visualize the actual cluster distribution among observations. Multidimensional scaling (MDS) is a technique of multivariate statistics which allows to map objects of an $\mathbb{R}^p$ space to $\mathbb{R}^q$ with $q \ll p$. This allows, for instance, to investigate dependent structures in similarity matrices like pairwise distance measurements among time series or multivariate data sets. It also supports the visualization of clustering results especially when arbitrary metrics are involved. The input of MDS are pairwise distance measurements between observations. The output of an MDS is a spatial layout, in which the data is represented as points. These points are arranged in such a way that the pairwise distances in the spatial representation are maintained with respect to the pairwise distances according to the similarity matrix. Hence, similar objects are mapped closer together than dissimilar objects.

Following the formal notation of Borg and Groenen (1997), given the data matrix $\mathbf{X} = \{\vec{x}_1, \vec{x}_2, \ldots, \vec{x}_n\}$, $\vec{x}_i \in \mathbb{R}^d$ of $n$ points in a $d$-dimensional Euclidean space. The squared Euclidean distance be-

tween $\vec{x}_i$ and $\vec{x}_j$ is then

$$\begin{aligned} d_{ij} &= ||\vec{x}_i - \vec{x}_j||^2 \\ &= (\vec{x}_i - \vec{x}_j)^\top (\vec{x}_i - \vec{x}_j) \\ &= \vec{x}_i^\top \vec{x}_i - 2\vec{x}_i^\top \vec{x}_j + \vec{x}_j \vec{x}_j. \end{aligned} \tag{3.36}$$

leading to the pairwise squared distance matrix

$$\begin{aligned} \mathbf{D}^{(2)} &= \vec{1}\mathrm{diag}(\mathbf{X}^\top\mathbf{X})^\top - 2\mathbf{X}^\top\mathbf{X} + \mathrm{diag}(\mathbf{X}^\top\mathbf{X})\vec{1}^\top \\ &= \vec{1}\mathrm{diag}(\mathbf{B})^\top - 2\mathbf{B} + \mathrm{diag}(\mathbf{B})\vec{1}^\top \end{aligned} \tag{3.37}$$

where $\vec{1}$ is a column vector containing all ones, $\mathrm{diag}(\mathbf{B})$ denoting the main diagonal of $\mathbf{B}$ and for convenience $\mathbf{B} = \mathbf{X}^\top\mathbf{X}$.

The main idea behind MDS is to reconstruct the coordinate matrix $\mathbf{X}$ from the given distance matrix $\mathbf{D}$ for any given metric. MDS takes advantage of the fact that $\mathbf{X}$ can be derived by eigenvalue decomposition of a scalar product matrix $\mathbf{B} = \mathbf{X}^\top\mathbf{X}$. Substituting $\vec{c} = \mathrm{diag}(\mathbf{B})$ and applying the *centering matrix* $\mathbf{J} = \mathbf{I} - n^{-1}\vec{1}\vec{1}^\top$, with $\mathbf{I}$ the Identity matrix, to both sides of Equation 3.37 and multiplying by $-\frac{1}{2}$ yields

$$\begin{aligned} -\frac{1}{2}\mathbf{J}\mathbf{D}^{(2)}\mathbf{J} &= -\frac{1}{2}\mathbf{J}(\vec{1}\vec{c}^\top - 2\mathbf{B} + \vec{c}\vec{1}^\top)\mathbf{J} \\ &= -\frac{1}{2}\mathbf{J}\vec{1}\vec{c}^\top\mathbf{J} - \frac{1}{2}\mathbf{J}\vec{c}\vec{1}^\top\mathbf{J} + \frac{1}{2}\mathbf{J}(2\mathbf{B})\mathbf{J} \\ &= -\frac{1}{2}\vec{0}\vec{c}^\top\mathbf{J} - \frac{1}{2}\mathbf{J}\vec{c}\vec{0}^\top + \mathbf{J}\mathbf{B}\mathbf{J} = \mathbf{B} \end{aligned} \tag{3.38}$$

where, $\mathbf{D}^{(2)}\mathbf{J}$ removes the distance average by row and $\mathbf{J}\mathbf{D}^{(2)}$ removes the distance average by column. Since $\mathbf{J}\vec{1}$ respectively $\vec{1}^\top\mathbf{J}$ equals $\vec{0}$, a null-vector, the first two terms of Equation 3.38 are zero and hence $\mathbf{B}$ can be expressed in terms of the pairwise distance matrix $\mathbf{D}^{(2)}$

The coordinate Matrix $\mathbf{X}$ can then be found by performing an eigenvalue decomposition of

$$\mathbf{B} = \mathbf{U}\mathbf{\Lambda}\mathbf{U}^\top. \tag{3.39}$$

Let $\lambda_1, \ldots, \lambda_q$ be the $q$ largest positive eigenvalues and $\vec{u}_1, \ldots, \vec{u}_q$ be the corresponding eigenvectors. The coordinate matrix of dimension $\mathbb{R}^q$ is then defined as

$$\mathbf{X}_q = \mathbf{\Lambda}_q^{\frac{1}{2}}\mathbf{U}_q^\top \tag{3.40}$$

where $\mathbf{\Lambda}_q$ is a diagonal matrix of $q$ eigenvalues and $\mathbf{U}_q^\top$ the matrix of corresponding eigenvectors. Typical values for $q$ are two or three since higher orders can hardly be visualized.

For demonstration purposes, imagine a two-dimensional data set as can be seen in Figure 3.8 (top left). Since the initial data set is two-dimensional, it is easy to visualize it as a map layout for given coordinates $\vec{x}$ and $\vec{y}$. The calculation of the Euclidean distance between each data point results in the pairwise distance matrix $\mathbf{D}_{\mathrm{EUK}}$ (Figure 3.8 top right). Let's further suppose, the initial map layout of the data set is not available since it is more dimensional or cannot be visualized easily. Instead, only the pairwise distance matrix is given. Especially if arbitrary distance metrics, like DTW or AR-metric, are used, it is difficult to visualize similarity structures among a data set. By applying MDS to the pairwise distance matrix $\mathbf{D}_{\mathrm{EUK}}$ and

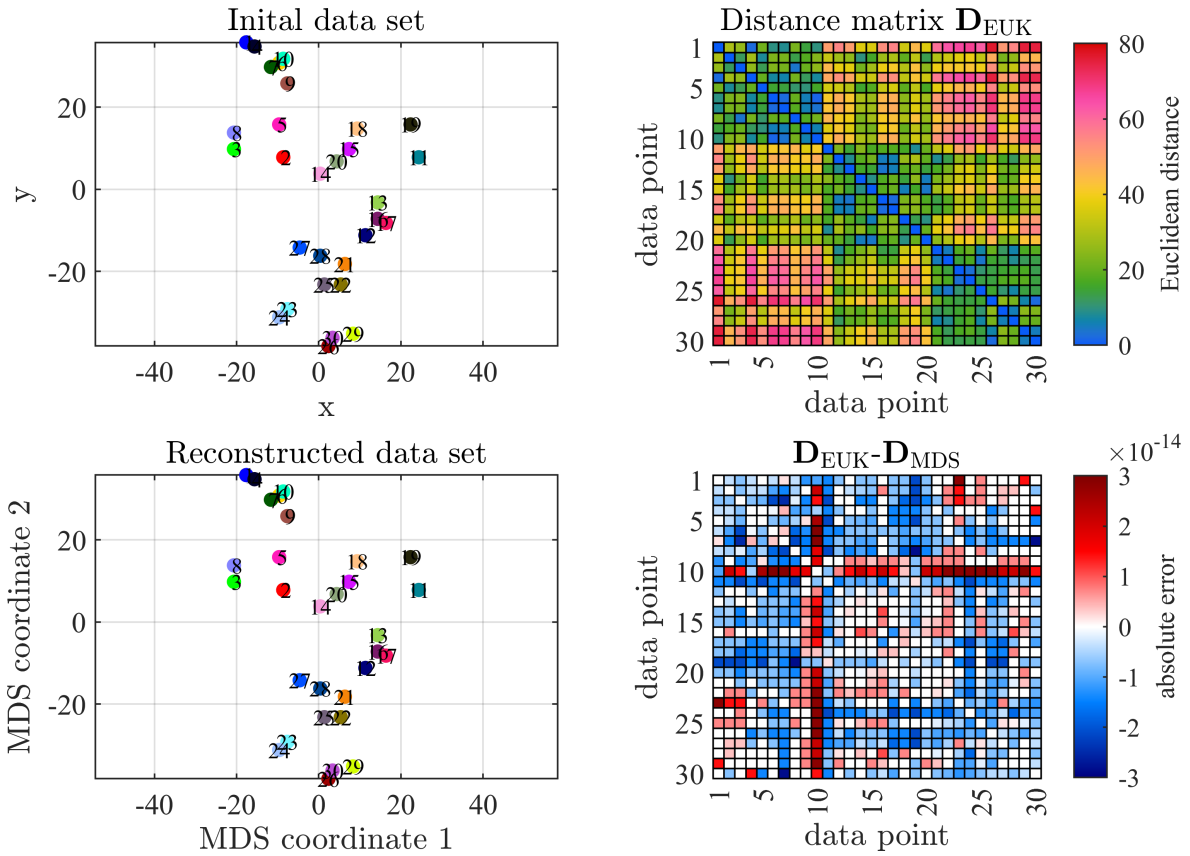


**Fig. 3.8.:** Calculated MDS coordinates (bottom left) based on the Euclidean pairwise distance matrix $\mathbf{D}_{EUK}$ (top right) of the initial data set (top left) and absolute differences between the Euclidean distance matrix $\mathbf{D}_{EUK}$ and the MDS distance matrix $\mathbf{D}_{MDS}$ (Euclidean metric) (bottom right).

choosing a dimensional reduction from $d = 30$ to $q = 2$, a map can be reconstructed showing the internal structure between the objects based on the pairwise distance measurements (Figure 3.8 bottom left). Rotating and mirroring the MDS coordinates, results in a good fit to the actual location of the data points in MDS coordinates. We can do so, since distances are invariant to rotational and mirroring operations. The absolute error of the initial Euclidean distance matrix $\mathbf{D}_{EUK}$ and the recalculated distance matrix $\mathbf{D}_{MDS}$ from MDS coordinates (Figure 3.8 bottom right) is less than $\pm 3 \cdot 10^{-14}$ and indicates a perfect reconstruction of the initial map layout. Therefore, MDS is an appropriate tool to visualize similarity structures among data sets based on their pairwise distance measurements even if the data cannot be visualized easily due to its multidimensional structure.

### 3.2.3. Estimating the optimal number of clusters

While partitioning clustering methods are provided a number of clusters prior to clustering, hierachical clustering methods construct a full data hierachy and the user decides the number of clusters by visual interpretation of the dendrogram. Both approaches are counter-intuitive. For the former, the optimal number of clusters cannot be identified since the data is purely divided based on the specified number of clusters $k$. For the latter, dendrograms are often misinterpreted since the information of merged clusters at a hierarchical level only provides the information that A is closer to C, rather than B. However, a dendrogram cannot provide an absolute statement of similarity. The subclusters A and C can still be far separated. A

more sophisticated approach to identify the optimal number of clusters is the use of statistical methods.

Let $\mathbf{X}$ be the previously defined data matrix in Equation 3.29 and let $d_{ij}$ be the distance between observation $\vec{x}_i$ and $\vec{x}_j$ (usually squared Euclidean distance, but any metric can be applied). Furthermore, the data is clustered into $k$ cluster $C_1, C_2, \ldots, C_k$ where $n_r$ denotes the number of observations assigned to cluster $C_r, r = 1, \ldots, k$. Let $S_r$ be the sum of pairwise distances of observations in cluster $C_r$ with

$$S_r = \sum_{i,j \in C_r} d_{ij} = \sum_{\vec{x}_i \in C_r} \sum_{\vec{x}_j \in C_r} ||\vec{x}_i - \vec{x}_j||^2 = 2n_r \sum_{\vec{x}_i \in C_r} ||\vec{x}_i - \vec{\mu}_r||^2 , \tag{3.41}$$

where $\vec{\mu}_r$ is denoting the centroid of cluster $C_r$. Then,

$$W_k = \sum_{r=1}^{k} \frac{1}{2n_r} S_r \tag{3.42}$$

is the within-cluster sum of squares with respect to the cluster means. With increasing number of clusters, $W_k$ gets successive smaller and hence the clusters are more compact. This approach is known as the "elbow" method. If the curve of $W_k$ resembles an arm shape, the optimal number of clusters is chosen at the inflection point of the curve (Figure 3.9 top middle). However, the optimal number of clusters might not be unambiguously identified since the successive change is too slow to clearly identify the inflection point.

Therefore, Tibshirani et al. (2001) proposed to choose the optimal number of clusters using the gap statistic. It is defined as

$$\text{Gap}(k) = E_n^* \{\log(W_k)\} - \log(W_k) . \tag{3.43}$$

The main idea is to standardize the $\log(W_k)$ curve by comparing it with a null reference distribution of the data (a distribution without obvious clusters). The optimal number of clusters is defined as the value of $k$ for which $\log(W_k)$ is at its first minimum below the reference curve $E_n^* \{\log(W_k^*)\}$ (Figure 3.9 top right). The reference data sets can be uniformly sampled from the initial data sets bounding box. The value $E_n^* \{\log(W_k)\}$ can then be found by calculating the $\log(W_k)$ curve for $B$ reference data sets resulting in

$$E_n^* \{\log(W_k^*)\} = \frac{1}{B} \sum_{b=1}^{B} \log(W_{kb}^*) . \tag{3.44}$$

Furthermore, the standard deviation of $E^* \{\log(W_k^*)\}$ is defined as

$$\text{sd}_k = \left( \frac{1}{B} \sum_{b=1}^{B} (\log(W_{kb}^*) - \bar{\ell})^2 \right)^{\frac{1}{2}} , \tag{3.45}$$

where $\bar{\ell} = \frac{1}{B} \sum_{b=1}^{B} \log(W_{kb}^*)$. The simulation error of $E_n^* \{\log(W_k^*)\}$ is expressed in terms of the standard deviation and is defined as

$$\text{s}_k = \text{sd}_k \sqrt{1 + \frac{1}{B}} . \tag{3.46}$$

The optimal number of clusters $k$ is then defined by the necessary condition such that $\text{Gap}(k) \geq \text{Gap}(k+1) - s_{k+1}$ and the sufficient condition of $\text{Gap}(k) \geq 0$. Table 3.3 summarize the necessary steps to calculate the gap statistics.

Applying the gap statistics to the example data set results in an optimal number of clusters $k = 3$ (Figure 3.9 bottom left), since $\text{Gap}(3) = 0.31$, and therefore greater than $\text{Gap}(4) - s_4 = 0.24 - 0.14 = 0.1$ (Figure 3.9 bottom right). The expected null reference distribution $E_n^*\{\log(W_k^*)\}$ was calculated for $B = 100$ reference data sets .

**Tab. 3.3.:** Outline of the computational implementation of the gap statistic.

**Calculation of the gap statistic**

1. Cluster observed data for $k = 1, \ldots, k_{max}$ and compute the within-cluster dispersion $W_k = \sum_{r=1}^{k} \frac{1}{2n_r} S_r$
2. Cluster $B$ reference data sets for $k = 1, \ldots, k_{max}$ and calculate the corresponding gap statistic $\text{Gap}(k) = (1/B) \sum_{b=1}^{B} \log(W_{kb}^*) - \log(W_k)$
3. Calculate the standard deviation $\text{sd}_k = ((1/B) \sum_{b=1}^{B} (\log(W_{kb}^*) - \bar{\ell})^2)^{1/2}$, with $\bar{\ell} = \frac{1}{B} \sum_{b=1}^{B} \log(W_{kb}^*)$.
4. Define $s_k = \text{sd}_k \sqrt{1 + (1/B)}$.
5. Choose the number of clusters as the smallest $k$ below the reference curve such that $\text{Gap}(k) \geq \text{Gap}(k+1) - s_{k+1}$ and $\text{Gap}(k) > 0$.

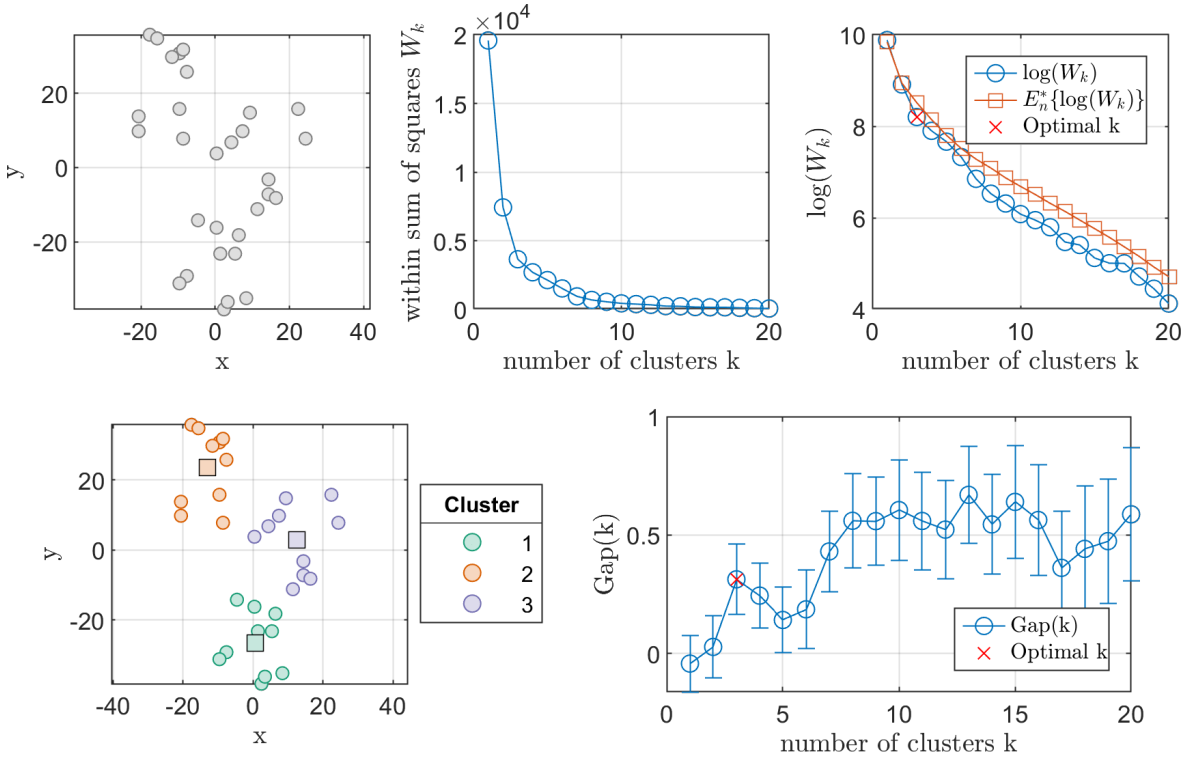


**Fig. 3.9.:** Clustering result (bottom left) of the example data set (top left) using the gap statistic (top right, bottom right) based on the logarithmic within-cluster dispersion (middle left).

**Note:** Matlab®'s implementation of the gap statistic is currently falsely implemented (up to version 2019b) and is still part of discussion with Matlab®'s support team (Hong and MathWorks Technical Support Department, 2020). Matlab®suggests $k = 1$ as an optimal number of clusters since it is only evaluating the necessary condition $\text{Gap}(k) \geq \text{Gap}(k+1) - s_{k+1}$. Since $\text{Gap}(1)$ is negative and therefore indicating that the within cluster dispersion $\log(W_k)$ is still above the expected within cluster dispersion $E_n^*\{\log(W_k)\}$, $k = 1$ does not fulfill the sufficient condition of $\text{Gap}(k) > 0$ and hence cannot be a valid solution. As stated by Tibshirani et al. (2001), negative gap values are an indicator of a random distribution of data points.

### 3.2.4. Cluster validation

Having decided on a reasonable number of clusters $k$ for the data set, either due to the gap statistic or specified by the user, the question if $k$ is suitable for the data set, still persists. Rousseeuw (1987) suggested the use of silhouettes in order to validate if a data point is well assigned to its cluster and to provide a quality measurement for this purpose.

Let $\mathbf{X}$ be the previously defined data matrix (Equation 3.29) and suppose it can be divided into $k$ clusters. Then every object $\vec{x}_i \in \mathbf{X}$ is assigned to one and only one cluster $C_i$ with the distance $d(\vec{x}_i, \vec{x}_j)$ between the objects $\vec{x}_i$ and $\vec{x}_j$. Furthermore, let $a(\vec{x}_i)$ be the average distance of $\vec{x}_i$ to every object in $C_i$ (intra-cluster-distance) and $b(\vec{x}_i)$ the average distance between $\vec{x}_i$ and every object in cluster $C_j \neq C_i$ (inter-cluster-distance). The smallest value for $b(\vec{x}_i)$ is then called the neighbor cluster of $\vec{x}_i$. Figure 3.10 gives a basic overview of the involved distances for calculating the silhouette value of $\vec{x}_i$ of cluster $A$ with respect to cluster $B$ and $C$. Whether the object $\vec{x}_i$ fits well to cluster $C_i$, can be calculated with the silhouette value, which is defined as

$$s(\vec{x}_i) = \frac{b(\vec{x}_i) - a(\vec{x}_i)}{\max(a(\vec{x}_i), b(\vec{x}_i))}. \tag{3.47}$$

For values of $s$ close to one, $\vec{x}_i$ is said to be *well assigned* to its cluster. If the value is close to zero, $a(\vec{x}_i)$ and $b(\vec{x}_i)$ are nearly identical and hence it is unclear if $\vec{x}_i$ should be assigned to $A$ or $B$. If the silhouette value is negative, $\vec{x}_i$ is miss-classified and should rather be assigned to $B$ than to $A$. The silhouette method can also be used to identify the best number of clusters by

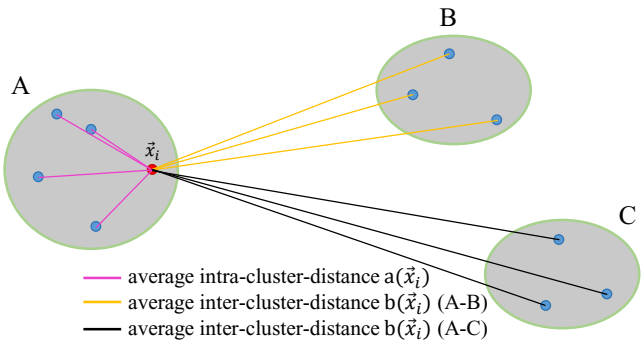


**Fig. 3.10.:** Overview of involved distances to calculate the silhouette value $s$ of object $\vec{x}_i$ assigned to cluster $A$ with respect to cluster $B$ and $C$ (after Rousseeuw (1987))

**Tab. 3.4.:** Interpretation for average silhouette width $\bar{s}(k)$ by Kaufman and Rousseeuw (1990)

| Value of $\bar{s}(k)$ | Interpretation |
|---|---|
| $0.7 \leq \bar{s}(k) \leq 1$ | A strong structure has been found |
| $0.5 \leq \bar{s}(k) \leq 0.7$ | A reasonable structure has been found |
| $0.25 \leq \bar{s}(k) \leq 0.5$ | The structure is weak and could be artificial |
| $\bar{s}(k) \leq 0.25$ | No substantial structure has been found |

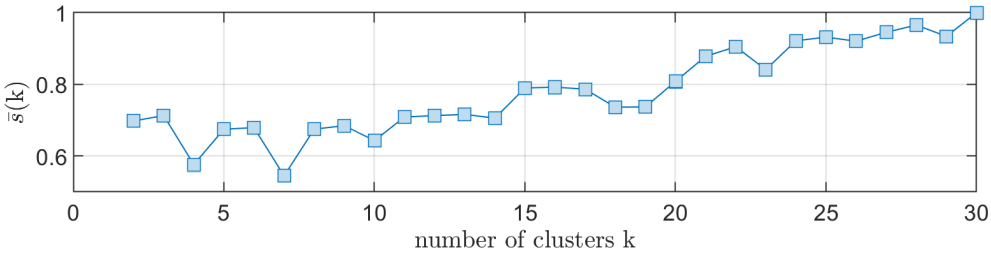


**Fig. 3.11.:** Average silhouette width $\bar{s}_k$ as a function of the number of clusters for the example data set.

calculating the average silhouette width $\bar{s}(k)$ of the entire silhouette values for cluster size $k$.

$$\bar{s}(k) = \frac{\sum_{i=1}^{n} s_i}{n}, \tag{3.48}$$

where $n$ is the number of data points. The optimal number of clusters is then chosen, such that $\bar{s}(k)$ is locally maximal. However, if $k$ equals the size of the data points, the average value reaches its global maximum of 1 (Figure 3.11). Therefore, other criteria like the gap statistic should be used in addition to verify the optimal number of $k$. Kaufman and Rousseeuw (1990) give an interpretation of the average silhouette width with respect to the cluster structure (Table 3.4).

According to the previous section, the gap statistic suggested $k = 3$ as an optimal number of clusters for the example data set.

Applying the k-means algorithm for $k = 2, 3$ and 4 to the sample data set, leads to the clustering result according to Figure 3.12 (top) and the corresponding silhouette values for each data point with respect to their cluster (bottom). For two and three clusters the silhouette values are all greater than zero and mostly above 0.5, indicating a good cluster assignment. Clustering the data set with four clusters leads to misclassified data points indicated by negative silhouette values for cluster one and two. Based on the mean silhouette value $\bar{s}(k)$, the clustering result for two clusters is 0.698, for three clusters 0.713 and for four clusters 0.576, indicating that the clustering result for three clusters is preferred over the result for two and four clusters.

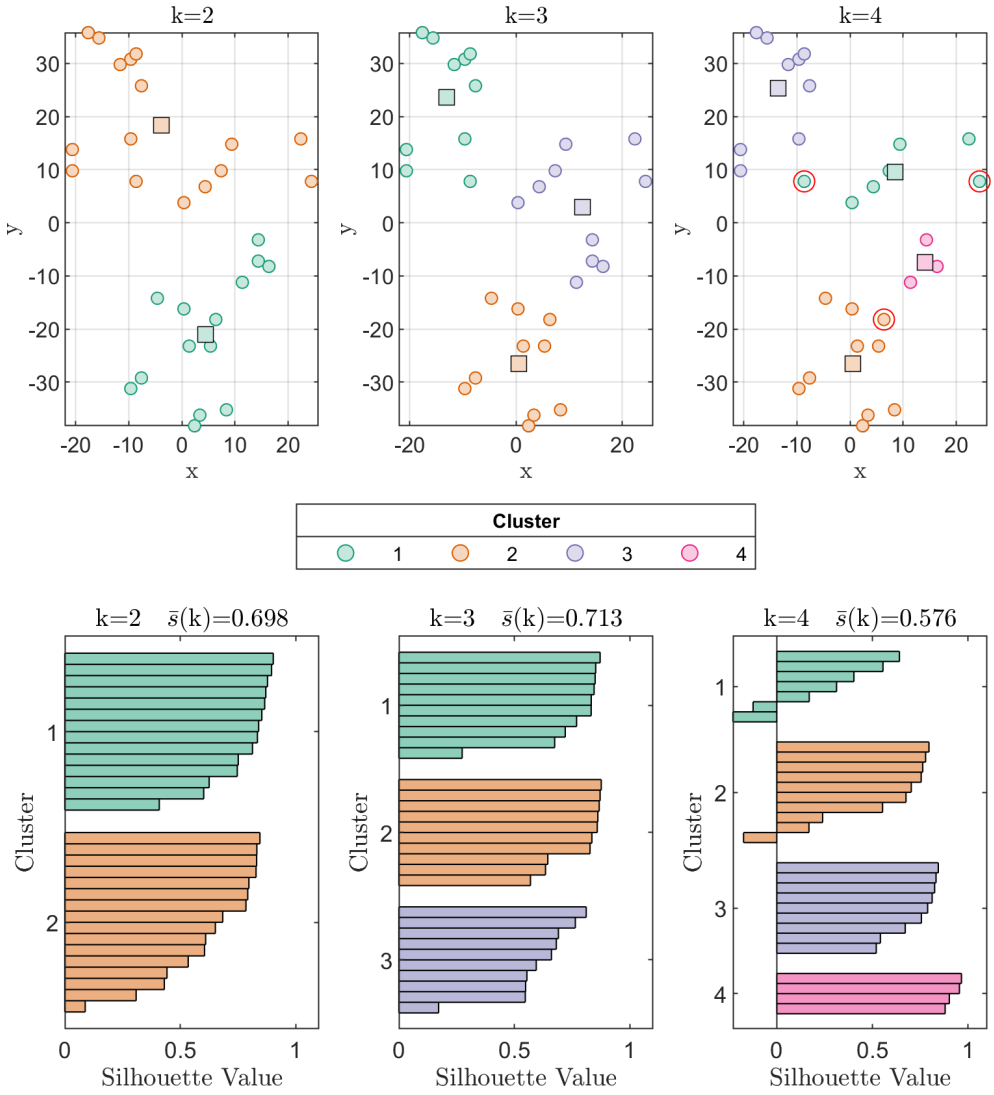


**Fig. 3.12.:** Classified color-coded data points (top) according to two (left), three (middle) and four (right) clusters marked as circles whereas squares mark cluster centers. Corresponding silhouette values $s(i)$ for each data point and the average silhouette width $\bar{s}_k$ according to the k-means clustering (bottom). Misclassified data points are marked with red circles

# 4. Determination of similarity of transient electromagnetic signals

In the following chapter different time series distance metrics are applied to synthetic semi-analytic transient electromagnetic responses. This allows to investigate the influence of different model parameters on distance metrics. Therefore, a statistical workflow based on cluster analysis is proposed featuring the necessary steps in order to determine similarity among transient electromagnetic measurements. The statistical workflow is further applied to a long-term monitoring data set conducted over a period of more than one year in Tharandter Wald located in Saxony (Germany).

## 4.1. Data transformation

Transient electromagnetic signals have a wide dynamic range in their amplitude of several magnitudes due to the fast decaying induced electromagnetic field in the subsurface. Therefore, it is necessary to reduce the dynamic range to achieve an equal influence of the data points. Otherwise, the results of various distance metrics would only be dominated by high amplitude data points. This can be compensated by applying a data transformation using the bijective area-sinus-hyperbolic function (Martin, 2009)

$$\operatorname{asinh}(\vec{x},a) = \log\left(\frac{\vec{x}}{a} + \sqrt{\left(\frac{\vec{x}}{a}\right)^2 + 1}\right) \tag{4.1}$$

to the measured data $\vec{x}$, where $a$ is a scaling factor. Here, the scaling factor is defined as the noise transition level of the transient electromagnetic response. Figure 4.1 (top) shows the asymptotic behavior of measured ambient noise ($5 \cdot 10^{-9}$ $\mathrm{V}/(\mathrm{A\,m^2})$) for logarithmically increasing time gates, which is referred to the "log-gating" technique. It is widely used for TEM receivers like the PROTEM system by Geonics (Genoics Limited, 2006), NanoTEM by Zonge (Zonge International, 2020) or SMARTem by EMIT (EMIT, 2020). The "log-gating" technique divides the receiver measurement window into separate time windows (gates) with different lengths. Early gates thereby have shorter time ranges than later gates, while the centers of the time gates are logarithmically equally spaced in time. This allows measuring the fast decaying electromagnetic field in the subsurface shortly after current turn-off with early short time gates, whereas later wider gates cover the more and more slowly decaying field. The measured value of a gate is an integrated value in its time width $\Delta t$ and is associated with the center of the gate. Since the width of the time gates increases over time, the mean value of the measured ambient Gaussian distributed noise (white noise) gets successively smaller and tends to $0\,\mathrm{V}/(\mathrm{A\,m^2})$ for $t \to \infty$. This behavior can be described in a logarithmic representation as a straight line with a slope of $\mathrm{t}^{-1/2}$ (Munkholm and Auken, 1996). The noise transition level is then defined as

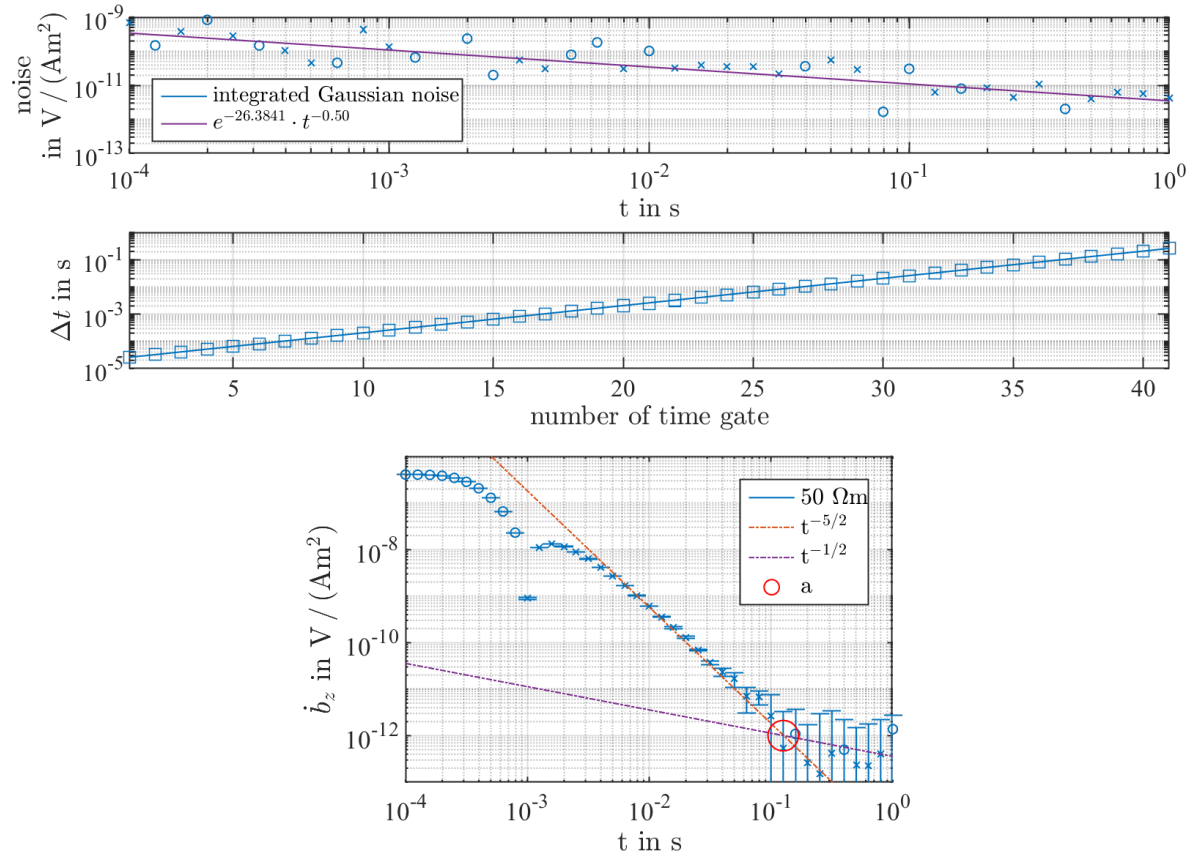


**Fig. 4.1.:** Asymptotic noise behavior for log-gating measurement technique (top) due to logarithmically increasing gate width $\Delta t$ (center). Vertical synthetic transient response of a 50 Ωm half-space with added ambient noise including late time and noise asymptotic as well as noise transition level $a$ indicated through red circle (bottom). Crosses mark positive and circles negative values.

the intersection between the late-time asymptotic of the transient electromagnetic response $\dot{\vec{b}}$ of $t^{-5/2}$ (Nabighian, 1989) and the noise asymptotic of $t^{-1/2}$. Figure 4.1 (bottom) shows a synthetic vertical transient response $\dot{b}_z$ with added white noise for a 50 Ωm half-space and the noise asymptotic for an ambient noise level of $5 \cdot 10^{-9}$ V/(Am$^2$). The noise transition level $a$ is about $1 \cdot 10^{-12}$ V/(Am$^2$) at $1.26 \cdot 10^{-1}$ s.

## 4.2. Statistical workflow for identifying similar TEM responses

Based on the concepts of time series analysis and cluster analysis, the following workflow (cf. Figure 4.2) is proposed to identify similar transient electromagnetic responses. First, the TEM responses are normalized to a common dipole-moment $m$ and to a common noise transition level $a$. By applying the area-sinus-hyperbolic function asinh(), equality of the influence of the data points is ensured with respect to the applied distance metric. In the next step the pairwise distance matrix **D** is constructed using any suitable time series distance metric (DTW, AR, NRMS, etc.). This step may include the interpolation of the transient responses in time from a logarithmic time grid to a linear time grid in order to meet the prerequisite of time series equally spaced in time for the AR and DTW distance metric. To determine the optimal number

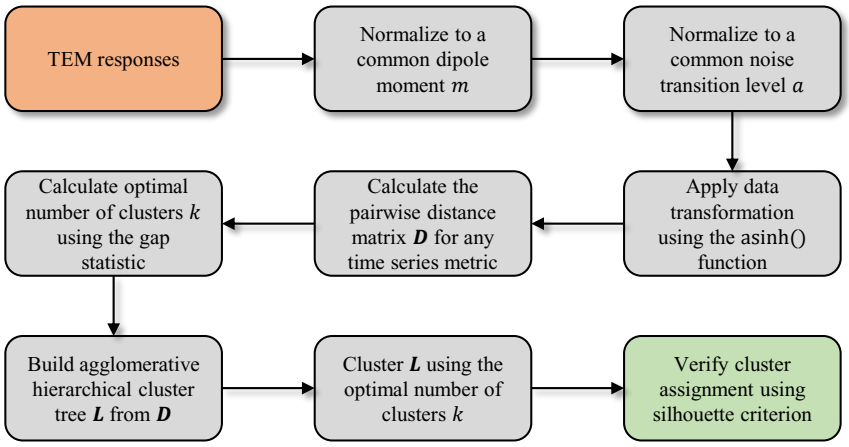


**Fig. 4.2.:** Overview of the statistical workflow for identifying similar transient electromagnetic responses based on concepts of time series analysis and cluster analysis.

of clusters $k$ of the data set, the gap statistic is applied. The agglomerative hierarchical cluster tree $\mathbf{L}$, constructed from the pairwise distance matrix, can then be clustered using the optimal number of clusters. To verify the clustering result, silhouette values and the average silhouette width are used.

## 4.3. Synthetic transient model responses

In order to investigate different time series distance metrics (see Chapter 3.1) with respect to transient electromagnetic responses, a synthetic data set is used. Although the statistical workflow emphasizes a dipole normalization in the first step, it is intentionally neglected in the upcoming study to investigate the effect on distance metrics.

The transient responses are obtained using em$\pi$mod. It is an open source Python-based electromagnetic modeler. "*The calculation is carried out in the wavenumber-frequency domain, and various Hankel- and Fourier-transform methods are included to transform the responses into the space-frequency and space-time domains*" (Werthmüller, 2017). The modeler is thereby capable of taking induced polarization effects (IP), based on the Cole-Cole model (Cole and Cole, 1941) or the Pelton model (Pelton et al., 1978), into account.

The data set consists of transient responses (vertical component) modeled for seven unique models. The reference model M1 is a homogeneous 10 $\Omega$m half-space for a point source at the surface with a dipole-moment of $1 \cdot 10^5$ A m$^2$ and a receiver-transmitter offset (Rx-Tx offset) of 300 m. Alterations of the model parameters thereby provide necessary information about their effect on the time series distance metrics. Therefore, the dipole-moment of M2 is double the dipole-moment of M1. This simulates either a double transmitter current or a transmitter loop with two wire turns. M3 represents an Rx-Tx offset of 250 m as a result of a misplaced receiver. M4 accounts for induced polarization effects represented by a Cole-Cole model with a chargability of $m_c = 0.65$, a relaxation time $\tau = 4 \cdot 10^{-3}$ and a frequency exponent $c = 0.6$. These

**Tab. 4.1.:** Overview of the model parameters of the synthetic transient responses.

| **Model** | **dipole-moment** [A m$^2$] | **Rx-Tx offset** [m] | **time shift** [µs] | **resistivity** [Ω m] |
|---|---|---|---|---|
| M1 | 100 000 | 300 | 0 | 10 |
| M2 | 200 000 | 300 | 0 | 10 |
| M3 | 100 000 | 250 | 0 | 10 |
| M4 | 100 000 | 300 | 0 | cole-cole model<br>$m_c = 0.65$, $\tau = 0.004$<br>$c = 0.6$, $\rho_0 = 20$ |
| M5 | 100 000 | 295 | 0 | 10 |
| M6 | 100 000 | 300 | 200 | 10 |
| M7 | 100 000 | 300 | 0 | 10, 200 m thickness<br>1, 20 m thickness<br>10, lower half-space |

parameters are in the range of magmatite or pyrrhotite rich soils or rocks. The Rx-Tx offset of M5 is 295 m, as a result of a misplaced receiver due to GPS accuracy (Department of Defense - United States of Amaerika, 2008). In dependence of the measurement system and the way to determine the output current turn-off time, time shifts can occur on a regular basis. To simulate this behavior, the model response of M6 is time shifted by 200 µs in positive time direction with respect to M1. In order to investigate the capability of detecting a different resistivity model, M7 is a response of a three-layered half-space consisting of a 10 Ω m layer with 200 m thickness followed by a 1 Ω m layer of 20 m thickness and a 10 Ω m lower half-space. Table 4.1 summarize the parameters of the investigated models. All model responses were calculated for the time interval $1 \cdot 10^{-4}$ s to $1 \cdot 10^{-1}$ s for a step size of $25 \cdot 10^{-6}$ s. The linear time resolution is thereby essential to meet the requirement of equally spaced time series in the DTW algorithm and the ARIMA modeling approach as well as for the NRMS distance metric. Figure 4.3 shows the vertical transient electromagnetic response $\dot{b}_z$ for M2 to M7 in comparison with the reference response of M1 and Figure 4.4 shows the transformed normalized vertical transient electromagnetic response

$$\operatorname{asinh}(\dot{b}_{z_{\text{norm}}}) = \operatorname{asinh}\left(\frac{\dot{b}_z}{a}\right). \tag{4.2}$$

Since no artificial noise is added to the synthetic data set, the noise transition level $a$ is defined as the smallest occurring value of the model responses ($1 \cdot 10^{-11}\,\mathrm{V}/(\mathrm{A\,m^2})$). Note, due to the normalization to the noise transition level, the quantity $\operatorname{asinh}(\dot{b}_{z_{\text{norm}}})$ is dimensionless.

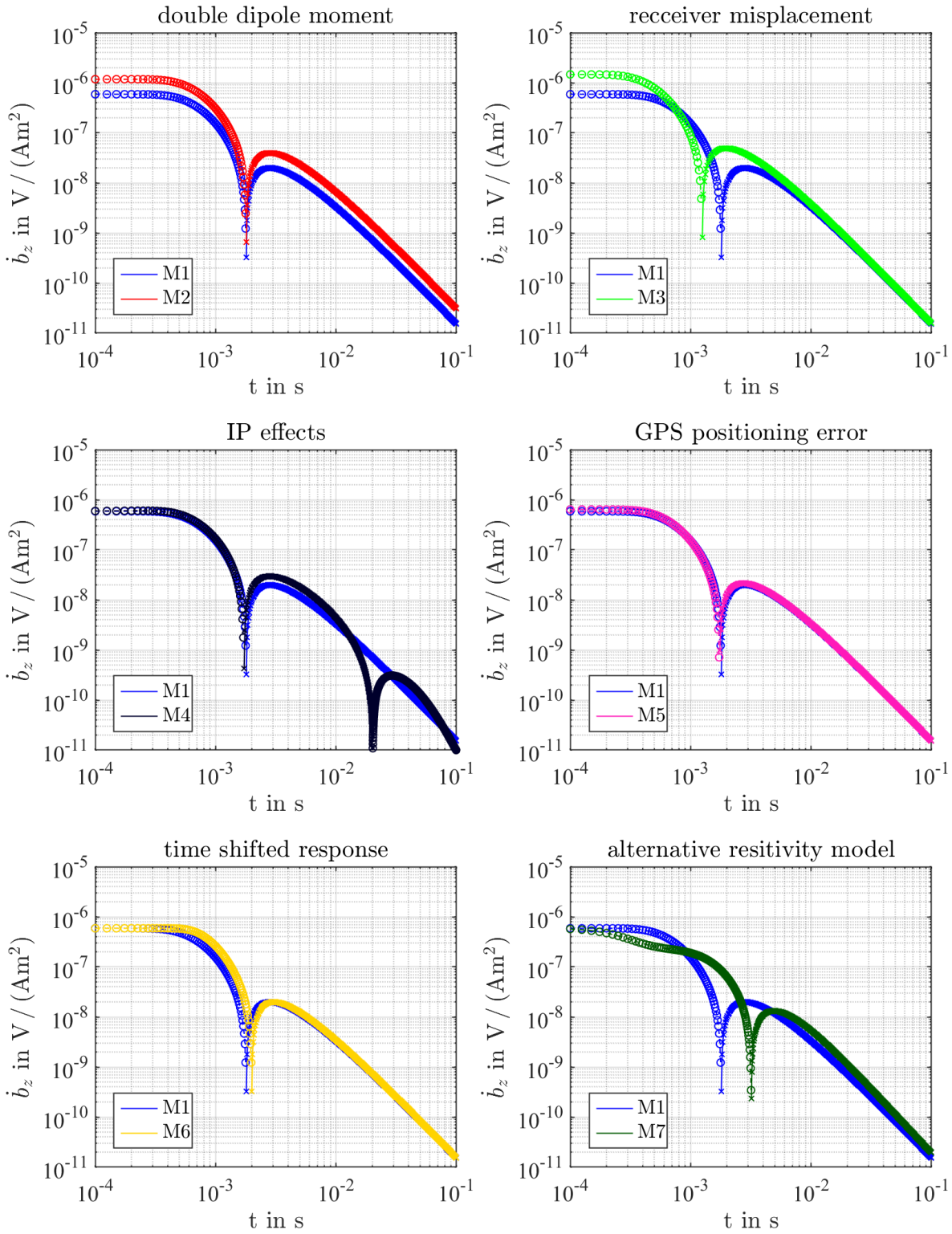


**Fig. 4.3.:** Vertical component of the transient response $\dot{b}_z$ in V/(A m$^2$) of the investigated synthetic models in comparison with the vertical component of the transient response of the reference model M1.

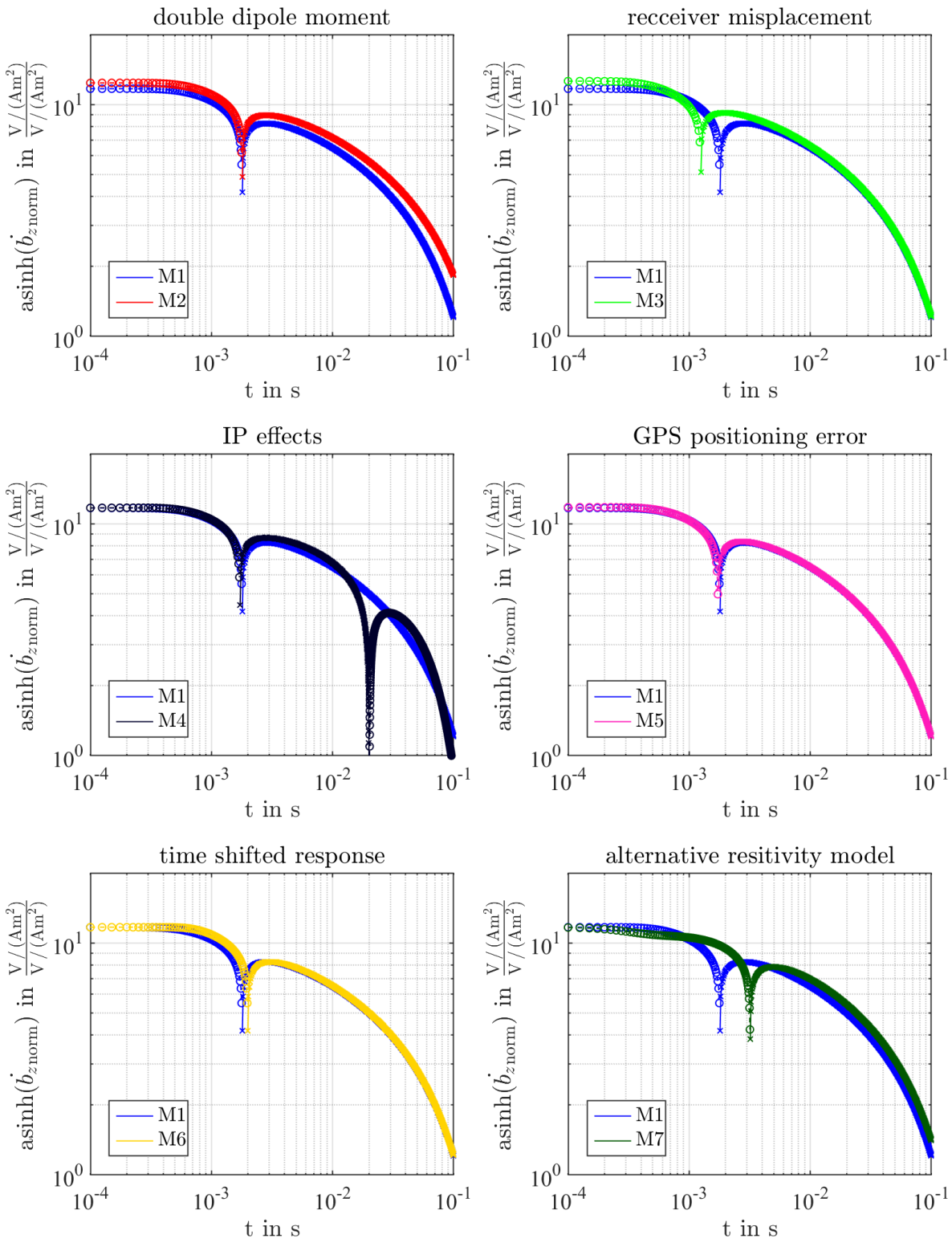


**Fig. 4.4.:** Vertical component of the transformed normalized transient responses asinh($\dot{b}_{z_{\mathrm{norm}}}$) of the investigated synthetic models in comparison with the vertical component of the transformed normalized transient response of the reference model M1.

In order to calculate the AR-distance, the corresponding ARIMA models of the synthetic transient responses have to be estimated. The ARIMA models were obtained using the R software package (R Core Team, 2020) in combination with the *forecast* library (Hyndman et al., 2019). Following the Box-Jenkins workflow for ARIMA modeling, the first step is to determine the degree of differencing in order to achieve a stationary time series. Therefore, the Kwiatkowski, Phillips, Schmidt, Shin (KPSS) test and the Dickey-Fuller (DF) test are applied. The test results, in terms of p-values, for the undifferenced ($\nabla^0$), first-order differenced ($\nabla^1$) and second-order differenced ($\nabla^2$) synthetic transient responses is provided in Table 4.2. In case of the KPSS test, the p-values are less than the significance level $\alpha = 0.05$ for the undifferenced time series. The null hypothesis (stationarity) is rejected in favor of the alternative hypothesis (non-stationarity). The null hypothesis is not rejected for higher order differenced time series except for M7. To support the results of the KPSS test, the DF test is applied in addition. The null hypothesis (non-stationarity) of the DF test is not rejected for undifferenced time series indicated by p-values larger the significance level $\alpha = 0.05$. However, the null hypothesis is rejected for higher order differenced time series in favor of the alternative hypothesis (stationarity) due to p-values less then $\alpha$. In conclusion, the degree of differencing is one for M1 to M6 and two for M7. The degree $p$ and $q$ of the ARIMA models are determined by maximizing the AIC criterion. The p-value of the Ljung-Box test statistic is high for all models, indicating no evidence for autocorrelation among the residuals between the fitted time series and the initial model responses. Hence, the models are well determined. The final estimated model parameters, including the p-value of the Ljung-Box test, are listed in Table 4.3. To support the Ljung-Box test results, the fitted ARIMA time series were back transformed using the sinus-hyperbolic function (inverse function of asinh) and by multiplication with the noise transition level $a$ through,

$$\dot{b}_z = \sinh(\dot{b}_{z_{\text{norm}}}) \cdot a\,. \tag{4.3}$$

Figure 4.5 shows the fitted ARIMA time series for M1 to M7 in comparison with its corresponding synthetic transient responses. The estimated ARIMA time series models show a good fit, except for slight variations at sign changes, compared to the synthetic transient responses.

**Tab. 4.2.:** KPSS and DF unit-root test results for the undifferenced ($\nabla^0$), first-order differenced ($\nabla^1$) and second-order differenced ($\nabla^2$) synthetic transient responses.

| **Model** | **KPSS test p-value** | | | **DF test p-value** | | |
|---|---|---|---|---|---|---|
| | $\nabla^0$ | $\nabla^1$ | $\nabla^2$ | $\nabla^0$ | $\nabla^1$ | $\nabla^2$ |
| M1 | 0.01 | 0.055 | 0.1 | 0.972 | 0.01 | 0.03 |
| M2 | 0.01 | 0.059 | 0.1 | 0.973 | 0.01 | 0.03 |
| M3 | 0.01 | 0.089 | 0.1 | 0.340 | 0.01 | 0.01 |
| M4 | 0.01 | 0.100 | 0.1 | 0.413 | 0.01 | 0.01 |
| M5 | 0.01 | 0.057 | 0.1 | 0.942 | 0.01 | 0.04 |
| M6 | 0.01 | 0.052 | 0.1 | 0.990 | 0.01 | 0.01 |
| M7 | 0.01 | 0.026 | 0.1 | 0.324 | 0.01 | 0.01 |

**Tab. 4.3.:** ARIMA estimates $\boldsymbol{\phi}$ and $\boldsymbol{\theta}$ of synthetic transient electromagnetic responses in Box-Jenkins notation including the Ljung-Box test results in terms of p-values.

| Model | p | d | q | $\boldsymbol{\phi_1}$ | $\boldsymbol{\phi_2}$ | $\boldsymbol{\theta_1}$ | $\boldsymbol{\theta_2}$ | $\boldsymbol{\theta_3}$ | Ljung-Box test p-value |
|---|---|---|---|---|---|---|---|---|---|
| M1 | 2 | 1 | 1 | 1.14 | -0.21 | 0.86 | 0.00 | 0.00 | 0.996 |
| M2 | 2 | 1 | 1 | 1.10 | -0.18 | 0.86 | 0.00 | 0.00 | 0.995 |
| M3 | 1 | 1 | 3 | -0.90 | 0.00 | 0.56 | 0.20 | 0.04 | 0.993 |
| M4 | 2 | 1 | 3 | 1.03 | -0.10 | 0.31 | 0.47 | 0.01 | 0.852 |
| M5 | 2 | 1 | 1 | 1.16 | -0.23 | 0.87 | 0.00 | 0.00 | 0.999 |
| M6 | 2 | 1 | 1 | 1.08 | -0.17 | 0.82 | 0.00 | 0.00 | 0.998 |
| M7 | 1 | 2 | 3 | 0.75 | 0.00 | 1.49 | -0.43 | -0.07 | 0.979 |

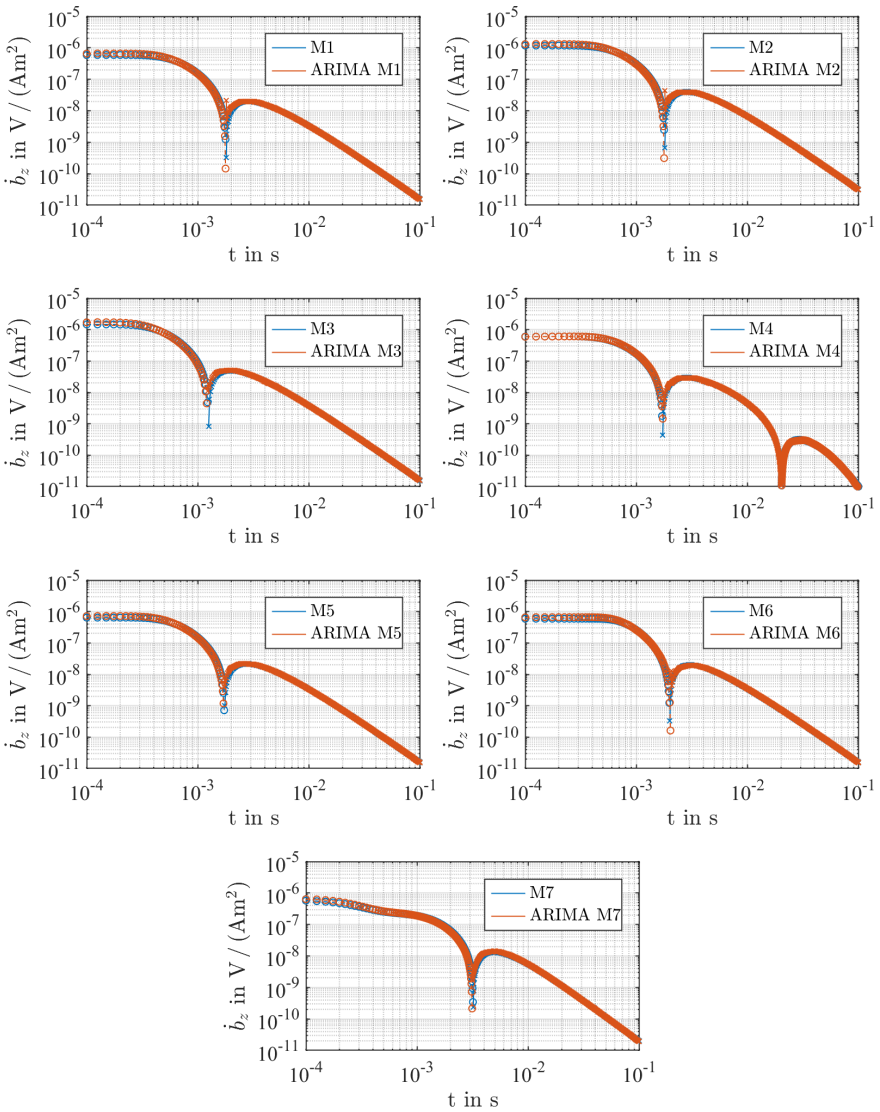


**Fig. 4.5.:** Fitted ARIMA time series models (orange) in comparison with the synthetic transient responses (blue). Circles mark negative and crosses mark positive values.

### 4.3.1. Cluster analysis

Depending on the applied distance metric and similarity criterion for each metric, the final cluster results may vary drastically. Applying the Euclidean, dynamic time warping, AR and normalized root-mean-square distance metric to the transformed normalized synthetic transient responses results in the pairwise distance matrices **D** shown in Figure 4.6.

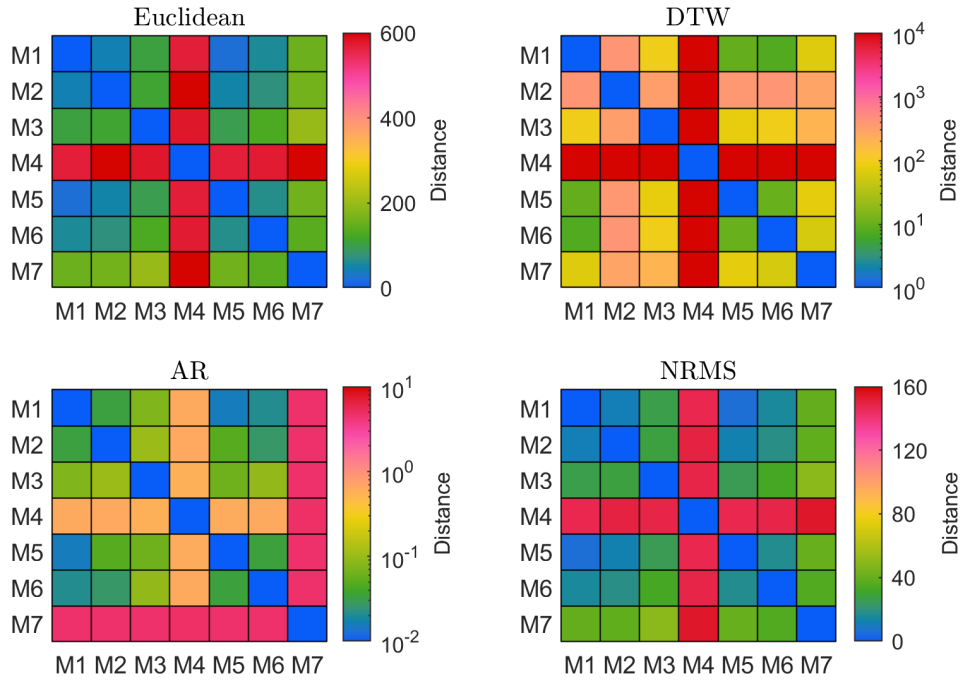


**Fig. 4.6.:** Calculated pairwise distance matrices **D** for Euclidean, DTW, AR and NRMS distance metric applied to the synthetic transient responses M1 to M7.

All metrics rank M4 with the largest, and for the AR-metric a large distance to all other models. Furthermore, M7 has the largest distance in the AR-metric and large distances for other metrics compared to all other models. Clustering the pairwise distances using an agglomerative hierarchical cluster algorithm with complete linkage criterion results in the hierarchical cluster trees shown in Figure 4.7.

For the Euclidean distance metric, M1 is closely matched with M5 since they have the smallest Euclidean distance. Successively, the time shifted response M6 is added to the tree followed by the amplitude shifted response M2. M7 and M4 are added at last with a significantly larger distance.

For the dynamic time warping distance metric M1, M6 and M5 are closely matched together (small DTW distances). M3, M7 and M2 are added successively, while M2 exhibits a large distance compared to M1, M6, M5, M3 and M7. M4 is added last with the largest DTW distance. Since dynamic time warping is a method of detecting similar shapes, it would have been expected that M2 is closely matched to M1, M6, and M5. However, the DTW metric fails in detecting similar shapes at a certain amplitude offset. As the offset increases, the warping path more and more matches the regular Euclidean point-to-point mapping. Therefore, an amplitude normalization is recommended.

The hierarchical cluster tree for the normalized root-mean-square distance metric is similar to the tree of the Euclidean distance metric, except that positions of M6 and M2 are swapped.

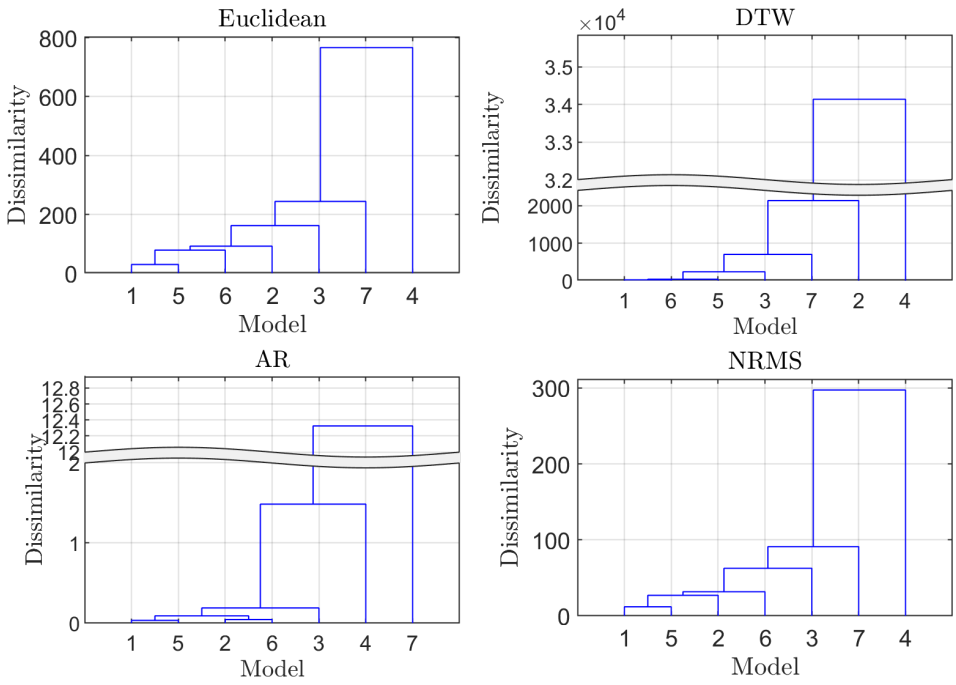


**Fig. 4.7.:** Dendrograms for the hierarchical cluster trees for Euclidean, DTW, AR and NRMS distance metric using the complete linkage method. For a better visualization the y-axis is split in the DTW and the Autoregressive (AR) tree.

Other than the previously mentioned distance metrics, the autoregressive metric is a model based similarity measurement. ARIMA models which represent similar time generating processes have a small distance compared to ARIMA models with a different time generating process. Hence M1 and M5 as well as M2 and M6 are matched closely together, indicating a high similarity between the model responses. M3, M4, and M7 are added successively while M7 has the largest AR distance to all other models.

As previously mentioned in Chapter 3.2.2, dendrograms are not intuitive for cluster interpretation, especially for the Euclidean and NRMS distance metric since no obvious structure is noticeable. Therefore, the optimal number of clusters is identified using the gap statistic (Figure 4.8) and for better visualization of the internal cluster structure, the pairwise distance metrics are transformed using multidimensional scaling (Equation 3.40) with a dimensional reduction from 7 to 2 (Figure 4.9). The optimal number of clusters for the Euclidean and NRMS distance metric is three, whereas the optimal number of clusters for DTW is five and four for the AR-metric. In all MDS representations M4 and M7 are far separated between each other and to all other models, forming separate clusters for each distance metric. The Euclidean distance metric fails to separate the dissimilar model response M3 from the remaining similar model responses M1, M2, M5, and M6. A similar behavior can be observed for the NRMS metric. The DTW distance metric can clearly separate M3 from the remaining model responses. As previously discussed, DTW fails in detecting M2 as a similar model response compared to M1, M5, and M6, due to the constant amplitude offset. This can be avoided by applying an amplitude normalization to the data. However, the AR-metric is capable in detecting the expected cluster distribution among the synthetic transient responses. It clearly separates M3, M4, and M7, each as separate cluster, from the cluster formed by the similar model responses M1, M2, M5, and M6. Table 4.4 shows the final cluster assignment for each model response. In addition to verify the quality of the cluster assignment, silhouette plots are provided (cf. Figure 4.10). The silhouette values are all positive and high for every distance metric, indicating well assigned

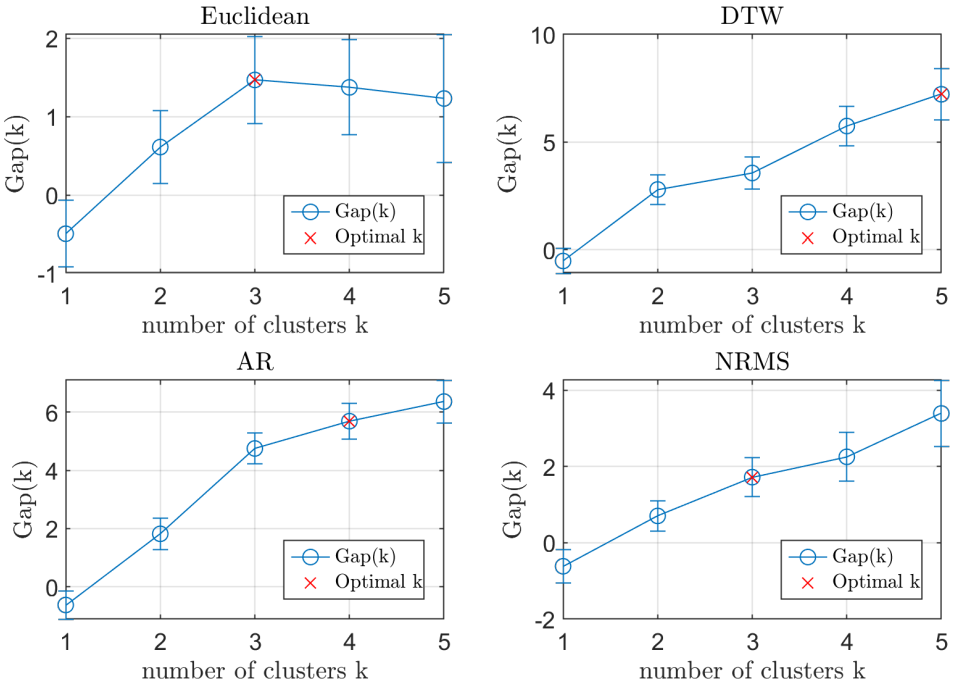


**Fig. 4.8.:** Optimal number of clusters, marked as blue dot, based on the gap statistic for hierarchical clustering for Euclidean, DTW, AR and NRMS distance metric using the complete linkage method.

responses with respect to their clusters. The average silhouette width is also high indicating a strong structure based on the interpretation by Kaufman and Rousseeuw (1990).

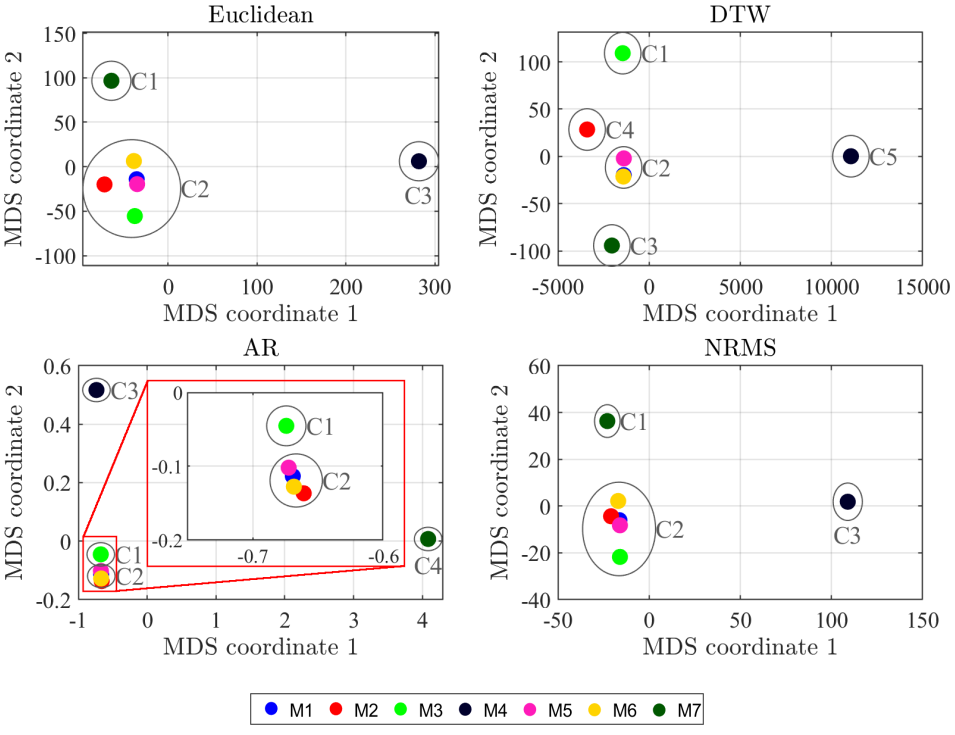


**Fig. 4.9.:** Identified clusters of synthetic transient responses for Euclidean, DTW, AR, and NRMS distance metric using the optimal number of clusters provided by the gap statistic.

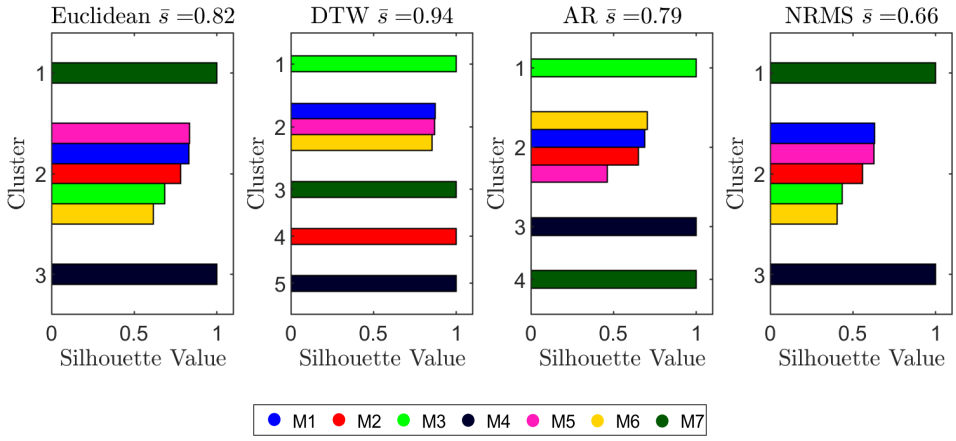


**Fig. 4.10.:** Silhouette values of synthetic transient responses for identified clusters based on the Euclidean, DTW, AR, and NRMS distance metric.

**Tab. 4.4.:** Cluster assignment of synthetic transient responses for the Euclidean, DTW, AR and NRMS distance metric obtained by hierarchical clustering using the complete linkage method and the optimal number of clusters provided by the gap statistic.

| Model | Euclidean | DTW | AR | NRMS |
|---|---|---|---|---|
| M1 | C2 | C2 | C2 | C2 |
| M2 | C2 | C4 | C2 | C2 |
| M3 | C2 | C1 | C1 | C2 |
| M4 | C3 | C5 | C3 | C3 |
| M5 | C2 | C2 | C2 | C2 |
| M6 | C2 | C2 | C2 | C2 |
| M7 | C1 | C3 | C4 | C1 |

### 4.3.2. Conclusions

In conclusion, the ARIMA modeling approach is capable of detecting similar time generating processes superior over the DTW, Euclidean, and NRMS distance metric. In return, a much higher computational effort is required to achieve the result since the ARIMA modeling approach can hardly be automated and requires serious user interaction and verification, especially for identifying the optimal parameter set (p,d,q). If time series exhibit similar shapes with even amplitude levels, the dynamic time warping distance metric is also capable of detecting similar time generating processes at a much faster speed and less computational effort. However, no distance metric is capable of distinguishing between different physical processes. The distance between a minor time shifted transient response (M6) and the reference model response M1 is similar to that of a slightly misplaced receiver (M5) and M1. The Euclidean and NRMS distance metric fail in identifying M3 as a single cluster. All metrics successfully identified M4 and M7 as dissimilar time series apart from the remaining model responses.

## 4.4. TEM monitoring at Tharandter Wald

In preparation of a repeat measurement survey at the $CO_2$-sequestration site Field Research Station (FRS) in Brooks, Alberta/Canada, a monitoring study was carried out in Germany. It

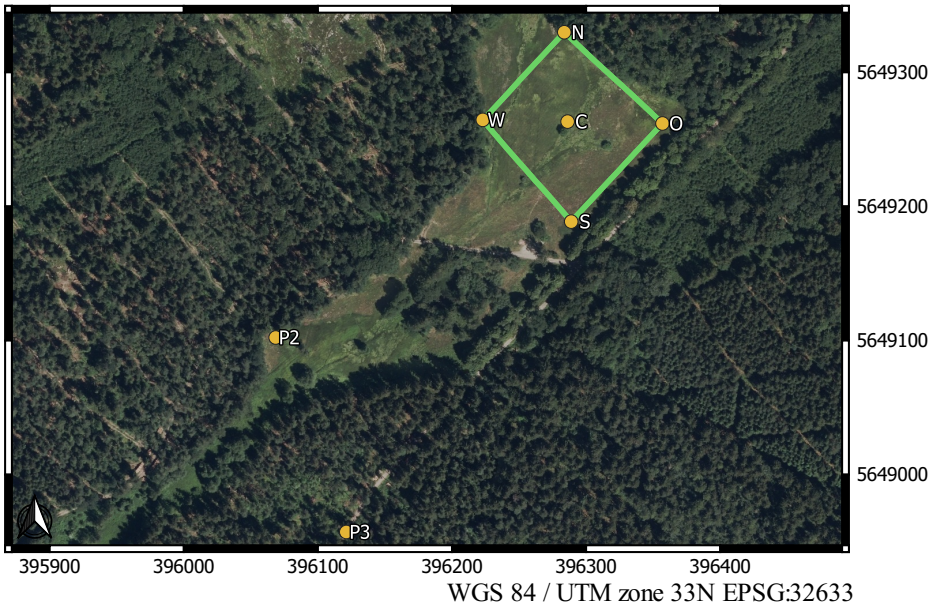


**Fig. 4.11.:** Overview of the transient electromagnetic monitoring setup at Tharandter Wald, Saxony, Germany (GeoSN, 2020).

was tested, if the transient responses of the successive measurements are similar and if the PROTEM system by Geonics exhibits changes over time. Further details of the PROTEM system are listed in Appendix B.

The measurements were conducted in a nature reserve at Tharandter Wald, Saxony (Figure 4.11) over more than one year for central loop and separate loop configurations. Thereby, the transmitter loop location as well as the receiver positions where kept identical for all measurements. The corresponding coordinates are listed in Table 4.5. It was ensured that the survey site does not change during monitoring with regard to urban or agricultural influences. These could cause changes in the transient electromagnetic response and would violate the repeatability conditions. Table 4.6 summarizes the basic survey parameters for each acquisition date. The TEM47 transmitter, operating at 2 A output current, was used for central loop measurements at observation point C in conjunction with the high-frequency receiver coil (HF-coil). For separate loop measurements at observation point P2 and P3 the TEM57-MK2 transmitter was used, operating at 17 A output current, in combination with the low-frequency receiver coil (LF-coil). A single turn square loop with a side length of 100 m served as transmitter loop. A second turn was added to the transmitter loop, enhancing the dipole moment by a factor of two, on 4th April 2018 to investigate changes in the electromagnetic response due to modifications of the transmitter loop. However, due to a major malfunction of the power generator, the test was only carried out for observation point P2 and P3. For each acquisition date and observation point, 25 measurements were conducted and stacked through averaging. Each measured single response consists of 400 transients resulting in 10000 per stack. Since the PROTEM system does not provide any information about data errors, the standard deviation of the consecutive measurements is used.

**Tab. 4.5.:** Coordinates of observation points and transmitter loop location. Coordinates are given in WGS84/UTM zone 33N (EPSG:32633) coordinate system.

| ID | Easting | Northing | Elevation [m] |
|---|---|---|---|
| N | 396283,.68 | 5649329.87 | 406.80 |
| O | 396356.94 | 5649261.82 | 405.45 |
| S | 396288.86 | 5649188.60 | 401.40 |
| W | 396222.89 | 5649264.50 | 402.91 |
| C | 396286.16 | 5649263.21 | 403.03 |
| P2 | 396068.36 | 5649102.14 | 392.97 |
| P3 | 396121.07 | 5648957.05 | 396.69 |

**Tab. 4.6.:** Survey parameters of the TEM monitoring at Tharandter Wald.

| **Name** | **Date** | **Transmitter** | **dipole-moment** [A m$^2$] | **Observation points** | **number of repeat measurements** |
|---|---|---|---|---|---|
| R1 | 26.10.2017 | TEM47 / TEM57 | $20 \cdot 10^3$ / $170 \cdot 10^3$ | C, P2, P3 | 25 |
| R2 | 15.11.2017 | TEM47 / TEM57 | $20 \cdot 10^3$ / $170 \cdot 10^3$ | C, P2, P3 | 25 |
| R3 | 09.12.2017 | TEM47 / TEM57 | $20 \cdot 10^3$ / $170 \cdot 10^3$ | C, P2, P3 | 25 |
| R4 | 24.01.2018 | TEM47 / TEM57 | $20 \cdot 10^3$ / $170 \cdot 10^3$ | C, P2, P3 | 25 |
| R5 | 25.01.2018 | TEM47 / TEM57 | $20 \cdot 10^3$ / $170 \cdot 10^3$ | C, P2, P3 | 25 |
| R6 | 21.02.2018 | TEM47 / TEM57 | $20 \cdot 10^3$ / $170 \cdot 10^3$ | C, P2, P3 | 25 |
| R7 | 15.03.2018 | TEM47 / TEM57 | $20 \cdot 10^3$ / $170 \cdot 10^3$ | C, P2, P3 | 25 |
| R8 | 04.04.2018 | TEM47 / TEM57 | $20 \cdot 10^3$ / $340 \cdot 10^3$ | C, P2, P3 | 25 |
| R9 | 11.06.2018 | TEM47 / TEM57 | $20 \cdot 10^3$ / $170 \cdot 10^3$ | C, P2, P3 | 25 |
| R10 | 06.12.2018 | TEM47 / TEM57 | $20 \cdot 10^3$ / $170 \cdot 10^3$ | C, P2, P3 | 25 |

### 4.4.1. Cluster analysis

The cluster analysis is identical as demonstrated for the synthetic transient model responses following the statistical workflow for identifying similar time series (Chapter 4.2). First, the stacked responses are normalized to a common dipole-moment $m$ and noise transition level $a$. For data balancing, the stacked normalized responses are transformed applying the area-sinus-hyperbolic function. Furthermore, the stacked responses are interpolated from a logarithmic to a linear equally spaced time raster in order to meet the requirements of the DTW algorithm and ARIMA modeling approach. Data points below the noise transition zone or data points affected by oversaturated gates are removed. The pairwise distance matrix $\mathbf{D}$ is then calculated for the Euclidean, DTW, AR, and NRMS distance metric and the hierarchical tree $\mathbf{L}$ is constructed using an agglomerative hierarchical cluster algorithm. For identifying the optimal number of clusters $k$, the gap statistic is used. Furthermore, the pairwise distance matrices are transformed using multidimensional scaling with a dimensional reduction from 10 to 2. This allows for a better cluster visualization compared to dendrogram plots. The clustering results are validated using silhouette values and silhouette plots.

### Central loop measurements

Figure 4.12 shows the stacked vertical transient responses $\dot{b}_z$ including the standard deviation for each gate as error bar and the interpolated vertical transient responses at observation point C. The responses are well aligned except for the first three time gates. The HF-coil operates in its intended working tuning range but due to inconsistencies caused by reference cable synchronization mode between receiver and transmitter (see Appendix B), the first gate at 6.8 µs is located in the turn-off ramp of the transmitter. This leads to a partially oversaturated first gate affecting the next two to three gates (Levy and McNeil, 1984). The noise transition level is at $1 \cdot 10^{-8}$ V/m$^2$. Therefore, the first four gates and the last five gates (values below the noise transition level) are not considered in the cluster analysis. Table 4.7 shows the estimated ARIMA models for the central loop measurements including the Ljung-Box statistic. Due to the high p-value of the Ljung-Box test, there is no indication of autocorrelation present in the residuals between the measured responses and the fitted ARIMA time series indicating well estimated ARIMA models (see Figure A.7).

Calculating the pairwise Euclidean, DTW, AR, and NRMS distances of the transformed normalized transient responses and successice clustering leads to the hierarchical cluster trees shown in Figure 4.13. None of the dendrograms indicates obvious cluster structures. This is also supported by the gap statistic. The optimal number of clusters is one for all metrics (Figure 4.14). All gap values are negative, except for Gap(1) for DTW, indicating that the responses are randomly distributed. Figure 4.15 shows the MDS representation of the pairwise distance matrices and the identified cluster. The MDS coordinates are randomly distributed, supporting the one cluster hypothesis. A verification of the cluster result using silhouette values cannot be provided, since the silhouette calculation requires at least two clusters.

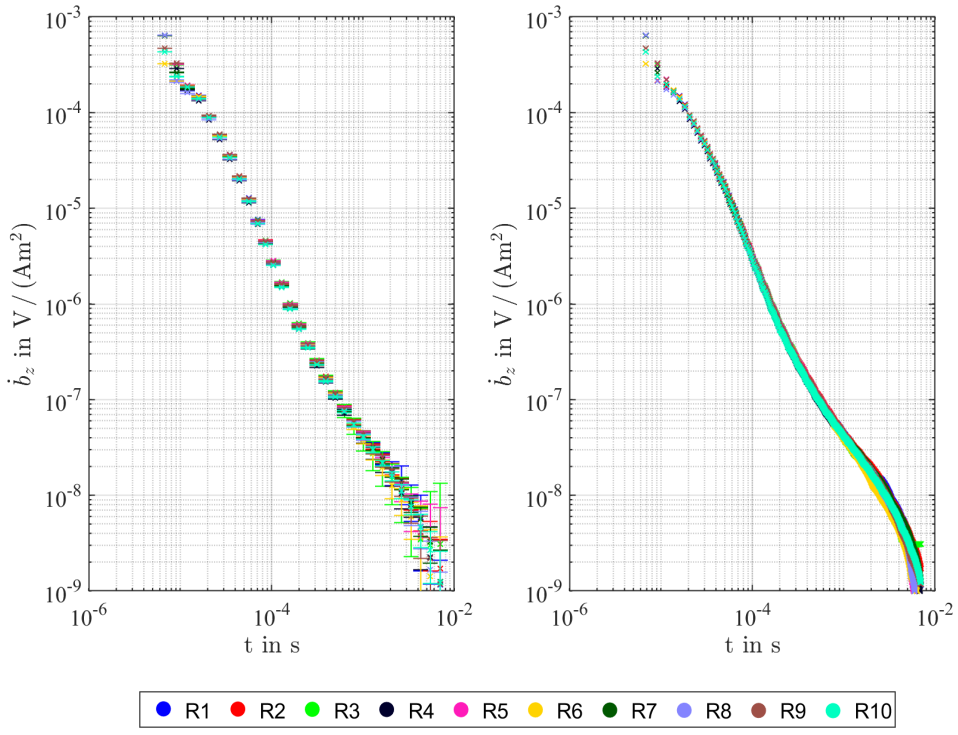


**Fig. 4.12.:** Stacked vertical TEM responses $\dot{b}_z$ in V/m$^2$ including the standard deviation as error bar (left) and interpolated responses (right) for central loop measurements.

**Tab. 4.7.:** ARIMA estimates $\boldsymbol{\phi}$ in Box-Jenkins notation including the Ljung-Box test results in terms of p-values ($\alpha = 0.05$) for central loop measurements.

| ARIMA model | p | d | q | $\boldsymbol{\phi}_1$ | Ljung-Box test p-value |
|---|---|---|---|---|---|
| R1 | 1 | 3 | 0 | -0.008 | 0.956 |
| R2 | 1 | 3 | 0 | 0.009 | 0.943 |
| R3 | 1 | 3 | 0 | 0.055 | 0.932 |
| R4 | 1 | 3 | 0 | 0.067 | 0.952 |
| R5 | 1 | 3 | 0 | 0.059 | 0.935 |
| R6 | 1 | 3 | 0 | 0.026 | 0.956 |
| R7 | 1 | 3 | 0 | 0.040 | 0.967 |
| R8 | 1 | 3 | 0 | 0.035 | 0.970 |
| R9 | 1 | 3 | 0 | -0.022 | 0.945 |
| R10 | 1 | 3 | 0 | 0.040 | 0.957 |

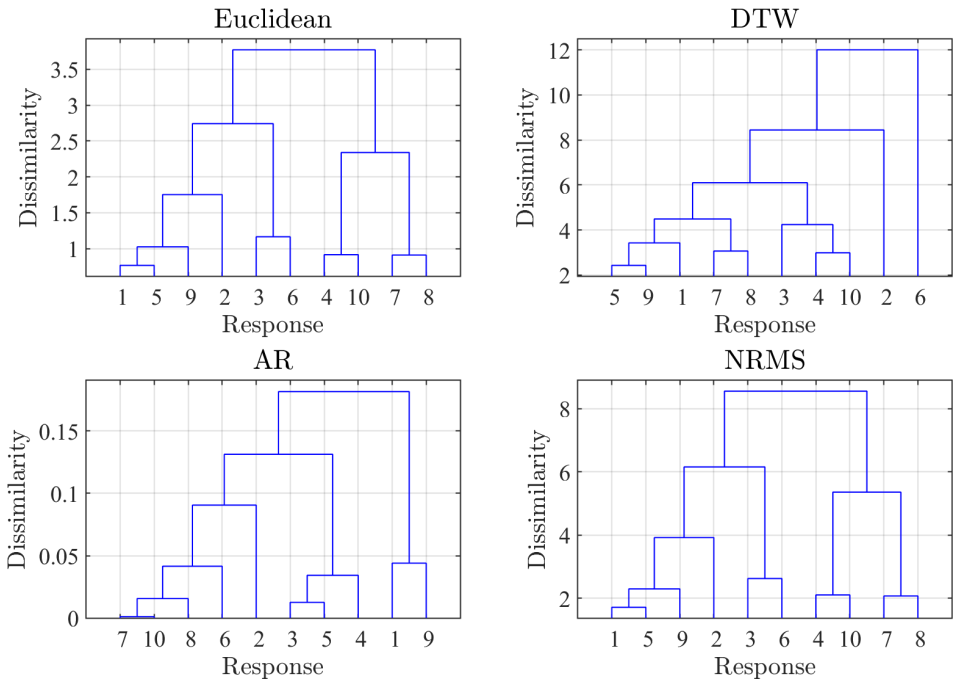


**Fig. 4.13.:** Hierarchical cluster trees for Euclidean, DTW, AR, and NRMS distance metric for central loop measurements.

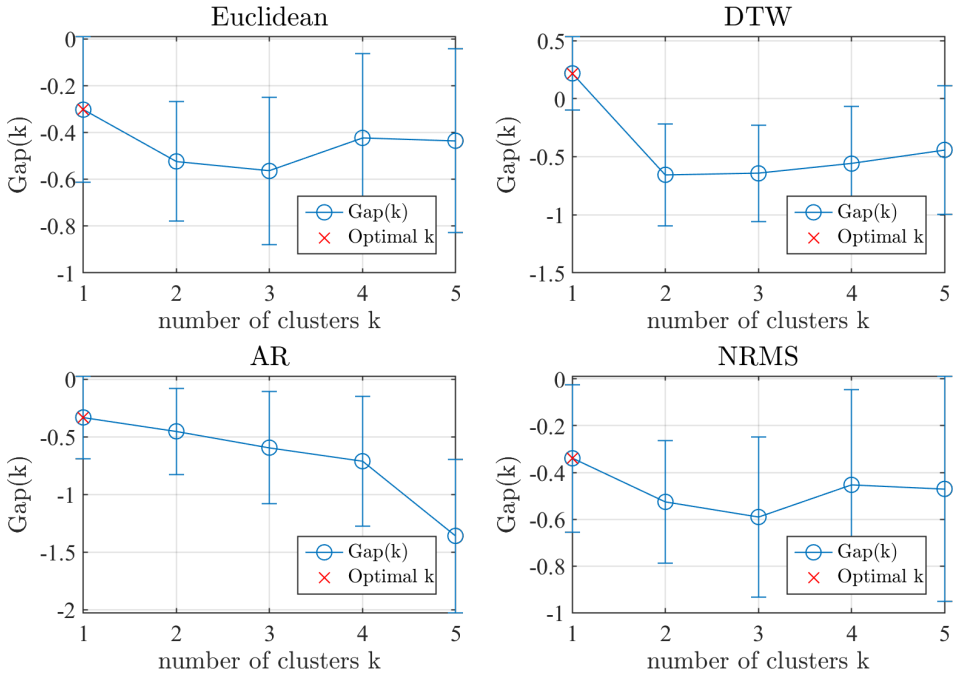


**Fig. 4.14.:** Optimal number of clusters for central loop measurements based on gap statistic for Euclidean, DTW, AR, and NRMS distance metric.

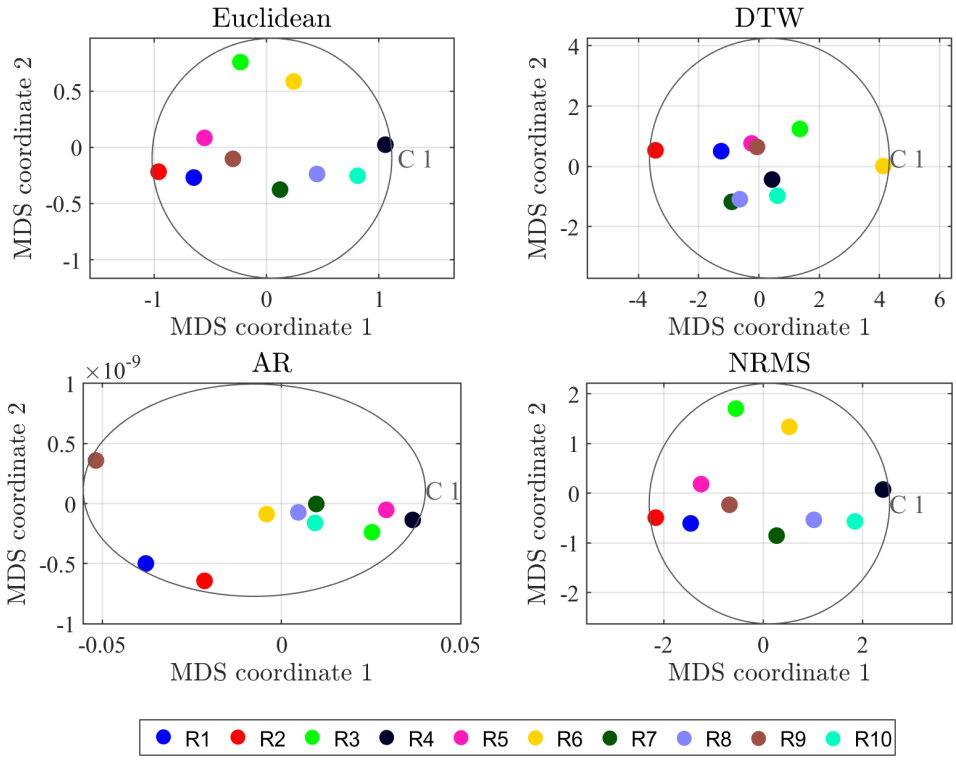


**Fig. 4.15.:** MDS representation of pairwise distance matrices for Euclidean, DTW, AR, and NRMS distance metric and identified cluster for central loop measurements.

### Separate loop measurements at P2

Figure 4.16 shows the vertical stacked transient responses including the standard deviation for each gate as error bar and the interpolated vertical response at observation point P2. The responses exhibit higher standard deviations for later gates in comparison to the central loop measurements. Due to the Rx-Tx offset the amplitude is decreased in general and the transient responses are much more affected by ambient noise. R1 has very high standard deviations after the first sign change and even features a second sign change at about $1 \cdot 10^{-3}$ s after transmitter current turn-off. The amplitudes of R8 for early gates are smaller and for later gates higher in comparison to the remaining responses. Furthermore, the sign change occurs slightly earlier. Measurements at observation point P2 were conducted with the low-frequency receiver coil which does not operate in its intended tuning range at 25 Hz repetition rate. Amplitudes for early times up to 40 µs are damped due to the LF-coil system response (cf. Figure B.1). The LF-coil has a much higher effective coil area (200 $\mathrm{m}^2$) compared to the HF-coil (31.4 $\mathrm{m}^2$) and thus is more sensitive to ambient noise. However, due to the fast decaying current system of the low conductive subsurface it is necessary to use a sensitive receiver coil in order to measure the small amplitudes of the transient response at late times. The noise transition level is about $1 \cdot 10^{-8}$ $\mathrm{V/m}^2$ . Based on the noise transition level and the tuning range of the LF-coil, the first seven and the last five gates are not considered in the cluster analysis.

Table 4.8 shows the estimated ARIMA models including the Ljung-Box statistic. Since the p-Values of the Ljung-Box test are high, the estimated ARIMA models are considered well-defined. This is also supported by the fitted ARIMA time series in comparison with the measured responses (see Figure A.8). Applying the pairwise Euclidean, DTW, AR, and NRMS distance metric to the transformed normalized transient responses and successive clustering, leads

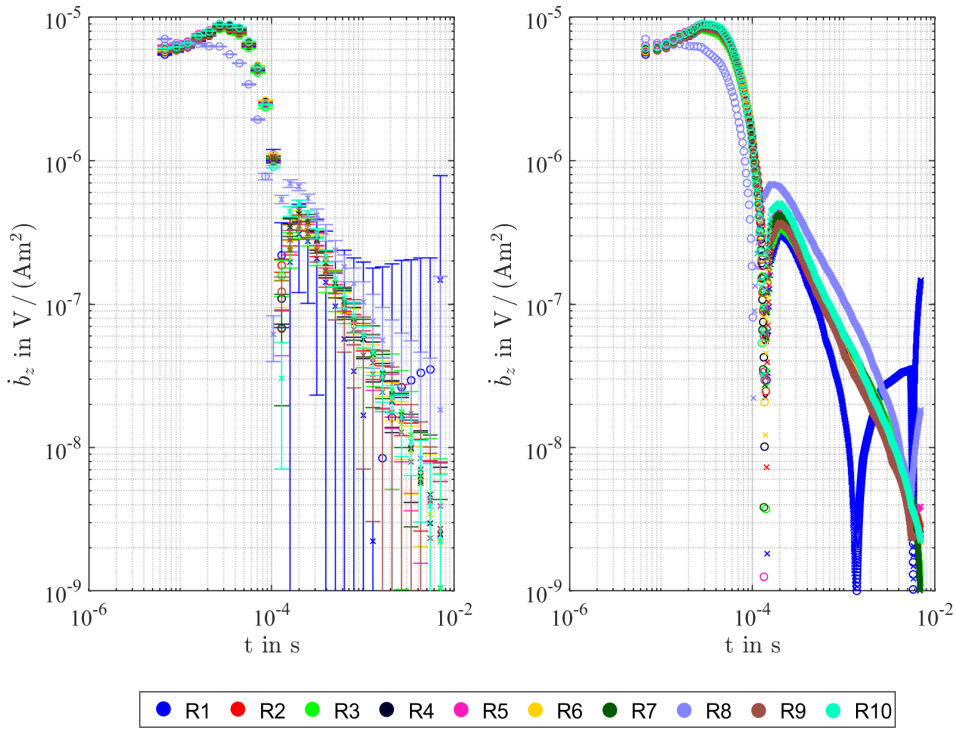


**Fig. 4.16.:** Stacked vertical TEM responses $\dot{b}_z$ in $\mathrm{V/m}^2$ including the standard deviation as error bar (left) and interpolated responses (right) for measurements at observation point P2. Crosses mark positive and circles mark negative values.

**Tab. 4.8.:** ARIMA estimates $\boldsymbol{\phi}$ and $\boldsymbol{\theta}$ in Box-Jenkins notation including the Ljung-Box test results in terms of p-values ($\alpha = 0.05$) for TEM measurements at P2.

| ARIMA model | p | d | q | $\boldsymbol{\phi_1}$ | $\boldsymbol{\theta_1}$ | $\boldsymbol{\theta_2}$ | Ljung-Box test p-value |
|---|---|---|---|---|---|---|---|
| R1 | 1 | 2 | 1 | 0.18 | 0.99 | 0 | 0.946 |
| R2 | 1 | 1 | 1 | 0.57 | 0.42 | 0 | 0.998 |
| R3 | 1 | 1 | 1 | 0.61 | 0.48 | 0 | 0.999 |
| R4 | 1 | 1 | 1 | 0.62 | 0.49 | 0 | 0.999 |
| R5 | 1 | 1 | 1 | 0.65 | 0.53 | 0 | 0.999 |
| R6 | 1 | 1 | 1 | 0.65 | 0.54 | 0 | 0.999 |
| R7 | 1 | 1 | 1 | 0.66 | 0.55 | 0 | 0.999 |
| R8 | 1 | 1 | 2 | 0.81 | 0.70 | 0.04 | 0.998 |
| R9 | 1 | 1 | 1 | 0.60 | 0.46 | 0 | 0.998 |
| R10 | 1 | 1 | 1 | 0.64 | 0.51 | 0 | 0.999 |

to the hierarchical cluster trees shown in Figure 4.17. The dendrograms reveal an obvious distinguishable pattern. R1 and R8 are well separated from the remaining responses, indicated by large dissimilarity values. The optimal number of clusters is five for the Euclidean, and NRMS distance metric and three for the DTW, and AR distance metric (Figure 4.18). For a better visualization of the underlying cluster structure, Figure 4.19 shows the MDS representations of the pairwise distance matrices as well as the identified clusters. Each MDS representation shows well separated clusters, especially for R1 and R8. While measuring R1, a DGPS (Differential Global Positioning System) device was close to the receiver coil causing high ambient noise at later time gates. R8 was measured while a second turn was added to the transmitter loop. This leads to an enhanced inductance and capacitance of the transmitter loop system (Helwig and Kozhevnikov, 2003; Oelschlägel, 2015), leading to a different transmitter current function and a slightly different electromagnetic response.

The MDS representation of the Euclidean and NRMS pairwise distance matrices are almost identical. Due to slight amplitude variations throughout the remaining responses, the data is divided into five clusters. However, the DTW and AR distance metric identify three distinct clusters. Cluster one is formed by R8, cluster three is formed by R1 and the remaining responses are forming cluster two (cf. red boxes Figure 4.19 top right, bottom left). The clustering results are validated using silhouette plots (Figure 4.20). The silhouette values are all positive and high for each metric, indicating well assigned responses with respect to their clusters. A strong structure is indicated by high average silhouette widths. However, a cluster result containing more than three clusters seems unreasonable, since the survey side did not change over the monitoring period and no changes in the transient responses, besides R1 and R8, are expected. Changes may only occur due to slight noise variations during measurements resulting in more detected clusters for the Euclidean and NRMS distance metric.

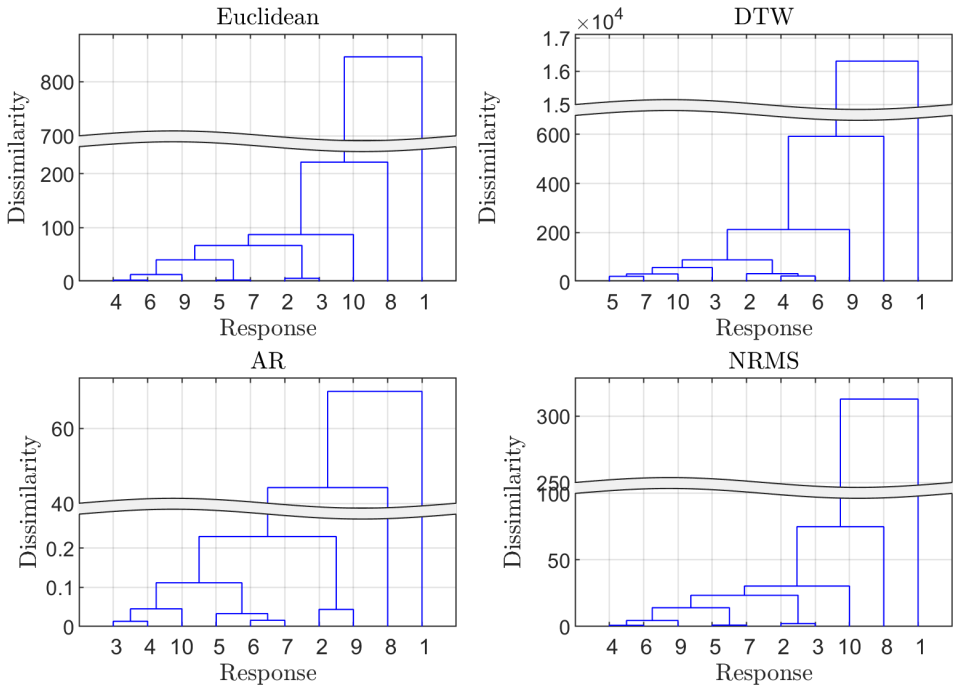


**Fig. 4.17.:** Hierarchical cluster trees for Euclidean, DTW, AR, and NRMS distance metric for TEM measurements at P2.

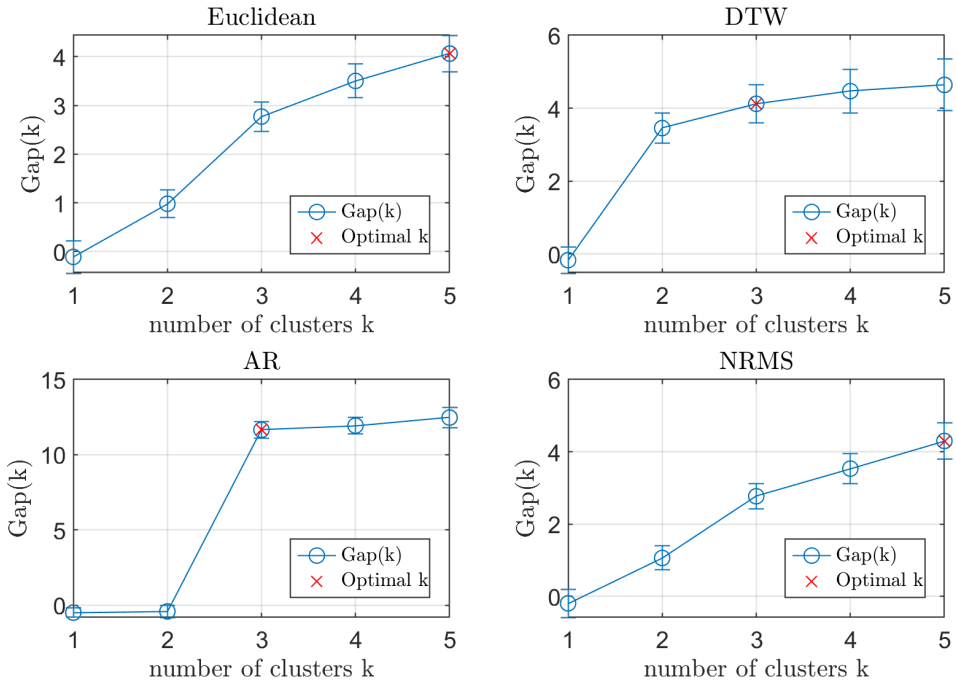


**Fig. 4.18.:** Optimal number of clusters for TEM measurements at P2 based on gap statistic for Euclidean, DTW, AR, and NRMS distance metric.

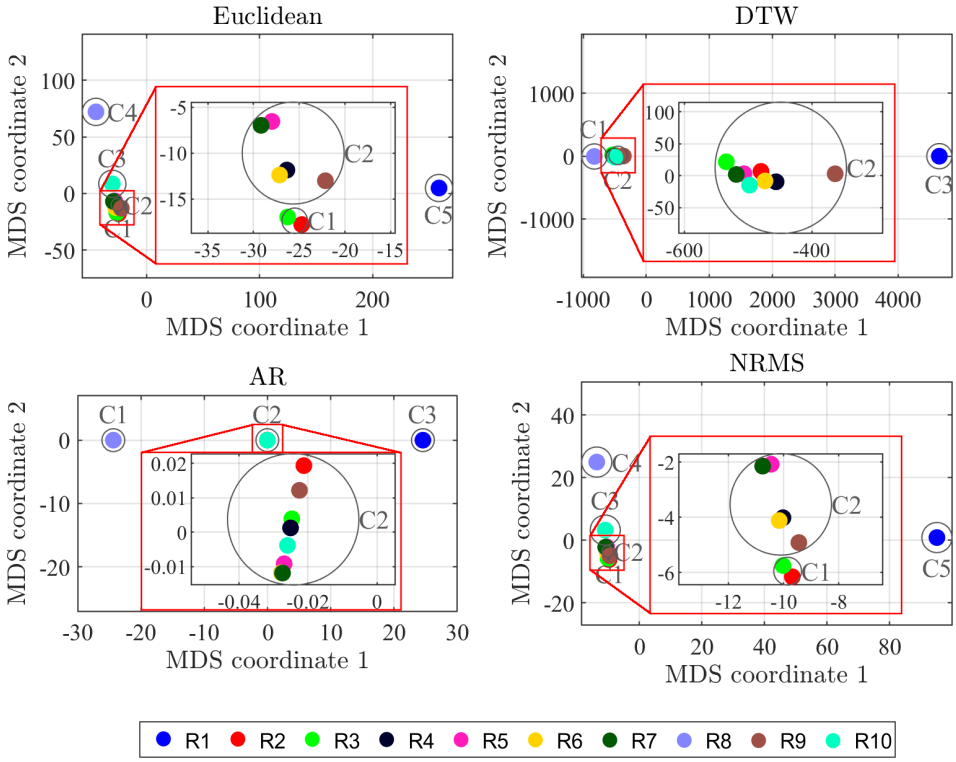


**Fig. 4.19.:** MDS representation of pairwise distance matrices and identified clusters for Euclidean, DTW, AR, and NRMS metric for TEM measurements at P2.

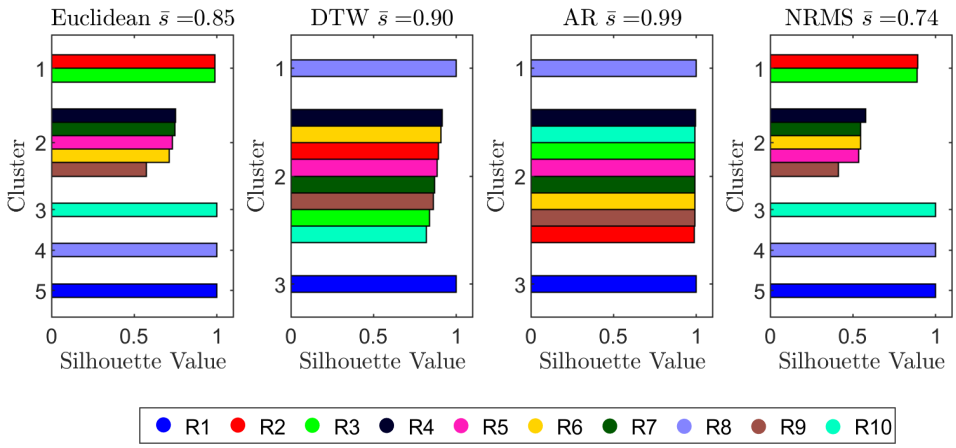


**Fig. 4.20.:** Silhouette values according to identified cluster for Euclidean, DTW, AR and NRMS metric for TEM measurements at P2.

### Separate loop measurements at P3

Figure 4.21 shows the stacked vertical transient responses including the standard deviation for each gate as error bar and the interpolated vertical response (right). All responses exhibit a good amplitude and time alignment except R8, due to the double dipole-moment of the transmitter loop exhibiting a similar behaviour like R8 at observation point P2. The noise transition level is about $1 \cdot 10^{-8}$ V/m$^2$. Based on the tuning range of the LF-coil and noise transition level, the first seven and last five gates are not considered in cluster analysis.

Table 4.9 shows the estimated ARIMA models including the Ljung-Box statistic. The p-Values of the Ljung-Box test are high, indicating well-defined ARIMA models. This is also supported by the actual fitted ARIMA time series in comparison with the measured responses (see Figure A.9). Figure 4.24 shows the hierarchical cluster trees for TEM measurements at observation point P3. For all metrics, R8 is clearly separated by the remaining responses, indicating a single cluster assignment. This is also supported by the gap statistic. For the Euclidean and NRMS distance metric the optimal number of clusters is four and two for the DTW and AR metric (4.22). In addition to verify the optimal number of clusters, silhouette plots are provided (cf. Figure 4.20). The silhouette values are all positive and high throughout every metric, indicating well assigned responses with respect to their clusters. The average silhouette width is also high indicating a strong to reasonable cluster structure. However, a cluster number of four seems unreasonable since changes in the transient responses can only be attributed to noise. Therefore, a clustering result with two clusters is much more likely.

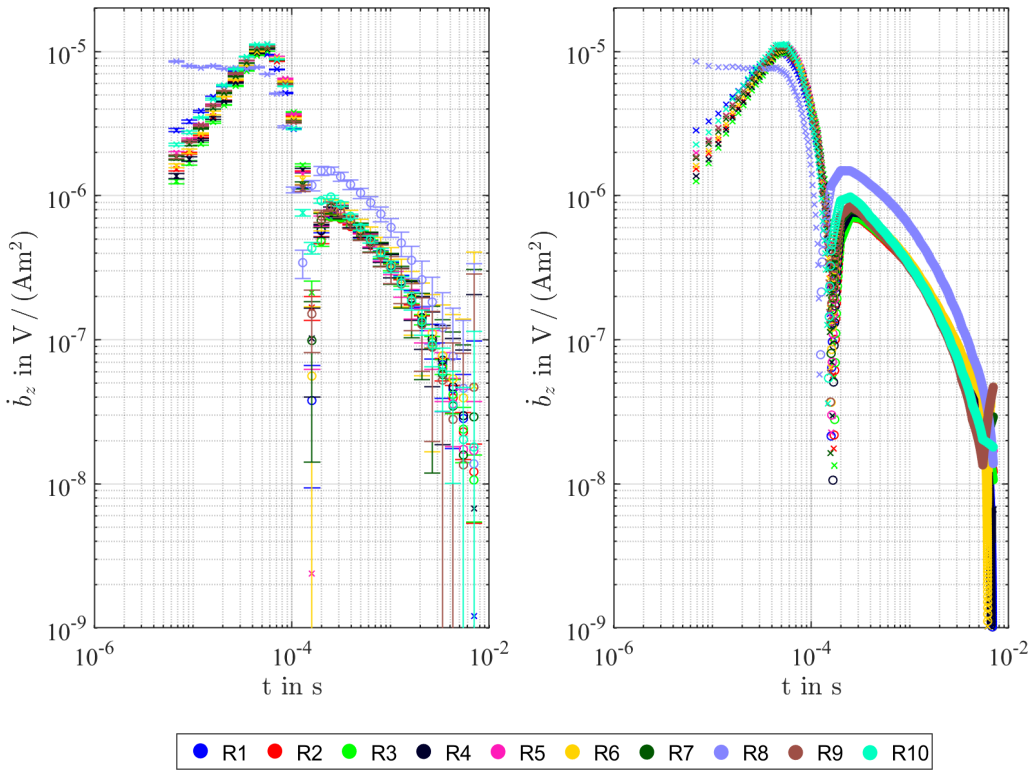


**Fig. 4.21.:** Stacked vertical TEM responses $\dot{b}_z$ in V/m$^2$ including the standard deviation as error bar (left) and interpolated responses (right) for measurements at observation point P3. Crosses mark positive and circles mark negative values.

**Tab. 4.9.:** ARIMA estimates $\boldsymbol{\phi}$ and $\boldsymbol{\theta}$ in Box-Jenkins notation including the Ljung-Box test results in terms of p-values ($\alpha = 0.05$) for TEM measurements at P3.

| ARIMA model | p | d | q | $\boldsymbol{\phi_1}$ | $\boldsymbol{\phi_2}$ | $\boldsymbol{\theta_1}$ | $\boldsymbol{\theta_2}$ | Ljung-Box test p-value |
|---|---|---|---|---|---|---|---|---|
| R1 | 1 | 2 | 2 | 0.62 | 0 | 1.03 | -0.05 | 0.851 |
| R2 | 1 | 2 | 2 | 0.57 | 0 | 0.83 | 0.15 | 0.609 |
| R3 | 2 | 2 | 2 | 0.36 | 0.14 | 0.38 | 0.60 | 0.705 |
| R4 | 2 | 2 | 2 | 0.38 | 0.12 | 0.17 | 0.80 | 0.584 |
| R5 | 1 | 2 | 2 | 0.57 | 0 | 0.86 | 0.12 | 0.645 |
| R6 | 1 | 2 | 2 | 0.57 | 0 | 0.90 | 0.09 | 0.655 |
| R7 | 1 | 2 | 2 | 0.60 | 0 | 1.08 | -0.09 | 0.842 |
| R8 | 1 | 2 | 1 | 0.44 | 0 | 0.98 | 0 | 0.871 |
| R9 | 1 | 2 | 2 | 0.56 | 0 | 0.99 | -0.003 | 0.800 |
| R10 | 1 | 2 | 2 | 0.45 | 0 | 0.66 | 0.31 | 0.618 |

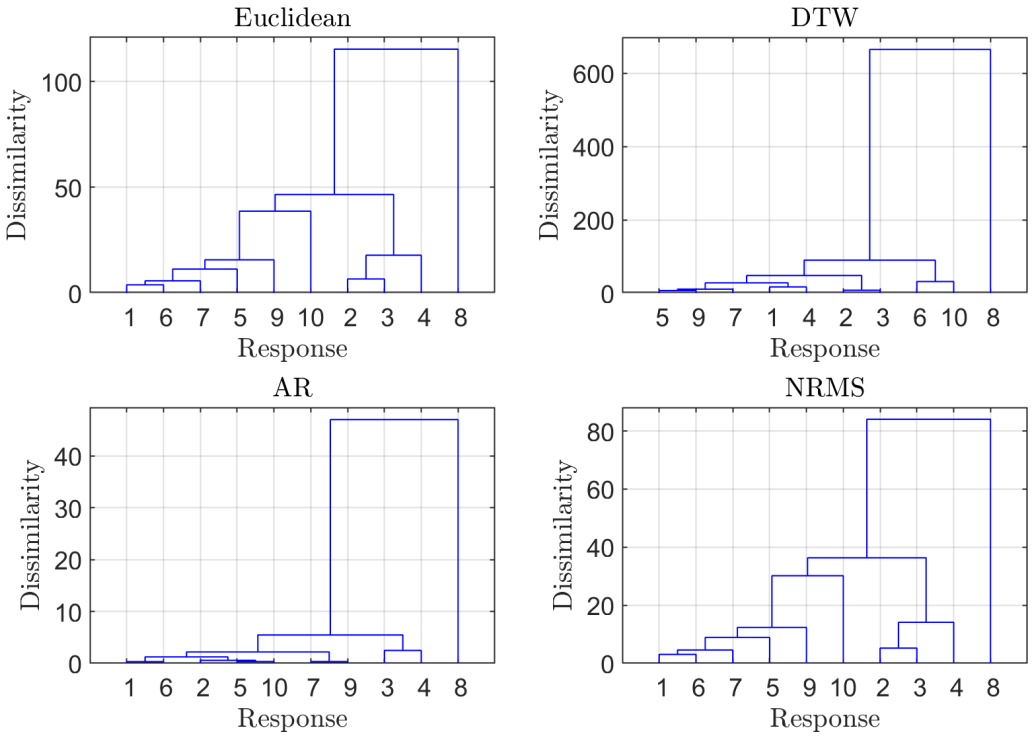


**Fig. 4.22.:** Hierarchical cluster trees for Euclidean distance, DTW, AR and NRMS distance for TEN measurements at P3.

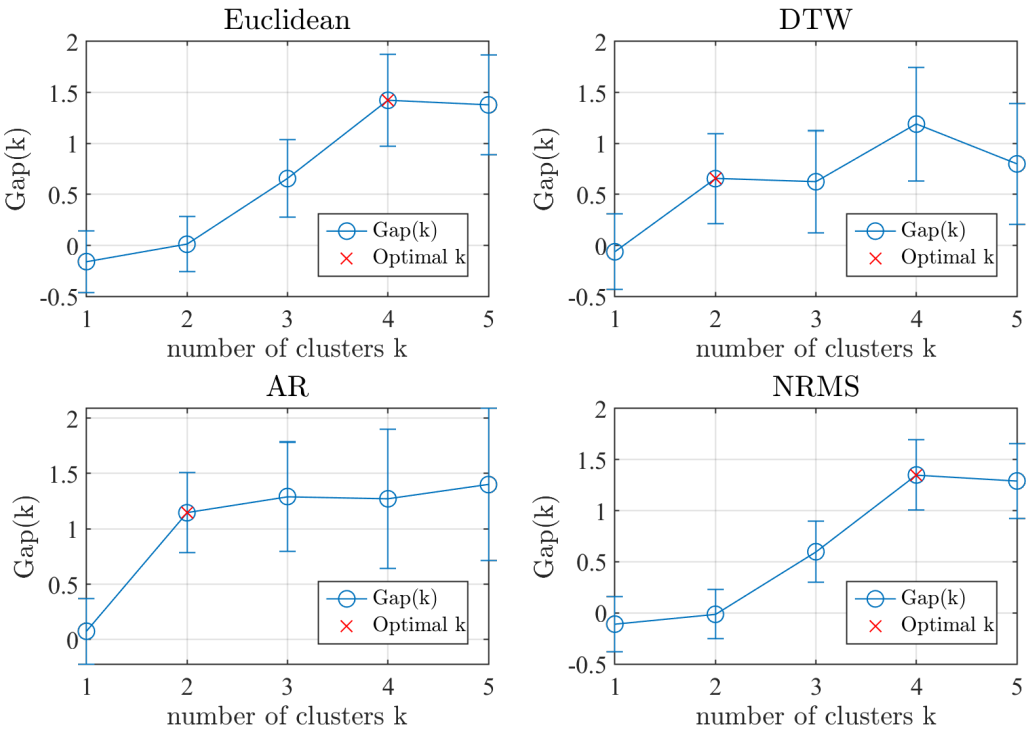


**Fig. 4.23.:** Optimal number of clusters for TEM measurements at P3 based on gap statistic for Euclidean, DTW, AR, and NRMS distance metric.

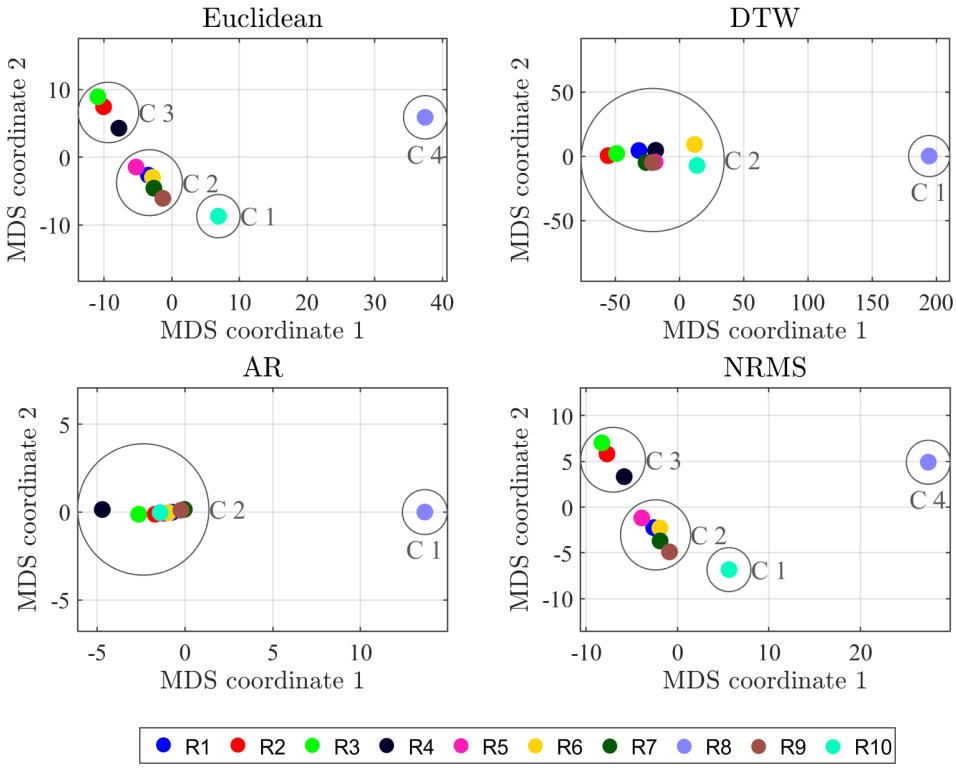


**Fig. 4.24.:** MDS representation of pairwise distance matrices and identified clusters for Euclidean, DTW, AR, and NRMS metric for TEM measurements at P3.

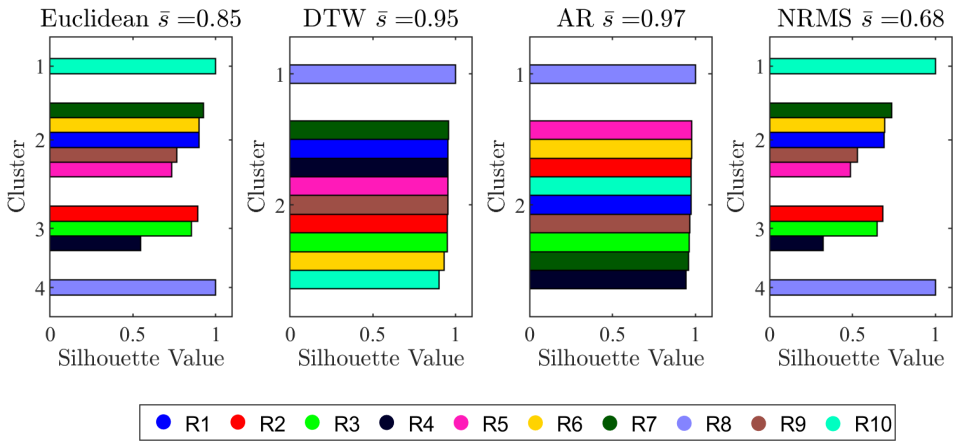


**Fig. 4.25.:** Silhouette values according to identified cluster for Euclidean, DTW, AR, and NRMS metric for TEM measurements at P3.

### 4.4.2. Conclusions

The developed workflow for identifying similar transient electromagnetic responses, was successfully applied to the long-term monitoring data set of Tharandter Wald. After removing oversaturated gates and gates in the noise transition zone, the repeated measurements for central loop configuration, using the TEM47 transmitter and the high-frequency receiver coil, are unambiguously statistically reproducible in the context of cluster analysis (optimal number of clusters of one) for the Euclidean, DTW, AR, and NRMS distance metric. However, the Euclidean and NRMS distance metric are very sensitive to noise affected data, resulting in more number of clusters than expected, especially for separate loop measurements. In this context, they are not well suited as similarity criterion for transient electromagnetic responses. Based on the DTW and AR metric, the optimal number of clusters for measurements at observation point P2 is three. The Responses R1 and R8 can clearly be identified as separate clusters due to large ambient noise (DGPS device) respectively a different transmitter loop setup (double wire turn). The remaining responses are similar. Measurements conducted at observation point P3 are considered reproducible for the DTW and AR metric, except for response R8. Based on the clustering results, the DTW and AR distance metric are superior in detecting similar transient responses compared to the Euclidean and NRMS distance metric.

# 5. Borehole TEM measurements at the CMC Field Research Station

The measurements presented in this chapter were conducted in the context of a collaborative project between the Institute of Geophysics and Geoinformatics at the Technical University Bergakademie Freiberg and the Carbon Management Canada Research Institutes (CMC). The aim of this project was to investigate a new approach to quantitative $CO_2$ injection monitoring using borehole electromagnetic measurements (CMC Project C394) in order to investigate if electromagnetic monitoring is feasible and possibly advantageous to seismic monitoring. The key goals are

- the refinement of existing and the development of new monitoring technologies to determine the detection threshold of gaseous $CO_2$ in the subsurface,
- the development of monitoring technologies with respect to enhanced oil recovery and
- the risk reduction of carbon sequestration in general (Lawton et al., 2017).

Therefore, a pilot Carbon Capture and Storgae (CCS) site was established by CMC including a Field Research Station (FRS) operated by the Containment and Monitoring Institute (CaMI) near Brooks, Alberta (Canada). It provides an experimental environment for a multitude of different experiments. Originally, it was planned to sequestrate 600 t gaseous $CO_2$ over one year into a saline aquifer at a depth of around 300 m. The shallow target was particularly chosen to test trapping mechanisms of gaseous $CO_2$ and to initiate a controlled leakage to investigate migration patterns of $CO_2$ in the subsurface. The injection phase was intended to be split into three-month periods of continuous injection followed by a one-month enclosure period to allow the reservoir pressure to dissipate (Dongas and Lawton, 2016). In order to detect changes in the conductivity due to sequestrated $CO_2$, surface-to-borehole transient electromagnetic measurements were conducted. First baseline measurements at the FRS were obtained from June to July 2016 before $CO_2$ injection. Due to a failure of the main output stage of the power transmitter, only a rather small part of the originally planned baseline data set could be obtained during the 2016 field survey. However, the baseline measurements could be repeated in 2018, as only an insignificant amount of $CO_2$ ($\sim$4 t) had been injected into the reservoir due to technical problems at the well site. At the time of writing, a post-injection repeat survey is still lacking but would be highly desirable as $CO_2$ is being continuously injected since March 2020.

In the first section of this chapter, a general geological site characterization at the FRS is given followed by a description of the electrical rock properties of the local subsurface. Furthermore, the influence of $CO_2$ on the reservoir conductivity is investigated and the rock volume occupied by 600 t $CO_2$ is estimated. 3D finite element simulations for the baseline state (no $CO_2$ injected) and the injected state are evaluated to estimate the influence of $CO_2$ on the transient response. At the end of this chapter, the baseline measurements and the repeat measurements

are evaluated based on the statistical workflow to detect repeatability of the measurements presented in Chapter 4. Furthermore, the relative and absolute differences between the baseline and the repeat measurements are compared with the 3D finite element simulations based on a total amount of 4 t sequestrated $CO_2$.

## 5.1. Geological site characterization

Alberta is well known for its high occurrence of potent natural oil, coal, and gas deposits. They are mainly distributed over the Western Canada Sedimentary Basin (Figure 5.1), which extends from the northern U.S.A. to the northwest of Canada. The Western Canada Sedimentary Basin developed in two major phases. Firstly, by miogeosyncline and a platform phase during the upper Precambrian through Middle Jurassic. Secondly, by a foreland phase during Upper Jurassic through Tertiary (Bustin, 1991). Thereby, large natural gas fields were formed which are mainly located in sand lenses. The Brooks gas field, for instance, in the County of Newell is the third-largest in Alberta. The gas-bearing zone is formed by sandy shale (Ley, 1935). Thus, the County of Newell has a high potential for applying CCS-technologies since the depleted hydrocarbon reservoirs can serve as $CO_2$ reservoir rocks.

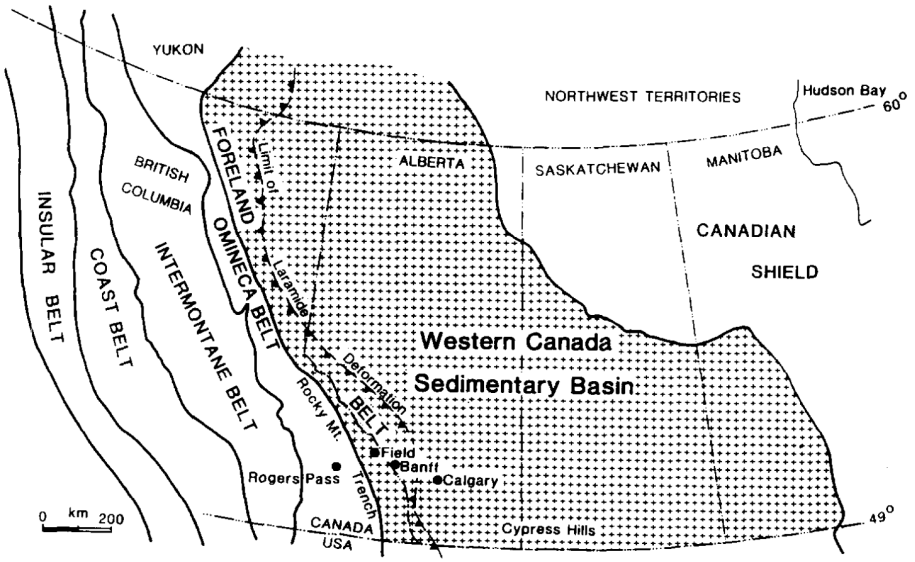


**Fig. 5.1.:** Overview of the regional extend of the Western Canada Sedimentary Basin (Bustin, 1991).

The Field Research Station (FRS) is located in the southeast of Alberta in the County of Newell, ∼20 km southwest of Brooks (Figure 5.2). The coordinates and the unique well identifier (UWI) of the well infrastructure at the FRS are listed in Table 5.1. Since observation well #1 is steel-cased, only observation well #2 is used for transient electromagnetic measurements. Figure 5.3 shows the geological and hydrological units in the County of Newell, Alberta (WorleyParsonsKomex, 2008). In the following, the geological units are briefly described.

**The Overburden** in the region of Newell County is formed by unconsolidated sediments (mainly gravel, till, silt, sand, and clay) overlaying the bedrock. The sediments were deposited in the Quaternary due to glacial activity and were subsequently reworked by eolian and fluvial processes (WorleyParsonsKomex, 2008; Dongas et al., 2014).

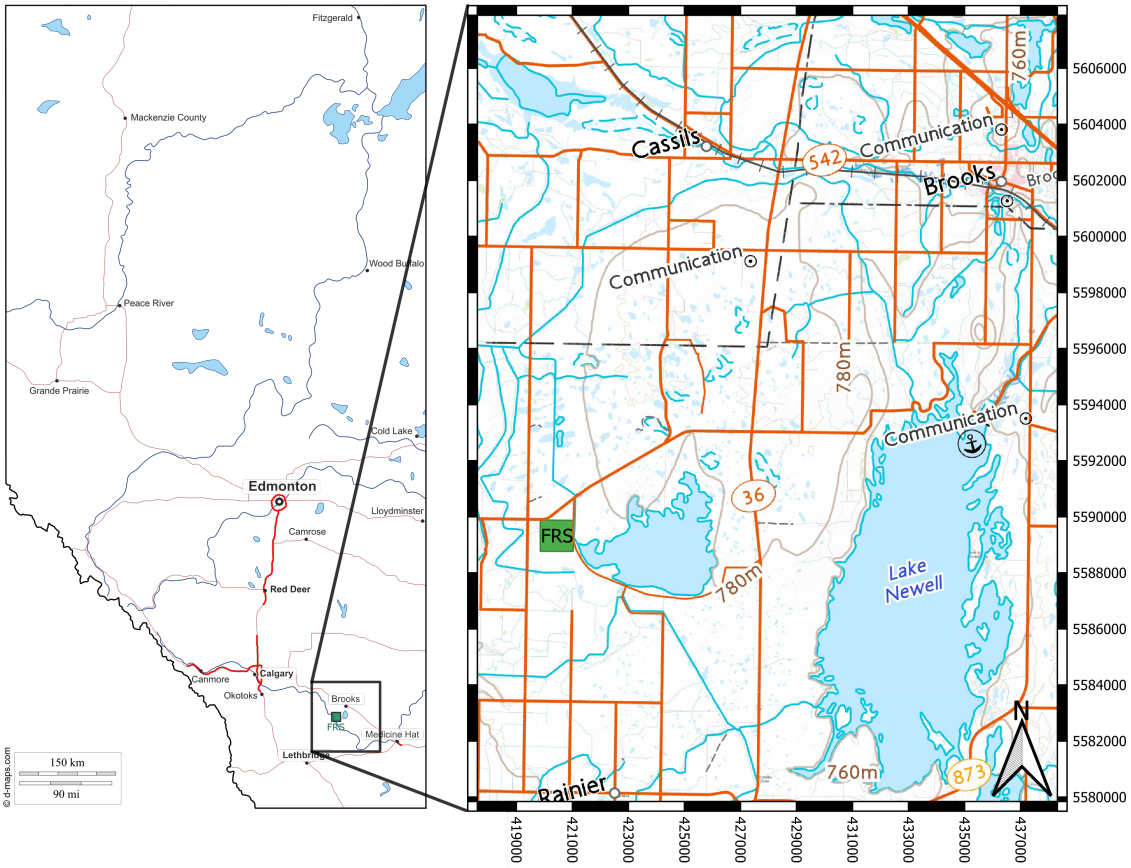


**Fig. 5.2.:** General overview of the Field Research Station in the County of Newell, located SE of Alberta (left). The FRS is located ~20 km southwest of Brooks (right). Coordinate system EPSG:32612 - WGS84/UTM 12N

**Tab. 5.1.:** Coordinates of the well infrastructure at the Field Research Station. Coordinate system EPSG:32612 - WGS84/UTM 12N (D'Gis Group, 2019).

| Well | UWI | Easting | Northing | Elevation [m] |
|---|---|---|---|---|
| Injection Well | 02/10-22-017-16W/0 | 420438 | 5589312 | 779.6 |
| Observation Well #1 | 1F1/10-22-017-16W4/00 | 420459 | 5589333 | 779.7 |
| Observation Well #2 | 1F2/10-22-017-16W4/00 | 420423 | 5589299 | 779.6 |

**The Horseshoe Canyon Formation** consists of fluvial sediments and can reach a thickness of up to 80 m. The sandstones are well-sorted, very fine to medium-grained, and of pale gray appearance. Abundant coal beds, siltstones, and gray to greenish mudstones are interbedded between sandstones (Hamblin, 1998).

**The Bearpaw Formation** underlays the Horseshoe Canyon Formation and is dominated by gray to dark gray silty mudstones and marine shales. Only few potential aquifers may occur due to locally thin distributed Horseshoe Canyon sandstone lenses (Hamblin, 1998; WorleyParsonsKomex, 2008).

**The Oldman Formation** has a maximum thickness of 140 m and can be divided into four members. From uppermost to lowermost: Lethbridge Coal Zone, Dinosaur Park Formation, Siltstone Member, Comrey Sandstone. The Dinosaur Park Formation occupies approximately half of the thickness. Gray to dark-greenish thin interbedded mudstone and medium-grained

| Unit | | Member | Dominant Lithology | Aquifer/Aquitard | Thickness |
|---|---|---|---|---|---|
| Overburden | | | Clay, Till, Silt, Sand, Gravel | Aquifer/Aquitard | 1 to 120 m |
| | | Sand and Gravel | Sand, Gravel | Aquifer | 0 to 40 m |
| Horseshoe Canyon Formation | | | Sandstone, Siltstone, Coal | Aquifer | <80 m |
| Bearpaw Formation | | | Shale | Aquitard | <140 m |
| Belly River Group | Oldman Formation | Lethbridge Coal Zone | Coal | Aquifer | <20 m |
| | | Dinosaur Park | Sandstone, Siltstone, Mudstone | Aquifer | <50 m |
| | | Siltstone | Siltstone, Shale, Minor Sandstone | Aquitard | <20 m |
| | | Comrey Sandstone | Sandstone, Siltstone | Aquifer | <20 m |
| | Foremost Formation | Taber Coal Zone | Coal | Aquifer | <15 m |
| | | | Siltstone, Shale, some Sandstone | Aquifer | <110 m |
| | | McKay Coal Zone | Coal | Aquifer | 35 m |
| | | Basal Belly River | Sandstone | Aquifer | 20 m |
| Lea Park/Pakowki Formation | | | Shale | Aquitard | 175 – 200 m |

**Fig. 5.3.:** Hydrological and geological units in the County of Newell, Alberta (WorleyParsonsKomex, 2008)

sandstone beds are forming the 30 m to 40 m upper part of the Dinosaur Park Formation which is well known for its large amounts of well-preserved fossils. The lower part is generally 40 m to 50 m thick and consists of fluvial, well-sorted, brown-gray, fine-grained, "salt and pepper" sandstones, interbedded with sandy siltstone (WorleyParsonsKomex, 2008). The underlying Siltstone Member is dominated by pale-colored, thinly interbedded mudstone and fine-grained sandstone. The thickness of the Siltsone Member highly depends on the localized level of erosion of the Dinosaur Park Formation. The Comrey Sandstone consists of thick, sharp-based, sandy bodies separated by thin shale units. Hamblin (1997) states further, that the Comrey Sandstone is a light-gray, quartz-rich, well-sorted sandstone containing aquifers up to 20 m thickness.

**The Foremost Formation** exhibits two coal zones. The Taber Coal Zone is located at the top of the Foremost Formation with a thickness up to 15 m. The McKay Coal Zone separates the fine-grained siltstone and carbonaceous shales of the upper part of the Foremost Formation from the high permeable Basal Belly River Formation at the bottom of the Foremost Formation. There are no significant aquifers expected in the upper part of the Foremost Formation. If aquifers are present, they would be predominantly expected in the Basal Belly River Formation (WorleyParsonsKomex, 2008). The Basal Belly River Sandstone (BBRS) dominantly consists of fine to medium-grained rock with poorly to well-sorted grains. The sandstone framework is characterized by 30 % quartz, 25 % feldspar and 45 % rock fragments (see Figure 5.4).

**The Lea Park/Pakowki Formation** dominantly consists of gray shale and siltstone forming an extensive aquitard throughout the region acting as the base of groundwater protection (WorleyParsonsKomex, 2008).

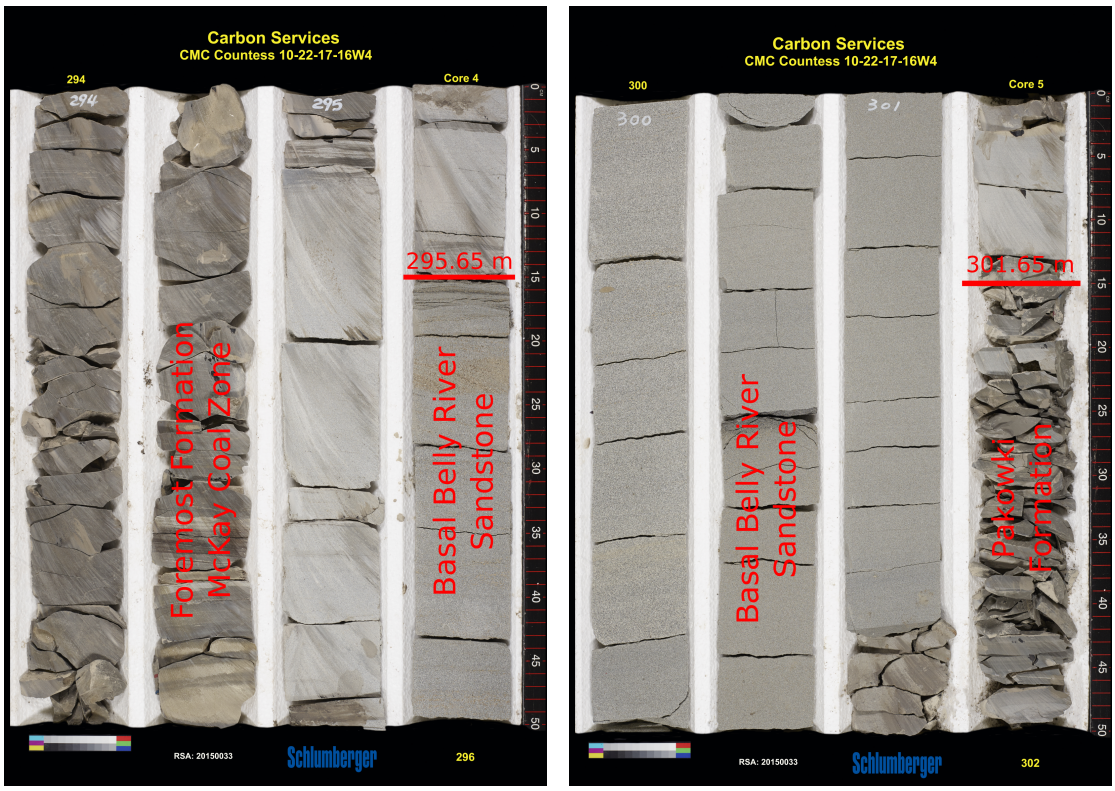


(a) Identified caprock boundary between McKay Coal Zone and BBRS in 295.65 m bKB.

(b) Identified lower sealing boundary between BBRS and Pakowki Formation in 301.65 m bKB.

**Fig. 5.4.:** Core samples showing identified reservoir boundaries formed by the McKay Coal Zone as caprock (a) and the lower sealing by the Pakowki Formation (b).

## 5.2. Electrical rock properties

The reservoir is identified at a depth of 295.65 m to 301.65 m below kelly bushing (bKB) [1,2] and has a porosity of 10 % to 25 % with an intrinsic permeability of 0.57 mD and a reservoir pressure of 3 MPa, based on the hydrostatic pressure gradient (Dongas et al., 2014; Dongas and Lawton, 2016). It contains brackish groundwater with up to 1000 mg/L to 3500 mg/L total dissolved solids (TDS) (WorleyParsonsKomex, 2008). The cap rock is formed by the upper part of the Foremost Formation with a porosity of 11.5 % and a permeability of 0.001 mD (Dongas and Lawton, 2016).

After well drilling completion, four-foot array induction logs (AIF) were conducted in observation well #1 and #2 by CaMI. The log indicates small variations of the electric formation resistivity $\rho_{\mathrm{AIF}}$ ranging from about 3 Ωm to 20 Ωm throughout the observation wells (Figure 5.5). In general, the observed resistivities are low. This is in good agreement with the expected resistivity values due to the high observed porosities in the subsurface and the large amounts of highly conductive groundwater throughout the region. Based on the well logs of both observation wells (Schlumberger Limited, 2016), the bottom-hole temperature is 20.3 °C at 350 m depth. Assuming a geothermal gradient of 3 °C per 100 m (Kertz, 1969), the temperature inside the reservoir is ∼18.5 °C. Table 5.2 shows a summary of the mean resistivities based on the

[1] An elevated adapter on the rig floor connecting the rotary table to the kelly (Ramsey, 2020).
[2] Conversion to meter below ground level (bgl): 0 m (bKB) = −4.9 m (bgl) (Appendix C.1)

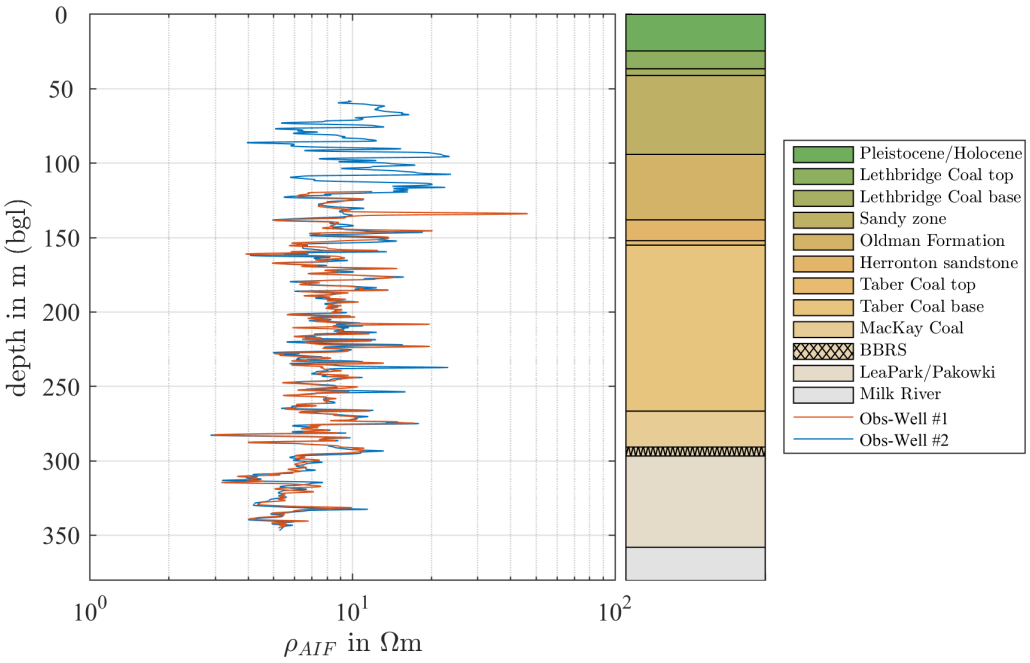


**Fig. 5.5.:** Four-foot array induction log (left) for observation well #1 and #2 in comparison with identified lithological units (right).

AIF-log of observation well #2, the thickness, and the depth of the top layer for each identified lithological unit (Osadetz et al., 2017).

### 5.2.1. Influence of $CO_2$ on reservoir conductivity

A crucial aspect of reservoir monitoring using electromagnetic methods is predicting conductivity changes of the target formation once $CO_2$ is injected. The calculated conductivity change and the estimated rock volume occupied by $CO_2$ are essential parameters for the later transient electromagnetic 3D forward simulations.

The electrical conductivity $\sigma_0$ of water-bearing clay-free porous rocks is proportional to the electrical conductivity $\sigma_w$ of the pore water and can be described by Archie's law (Archie, 1942)

$$\sigma_0 = S_w^n \Phi^m \sigma_w, \tag{5.1}$$

where $S_w$ denotes the pore water saturation, $\Phi$ the porosity, $m$ the cementation exponent and $n$ the saturation exponent. The pore water conductivity depends on the amount and type of dissolved salts and temperature. However, Equation 5.1 is only valid, if the pore water is brine or water and if it is the only available electrical conductor in the rock. In the presence of a reactive gas like $CO_2$, the pore water conductivity is far more complex due to dissolution and partial dissociation of $CO_2$ into the pore water. Based on laboratory experiments, Börner et al. (2013) developed an adapted conductivity model based on Archie's law, which accounts for the physicochemical processes of pore water in presence of $CO_2$ under reservoir conditions. It is defined as

$$\sigma_{\text{reservoir}} = S_w^n \Phi^m \sigma_w \sigma_w^{\text{norm}}, \tag{5.2}$$

where $\sigma_w^{\text{norm}}$ is the conductivity contrast. It is a semi-analytical formulation based on an extensive laboratory study. Additionally to the semi-analytical formulation, J.H. Börner, 2015

**Tab. 5.2.:** Overview of the thickness, depth to top layer below ground level, and mean resistivity for each identified lithological unit at the FRS.

| **Formation** | **Member** | **Thickness** [m] | **Depth to TOP** [m (bgl)] | **Mean resistivity** [Ω m] |
|---|---|---|---|---|
| Pleistocene Holocene | | 24.60 | 0.00 | NA |
| Dinosaur Park Formation | Lethbridge Coal Zone top | 12.00 | 24.60 | NA |
| | Lethbridge Coal Zone base | 4.50 | 36.60 | NA |
| | Sandy zone | 53.00 | 41.10 | $8.26 \pm 4.47$ |
| Oldman Formation | | 44.00 | 94.10 | $10.60 \pm 3.83$ |
| Foremost Formation Belly River Group | Herronton Sandstone | 14.00 | 138.10 | $9.52 \pm 2.31$ |
| | Taber Coal Zone top | 3.00 | 152.10 | $8.48 \pm 2.90$ |
| | Taber Coal Zone base | 111.50 | 155.10 | $7.99 \pm 1.60$ |
| | McKay Coal Zone | 24.15 | 266.60 | $7.64 \pm 2.07$ |
| | Basal Belly River Sandstone | 6.00 | 290.75 | $9.67 \pm 1.63$ |
| Lea Park Pakowki Formation | | 61.35 | 296.75 | $5.55 \pm 0.97$ |

provides an empirical formulation for the conductivity contrast. It can be expressed in terms of salinity $c_{\mathrm{NaCl}}$, temperature $T$ and pore pressure $p$ of the target formation:

$$\sigma_w^{\mathrm{norm}} = 1 + \frac{q_1 + q_2 T + q_3 p}{c_{\mathrm{NaCl}}} \left(1 - \exp[-(q_4 + q_5 T)\, p]\right) - (q_6 + q_7 T)\left(1 - \exp[-q_8 p]\right) \quad (5.3)$$

The empirical determined parameters $q_i$, according to J.H. Börner, 2015, are listed in Table 5.3.

The conductivity in the BBRS Formation under the presence of $CO_2$ can then be calculated using Equation 5.2 and the characteristic reservoir parameters according to Table 5.4. Since

**Tab. 5.3.:** Parameter values for the empirical formulation of the normalized electrical conductivity $\sigma_w^{\mathrm{norm}}$ (J.H. Börner, 2015).

| **Parameter** | **Value** |
|---|---|
| $q_1$ | $2.65 \cdot 10^{-1}\,\mathrm{g/L}$ |
| $q_2$ | $-5.49 \cdot 10^{-4}\,\mathrm{g/(L\,K)}$ |
| $q_3$ | $1.23 \cdot 10^{-3}\,\mathrm{g/(L\,MPa)}$ |
| $q_4$ | $3.24 \cdot 10^{0}\ \ 1/\mathrm{MPa}$ |
| $q_5$ | $-7.74 \cdot 10^{-3}\,\mathrm{MPa/K}$ |
| $q_6$ | $5.18 \cdot 10^{-1}$ |
| $q_7$ | $-1.25 \cdot 10^{-3}\,1/\mathrm{K}$ |
| $q_8$ | $3.28 \cdot 10^{-1}\,1/\mathrm{MPa}$ |

no information about the cementation and saturation exponents are given, literature values for sandstone of $n = 2$ and $m = 1.4$ are assumed (Schön, 1996). Furthermore, the pore water saturation is assumed to be 0.5 (Macquet et al., 2018) and the conductivity $\sigma_w = 0.6\,\mathrm{S/m}$ is given by Hamann and Vielstich (1998) based on a TDS value of 3000 mg/L. This leads to a reservoir conductivity of about 0.01 S/m respectively 100 Ωm after $CO_2$-injection.

Given the total mass $m_{CO2}$, the density $\rho_{CO2}$, the $CO_2$ saturation $S_{CO2}$ inside the target formation and the reservoir porosity $\Phi$, the rock volume occupied by $CO_2$ can be calculated by

$$V_{\mathrm{rock}} = \frac{V_{\mathrm{CO2}}}{S_{\mathrm{CO2}} \cdot \Phi} = \frac{V_{\mathrm{CO2}}}{(1 - S_w) \cdot \Phi}, \tag{5.4}$$

where

$$V_{\mathrm{CO2}} = \frac{m_{\mathrm{CO2}}}{\rho_{\mathrm{CO2}}}. \tag{5.5}$$

The density $\rho_{CO2}$ is thereby a function of temperature and pressure, and can be calculated using the equation of state for real gases after Peng and Robinson (1976) (see Appendix C.2 for further details). For the given initial parameters, the total rock volume occupied by $CO_2$ is 120 000 $m^3$. Since the ratio of the vertical to horizontal hydraulic permeability of the BBRS Formation $k_V/k_H = 0.1$ and laboratory core measurements indicating small migration capabilities into the Foremost and Pakowki Formation (Dongas and Lawton, 2016), the $CO_2$ will predominately migrate horizontally. As a result, the $CO_2$-plume is assumed to be of cylindrical shape with a radius of 80 m and a height of 6 m. These values are in good accordance with reservoir simulations conducted by CaMI for 600 t sequestrated $CO_2$, one year after injection (Figure 5.6, after Dongas and Lawton (2016)).

**Tab. 5.4.:** Overview of assumed parameter values for reservoir conductivity and rock volume calculation.

| Parameter | Value | |
|---|---|---|
| porosity $\Phi$ | 0.15 | |
| porewater saturation $S_w$ | 0.5 | |
| porewater conductivity $\sigma_w$ | 0.6 | S/m |
| conductivity contrast $\sigma_w^{\mathrm{norm}}$ | 0.94 | |
| cementation exponent m | 1.4 | |
| saturation exponent n | 2 | |
| mass $CO_2$ | 600 000 | kg |
| reservoir pressure | 3 | MPa |
| reservoir temperature | 18.5 | °C |
| salinity $c_{\mathrm{NaCl}}$ | 3000 | mg/L |
| physical state of $CO_2$ | gaseous | |

## 5.3. 3D forward TEM simulations

In order to investigate the effect of sequestrated $CO_2$ on transient electromagnetic measurements, 3D-simulations are carried out for various transmitter locations. The 3D finite element code uses curl-conforming, first-kind Nédélec elements as spatial discretization of the quasi-static Maxwell's equations on a tetrahedral mesh in combination with a time integration using

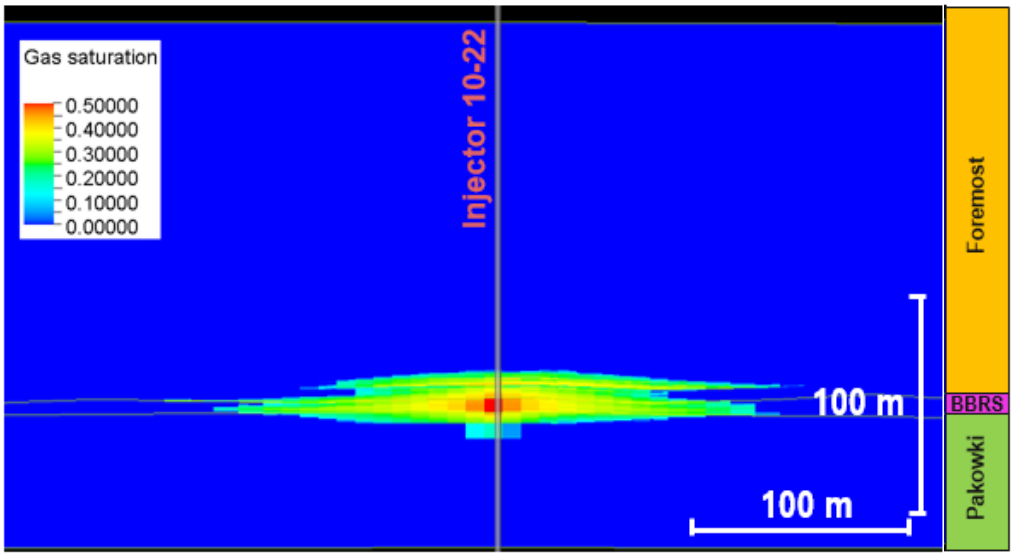


**Fig. 5.6.:** $CO_2$ saturation profile in the Basal Belly River Sandstone 1-year after injection. Modified after (Dongas and Lawton, 2016)

rational Krylov methods (R.U. Börner, 2015). The finite element mesh is constructed using ANSYS Workbench. For each identified geological unit, a 1 km × 1 km isosurface based on refraction seismic measurements exists (Dongas and Lawton, 2015). However, incorporating each geological unit separately in the model is impracticable. Firstly, the thin layer thicknesses would cause either a large amount of elements or elements exhibiting high aspect ratios which would negatively affects the numerical solution. Secondly, the observed resistivity changes between the identified geological units are very small and would hardly be noticeable in actual measurements. To reduce the number of tetrahedral elements and thus, the amount of degrees of freedom, a simplified model of the AIF resistivity model (Table 5.2) is used. The model dimensions are 5000 m × 5000 m × 5000 m including an 5000 m × 5000 m × 2500 m air half-space with a resistivity of $1 \cdot 10^9\,\Omega$m.

Based on the previous resistivity calculation of the $CO_2$-plume, two scenarios are simulated. The first scenario covers the baseline state where no $CO_2$ is injected whereas the second scenario covers the case of a $CO_2$ filled reservoir. The baseline response $\vec{b}_{\text{base}}$ is the transient response of a homogeneous 10 Ωm half-space whereas for the post-injection response $\vec{b}_{\text{inj}}$ a $CO_2$-plume of cylindrical shape with a radius of $r = 80$ m, a height of $h = 6$ m and a resistivity of 100 Ωm is additionally included in the homogeneous half-space. The $CO_2$-plume is centered at 294 m depth. Both scenarios are simulated for two square transmitter loops of 400 m and 100 m side length at different locations with respect to the observation well. Thereby, the 400 m×400 m transmitter loop provides a large dipole moment to increase the signal-to-noise ratio for real measurements, whereas the 100 m×100 m transmitter loop is intended to provide a much more focused setup with respect to the reservoir. The numerical solutions are evaluated along observation well #2 for 0 m to 330 m depth in 5 m steps in a time interval from 250 µs to 100 ms after transmitter current turn-off. Figure 5.7 shows the sliced 3D-models at observation well #2 for both transmitter setups without the air half-space.

Since numerical solutions are only an approximation of the true solution, suitable methods are needed to evaluate the numerical solution with respect to its accuracy. The main contributions to the numerical error originate from the spatial discretization error and from the conductiv-

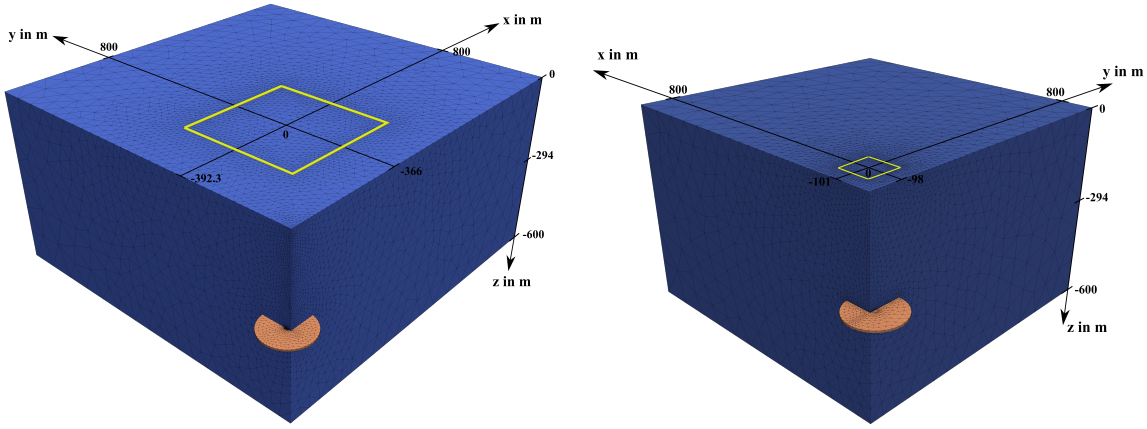


(a) Meshed 3D-model without air half-space for the 400 m × 400 m transmitter loop setup sliced at observation well #2.

(b) Meshed 3D-model without air half-space for the 100 m × 100 m transmitter loop setup sliced at observation well #2.

**Fig. 5.7.:** Overview of meshed 3D-models without air half-space for the large transmitter loop setup (a) and the small transmitter loop setup (b) sliced at observation well #2. The cylindrical shaped 100 Ω m $CO_2$ reservoir (orange) in a depth of 294 m (bgl) below the injection well is embedded in a 10 Ω m homogeneous half-space (blue). Yellow lines mark the transmitter loop.

ity contrasts in the model (Spitzer and Wurmstich, 1999). One way of evaluating the quality of the numerical solution is the comparison with respect to the corresponding analytical solution. However, for complex model geometries an analytical solution does not necessarily exist. Therefore, a constant resistivity value of 10 Ω m is applied to all model cells and the calculated numerical solution is compared to the analytical solution of a homogeneous half-space with the same resistivity value. The left subplots of Figure 5.8 show the numerically computed vertical component of the transient response in comparison with the corresponding analytical solution (black) at 2.5 ms (blue) and 25 ms (orange) after current turn-off as well as the relative deviation of the numerical solution with respect to the analytical solution in percent along the observation borehole for the large (a) and the small (b) transmitter loop setup. The right subplots show the vertical component of the transient responses in a depth of 285 m inside the observation well as a function of time. The numerical solution deviates about ±5 % for early times and less than ±1 % for late times in comparison with the analytical solution. Since the changes are small, the numerical solutions are expected to be still reliable and accurate enough to yield meaningful interpretations for the investigated model scenarios.

In order to track changes caused by $CO_2$ injection with respect to time and depth of the transient response, the relative changes between the response of the baseline state (base) and the injected state (inj) are calculated by

$$\delta|\dot{\vec{b}}|^{\text{inj}}_{\text{base}} = \frac{|\dot{\vec{b}}|_{\text{inj}} - |\dot{\vec{b}}|_{\text{base}}}{|\dot{\vec{b}}|_{\text{base}}} \cdot 100\%\,, \tag{5.6}$$

expressed in terms of percentage deviation as well as the absolute changes

$$\Delta|\dot{\vec{b}}|^{\text{inj}}_{\text{base}} = |\dot{\vec{b}}|_{\text{inj}} - |\dot{\vec{b}}|_{\text{base}} \tag{5.7}$$

in $\mathrm{V}/(\mathrm{A\,m^2})$.

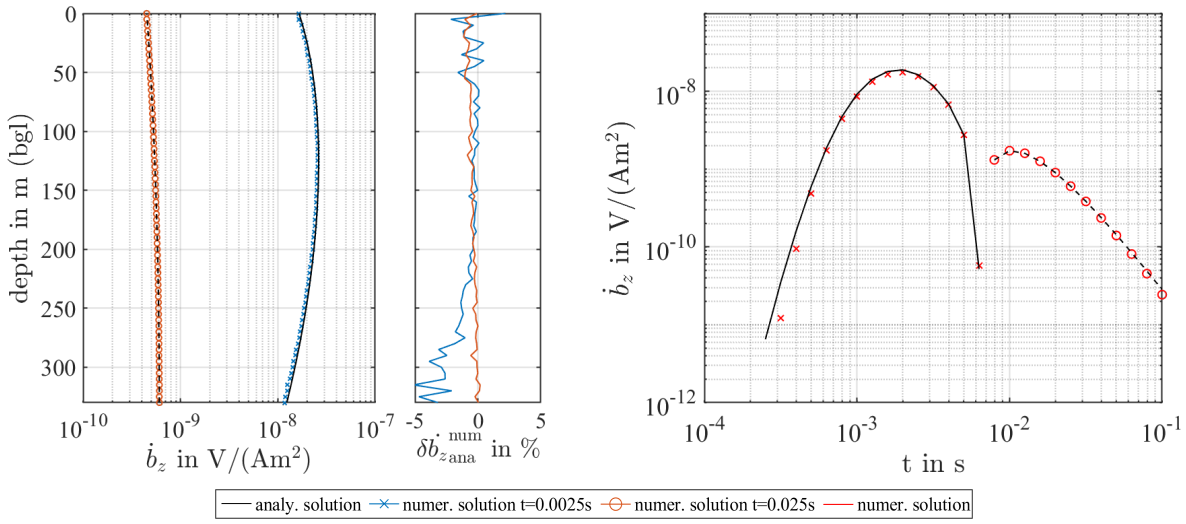


(a) Evaluation of the numerical solution for the large transmitter setup.

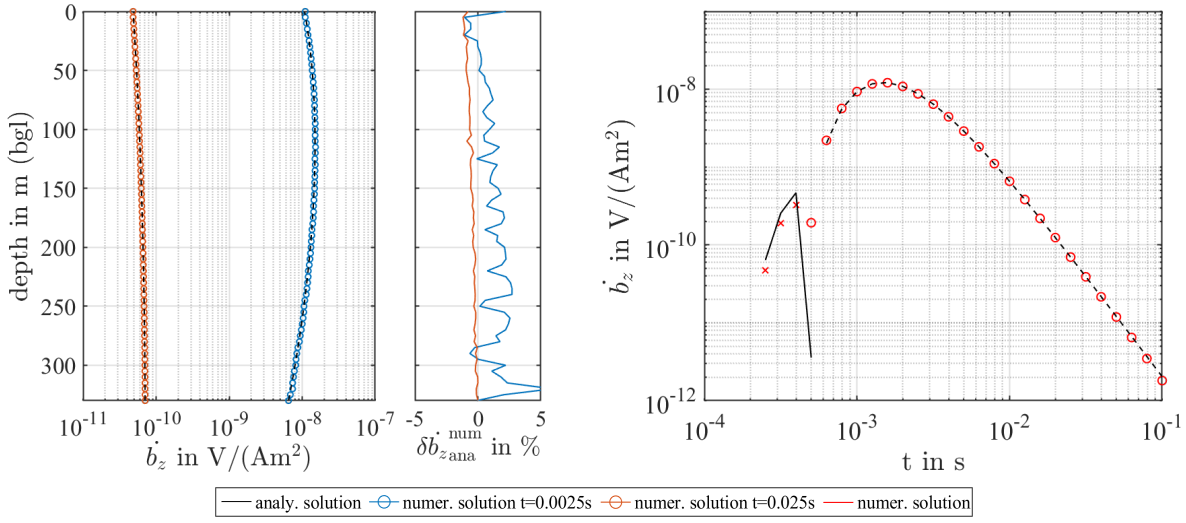


(b) Evaluation of the numerical solution for the small transmitter setup.

**Fig. 5.8.:** (Left) Vertical component $\dot{b}_z$ 2.5 ms (blue) and 25 ms (orange) after current switch-off along the observation borehole for the large (a) and small (b) transmitter setup. The analytical solution for a 10 Ωm half-space is indicated as black line. (Middle) Relative deviation (cf. Equation 5.6) between the numerical and analytical solutions of $\dot{b}_z$ according to the left illustration. (Right) Vertical transient response $\dot{b}_z$ at a depth of 285 m (bgl) within the observation borehole between 250 µs and 100 ms (red numerical, black analytical). Circles and dashed lines indicate negative values whereas crosses and solid lines represent positive values.

Figure 5.9 shows absolute changes $\Delta|\vec{\dot{b}}|_{\mathrm{base}}^{\mathrm{inj}}$ (left) and relative changes $\delta|\vec{\dot{b}}|_{\mathrm{base}}^{\mathrm{inj}}$ (right) of the vertical (top) and radial (bottom) component as a function of depth and time between the baseline and injection state evaluated at observation well #2 for the large transmitter loop setup. The simulated response pattern is complex. At early times, the vertical component $\dot{b}_z$ of the injected response is larger than the background response, indicated by positive absolute changes whereas for later times the absolute changes are lower compared to the background response. Due to the presence of $CO_2$ in the reservoir, the diffusivity is enhanced near the reservoir which results in a faster decay rate of the vertical induced field. This leads to relative changes of 5 % to 20 % for early times and larger than ±40 % at $6.3 \cdot 10^{-3}$ s, the time of sign change in the vertical component. In contrast, the radial component $\dot{b}_r$ of the transient response for the injection state is smaller above and larger below the reservoir compared to the background response for

early times. The horizontal current system, produced by the transmitter loop at the Earths surface, avoids low conductive regions and is therefore consequently deflected above and below the $CO_2$ filled reservoir. This causes relative changes of $-15\,\%$ to $20\,\%$ at early times close to the reservoir and about $\pm 20\,\%$ at the time of sign change in the transient responses.

A similar pattern can be observed for the small transmitter loop setup (see Appendix C.3.1, Figure C.1). However, relative changes of $\pm 15\,\%$ in the radial component can be observed over a much wider time range compared to the large transmitter setup and do exceed values of $\pm 20\,\%$ at times close to the sign change in the transient responses. Since the transmitter is positioned closer to observation well #2, the pattern occurs slightly earlier in time compared to the large transmitter setup.

Based on the 3D simulation results, the following conclusions can be drawn for the real measurements. In a depth from 0 m to 150 m a very large probe spacing can be used since there are no major relative differences expected. A very small probe spacing (1 m to 2 m) should be applied in close vicinity of the reservoir since the relative changes are predominantly noticeable close to the reservoir and are changing rapidly over depth, especially in the radial component of the transient response. Due to the transmitter positioning, the pattern of the relative and absolute changes can be observed at different times. In general, detectability of 600 t $CO_2$ can be expected, if the ambient noise level for real measurements is small.

However, only an insignificant amount of $CO_2$ ($\sim$4 t) was sequestrated during 2016 and 2018 and the Containment and Monitoring Institute reported an unsuccessful trapping of the injected $CO_2$ in the target formation which resulted in partial upward migration of the $CO_2$ along the injector well casing. Therefore, the reservoir simulations and the resistivity calculations are updated based on a conservative total amount of 4 t $CO_2$. The $CO_2$ occupies 800 $m^3$ reservoir rock resulting in a $CO_2$-plume of cylindrical shape with a radius of 6.5 m at a height of 6 m. Figure 5.10 and 5.11 show the relative and absolute changes of the vertical and radial component for the large and small transmitter setup. No major relative differences can be observed. Due to ambient electromagnetic noise at the FRS, the small relative and absolute changes can be masked and therefore, detectability of the small amount of $CO_2$ cannot be expected.

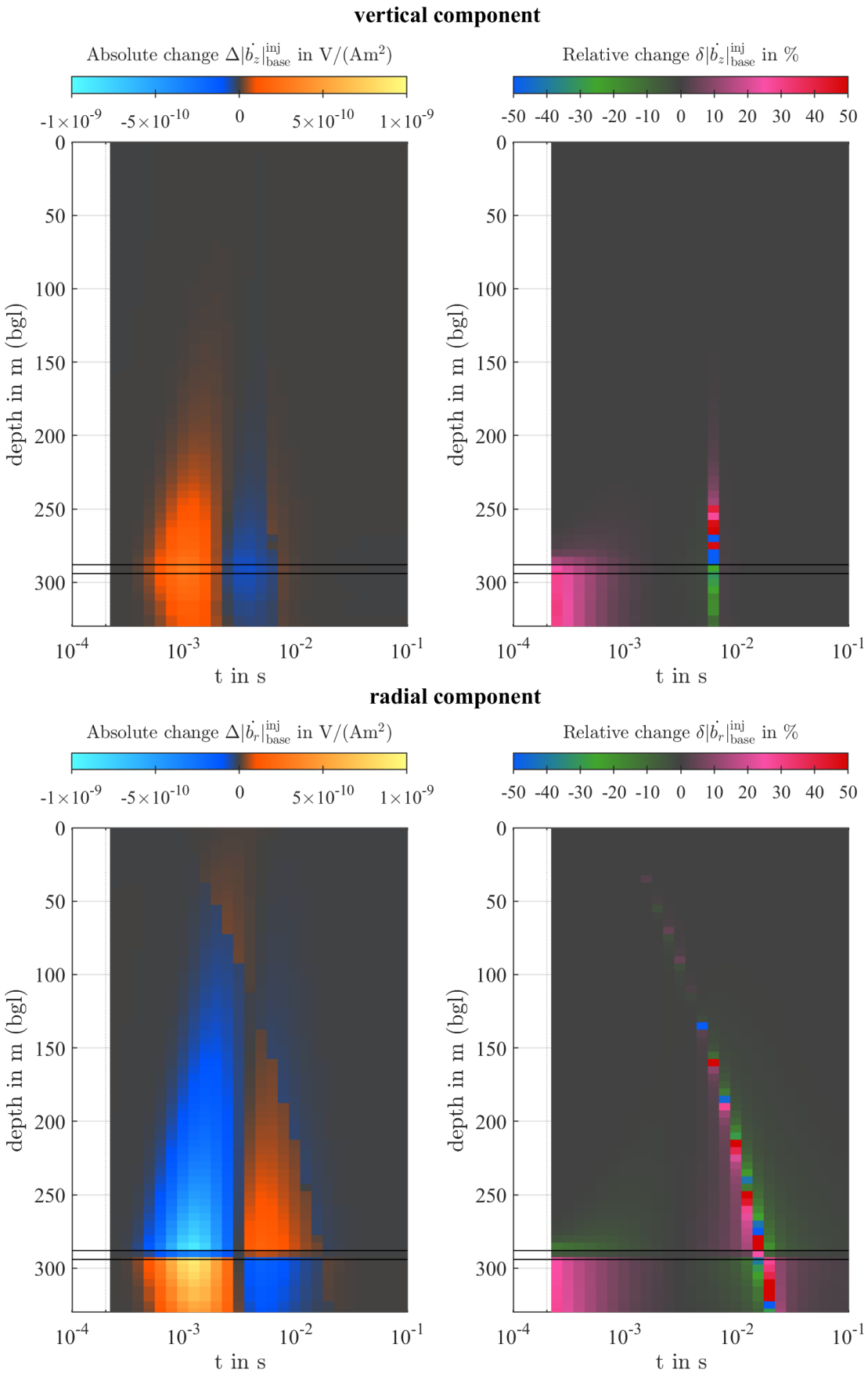


**Fig. 5.9.:** Absolute changes $\Delta|\dot{\vec{b}}|^{\text{inj}}_{\text{base}}$ (left) and relative changes $\delta|\dot{\vec{b}}|^{\text{inj}}_{\text{base}}$ (right) of the vertical (top) and radial (bottom) component of the transient response as a function of depth and time between the baseline and injection state evaluated at observation well #2 for the large transmitter loop setup. The total amount of injected $CO_2$ is 600 t.

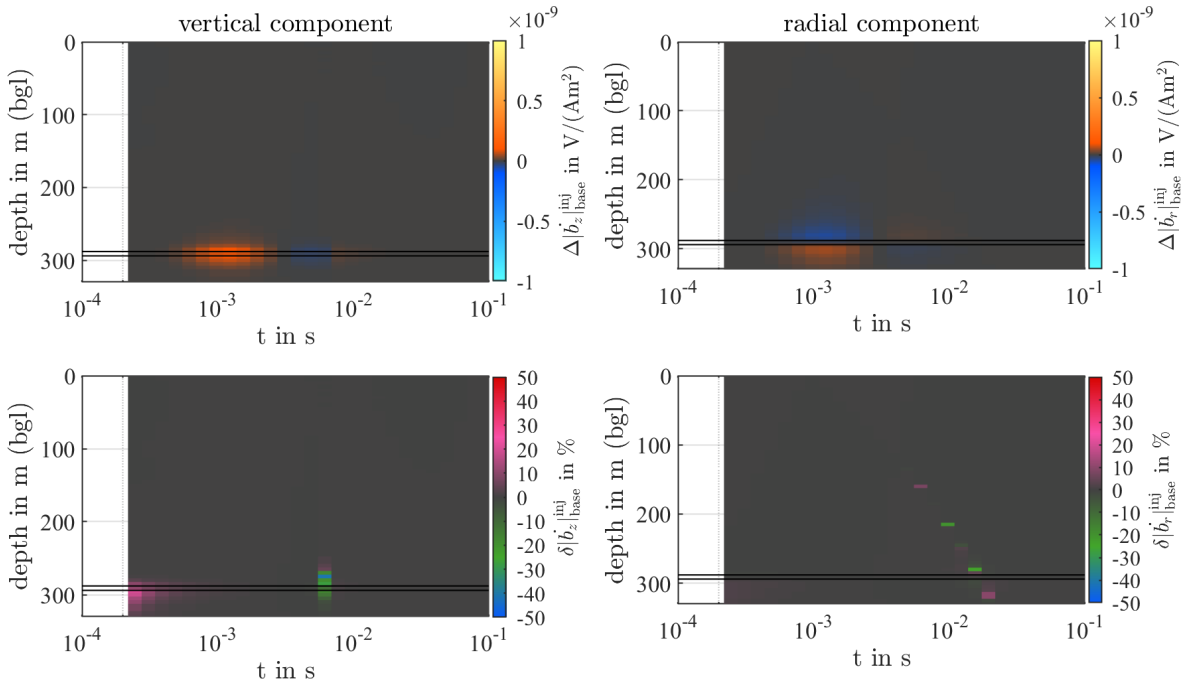


**Fig. 5.10.:** Absolute changes $\Delta|\dot{\vec{b}}|^{\text{inj}}_{\text{base}}$ (top) and relative changes $\delta|\dot{\vec{b}}|^{\text{inj}}_{\text{base}}$ (bottom) of the vertical (left) and radial (right) component of the transient response as a function of depth and time between the baseline and injection state evaluated at observation well #2 for the 400 m side length square transmitter loop setup. The total amount of $CO_2$ is 4 t.

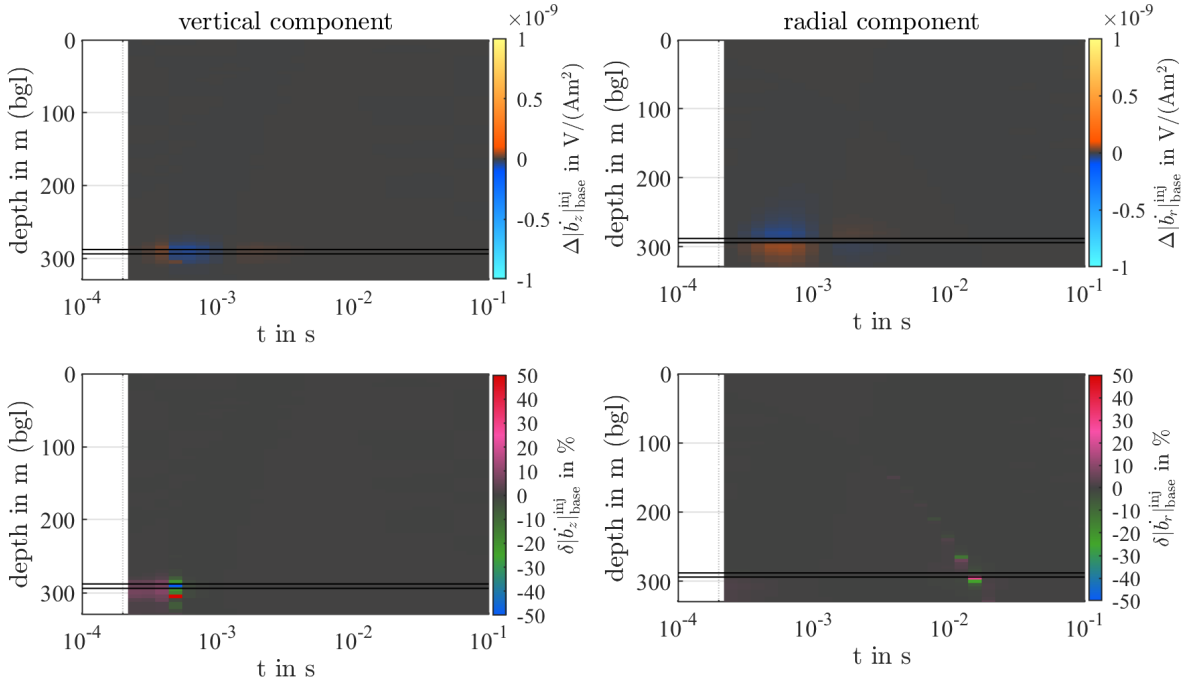


**Fig. 5.11.:** Absolute changes $\Delta|\dot{\vec{b}}|^{\text{inj}}_{\text{base}}$ (top) and relative changes $\delta|\dot{\vec{b}}|^{\text{inj}}_{\text{base}}$ (bottom) of the vertical (left) and radial (right) component of the transient response as a function of depth and time between the baseline and injection state evaluated at observation well #2 for the 100 m square transmitter loop setup. The total amount of $CO_2$ is 4 t.

## 5.4. Data acquisition

Borehole transient electromagnetic measurements were conducted from June to July in 2016 for the baseline state and a repeat survey from September to October in 2018 with the PROTEM system by the manufacturer Geonics Limited using the TEM57 and TEM67 transmitter and the 3-component borehole sensor BH43-3D. Figure 5.12 shows the survey layout at the FRS. It consisted of four two turn square transmitter loops (TEM67) with a side length of 400 m, located NE, SE, SW and NW of the FRS. In addition, four one turn square transmitter loops (TEM57) with 100 m side length were centered around observation well #2. The dipole moment was $220 \cdot 10^3$ A m$^2$ for the TEM57 transmitter setup operating at 22 A and $6.4 \cdot 10^6$ A m$^2$ for the TEM67 transmitter setup operating at 20 A. The downhole probe spacing inside the observation well varied between 1 m and 20 m according to the target of interest. Since the reservoir is very thin, a smaller spacing of 1 m for small dipole moments and 2 m for large dipole moments was used close to reservoir depth, whereas a larger probe spacing of 5 m to 20 m was used with increasing distance to the reservoir. Due to a failure of the main output stage of the TEM57-MK2 power transmitter, only a rather small part of the originally planned baseline data set could be obtained during the 2016 field survey (TEM67 NE and TEM57 NW). However, the baseline measurements could be repeated in 2018, as only an insignificant amount of $CO_2$ ($\sim$4 t) had been injected into the reservoir due to technical problems at the well site. The repeat measurements in 2018 were conducted according to the planned survey layout. Table 5.5 gives an overview of the total amount of acquired TEM measurements for the field surveys in 2016 and 2018.

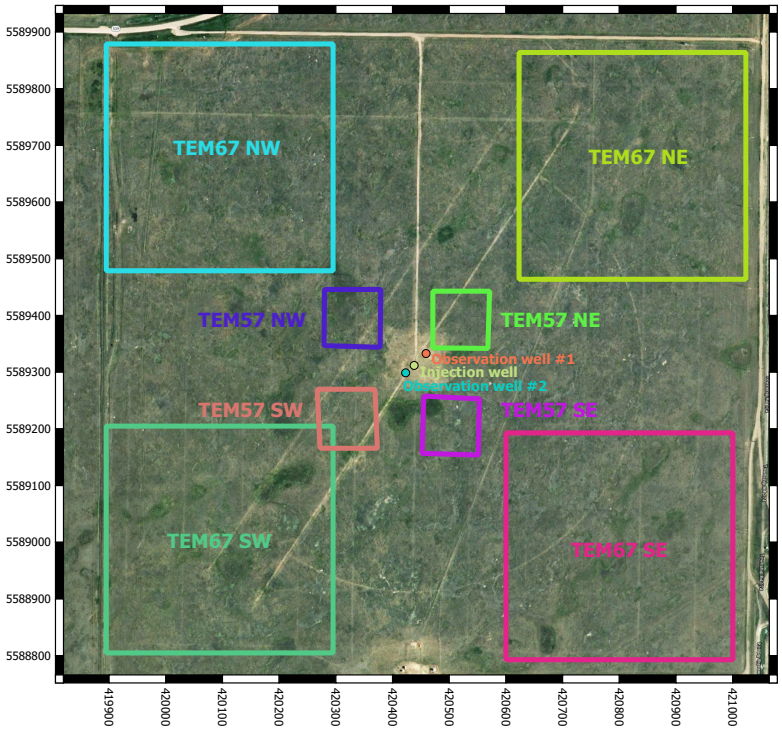


**Fig. 5.12.:** Plan view of the survey layout at the $CO_2$-sequestration site at FRS. Coordinate system EPSG:32612 - WGS84/UTM 12N.

**Tab. 5.5.:** Overview of the acquired transient electromagnetic data set of the field surveys in 2016 and 2018.

| | 2016 | | 2018 | |
|---|---|---|---|---|
| | TEM57 | TEM67 | TEM57 | TEM67 |
| number of TX positions | 1 | 1 | 4 | 4 |
| number of repeated measurements | 5 | 5 | 5 | 5 |
| depth range [m] | 320-270 | 320-170 | 320-60 | 320-60 |
| total depths measured | 26 | 22 | 46 | 43 |
| total raw measurements | 130 | 110 | 920 | 860 |

## 5.5. Data processing

A measured physical quantity is typically afflicted with errors. In general, one can distinguish between two types of error. These are random errors and systematic errors. Random errors can afflict the measured value as a consequence of random instrumental behavior or due to influences of natural occurrence. Typical random errors for TEM are

- electromagnetic noise from natural sources (lightning discharges, sferics),
- electromagnetic noise from cultural sources (nearby industrial machines, radio transmitters, power lines) and
- random transmitter output current instabilities.

On the contrary, systematic errors are a consequence of the measurement device or are caused through erroneous equipment handling. Typical systematic errors for TEM measurements are

- calibration errors of the receiver unit,
- voltage drifts through changing ambient temperature or self-heating of the transmitter or receiver,
- a flawed data recording as a consequence of faulty synchronization between transmitter and receiver or
- a constant decrease of the output current amplitude for battery powered transmitters.

In case of the PROTEM system, the major reason for applying data processing is the imprecise determination of the current turn-off time $T_0$, which defines the actual time position of the first measurement gate with respect to the current turn-off.

For the TEM57-MK2 respectively the TEM67 transmitter, $T_0$ is displayed on a liquid-crystal display (LCD). The displayed value is then entered manually into the digital receiver. If the repetition rate or the survey layout changes, $T_0$ is changing as well and has to be reentered into the receiver. Furthermore, the displayed value on the LCD does fluctuate over time due to insolation, ambient temperature, and is highly influenced by the chosen repetition rate of the transmitter. However, monitoring tests of the current output function at Tharandter Wald in 2018 have shown, that the turn-off ramp is indeed very stable and no fluctuations of the

turn-off time occur, even if the displayed value of the LCD changes. The output current time stability could be verified by a second current monitoring in Cologne during collaborative TEM measurements with the Institute of Geophysics and Meteorology of the University of Cologne. For measurements at the FRS in 2016, the turn-off time $T_0$ was entered into the receiver as it was displayed on the LCD (including $T_0$ changes over time) while for measurements in 2018 a fixed measured $T_0$ time (determined by oscilloscope measurements) was entered into the receiver.

As a result, successive measurements at different depth have varying reference times for the receiver measurement window. This behavior was also observed by Foged et al. (2013) and therefore requires minor time shifts if different $T_0$ times are used for successive measurements. Since the true turn-off times of the measurements at the field survey in 2016 are unknown, the transient responses are shifted to the measured $T_0$ times of the field survey in 2018 to ensure comparability. Hence, the transient responses of 2016 are time shifted by the difference of the turn-off times with respect to measurements conducted in 2018 and interpolated to the original gate center times of the PROTEM system. The displayed turn-off time of the TEM57 transmitter setup in 2016 varied between 5 µs to 15 µs whereas the true measured turn-off time in 2018 for the identical setup was 56 µs. For the TEM67 transmitter setup, the displayed turn-off time at the field survey in 2016 ranged between 650 µs to 700 µs. The measured turn-off time for the TEM67 transmitter setup in 2018 was 755 µs. The large differences between the displayed turn-off times of 2016 and the measured turn-off time in 2018 may also be a consequence of the damaged TEM57-MK2 and TEM67 transmitters in 2016. Figure 5.13 shows the measured vertical component of the transient responses at ∼290 m depth for the TEM57 (top left) and at ∼210 m depth for the TEM67 transmitter setup (bottom left) as well as the turn-off time corrected responses (top right, bottom right). The effect is significantly noticeable for both transmitter configurations, but especially for the TEM67 transmitter setup at early times. Further details and descriptions of the current output function and general information about the PROTEM system can be found in Appendix B.

The borehole measurements at the FRS were conducted using the three-component BH43-3D sensor of the PROTEM system. Although the BH43-3D sensor is equipped with tilt-meters to reorient the x- and y-component of the transient response, they do not provide a sufficient reading for very steep boreholes as it is the case for observation well #2 (Levy and McNeil, 1984). Instead, besides the vertical component, the magnitude of the radial component

$$|\dot{b}_r| = \sqrt{\dot{b}_x^2 + \dot{b}_y^2} \tag{5.8}$$

is used for comparison. Since the radial component is indirectly determined by the measured x- and y-component, which are error affected quantities exhibiting absolute uncertainties, the propagation of uncertainty needs to be applied in order to calculate the error of the radial component.

For a quantity $c = f(a,b)$ which is indirectly calculated of two error affected variables $a$ and $b$ exhibiting the absolute uncertainty $\Delta a$ and $\Delta b$, the uncertainty $\Delta c$ of the resulting variable is calculated by applying a linear approximation (Hering et al., 2004)

$$f(a+\Delta a, b+\Delta b) = f(a,b) + \frac{\partial f}{\partial a}\Delta a + \frac{\partial f}{\partial b}\Delta b\,. \tag{5.9}$$

where

$$\Delta c \approx \left|\frac{\partial f}{\partial a}\right| \Delta a + \left|\frac{\partial f}{\partial b}\right| \Delta b \tag{5.10}$$

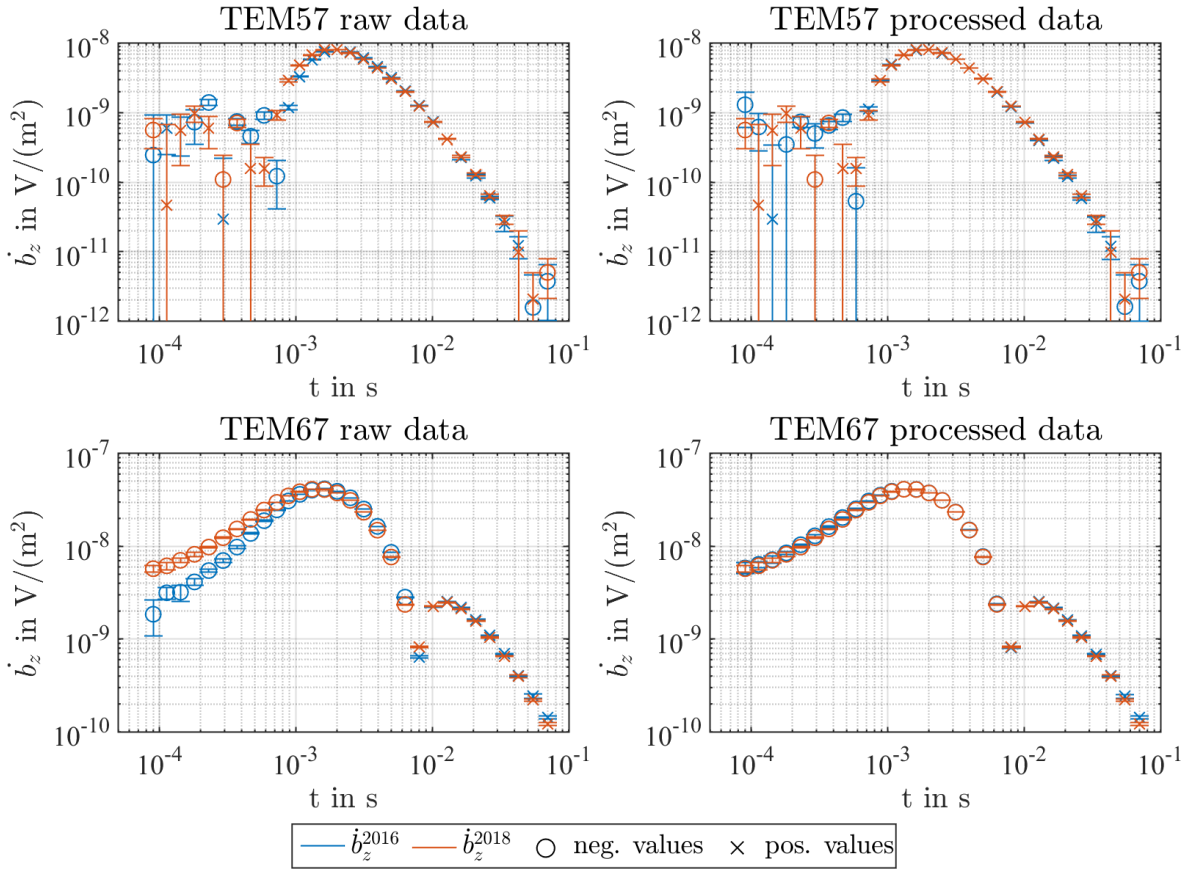


**Fig. 5.13.:** Vertical component $\dot{b}_z$ of the transient response at ∼290 m depth for the TEM57 transmitter (top left) and at ∼210 m depth for the TEM67 transmitter (bottom left) without turn-off time correction. Turn-off time corrected responses for the TEM57 transmitter (top right) and TEM67 transmitter (bottom right) according to measured turn-off times of 2018 survey.

Since uncertainties are composed additively, only absolute values are considered.

Evaluating Equation 5.10 with respect to the functional given in Equation 5.8, the error of the radial component is

$$\begin{aligned}
\Delta\dot{b}_r &= \left|\frac{\partial \dot{b}_r}{\partial \dot{b}_x}\right| \Delta\dot{b}_x + \left|\frac{\partial \dot{b}_r}{\partial \dot{b}_y}\right| \Delta\dot{b}_y \\
&= \left|\frac{\dot{b}_x}{\sqrt{\dot{b}_x^2 + \dot{b}_y^2}}\right| \Delta\dot{b}_x + \left|\frac{\dot{b}_y}{\sqrt{\dot{b}_x^2 + \dot{b}_y^2}}\right| \Delta\dot{b}_y \\
&= \left|\frac{\dot{b}_x}{|\dot{b}_r|}\right| \Delta\dot{b}_x + \left|\frac{\dot{b}_y}{|\dot{b}_r|}\right| \Delta\dot{b}_y
\end{aligned} \tag{5.11}$$

## 5.6. Data quality

Measurements conducted with the PROTEM system are internally pre-stacked. However, the system does not provide an error estimate of this stacking process. Therefore, at each probe location five consecutive measurements were conducted and then post-stacked in terms of averaging. As error estimate, the standard deviation of the post-stacking process is used.

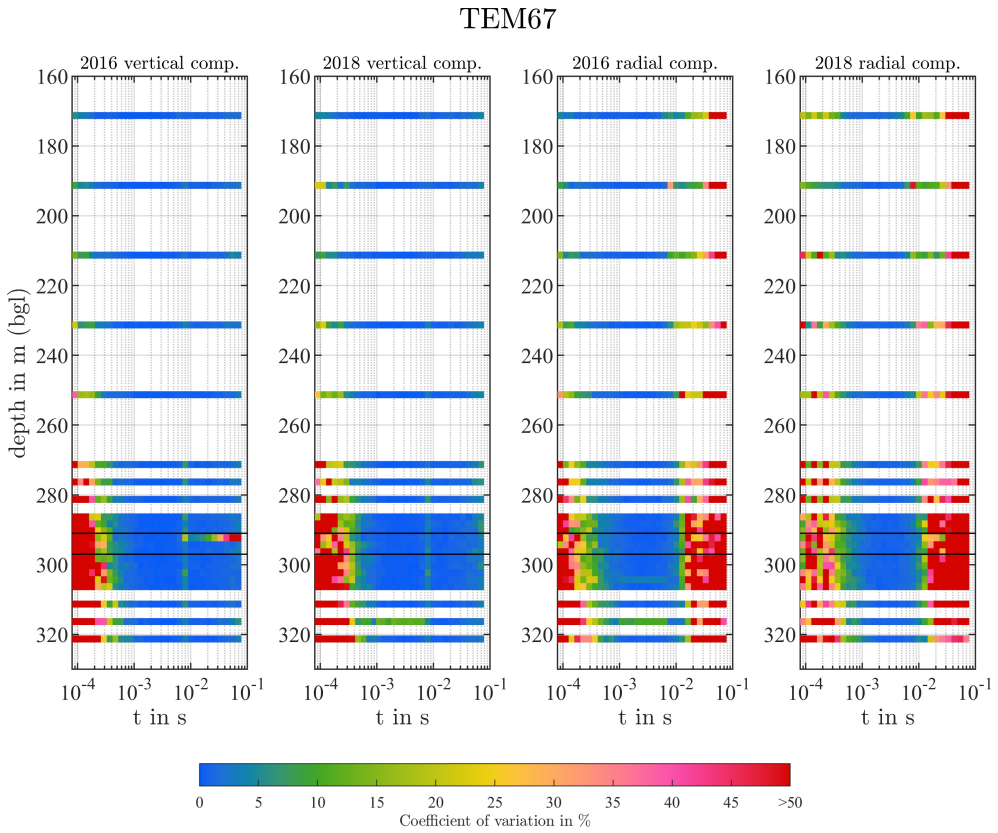


**Fig. 5.14.:** Coefficients of variation for the vertical and radial component of the transient response of 2016 and 2018 as a function of depth and time for the TEM67 transmitter setup.

To evaluate the quality of the measurements, the coefficient of variation (cv), also known as the relative standard deviation,

$$\mathrm{cv}_i = \frac{\mathrm{std}(\dot{b}_i)}{|\mathrm{mean}(\dot{b}_i)|}, \tag{5.12}$$

which is defined as the ratio of the sample standard deviation to the absolute value of the sample mean of $\dot{b}_i$, where $i$ denotes either the vertical or the radial component is used. Thereby, low values of the coefficients of variation indicate small variations of the mean values of the receiver gates. The coefficients of variation are further used to restrict the data set for the upcoming repeatability studies.

Figure 5.14 shows the coefficients of variation for the vertical and radial component of the transient response of 2016 and 2018 as a function of depth and time for the TEM67 and TEM57 transmitter setup. In general, the coefficients of variation are similar between both surveys. Due to the large dipole moment of the TEM67 transmitter setup, the vertical component has very low coefficients of variation close to 0 % over a wide time range except for very early times at depths greater than 260 m. For the radial component, the coefficients of variation are high for very early and late times restricting the time window with low coefficients of variation from about $6.5 \cdot 10^{-4}$ s to $9 \cdot 10^{-3}$ s. Since the dipole moment of the TEM57 transmitter setup is 30 times smaller compared to the TEM67 transmitter setup, the vertical and radial component are much more noise affected, resulting in smaller time windows with low coefficients of variation. For the vertical component, the effective time window is $8 \cdot 10^{-4}$ s to $1.5 \cdot 10^{-2}$ s and for the radial component $6.5 \cdot 10^{-4}$ s to $3 \cdot 10^{-3}$ s.

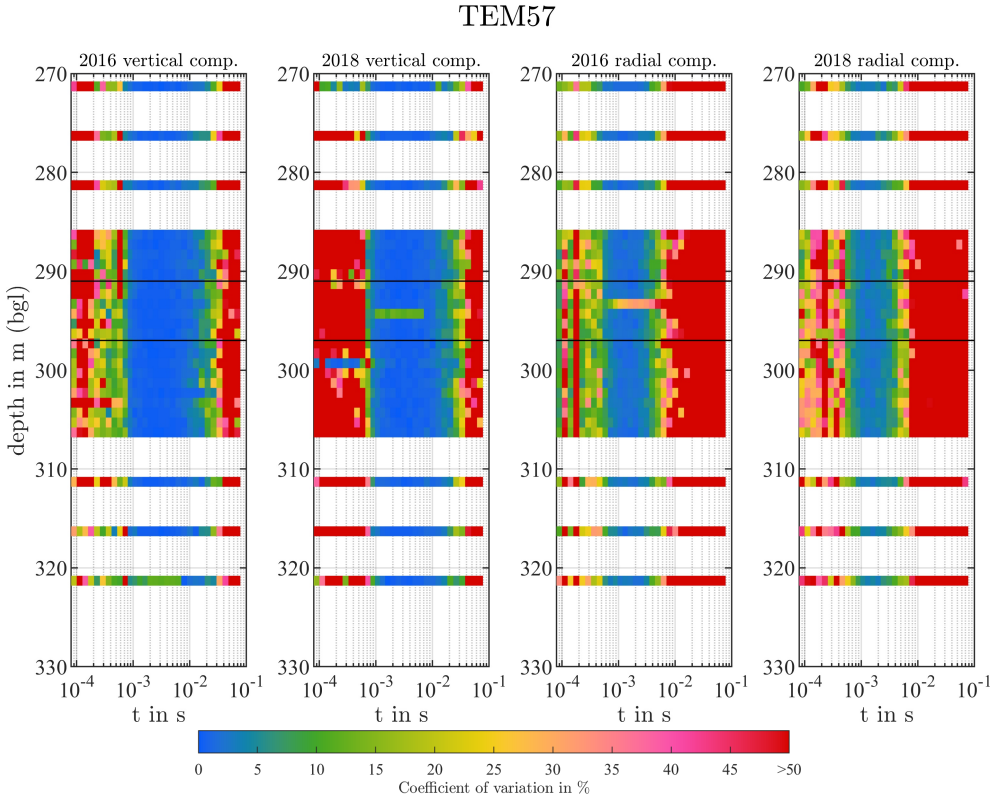


**Fig. 5.15.:** Coefficients of variation for the vertical and radial component of the transient response of 2016 and 2018 as a function of depth and time for the TEM57 transmitter setup.

## 5.7. Evaluation of repeatability

In the following section the repeatability of the two baseline measurements at the FRS are compared in two different ways. Firstly, by evaluating the relative and absolute differences between the stacked transient responses for each depth for the TEM67 and TEM57 transmitter location. Secondly, by clustering the individual consecutive measurements (five raw measurements each for 2016 and 2018, ten in total) for each depth separately according to the developed statistical workflow, presented in Chapter 4, using the dynamic time warping distance metric.

### 5.7.1. Relative and absolute changes

For evaluating the relative and absolute changes of the transient responses according to Equation 5.6 and 5.7, the data set is restricted to data points with coefficients of variation less than 5 % for both the 2016 and 2018 measurements. Thereby, the 5 % error floor serves as the minimal detection threshold since only small relative changes are expected, based on the 3D forward simulations. Furthermore, the 5 % error floor ensures the most acceptable data range of low error affected measurements over a wide time range (cf. Figure 5.14). As a consequence, relative changes between 5 % and $-5$ % are considered not significant since they are in the range of the error margins.

Figure 5.17 and Figure 5.18 show the absolute differences $\Delta|\dot{b}|^{2018}_{2016}$ and relative differences $\delta|\dot{b}|^{2018}_{2016}$ between the transient responses for the vertical and radial component of the field sur-

veys in 2016 and 2018 for the TEM67 transmitter setup as well as transient responses below, inside, above and far above the reservoir. For the vertical component relative changes in the range of $-20\,\%$ to $5\,\%$ can be observed. However, relative changes above the error margins only occur at late times close to the noise transition level. Furthermore, the vast majority of all relative changes (about $93\,\%$) are in the range of $\pm 5\,\%$ which is below the error margins (cf. Figure 5.16 (top left)). For the radial component, only relative changes in the range of $\pm 5\,\%$ can be observed. In other words, all relative changes for the radial component are below the error floor and are therefore considered not significant.

A similar behavior can be observed for measurements for the TEM57 transmitter location. For the vertical component, relative changes larger than $\pm 5\,\%$ can be observed for early and late times. However, these time gates are heavily affected by previous or later data points exhibiting high coefficients of variation. For the radial component, the available data is very limited (87 data points). However, approximately $97\,\%$ of the observed relative changes are below $5\,\%$.

Based on the $5\,\%$ error floor, the vast majority of the observed relative differences in both the vertical and radial component for the TEM67 and TEM57 transmitter setup are below the error margins and therefore are considered not significant. Relative changes above the error margins only occur for data points close to the noise transition level and are therefore considered to be no reliable data points even if the coefficient of variation is acceptable. In conclusion, repeatability of the baseline measurements of 2016 and 2018 can be detected.

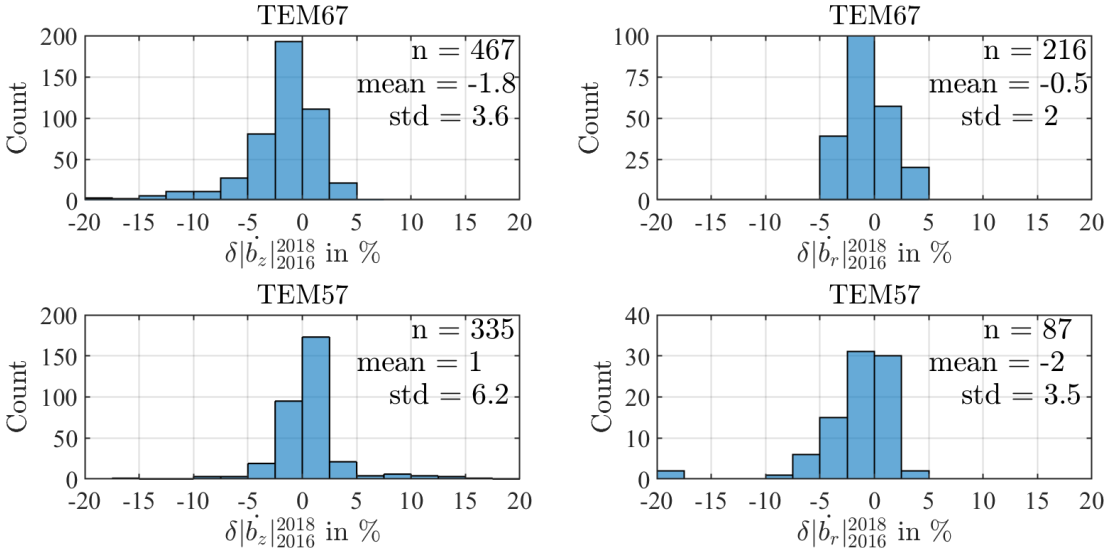


**Fig. 5.16.:** Distribution of relative changes for the vertical (left) and radial component (right) of the transient responses between the field surveys in 2016 and 2018 for the TEM67 (top) and TEM57 (bottom) transmitter setup.

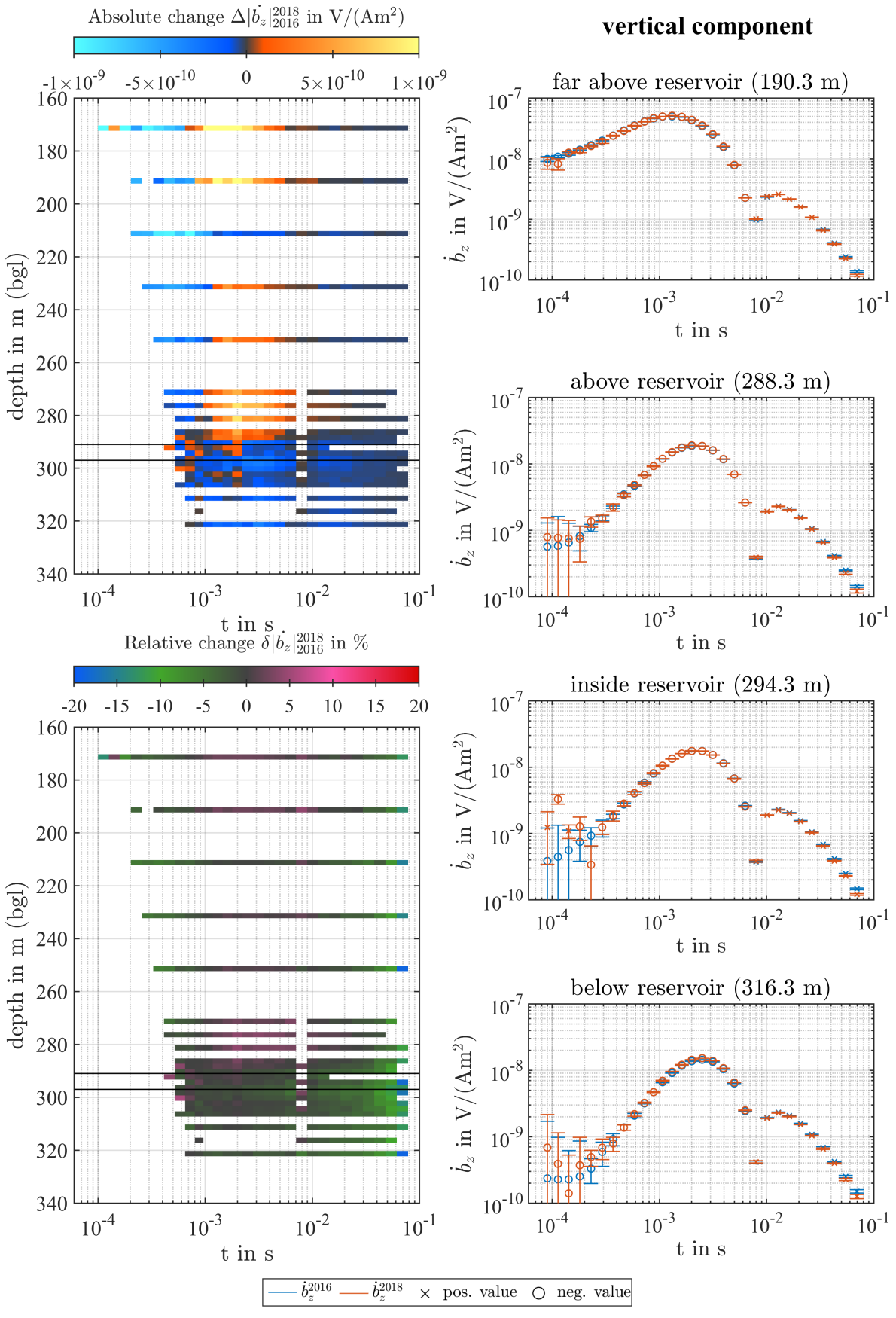


**Fig. 5.17.:** (Left) Absolute differences $\Delta|\dot{b}_z|^{2018}_{2016}$ (top left) and relative differences $\delta|\dot{b}_z|^{2018}_{2016}$ (bottom) between the absolute values of the vertical TEM responses of field surveys in 2016 and 2018 for the TEM57 transmitter setup limited to coefficients of variation $\leq$5 %. Black lines indicate identified reservoir limits. (Right) TEM responses $\dot{b}_z$ below, inside, above and far above the reservoir.

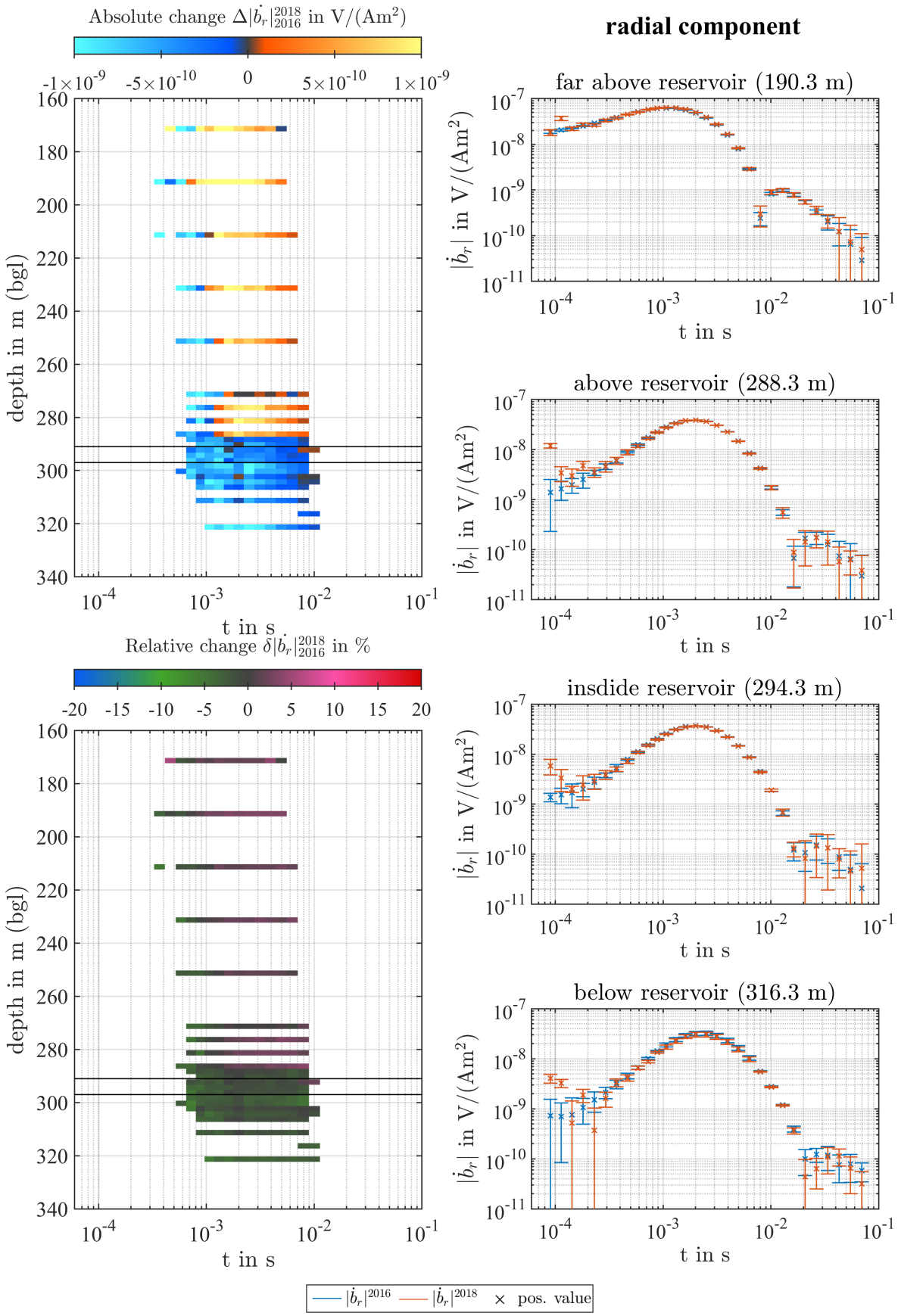


**Fig. 5.18.:** (Left) Absolute differences $\Delta|\dot{b}_r|^{2018}_{2016}$ (top) and relative differences $\delta|\dot{b}_r|^{2018}_{2016}$ (bottom) between the absolute values of the vertical TEM responses of field surveys in 2016 and 2018 for the TEM67 transmitter setup limited to coefficients of variation $\leq$5 %. Black lines indicate identified reservoir limits. (Right) TEM responses $|\dot{b}_r|$ below, inside, above and far above the reservoir.

### 5.7.2. Statistical evaluation

In addition to the determination of repeatability based on the relative and absolute changes of the transient responses of the 2016 and 2018 field surveys, the developed statistical workflow is applied to the raw data sets. Repeatability is thereby determined by clustering the individual consecutive measurements (five raw measurements each for 2016 and 2018, ten in total) for each depth separately. The maximum number of clusters is restricted to two, since we are only interested if the individual measurements of each survey are assigned to different clusters or if all ten measurements are merged in a single cluster. However, the previously defined limiting condition for data points based on the coefficient of variation cannot be applied in this case, since the DTW distance metric has the prerequisite of an equally sampled time series. This is achieved by interpolating the transient response from a logarithmic to a linear equally spaced time raster. Thus, removing in between data points would cause a loss of information and hence false interpolated responses. Instead, the data set for the TEM67 transmitter setup is limited to the 8th to 30th time-gate for the vertical and to the 8th to 22th time-gate for the radial component of the transient response. For measurements of the TEM57 transmitter setup the data set is limited to the 14th to 24th time-gate for the vertical and to the 10th to 20th time-gate for the radial component of the transient response. These time windows roughly correspond to the lowest coefficients of variation in each component. The noise transition level $a$ is about $1 \cdot 10^{-10}\,\mathrm{V}/(\mathrm{A\,m^2})$.

In general, three types of clustering results can be distinguished. If all ten consecutive measurements are assigned to only one cluster, repeatability of the baseline measurements of 2016 and 2018 is indicated (Type 1). For type number two, only one response is assigned to a separate cluster while the remaining responses are merged into one cluster. Thereby, the single clustered response can be identified as an outlier (Type 2). If consecutive measurements of 2016 and 2018 are assigned to separate clusters where one cluster only features 2016 and the second cluster only features 2018 measurements, no repeatability between the baseline measurements of 2016 and 2018 is indicated (Type 3). Figure 5.19 shows the three possible types of clustering results for example transient responses at certain depths.

Table 5.6 shows an overview of the clustering results, listed by type of classification, component and transmitter type. For the vertical and radial component of the transient response for the TEM67 transmitter setup, four Type 2 clustering results can be observed. These depths clearly feature an outlier in the measurements. For the vertical component of the transient response for the TEM57 transmitter setup, two Type 2 clustering results and one Type 3 clustering result can be observed (see Figure 5.19 c). However, for the Type 3 clustering result, the separation between the clustered measurements of 2016 (orange) and 2018 (blue) occur at relatively late times close to data points exhibiting large coefficients of variation. In total 89 individual repeat measurements at different depths are identified as Type 1 clustering result, indicating repeatability between the baseline measurements of 2016 and 2018. A complete overview of

**Tab. 5.6.:** Overview of the clustering results, listed by type of classification, component of the transient response and transmitter type.

| | vertical component | | | radial component | | |
|---|---|---|---|---|---|---|
| Type | 1 | 2 | 3 | 1 | 2 | 3 |
| TEM67 | 20 | 2 | 0 | 20 | 2 | 0 |
| TEM57 | 23 | 2 | 1 | 26 | 0 | 0 |

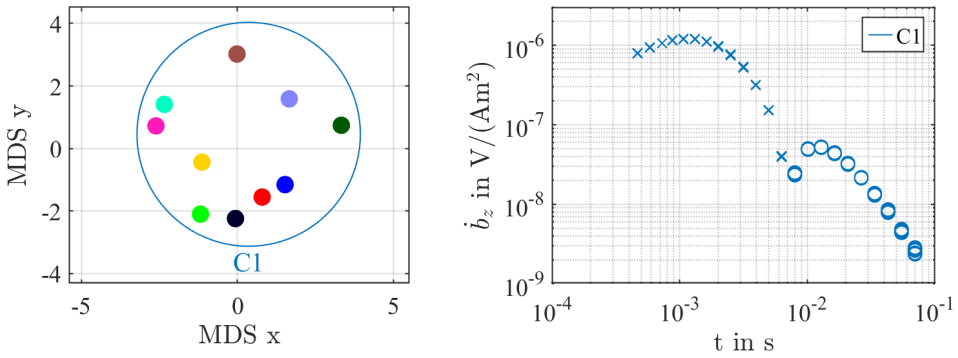


(a) Illustration of the Type 1 clustering result for the vertical component of the transient response (TEM67) measured at 171.3 m depth.

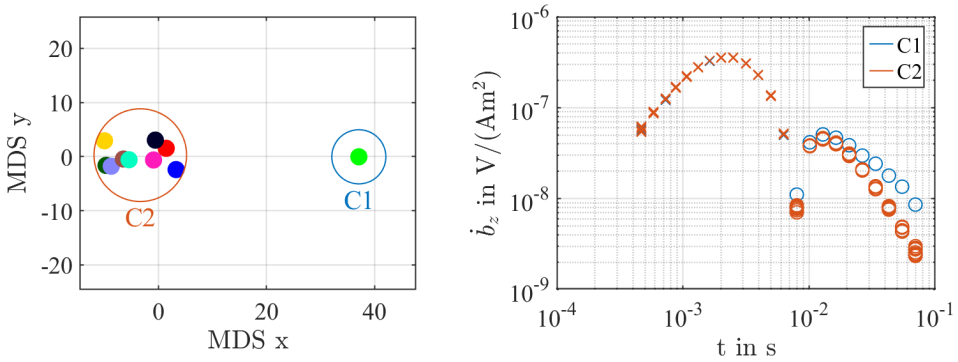


(b) Illustration of the Type 2 clustering result for the vertical component of the transient response (TEM67) measured at 292.3 m depth.

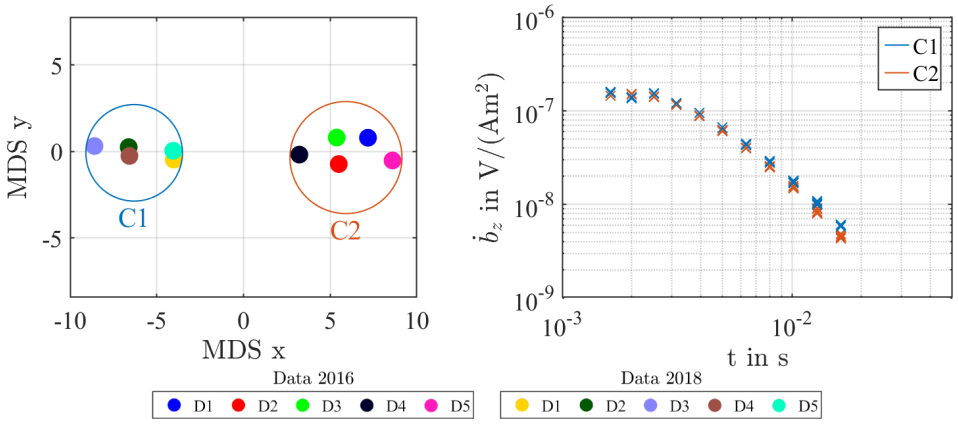


(c) Illustration of the Type 3 clustering result for the vertical component of the transient response (TEM57) measured at 299.3 m depth.

**Fig. 5.19.:** Overview of the different types of observed clustering results based on the statistical workflow for identifying similar transient responses. Type 1 indicates repeatability of the baseline measurements, Type 2 indicates an outlier and Type 3 indicates no repeatability of the baseline measurements of 2016 and 2018. (Left) Identified clusters in the MDS representation. (Right) Vertical component of the transient response colored according to their cluster assignment.

the clustering results of the vertical and radial component at each depth for both transmitter setups are shown in Appendix C.5 (Figure C.4 to Figure C.13).

### 5.7.3. Conclusion

Based on the updated 3D forward simulations of the 4 t sequestrated $CO_2$ scenario, no major relative differences are expected between the baseline state and the injected state. The evaluations of the relative changes between the transient responses of the field surveys in 2016 and 2018 have shown, that the vast majority of observed relative changes are in-between the defined error floor limits of $\pm 5\,\%$. Furthermore, the statistical evaluation in terms of clustering the individual consecutive measurements of 2016 and 2018 have shown, that only one repeat measurement could be identified as Type 3 clustering result. The Type 2 clustering results (six in total) can be related to single outliers for unknown reasons. The remaining 89 repeat measurements are identified as Type 1 clustering results.

In conclusion, repeatability between the baseline measurements of 2016 and the repeat measurements of 2018 can be detected.

# 6. Summary and conclusions

We live in a society with a constantly growing population that has a high demand for energetic raw materials. As a consequence, sustainable strategies have to be developed to counteract the growing trend of greenhouse gas emission, especially $CO_2$. Strategies to slow down the emission of $CO_2$ are CCS-technologies and the storage of $CO_2$ in suitable subsurface reservoirs. However, these reservoirs harbor the risk of leakage. Therefore, it is essential to monitor the injection horizons with suitable geophysical methods to initiate early countermeasures if leakage occurs. Electromagnetic methods are particularly sensitive to changes in the subsurface conductivity, making them well-suited for monitoring the migration of poorly conductive $CO_2$ in well-conducting brine. In this thesis the transient electromagnetic method in various configurations (surface-to-surface, surface-to-borehole) is used for monitoring experiments. A crucial aspect of monitoring is the assignment of measured data to certain events occurring (leakage, migration, etc.). Especially if the changes in the measured data is small due to e.g. small amounts of injected $CO_2$, suitable statistical methods are needed to distinguish between certain events.

Since there does not seem to be a standardized workflow of detecting similar transient electromagnetic responses from successive repeat measurements, a new statistical workflow based on cluster analysis is proposed. Since transient electromagnetic measurements are time series, the similarity criterion between two measurements is a time series distance. In this thesis the dynamic time warping, the autoregressive distance based on ARIMA time series models and the normalized root-mean-square time series distance metric are investigated and compared to the classic Euclidean norm. Since transient electromagnetic signals exhibit a high dynamic range in amplitude, a data normalization based on the area-sinus-hyperbolic function is crucial in order to achieve an equal influence of the data points. Otherwise, the resulting distances of the time series distance metrics are dominated by high amplitude data points which do not necessarily represent the full information of the transient signal. The pairwise distances are then clustered using a hierarchical clustering algorithm and the optimal number of clusters is determined by applying the gap statistic. To validate the clustering results, silhouette plots and the average silhouette width are used. The workflow is applied to a synthetic data set and a long-term monitoring data set as well as repeat measurements at a pilot $CO_2$-sequestration site in Canada.

The evaluation of the clustering results for the synthetic data set indicate, that the autoregressive distance metric is superior in detecting the correct number of similar transient responses compared to the dynamic time warping. By using the autoregressive distance metric, identical responses which are time and amplitude shifted can be successfully identified as similar objects compared to the reference model response. However, the computational effort is much higher compared to dynamic time warping since the ARIMA time series model identification and verification can hardly be automated and requires serious user interaction during the process. The Euclidean and normalized root-mean-square distance metric fail in detecting the correct number of similar transient responses due to their sensitivity to signal transformations (e.g. shifting,

uniform and non-uniform amplitude scaling, uniform time scaling, uniform bi-scaling). In order to test the statistical workflow on real data, a long term monitoring data set was measured from 2017 to 2018 at Tharandter Wald in Saxony for a $100 \times 100$ m$^2$ transmitter loop. The statistical evaluation indicates repeatability of the measurements. Measurements which can clearly be related to certain events, like nearby DGPS devices or a changed survey layout, are successfully identified and marked as dissimilar time series. Furthermore, it can be shown, if amplitude normalization is taken into account, the dynamic time warping distance metric can also be taken into consideration as a suitable time series distance metric for detecting similarity among transient signals.

In preparation of a field survey at the pilot $CO_2$ sequestration site FRS in Canada, 3D forward simulations for a total amount of 600 t $CO_2$ are conducted. Based on the reservoir conductivity calculations and the geological conditions, a $CO_2$-plume of cylindrical shape with a radius of 80 m and a height of 6 m with a conductivity of 0.01 S/m can be expected. The conductivity is reduced by a factor of 10 compared to the initial undisturbed environment where no $CO_2$ is sequestrated. Relative changes of about $\pm 20$ % in the transient response are predicted once $CO_2$ is sequestrated. Thereby, the changes in the radial component are more pronounced than in the vertical component of the transient response. Since only an insignificant amount of $CO_2$ was sequestrated from 2016 to 2018, the 3D simulations were updated based on a total amount of 4 t $CO_2$. The comparison of the simulation results between the baseline state and the injection state show, that no major relative differences in the transient responses can be expected. The relative changes are in the range of $\pm 5$ %. Measurements for the baseline state were conducted in 2016 and repeat measurements in 2018. The evaluation of the relative differences of the transient responses between the baseline measurements of 2016 and the repeat measurements of 2018 at the pilot $CO_2$-sequestration site successfully indicate repeatability based on a 5 % error floor. The statistical evaluation in terms of clustering the individual consecutive measurements of 2016 and 2018 show, that only one set of repeat measurements at one depth is identified as Type 3 clustering result. This is caused by high ambient noise for data points at late times of the transient responses. The Type 2 clustering results (six in total) can be related to single outliers for unknown reasons. The remaining 89 repeat measurements are identified as Type 1 clustering results. In conclusion, repeatability between the baseline measurements of 2016 and the repeat measurements of 2018 can be detected. Thus, the data sets of 2016 and 2018 can be merged and used as baseline data set for a possible monitoring study at the pilot $CO_2$-sequestration site.

For the future, it is recommended to apply the statistical workflow for a $CO_2$-sequestration monitoring setup. Furthermore, strategies need to be developed for automating the process of ARIMA model identification and verification. This would greatly reduce the computation time and user interaction. Additional methods like functional data analysis should be considered and compared to the time series distance metrics investigated in this thesis.

# A. Statistics and time series models

## A.1. Unit root testing for time series

Considering a first order autoregressive process and a time series $\vec{X} = \{x_1, x_2, \ldots, x_n\}$. Then the AR(1) process is defined as

$$\phi(B)x_t = a_t, \tag{A.1}$$

with $\phi(B) = 1 - \phi_1 B$ yields

$$x_t = \phi_1 x_{t-1} + a_t, \tag{A.2}$$

where $\phi_1$ is the autoregressive parameter and $a_t$ a "random shock". A random shock is a normally and independently distributed variable from a fixed distribution with mean $\mu$ and variance $\sigma^2$ (e.g. NID$(0, \sigma^2)$). If $\phi_1 = 1$ the model is called the "random walk model"

$$x_t = x_{t-1} + a_t, \tag{A.3}$$

with $x_0 = 0$. Successive recursion of equation A.3 yields

$$x_t = t\sigma^2, \tag{A.4}$$

which is a non-stationary time series. However, the time series is stationary if $|\phi_1| < 1$ (Figure A.1). If the lag polynomial $\phi(B)$ has one root equal to one, it is called a **unit root** process. If a unit root is present the time series is non-stationary. However, taking the first difference of the random walk model results in a stationary time series. Therefore, the random walk process is called a process of integrated order one $I(1)$. The problem of stationarity testing reduces to test if the time series exhibits a unit root.

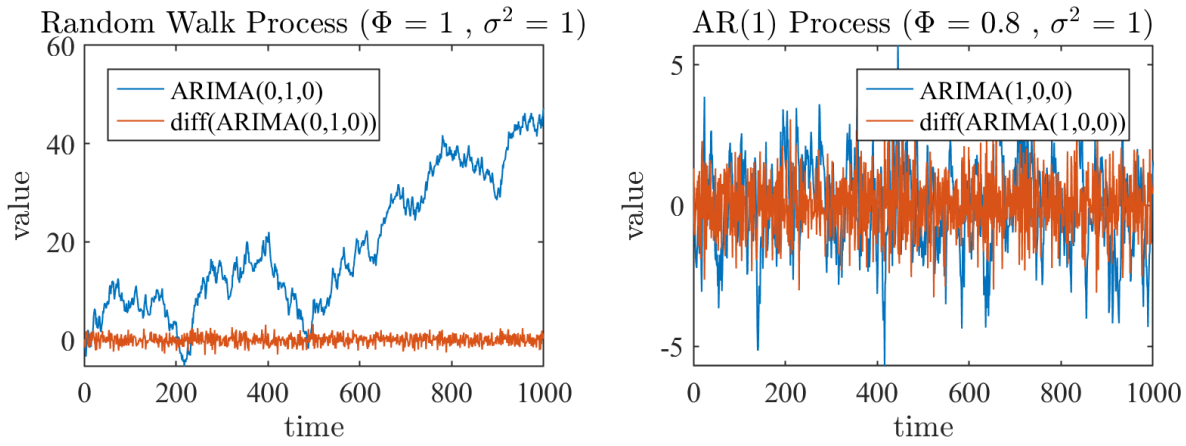


**Fig. A.1.:** Simulated non-stationary random walk process with $\phi = 1, \sigma^2 = 1$ and it's corresponding first order difference (left) vs. a stationary first order autoregressive process with $\phi = 0.8$, $\sigma^2 = 1$ and it's corresponding first order difference (right).

### A.1.1. Dickey-Fuller test

Taking the first difference of an $AR(1)$ process yields

$$x_t - x_{t-1} = \phi x_{t-1} + a_t - x_{t-1} = (1-\phi)x_{t-1} + a_t \tag{A.5}$$

or rewritten

$$\Delta x_t = \rho x_{t-1} + a_t. \tag{A.6}$$

If $\vec{X}$ is a non-stationary random walk process then $\rho$ equals zero and if $\vec{X}$ is an $AR(1)$ process $\rho$ is negative. This leads to the following hypothesis of the Dickey-Fuller test

$\mathbf{H_0}$ : $\rho = 0$ (equivalent to $\phi = 1$)

$\mathbf{H_1}$ : $\rho < 0$ (equivalent to $\phi < 1$)

The test statistic $\hat{\tau}$ is given by Dickey and Fuller (1979) as

$$\hat{\tau} = \frac{(\hat{\rho}-1)\sqrt{\sum_{t=2}^{n} x_{t-1}^2}}{S_e}, \tag{A.7}$$

with

$$S_e^2 = \frac{\sum_{t=2}^{n}(x_t - \hat{\rho}x_{t-1})^2}{n-2}, \tag{A.8}$$

and

$$\hat{\rho} = \frac{\sum_{t=1}^{n} x_t x_{t-1}}{\sum_{t=1}^{n} x_{t-1}^2}, \tag{A.9}$$

where $\hat{\rho}$ is the maximum likelihood estimator of $\rho$, and $n$ the sample size of $\vec{X}$. If $\hat{\tau}$ is less than a critical value of table A.1, the null hypothesis is rejected and the time series is a stationary process.

**Tab. A.1.:** Critical values in dependence of the sample size for the Dickey-Fuller test statistic for different significance levels $\alpha$ (Fuller, 1995).

| **Sample Size** | **Critical values for significance level** | | | |
|---|---|---|---|---|
| | **0.01** | **0.025** | **0.05** | **0.10** |
| 25 | -2.65 | -2.26 | -1.95 | -1.60 |
| 50 | -2.62 | -2.25 | -1.95 | -1.61 |
| 100 | -2.60 | -2.24 | -1.95 | -1.61 |
| 250 | -2.58 | -2.24 | -1.95 | -1.62 |
| 500 | -2.58 | -2.23 | -1.95 | -1.62 |
| $\infty$ | -2.58 | -2.23 | -1.95 | -1.62 |

For the time series in Figure A.1, the Dickey-Fuller test provides the results listed in Table A.4 at significance level $\alpha = 0.05$.

The test also supports the assumption of stationarity in case of the first order autoregressive process and non-stationarity in case of the random walk process, although the random walk process can be made stationary by taking the first difference.

**Tab. A.2.:** Dickey-Fuller test results for a random walk process, a first order autoregressive process and the first difference of the random walk model for significance level $\alpha = 0.05$.

| Time series | $\tau$-test statistic | critical value |
|---|---|---|
| Random Walk Process ARIMA(0,1,0) | 0.89 | -1.95 |
| Autoregressive Process ARIMA(1,0,0) | -10.52 | -1.95 |
| 1st difference of ARIMA(0,1,0) | -32.41 | -1.95 |

### A.1.2. Kwiatkowski, Phillips, Schmidt, Shin test

As an alternative to the DF test, Kwiatkowski, Phillips, Schmidt and Shin (KPSS test) introduced unit root test which is also capable of testing for linear trend stationarity as null hypothesis against the alternative of a non-stationary time series due to the presence of a unit root (Kwiatkowski et al., 1992).

Let $X_t = \{x_1, x_2, \ldots, x_n\}$, be a discrete observed time series. This series is assumed to be decomposed into a sum containing a linear deterministic trend $\xi t$ , a random walk part $r_t$, and a stationary error term $\varepsilon_t$:

$$x_t = \xi t + r_t + \varepsilon_t \,, \tag{A.10}$$

with

$$r_t = r_{t-1} + u_t. \tag{A.11}$$

where the $u_t$ are $iid(0, \sigma_u^2)$, independent and identically distributed with zero mean and fixed variance $\sigma_u^2$. Under the null hypothesis, the time series is said to be *trend-stationary* if $\sigma_u^2 = 0$, since $\varepsilon_t$ is assumed to be stationary itself. This implies that the random walk term $r_t$ is a constant and act as a model intercept. On the other hand, under the null hypothesis, the time series is said to be *level-stationary* if furthermore $\xi = 0$ is fulfilled.

$\mathbf{H_0} : \sigma_u^2 = 0$

$\mathbf{H_1} : \sigma_u^2 > 0$

The test statistic is then defined as

$$\eta = \frac{\sum_{t=1}^{T} S_t^2}{s^2 T^2} \tag{A.12}$$

where $S_t = \sum_{i=1}^{t} e_i$ are the partial sums of the estimation errors of the regression of $x_t$, either to a linear trend $\xi t$ or to a zero mean. Table A.3 shows critical values of the test statistic for different significance levels and the case of trend-stationarity $\eta_\tau$, respectively level-stationarity $\eta_\mu$.

For the time series in Figure A.1, the Kwiatkowski, Phillips, Schmidt, Shin test provides the results listed in Table A.4 for level stationarity $\eta_{mu}$ at significance level $\alpha = 0.05$.

The test supports the assumption of stationarity in case of the first order autoregressive process and non-stationarity in case of the random walk process, although the random walk process can be made stationary by taking the first difference.

**Tab. A.3.:** Critical values for different significance levels of the Kwiatkowski, Phillips, Schmidt, Shin test for the null hypothesis of level stationarity $\eta_\mu$ and trend stationarity $\eta_\tau$.

| **Significance level** | **Critical value** | |
|---|---|---|
| | **for $\eta_\mu$** | **for $\eta_\tau$** |
| 0.10 | 0.347 | 0.119 |
| 0.05 | 0.463 | 0.146 |
| 0.025 | 0.574 | 0.176 |
| 0.01 | 0.739 | 0.216 |

**Tab. A.4.:** Kwiatkowski, Phillips, Schmidt, Shin test results for a random walk process, a first order autoregressive process and the first difference of the random walk model for significance level $\alpha = 0.05$.

| **Time series** | **$\eta_\mu$-test statistic** | **critical value** |
|---|---|---|
| Random Walk Process ARIMA(0,1,0) | 1.74 | 0.463 |
| Autoregressive Process ARIMA(1,0,0) | 0.14 | 0.463 |
| 1st difference of ARIMA(0,1,0) | 0.076 | 0.463 |

## A.2. Ljung-Box test

As part of the model verification process in the Box-Jenkins approach for ARIMA modeling the Ljung-Box test (LB test) is commonly used to check for model accuracy. The Ljung-Box test is a portmanteau test which is used to identify autocorrelation among data. If the model is appropriate, Ljung and Box (1978) show that the test statistic

$$Q(\hat{\rho}_k) = n(n+2)\sum_{k=1}^{K}\frac{\hat{\rho}_k^2}{N-k} \tag{A.13}$$

approximately follows a $\chi^2(m)$ distribution where $\hat{\rho}_k$ are the sample autocorrelation coefficients with $k = (1,2,\ldots,K)$, $m = (K-p-q)$ the degree of freedom, $K$ the amount of lags, $p$ and $q$ the order of the underlying ARMA(p,q) model and $N = n-d$ with $n$ the sample length and $d$ the order of differencing. This leads to the following hypothesis of the Ljung-Box test.

$\mathbf{H_0}$ : The residuals are independently distributed

$\mathbf{H_1}$ : The residuals exhibit serial autocorrelation

The null hypothesis is rejected under the significance level $\alpha$, if the test statistic

$$Q(\hat{\rho}_k) > \chi^2_{1-\alpha,m} \tag{A.14}$$

is larger than the corresponding value of the $\chi^2(m)$ distribution.

Considering the monthly reported DAX values given in Figure A.2 (blue). Based on the Box-Jenkins approach, an ARIMA(1,1,1) model is compared with an ARIMA(1,0,0) model. Although, the fitted models (see Figure A.2 (orange)) visually look almost identical for both models, the ACF function of the residuals indicates a correlation for the ARIMA(1,0,0) model (see Figure A.3, first correlation at lag 1), whereas no autocorrelation is indicated by the ACF plot for the ARIMA(1,1,1) model (see Figure A.4). This result is also supported by the Ljung-

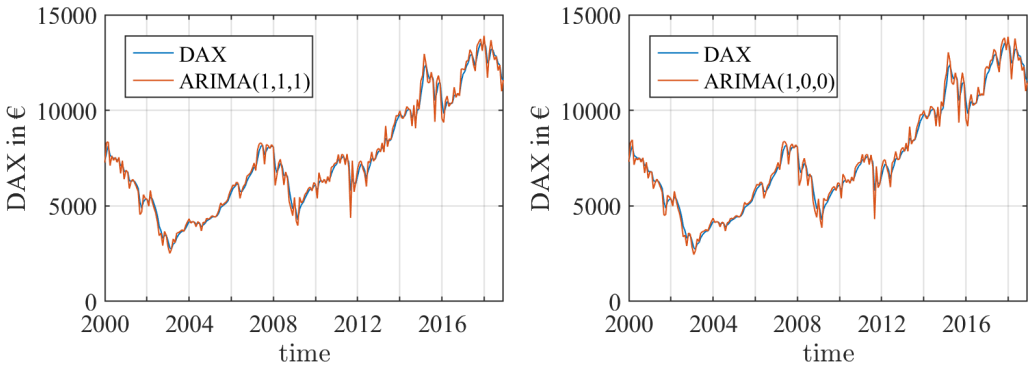


**Fig. A.2.:** Estimated ARIMA(1,1,1) model fit (left) and Estimated ARIMA(1,0,0) model fit (right) with respect to the monthly DAX prices.

Box test results (Table A.5). According to the test results an ARIMA(1,1,1) model is more appropriate to fit the DAX values than an ARIMA(1,0,0) model. This is also supported by the AIC and BIC value. Note, the model with the smallest of either criterion is preferred. However, a seasonal adjusted time series model (SARIMA) might be more accurate.

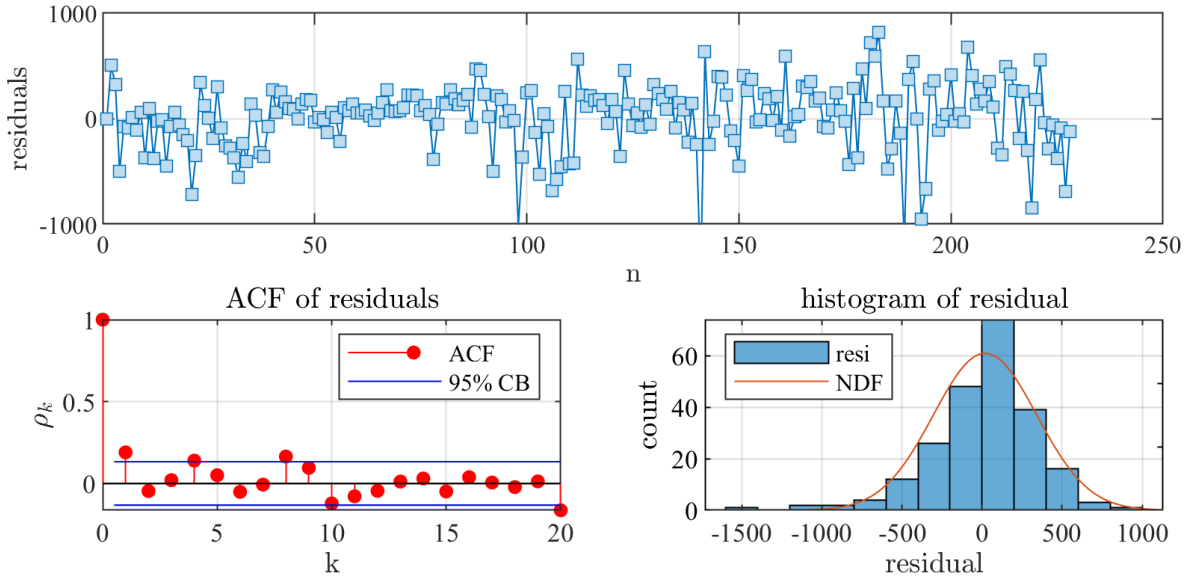


**Fig. A.3.:** Residual plot (top) for ARIMA(1,0,0) model with corresponding ACF plot (bottom left) and general distribution of residuals vs. a normal distribution function (bottom right).

**Tab. A.5.:** Ljung Box test result at 95% significance level for the time series models ARIMA(1,1,1) and ARIMA(1,0,0) fitted to the monthly DAX prices. The ARIMA (1,1,1) model is prefered over the ARIMA(1,0,0) model.

| Time series model | Q statistic | critical value | AIC | BIC |
|---|---|---|---|---|
| ARIMA(1,1,1) | 28.19 | 28.86 | 3277.3 | 3287.5 |
| ARIMA(1,0,0) | 36.95 | 30.14 | 4042.4 | 4045.8 |

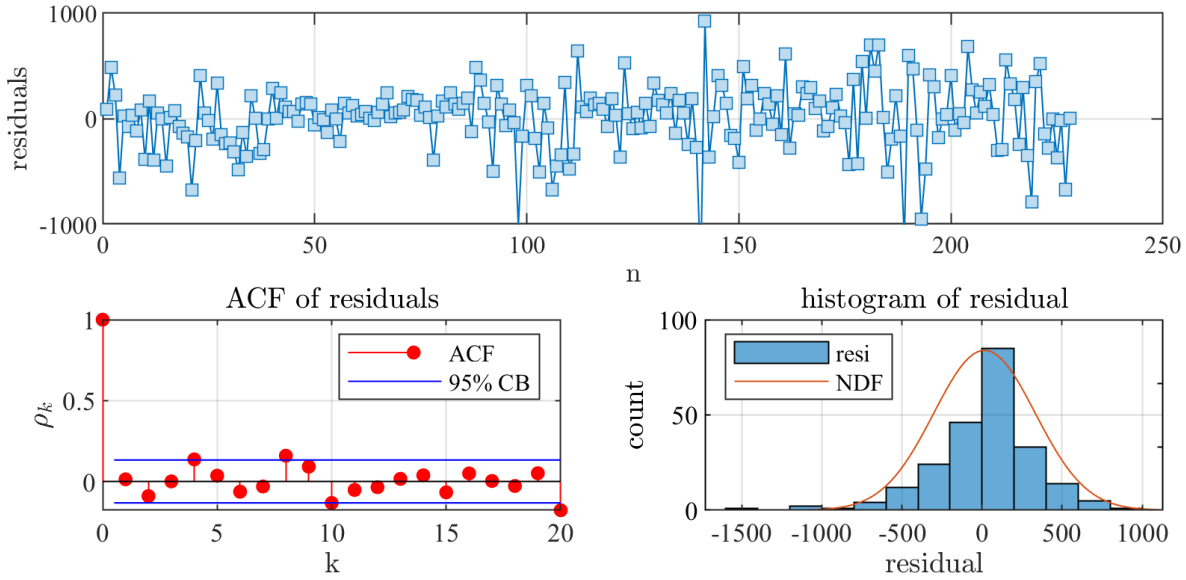


**Fig. A.4.:** Residual plot (top) for ARIMA(1,1,1) model with corresponding ACF plot (bottom left) and general distribution of residuals vs. a normal distribution function (bottom right).

## A.3. Duality between autoregressive and moving average processes

An autoregressive process

$$\phi(B)x_t = a_t \tag{A.15}$$

of order $p$, where $a_t$ can be represented as a finite weighted sum of previous values of $x_t$'s, can be converted to a moving average process

$$x_t = \phi^{-1}(B)a_t, \tag{A.16}$$

where the values of $x_t$ can be expressed as an infinite weighted sum of previous $a_t$.

Likewise, a moving average process

$$x_t = \theta(B)a_t \tag{A.17}$$

of order $q$, where $x_t$ can be represented as a finite weighted sum of previous $a_t$'s, can be converted to an autoregressive process

$$\theta^{-1}(B)x_t = a_t, \tag{A.18}$$

where the values of $a_t$ can be expressed as an infinite weighted sum of previous values of $x_t$ (Box et al., 2008).

**Exampel:** Converting an MA(1) process to an AR(∞) process
The MA(1) process defined as

$$x_t = \theta(B)a_t = (1-\theta_1 B)a_t = a_t - \theta_1 a_{t-1} \tag{A.19}$$

can be rewritten to

$$\theta^{-1}(B)x_t = \frac{x_t}{1-\theta_1 B} = a_t. \tag{A.20}$$

Remembering the geometric series

$$S = \sum_{k=0}^{\infty} a_0 q^k = a_0 + a_0 q + a_0 q^2 + \ldots, \tag{A.21}$$

converges to (Merziger and Wirth, 2006)

$$\lim_{k\to\infty} \sum_{k=0}^{\infty} a_0 q^k = \frac{a_0}{1-q} \quad \text{, if } |q| < 1. \tag{A.22}$$

Therefore, equation A.20 can be rewritten to an AR(∞) process

$$\frac{x_t}{1-\theta_1 B} = x_t + \theta_1 B x_t + \theta_1^2 B^2 x_t + \ldots \tag{A.23}$$

$$= (1 + \theta_1 B + \theta_1^2 B^2 + \ldots)x_t = a_t \tag{A.24}$$

respectively (see, equation 3.19)

$$x_t = -\theta_1 B x_t - \theta_1^2 B^2 x_t + \cdots + a_t = -\theta_1 x_{t-1} - \theta_1^2 x_{t-2} + \cdots + a_t \tag{A.25}$$

if $|\theta_1| < 1$. This is called the invertability condition.

## A.4. Maximum Likelihood Estimation

The maximum likelihood estimation method determines values for parameters of a given model in such a way that these estimated parameters maximize the likelihood that the process described by the model produce the data that were actually observed. Considering a casual ARMA(p,q) process

$$x_t = \phi_1 x_{t-1} + \phi_2 x_{t-2} + \cdots + \phi_p x_{t-p} - \theta_1 a_{t-1} - \theta_2 a_{t-2} - \cdots - \theta_q a_{t-q} - a_t \,, \tag{A.26}$$

where $a_t$ is a normally independently distributed variable (NID(0,$\sigma^2$)). Furthermore, let $\vec{\xi} = (\phi_1, \ldots, \phi_p, \theta_1, \ldots, \theta_q, \sigma^2)'$ denote the vector of model parameters and let $\vec{X} = (x_1, \ldots, x_N)$ be the observed series of size $N$. The probability that the data $\vec{X}$ is fitting the parameter vector $\xi$, is given by the multiplication of the individual probability density functions for each observation (Myung, 2003), which is

$$f(\mathbf{X} = (x_1, \ldots, x_N)|\xi) = f_1(x_1|\xi) f_2(x_2|\xi) \ldots f_N(x_N|\xi) = \prod_{i=1}^{N} f_i(x_i, \xi). \tag{A.27}$$

The inverse Problem then defined to find a suitable parameter vector for a given data set. Hence, the roles of $X$ and $\xi$ in equation A.27 are reversed

$$L(\xi, X) = f(\xi, X) = \prod_{i=1}^{N} L_i(\xi, x_i) \,, \tag{A.28}$$

where $L(\xi, X)$ is called the likelihood function. It represents the likelihood of the model parameter $\xi$ given the observed data $\mathbf{X}$. The maximum likelihood estimator $\hat{\xi}_{\text{MLE}}$ is then given by

$$\hat{\xi}_{\text{MLE}} = \underset{\xi \in \Xi}{\operatorname{argmax}} L(\xi, X) \,, \tag{A.29}$$

where $\Xi$ is the parameter space. To determine $\hat{\xi}_{\text{MLE}}$, the partial derivative of the likelihood function with respect to $\xi_i$ has to be evaluated and set to 0.

$$\frac{\partial L(\xi, X)}{\partial \xi_i} = 0 \tag{A.30}$$

For sake of simplicity, it is often convenient to work with the log-likelihood function $\log[L(\xi, X)]$.

For a general ARMA process the likelihood function is given by Neusser (2016) as

$$\begin{aligned} L(\xi, \mathbf{X}) &= (2\pi)^{-\frac{N}{2}} (\det \Gamma^{-\frac{1}{2}}) \exp\left(-\frac{1}{2} \mathbf{X}' \Gamma^{-1} \mathbf{X}\right) \\ &= (2\pi\sigma^2)^{-\frac{N}{2}} (\det G^{-\frac{1}{2}}) \exp\left(-\frac{1}{2\sigma^2} \mathbf{X}' G^{-1} \mathbf{X}\right) \end{aligned}$$

where $\Gamma$ is the variance matrix of the joint distribution functions $L_i$ and $G = \sigma^{-2}\Gamma$.

Detailed explanation of the derivitives can be found in (Tsay, 2010), Brockwell and Davis (1991), Box et al. (2008) or (Neusser, 2016)

# A.5. Clustering

## A.5.1. The complete linkage criterion for hierarchical clustering

In the following, a demonstration of the complete linkage criterion for an example data set is given. The data is clustered using an agglomerative hierarchical clustering algorithm.

Let A to E be the initial data points (Figure A.5) which should be clustered. In the first step, each sample is assigned to its initial cluster.

| | x | y |
|---|---|---|
| A | 25 | 79 |
| B | 34 | 51 |
| C | 22 | 53 |
| D | 27 | 78 |
| E | 33 | 59 |

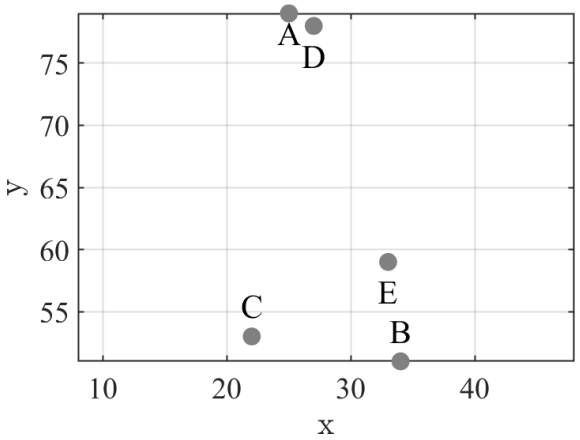


**Fig. A.5.:** Overview of the inital dataset.

### First iteration

Based on the pairwise Euclidean distance matrix $\mathbf{D}_1$, the first cluster merge occurs for sample A and D since the Euclidean distance is the smallest (2.24). Following the agglomerative

**Tab. A.6.:** Initial pairwise Euclidean distance matrix $\mathbf{D}_1$.

| | A | B | C | D | E |
|---|---|---|---|---|---|
| A | 0 | 29.41 | 26.17 | 2.24 | 21.54 |
| B | 29.41 | 0 | 12.17 | 27.89 | 8.06 |
| C | 26.17 | 12.17 | 0 | 25.50 | 12.53 |
| D | 2.24 | 27.89 | 25.50 | 0 | 19.92 |
| E | 21.54 | 8.06 | 12.53 | 19.92 | 0 |

hierachical clustering approach, the pairwise Euclidean distance matrix $\mathbf{D}_2$ is updated based on the initial distance matrix $\mathbf{D}_1$ using the complete linkage criterion

$$d_{CL}(C_1, C_2) = \max_{\substack{i \in C_1 \\ j \in C_2}} d_{ij} \,. \tag{A.31}$$

and calculating the distances between each element of the first cluster (A,D) and each of the remaining elements.

$$\mathbf{D}_2((A,D),B) = \max(\mathbf{D}_1(A,B),\mathbf{D}_1(D,B)) = \max(29.41,27.89) = 29.41$$
$$\mathbf{D}_2((A,D),C) = \max(\mathbf{D}_1(A,C),\mathbf{D}_1(D,C)) = \max(26.17,25.50) = 26.17$$
$$\mathbf{D}_2((A,D),E) = \max(\mathbf{D}_1(A,E),\mathbf{D}_1(D,E)) = \max(21.54,19.92) = 21.54$$

### Second iteration

Based on the updated pairwise Euclidean distance matrix $\mathbf{D}_2$, the next cluster merge occurs between sample B and E due to the smallest Euclidean distance of 8.06. Repeating the update

**Tab. A.7.:** Updated pairwise Euclidean distance matrix $\mathbf{D}_2$.

| | (A,D) | B | C | E |
|---|---|---|---|---|
| (A,D) | 0 | 29.41 | 26.17 | 21.54 |
| B | 29.41 | 0 | 12.17 | 8.06 |
| C | 26.17 | 12.17 | 0 | 12.53 |
| E | 21.54 | 8.06 | 12.53 | 0 |

procedure for recalculating the distances between the remaining samples and the former merged clusters leads to the pairwise Euclidean distance matrix $\mathbf{D}_3$.

$$\mathbf{D}_3((B,E),(A,D)) = \max(\mathbf{D}_2(B,(A,D)),\mathbf{D}_2(E,(A,D)) = \max(29.41,21.54) = 29.41$$
$$\mathbf{D}_3((B,E),C) = \max(\mathbf{D}_2(B,C),\mathbf{D}_2(E,C)) = \max(12.17,12.53) = 12.53$$

### Third iteration

The next cluster merge occurs between cluster (B,E) and sample C based on the minimal Euclidean distance in $\mathbf{D}_3$. Updating $\mathbf{D}_3$ using the former strategy leads to the final Euclidean

**Tab. A.8.:** Updated pairwise Euclidean distance matrix $\mathbf{D}_3$.

| | (A,D) | (B,E) | C |
|---|---|---|---|
| (A,D) | 0 | 29.41 | 26.17 |
| (B,E) | 29.41 | 0 | 12.53 |
| C | 26.17 | 12.53 | 0 |

distance matrix between cluster (A,D) and cluster ((B,E),C).

$$\mathbf{D}_4(((B,E),C),(A,D)) = \max(\mathbf{D}_3((B,E),(A,D)),\mathbf{D}_3(C,(A,D)) = \max(29.41,26.17) = 29.41$$

**Tab. A.9.:** Final pairwise Euclidean distance matrix $\mathbf{D}_4$.

| | (A,D) | ((B,E),C) |
|---|---|---|
| (A,D) | 0 | 29.41 |
| ((B,E),C) | 29.41 | 0 |

### Final iteration

In the final step, cluster (A,D) and ((B,E),C) are merged with the remaining distance between the clusters of 29.41. All samples are merged in a single cluster and the iteration process stops. Figure A.6 shows the final hierarchical cluster tree as dendrogram plot.

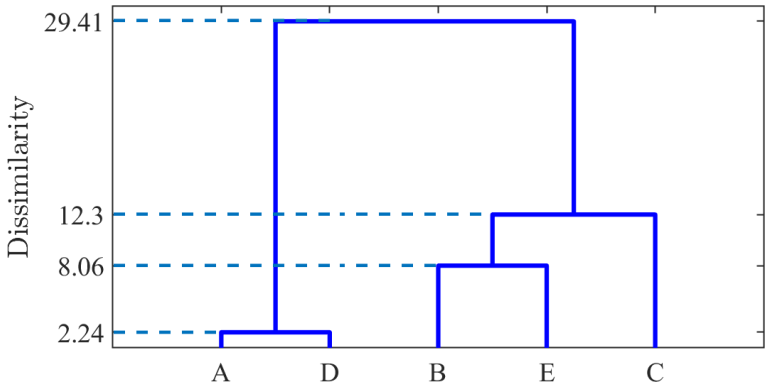


**Fig. A.6.:** Agglomerative hierarchical cluster tree **L** for the sample data set using the complete linkage criterion.

## A.6. Fitted ARIMA time series of measured TEM responses at Tharandter Wald

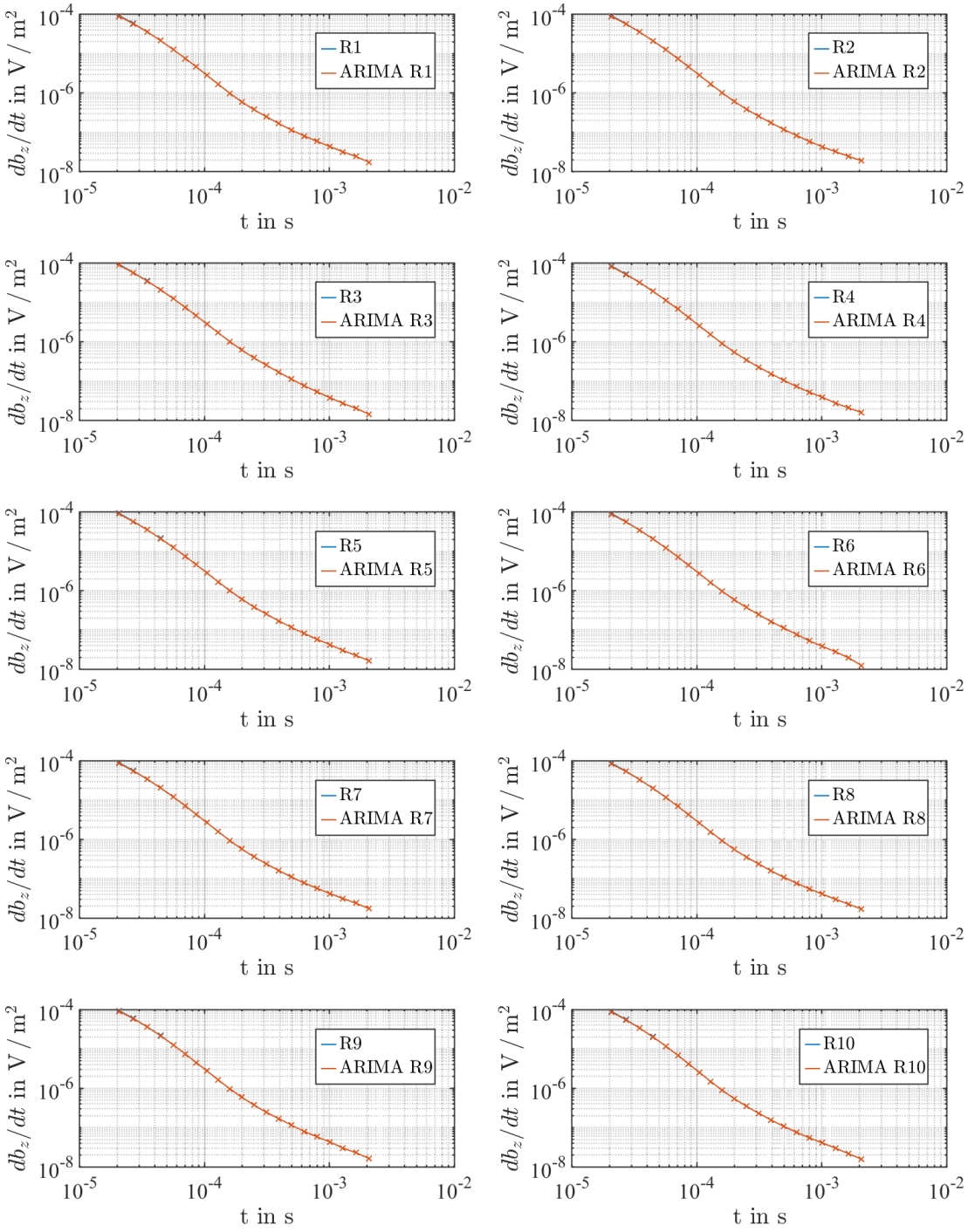


**Fig. A.7.:** Fitted ARIMA time series (orange) in comparison with measured transient electromagnetic responses for central loop measurements (blue).

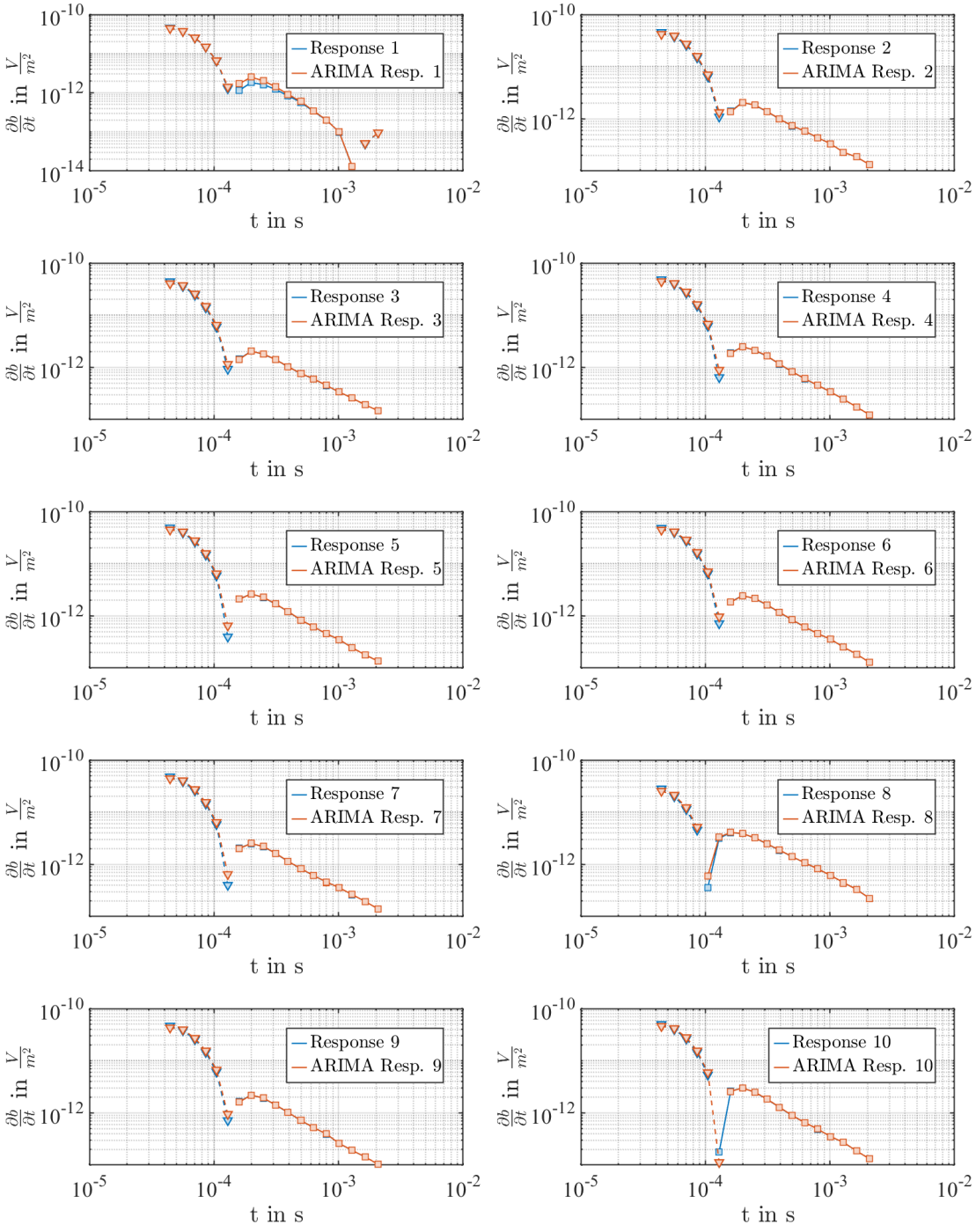


**Fig. A.8.:** Fitted ARIMA time series (orange) in comparison with measured transient electromagnetic responses at observation point P2 (blue).

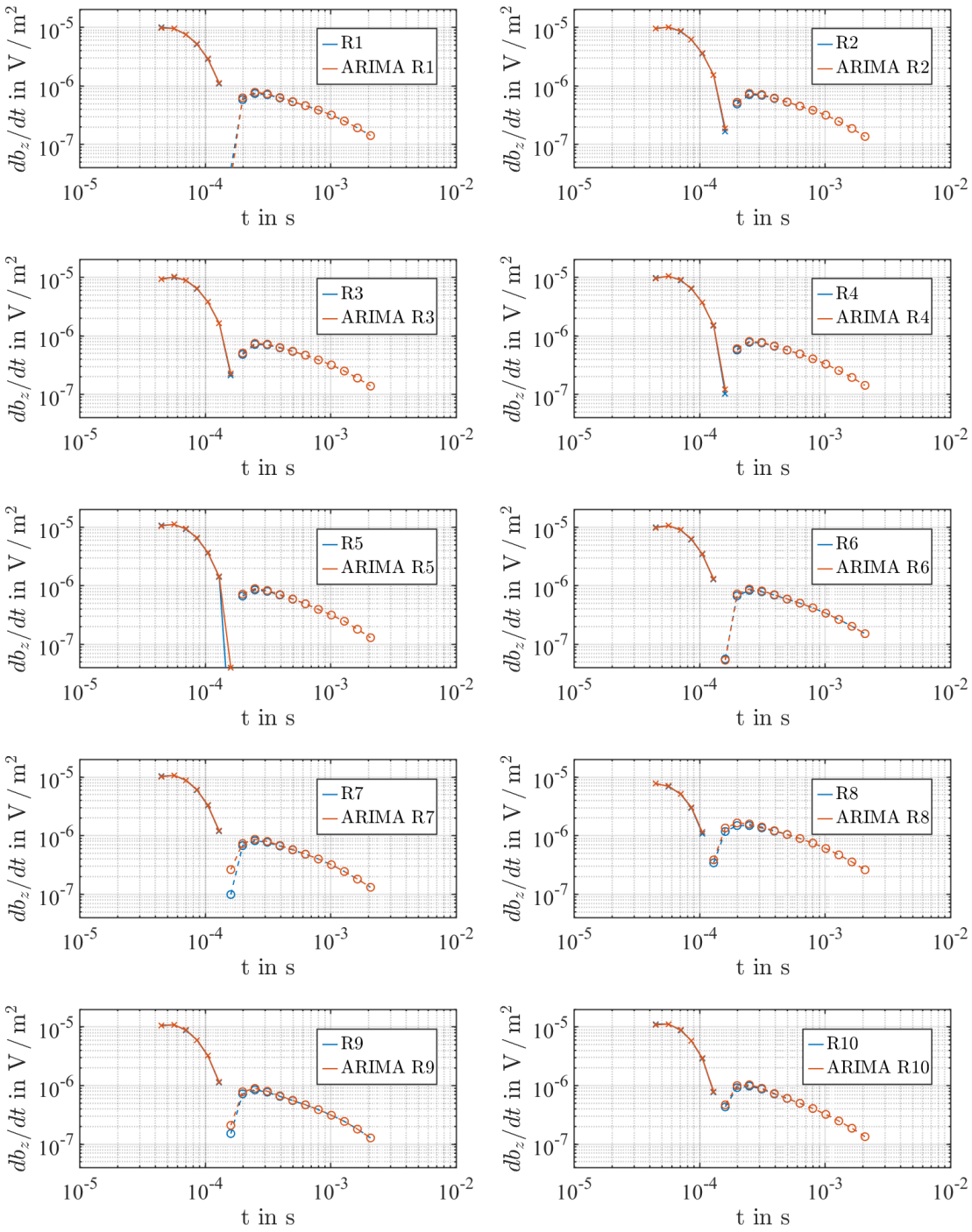


**Fig. A.9.:** Fitted ARIMA time series (orange) in comparison with measured transient electromagnetic responses at observation point P3 (blue).

# B. The PROTEM system by Geonics Ltd.

The PROTEM system, manufactured by Geonics Ltd., is a modular time domain electromagnetic measurement system consisting of a single digital receiver with multiple, interchangeable transmitter systems (Table B.1) and receiver coils (Table B.2). The TEM47 is a small, portable, battery-powered EM-transmitter with a maximum current output of 3 A and a fast current turn-off function ($\sim$5 µs), ideal for near-surface applications in the range of 5 m to 150 m sounding depth. For mid-range sounding applications (150 m to 500 m depth) the TEM57-MK2 transmitter is used. The maximum output current of the system is 25 A. For large transmitter loops, the TEM67 transmitter provides additional output voltage up to 100 V for the TEM57-MK2 transmitter in order to maintain the 25 A output current and hence providing large dipole moments. The TEM67 transmitter is therefore ideal for deep-range sounding applications up to 1000 m (Genoics Limited, 2006). Although the TEM57-MK2 and TEM67 transmitter are rated for 25 A, it is suggested to not exceed 20 A, since the output current function can get very unstable above 20 A (Oelschlägel, 2015). The synchronization between receiver and transmitter can either be obtained by a reference cable or the inbuilt quartz-crystal clock. The quartz-crystal clock synchronization thereby allows for long offset measurements between transmitter and receiver since the reference cable synchronization is limited to $\sim$50 m due to cable length.

**Tab. B.1.:** Overview of maximum output currents and voltages of the PROTEM transmitter systems.

| **Transmitter** | **Max. output current in A** | **Output voltage in VDC** | **Rx-Tx synchronization** |
|---|---|---|---|
| TEM47 | 3 | 0-9 | reference cable |
| TEM57-MK2 | 25 | 18-60 | reference cable/ quartz crystal |
| TEM67 | 25 | 18-160 | reference cable/ quartz crystal |

## B.1. System response

The system response can be described as a second order filter (Band-pass filter) with resonance frequencies $f_0$ and effective coil areas listed in Table B.2. The relative amplitude $|H(\omega)|$ is given by

$$|H(\omega)| = \frac{1}{\sqrt{1+\frac{1}{\tau^2}\left(\frac{\omega}{\omega_0}-\frac{\omega_0}{\omega}\right)^2}}, \tag{B.1}$$

the phase $\Phi$ by

$$\Phi(\omega) = -\arctan\left(\frac{2}{\tau}\frac{\omega}{\omega_0}+\sqrt{\frac{4}{\tau^2}-1}\right) - \arctan\left(\frac{2}{\tau}\frac{\omega}{\omega_0}-\sqrt{\frac{4}{\tau^2}-1}\right)+\frac{\pi}{2} \tag{B.2}$$

**Tab. B.2.:** Overview of effective coil areas and resonance frequencies for the PROTEM receiver coils.

| Induction coil | Effective coil area in $m^2$ | Resonance frequency $f_0$ in Hz |
|---|---|---|
| High Frequency (HF) | 31.4 | 702 000 |
| Low Frequency (LF) | 200 | 29 000 |
| BH43-3D (BH) | 100 | 10 000 |

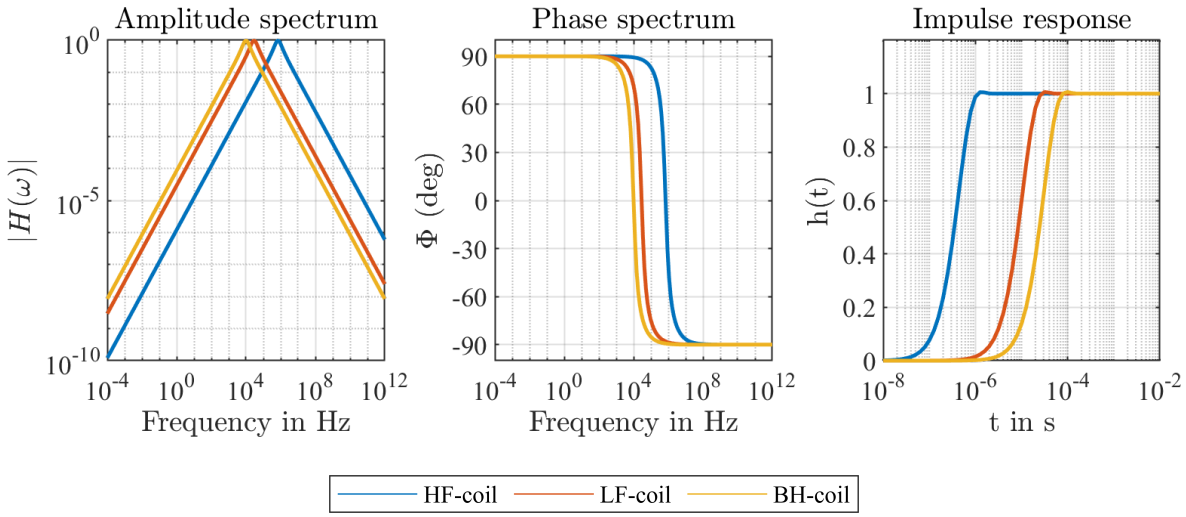


**Fig. B.1.:** Amplitude spectrum (left), phase spectrum (middle) and impulse response (right) of the high respectively low frequency receiver coil as well as the borehole receiver coil of the PROTEM system.

and the impulse response $h(t)$ by

$$h(t) = 1 - \left[ \left( \frac{e^{-\tau\omega_0 t}}{\sqrt{1-\tau^2}} \right) \cdot \sin\left( \omega_0 t \sqrt{1-\tau^2} + \arccos(\tau) \right) \right], \tag{B.3}$$

where $\tau = 0.85$ is a damping factor and $\omega_0 = 2\pi \cdot f_0$ is the characteristic coil frequency (Harris, 2013). Figure B.1 shows the amplitude spectrum, the phase spectrum, and the impulse response of the PROTEM receiver coils. The High-Frequency coil (HF) is trimmed to a high resonance frequency of 702 kHz resulting in a high sensitivity for early times whereas the Low-Frequency coil (LF) is trimmed to a lower resonance frequency of 29 kHz and the Borehole-sensor coil (BH) to 10 kHz resulting in an optimal detection range for intermediate to late-times. However, the amplitude of the induced voltage is damped for frequencies below or above the resonance frequency. From the impulse response $h(t)$ the following conclusions can be drawn. The HF-coil can effectively be used for very early times around 1 µs whereas the LF-coil is more suitable for intermediate at 40 µs and the BH-coil for late times at 100 µs. The characteristic impulse response of each receiver coil has to be taken into account for interpreting early times in the transient electromagnetic response since the amplitude is damped for earlier times than the characteristic response.

## B.2. Time stability of the output current function

The PROTEM system can operate at five different repetition rates (RR) ranging from 25 Hz to 0.25 Hz at 30 gate mode. The working cycle of one period $T = 1/RR$ includes a positive

and negative current turn-on, turn-off cycle as well as two receiver measurement cycles (see Figure B.2). Each cycle lasts a quarter of the transmitter period $T$. When the transmitter output current is switched off, the receiver starts the measurement cycle. Since the induced voltage in the receiver coil rapidly decays, the measurement gates are designed in such a way, that each gate has a different time interval. The width of the gates thereby increase logarithmically over time (Genoics Limited, 2006). Thus, early short time gates can measure the fast decaying field in the subsurface, while later wider time gates measure the more and more slowly decaying field. The first gate is positioned at a fixed time releative to the current turn-off time $T_0$. For instance, at a RR of 25 Hz, the first gate is positioned 6.8 µs after the current turn-off time $T_0$. Therefore, the turn-off time $T_0$ needs to be measured precisely to ensure comparability of repeated measurements during a monitoring experiment. The determination process of the turn-off time is chart-based for the TEM47 transmitter and digital for the TEM57-MK2 and TEM67 transmitter through a liquid-crystal display. However, the displayed value of the TEM57-MK2/ TEM67 transmitter fluctuates over time due to insolation, ambient temperature and the chosen repetition rate of the transmitter. For a 100 m × 100 m transmitter loop with an output current of 17 A, the displayed value can vary between ±15 µs around the actual turn-off time, depending

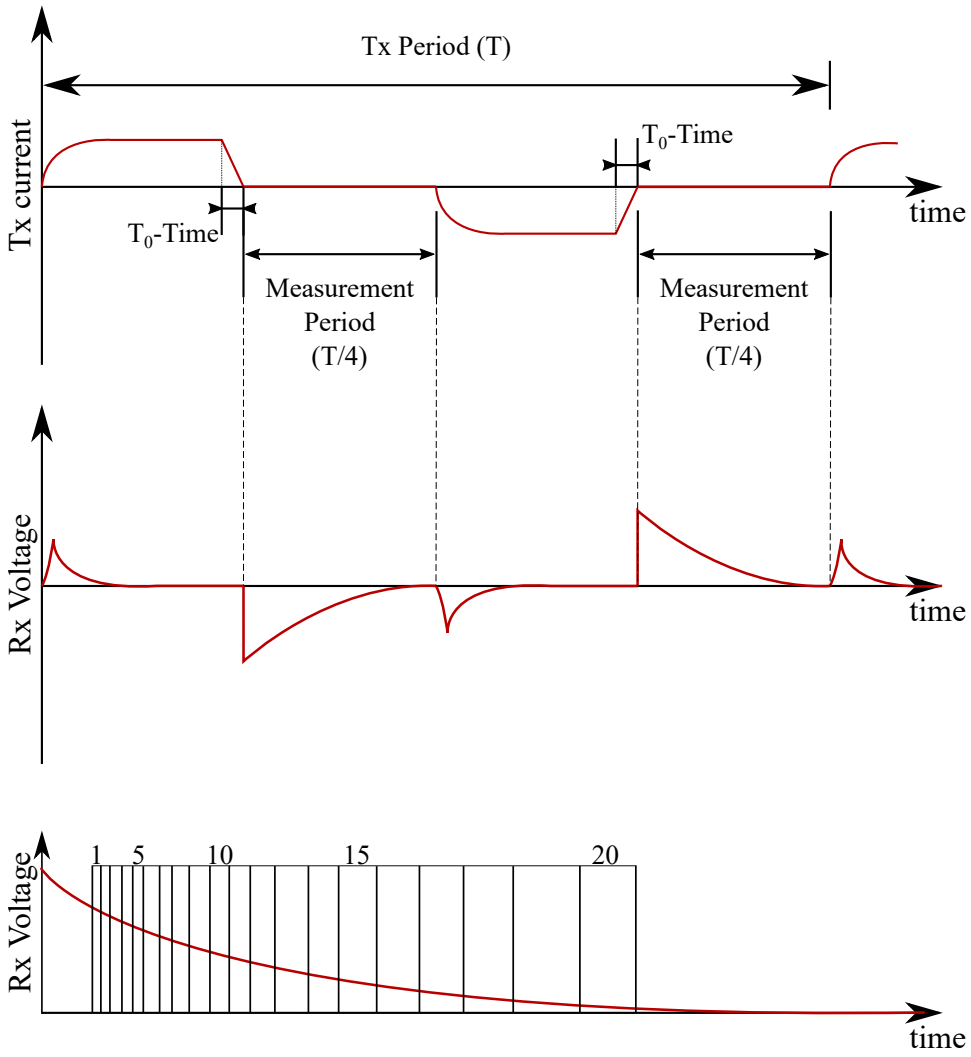


**Fig. B.2.:** Schematic diagram of the working cycle for the PROTEM transmitter systems. Current output function (top) vs. induced receiver voltage (middle) over time. Logarithmically increasing receiver gates over time (bottom) (Levy and McNeil, 1984).

on the subsurface conductivity. Thereby, for a high subsurface conductivity the range of the displayed turn-off time is larger than for a lower subsurface conductivity (see Chapter 5).

In an effort to measure the true turn-off time exactly, a current transductor (CKSR 25-NP) was used. This is a closed loop fluxgate-based transducer with responding times smaller 1 µs and therefore ideal for measuring fast current turn-off processes (Life Energy Motion, 2015). Figure B.3 shows the output current function of the TEM47 transmitter for each individual cycle at an output current of 3 A for an 100 m × 100 m transmitter loop. The turn-off time is 5 µs. This is in agreement with the chart-based value. Figure B.4 shows the current function of the TEM57-MK2 transmitter for each individual cycle for an 100 m × 100 m transmitter loop with an output current of 11 A in crystal clock synchronization mode. The turn-off time is 50 µs. However, the value of the LCD varies between 45 µs to 58 µs. Therefore, the LCD is not a reliable method to determine the true turn-off time $T_0$. Figure B.5 show the time dependency of the current turn-off function of the TEM57-MK2 transmitter measured over 2.5 hours in Tharandter Wald for an 100 m × 100 m transmitter loop with an output current of 17 A. The turn-off time $T_0$ of 56 µs and the amperage are constant during monitoring time. Discontinuities along the daytime axes are caused by trigger malfunction of the portable USB-oscilloscope. In collaboration with the Institute of Geophysics and Meteorology of the University of Cologne, the test was repeated at a survey in Cologne for an 100 m × 100 m transmitter loop with an output current of 10 A (Figure B.6). The turn-off time $T_0$ of 34 µs and the amperage are constant during the monitoring. In case of reference cable synchronization, a constant delay between the reference signal impulse and the actual turn-off cycle of the transmitter current of 5.6 µs can be measured. This effects the first gate at the 25 Hz repetition rate. The center of the first gate is positioned 6.8 µs after the reference cable impulse. However, due to the signal delay between transmitter and receiver, the first gate actually measures during the current shut down of the transmitter instead of its intended position 6.8 µs after the current turn-off time $T_0$ (Figure B.7). Therefore, depending on the current turn-off time, time gates can be oversaturated due to the high induced voltage in the receiver coil (saturation of the analog digital converter). Oversaturated time gates might affect later ones, therefore it is recommended to skip two or three gates after the last oversaturated gate.

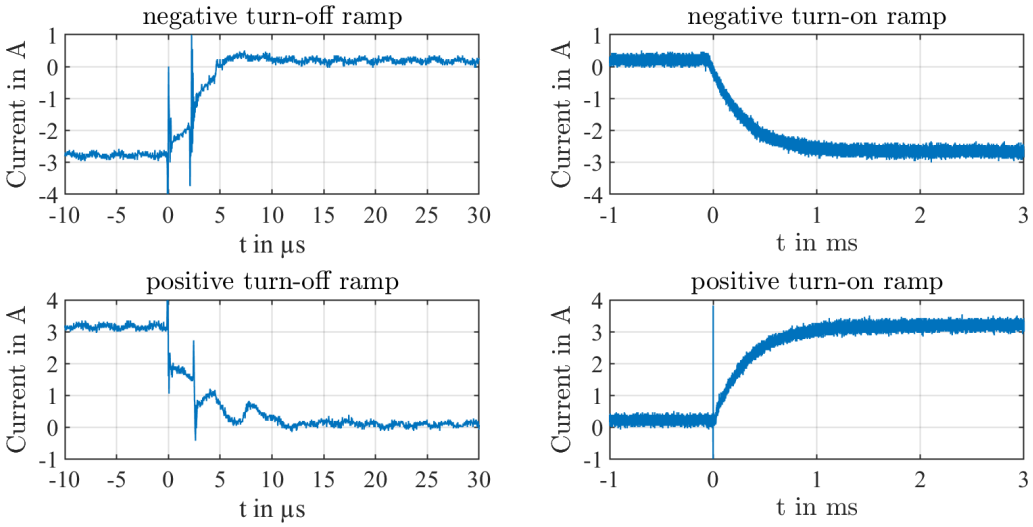


**Fig. B.3.:** TEM47 current ramp function for the negative turn-off, negative turn-on, positive turn-off, and positive turn-on cycle at 3 A output current for an 100 m × 100 m transmitter loop.

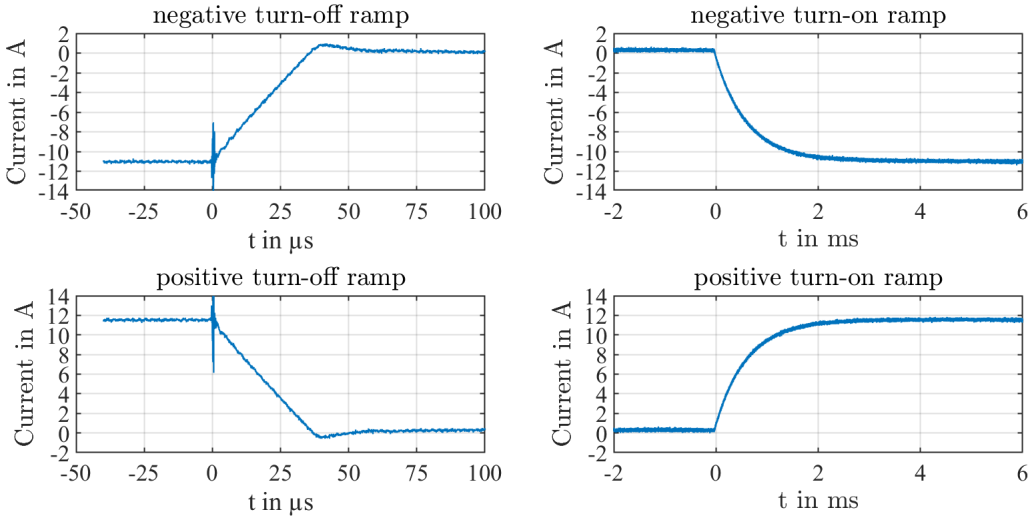


**Fig. B.4.:** TEM57-MK2l ramp function for the negative turn-off, negative turn-on, positive turn-off, and positive turn-on cycle at 11 A output current for an 100 m × 100 m transmitter loop.

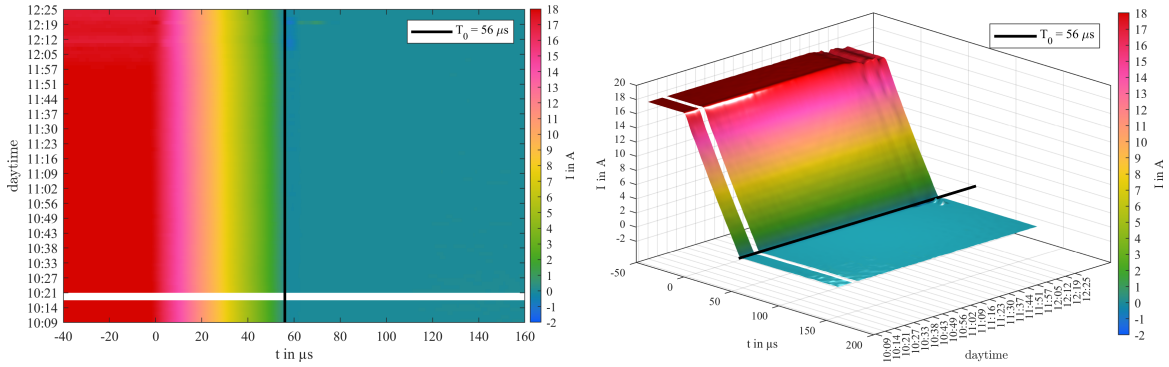


(a) (b)

**Fig. B.5.:** Measured time dependency of the TEM57-MK2 transmitter output current turn-off function (positive cycle) for a 100 m × 100 m transmitter loop at Tharandter Wald, Saxony as 2D plot (a) and 3D surface plot (b). The output current was set to 17 A at 25 Hz repetition rate.

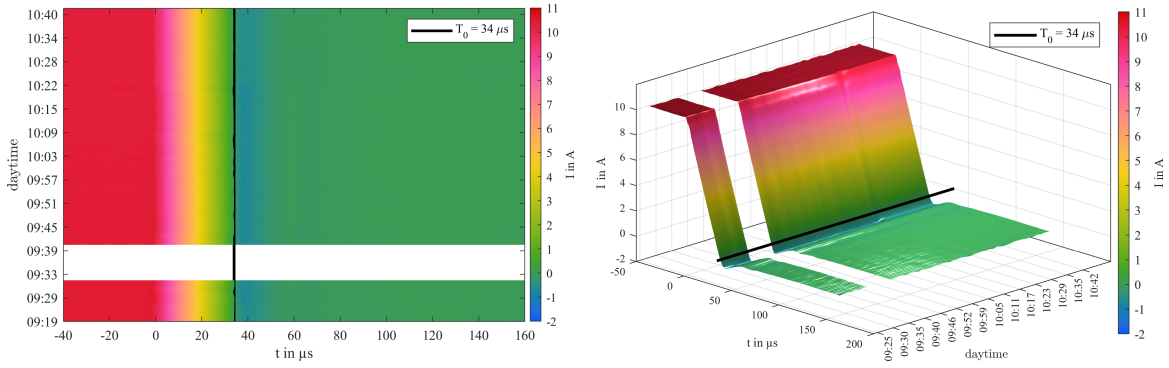


(a) (b)

**Fig. B.6.:** Measured time dependency of the TEM57-MK2 transmitter output current turn-off function (positive cycle) for an 100 m × 100 m transmitter loop at Vorgebirgspark, Collogne, as 2D plot (a) and 3D surface plot (b). The output current was set to 10 A at 25 Hz repetition rate.

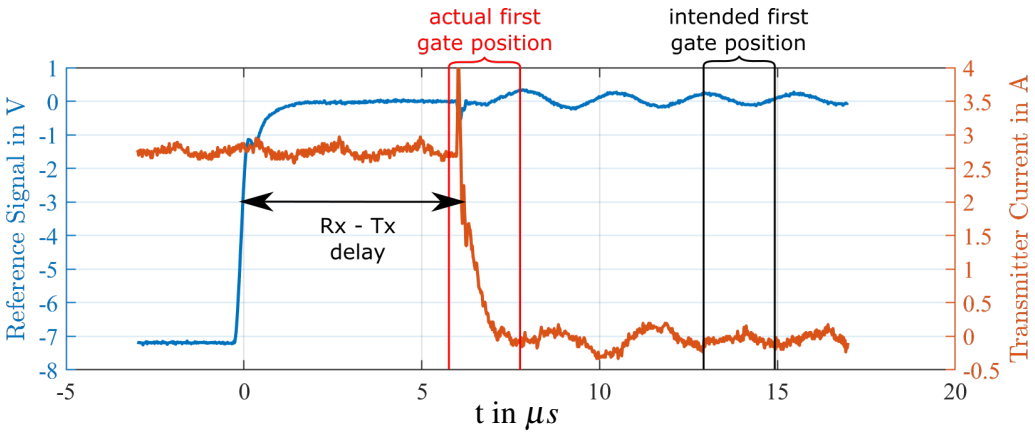


**Fig. B.7.:** Transmitter response delay between the reference cable signal impulse of the PROTEM digital receiver and the actual current turn-off cycle of the TEM47 transmitter in comparison with the first gate position at 25 Hz repetition rate.

# C. Borehole TEM measurements at the FRS in Brooks, Canada

## C.1. FRS Injection Well Completion Schematic

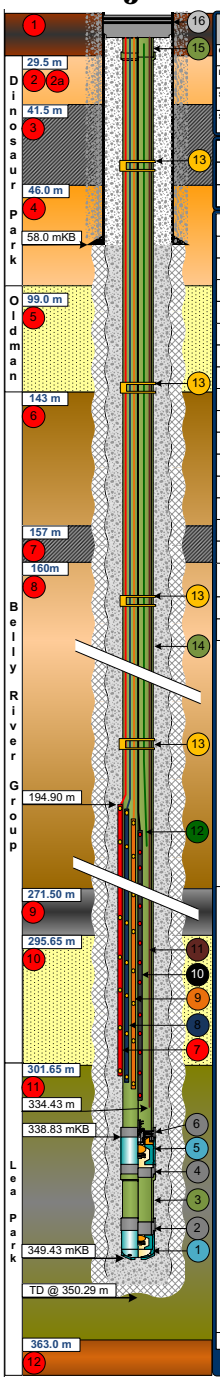


### Final FRS Injection Well Completion Schematic

| | | | |
|---|---|---|---|
| Company: CMC (Containment & Monitoring Institute) | | | Reference: Well Licence # 0478942 |
| Prepared for: Don Lawton | Client #: (403) 210-6671 | | Location: CMCRI 102 MW2 COUNTESS 10-22-17-16W4 |
| Sales Rep: | Vendor #: | | |
| Service Center: | Drawn by: Mark Woitt | Date: 5/14/2016 | Page: 1 |

| TUBULAR | Size | Weight | Grade | Thread | Depth |
|---|---|---|---|---|---|
| Casing | 298.4 mm OD/ 281.53 mm ID | 62.5 kg/m | J-55 | ST&C | 58 mKB |
| Casing | 114.3 mm OD/ 97.80 mm ID | 5.40 kg/m | Series 1750 Fiber Glass | EUE | 349.43 mKB |

| ITEM | DESCRIPTION | I.D. | O.D. | Length (m) |
|---|---|---|---|---|
| 1. | 114.3 mm Single Valve Float Shoe, 114.3 mm LTC Box Connection | N/A | 127.00 | .43 |
| 2. | 114.3 mm LTC Pin X 114.3 mm EUE Box X-Over | 101.6 | 139.70 | .29 |
| 3. | 1 Joint, 114.3 mm Fiber Glass Tubing, 114.3 mm 5.4 kg/m Series 1750 FG With EUE Box X Pin Connections | 97.80 | 154.90 | 9.22 |
| 4. | 114.3 mm LTC Box X 114.3 mm EUE Pin X-Over | 101.6 | 139.70 | .25 |
| 5. | 114.3 mm Single Valve Float Collar, 114.3 mm LTC Box X Pin Connections | N/A | 127.00 | .41 |
| 6. | 114.3 mm LTC Box X 114.3 mm EUE Pin X-Over | 101.6 | 139.70 | .25 |
| 7. | Geophone Array w/ Geo Space Technologies GS-32CT phones. 8 Geophones Spaced Between 194.9 and 299.9 mKB | | | |
| 8. | Geophone Array w/ Geo Space Technologies GS-32CT phones. 8 Geophones Spaced Between 119.9 to 304.9 mKB | | | |
| 9. | Geophone Array w/ Geo Space Technologies GS-32CT phones. 8 Geophones Spaced Between 204.9 and 309.9 mKB | | | |
| 10. | ERT Array. 16 Sensors Spaced Between 250.1 and 325.4 mKB | | | |
| 11. | Helical Would Fiber Optic Cable. Bottom At 334.43 mKB | | | |
| 12. | Encapsulated 6.35 mm DTS/ DAS Fiber Optic Line. Bottom At 248.59 mKB | | | |
| 13. | 37 Joints, 114.3 mm Fiber Glass Tubing, 114.3 mm 5.4 kg/m Series 1750 FG With EUE Box X Pin Connections | 97.80 | 154.90 | 336.03 |
| 14. | Cannon Over Coupling Protectors | | | |
| 15. | 114.3 mm Fiber Glass Pup Joint, 114.3 mm 5.4 kg/m Series 1750 FG With EUE Pin X Pin Connections | 97.80 | 154.90 | 1.03 |
| 16. | Nominal 346.07 mm X14.0 MPa StreamFlo Type Tubing Hanger With 114.3 mm EUE Box X Box Connections. Prepped With (3) 12.7 mm NPT Box Ports & (3) 19.05 mm NPT Box PortsFor Capillary Line Passage. | | | .30 |
| | KB To THF | | | 4.18 |
| | Casing End mKB | | | 349.43 |

NOTES

**Cementing Details;**
114.3 mm FG Casing Cemented w/ 21.3m$^3$ (26.4T) Pozz Fume G @ 1770kgm3 +0.1%Spc-12000_0.2% Fp-19+0.6% Fl-5+1%A-11+1%Cacl2, displaced w/2.56 m$^3$ H20, Plug down @ 14:07hrs. 5.5m$^3$ good cement returns,

298.4mm Surface Csg Cemented w/4.83m$^3$ (5T) Surf cem 1700@1730kg/m3 +0.15%fp-19+3%cacl2, Plug down @ 02:28hrs. 2m$^3$ good returns

**Geological Legend**
1) Pleistocene and Holocene (4.9 m KB)
2) Dinosaur Park Formation/Bedrock Surface (29.5 m)
2a) Dinosaur Park Formation, Lethbridge coal zone top (29.5 m)
3) Dinosaur Park Formation, Lethbridge coal zone base (41.5 m)
4) Dinosaur Park Formation, sandy zone (46 m)
5) Oldman Formation (99 m)
6) Foremost Formation (143 m)
7) Belly River Group, Foremost Formation, Herronton sandstone mbr. ? (143-149 m)
8) Belly River Group, Foremost Formation, top Taber Coal Zone (157 m)
9) Belly River Group, Foremost Formation, base Taber Coal zone (160 m)
10) Belly River Group, Foremost Formation, MacKay Coal Zone (271.5 m)
11) Belly River Group, Foremost Formation, Brosseau Mbr. (basal Belly River sst., 295.65 m)
12) Upper Lea Park Formation/Pakowki member (301.65 m)
13) Lower Lea Park Formation Alderson Member/Milk River shoulder (363.0 m)

Not To Scale

powerDRAW.net

## C.2. Calculation of the rock volume occupied by sequestrated $CO_2$

In the following, a short description is given how to calculate the rock volume occupied by $CO_2$ under reservoir conditions. Given the total injected mass $m_{CO2}$, the density $\rho_{CO2}$ of the sequestrated $CO_2$ under reservoir conditions and the $CO_2$ saturation $S_{CO2}$ inside the target formation as well as the reservoir porosity $\Phi$, the rock volume occupied by $CO_2$ can be calculated by

$$V_{\text{rock}} = \frac{V_{CO2}}{S_{CO2} \cdot \Phi}, \tag{C.1}$$

where

$$V_{CO2} = \frac{m_{CO2}}{\rho_{CO2}}. \tag{C.2}$$

The density $\rho_{CO2}$ in $[\text{kg/m}^3]$ is thereby a function of temperature and pressure, and can be calculated using the equation of state for real gases (Hering et al., 2004)

$$\rho_{CO2} = \frac{M \cdot p}{Z \cdot R \cdot T} \tag{C.3}$$

where

$M$ is the molar mass in $[\text{kg/mol}]$,

$p$ is the reservoir pressure in $[\text{Pa}] = \left[\text{kg/(m s}^2)\right]$,

$R$ is the gas constant in $\left[\text{kg m}^2/(\text{s}^2\,\text{mol K})\right]$,

$T$ is the reservoir temperature in $[\text{K}]$, and

$Z$ is the compressibility factor.

The compressibility factor $Z$ can be calculated by evaluating the roots of the Peng-Robinson equation of state (Peng and Robinson, 1976)

$$Z^3 - (1-B)Z^2 + (A - 3B^2 - 2B)Z - (AB - B^2 - B^3) = 0, \tag{C.4}$$

with

$$A = \frac{a\alpha p}{R^2 T^2},$$
$$B = \frac{bp}{RT},$$
$$a = \frac{0.45724 \cdot R^2 T_c^2}{p_c},$$
$$b = \frac{0.07780 \cdot RT_c}{p_c} \quad \text{and}$$
$$\alpha = (1 + (0.37464 + 1.54226\omega - 0.26992\omega^2)(1 - \sqrt{T/Tc}))^2,$$

where $p_c$ is the pressure and $T_c$ is the temperature of $CO_2$ at the critical point. The acentric factor $\omega$ is a dimensionless factor, which describes the deviation of the ideal spherical molecular form under thermodynamic influences ($\omega_{CO2} = 0.239$). Peng and Robinson (1976) further state, that Equation C.4 either yields one or three roots depending upon the number of phases in the system. In a two-phase system, the largest root accounts for the compressibility factor of the vapor while the smallest positive root corresponds to that of the liquid.

## C.3. 3D forward TEM simulations

### C.3.1. Simulation results for 600 t $CO_2$ for the small transmitter setup

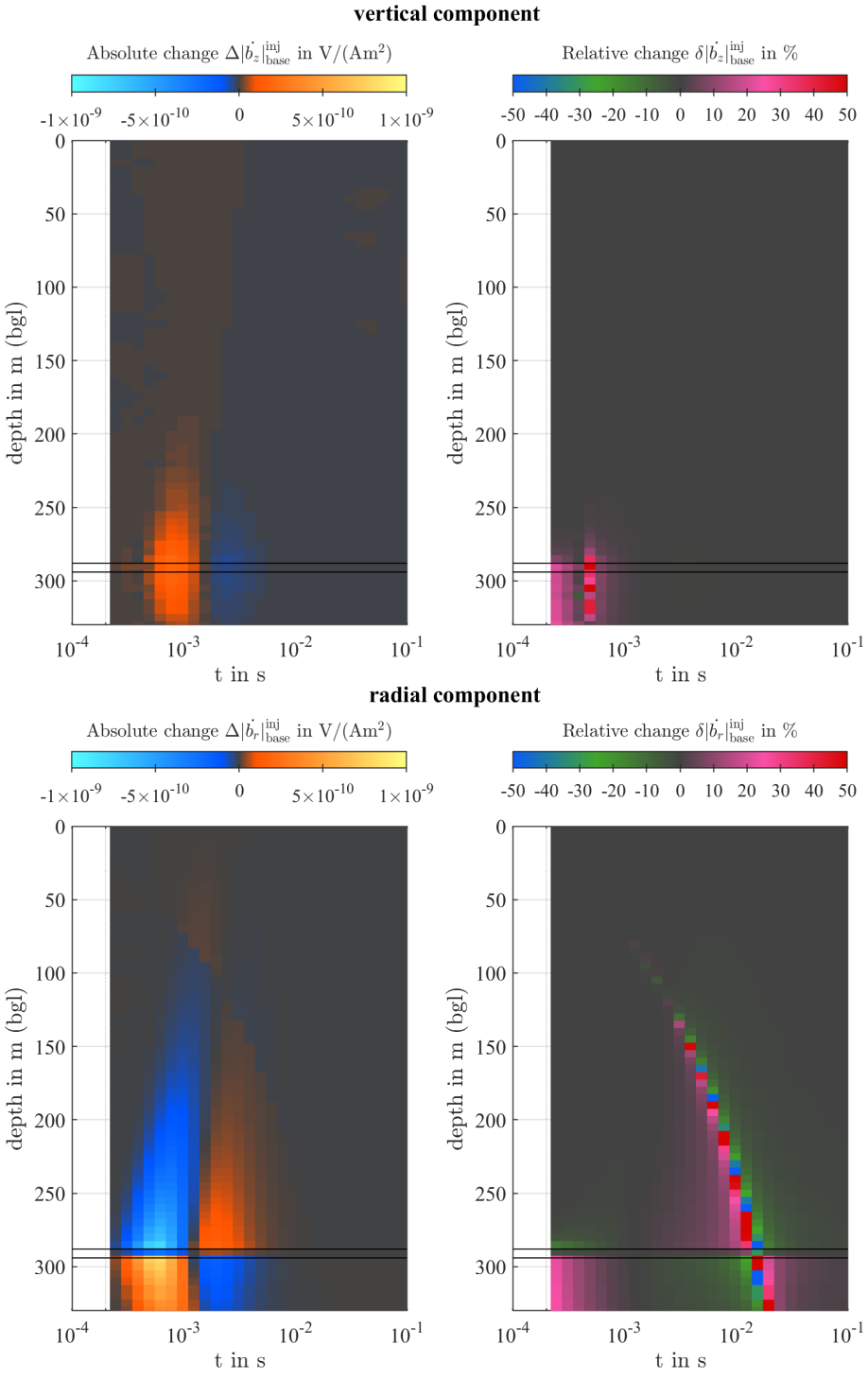


**Fig. C.1.:** Absolute changes $\Delta|\vec{\dot{b}}|^{\text{inj}}_{\text{base}}$ (left) and relative changes $\delta|\vec{\dot{b}}|^{\text{inj}}_{\text{base}}$ (right) of the vertical (top) and radial (bottom) component of the transient response as a function of depth and time between the baseline and injection state evaluated at observation well #2 for the small transmitter loop setup. The total amount of $CO_2$ is 600 t.

# C.4. Relative and absolute differences between 2016 and 2018 field survey for the TEM57 transmitter setup

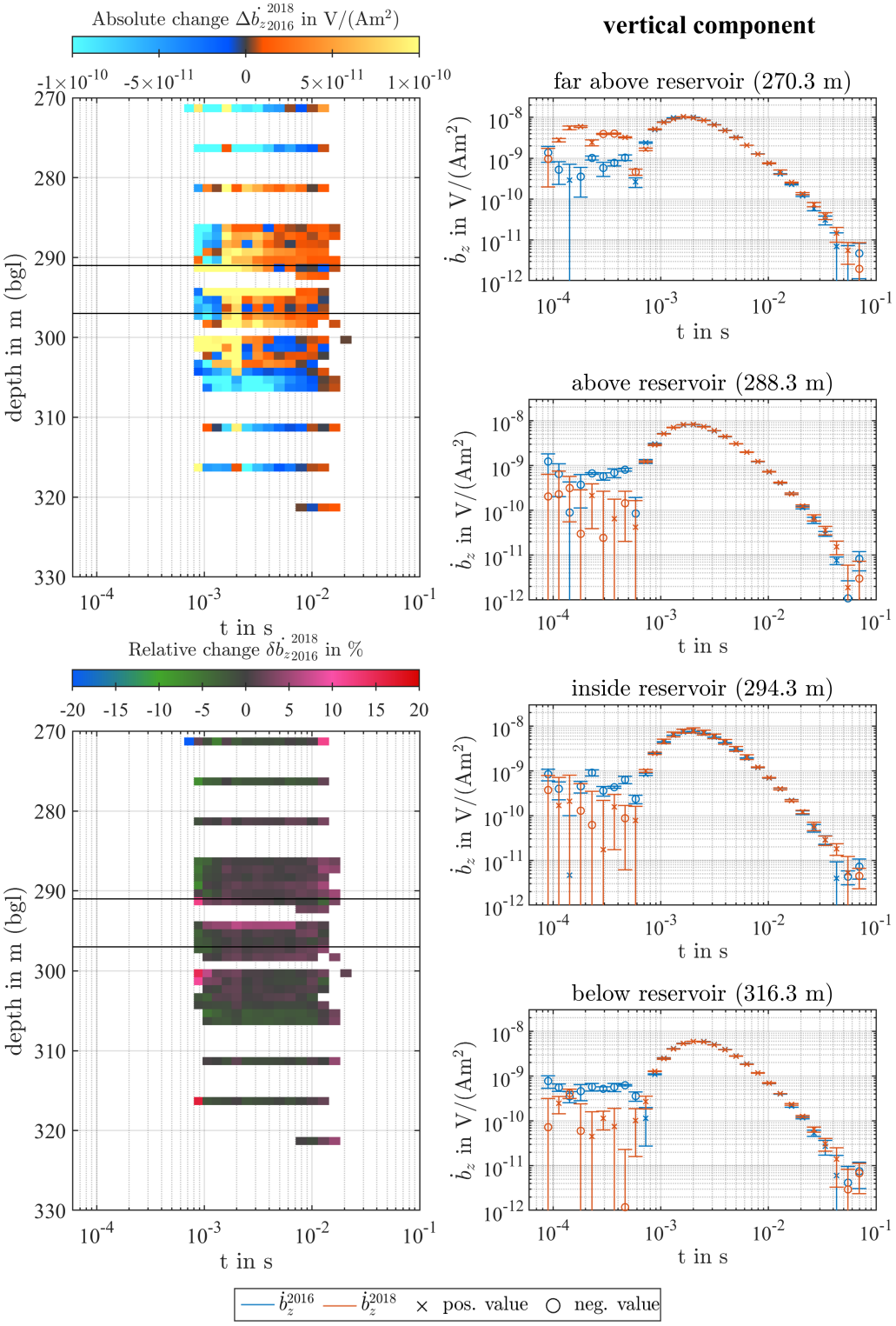


**Fig. C.2.:** (Left) Absolute differences $\Delta|\dot{b}_z|_{2016}^{2018}$ (top) and relative differences $\delta|\dot{b}_z|_{2016}^{2018}$ (bottom) between the absolute values of the vertical TEM responses of field surveys in 2016 and 2018 for the TEM57 transmitter setup limited to coefficients of variation $\leq 5\,\%$. Black lines indicate identified reservoir limits. (Right) TEM responses $\dot{b}_z$ below, inside, above and far above the reservoir.

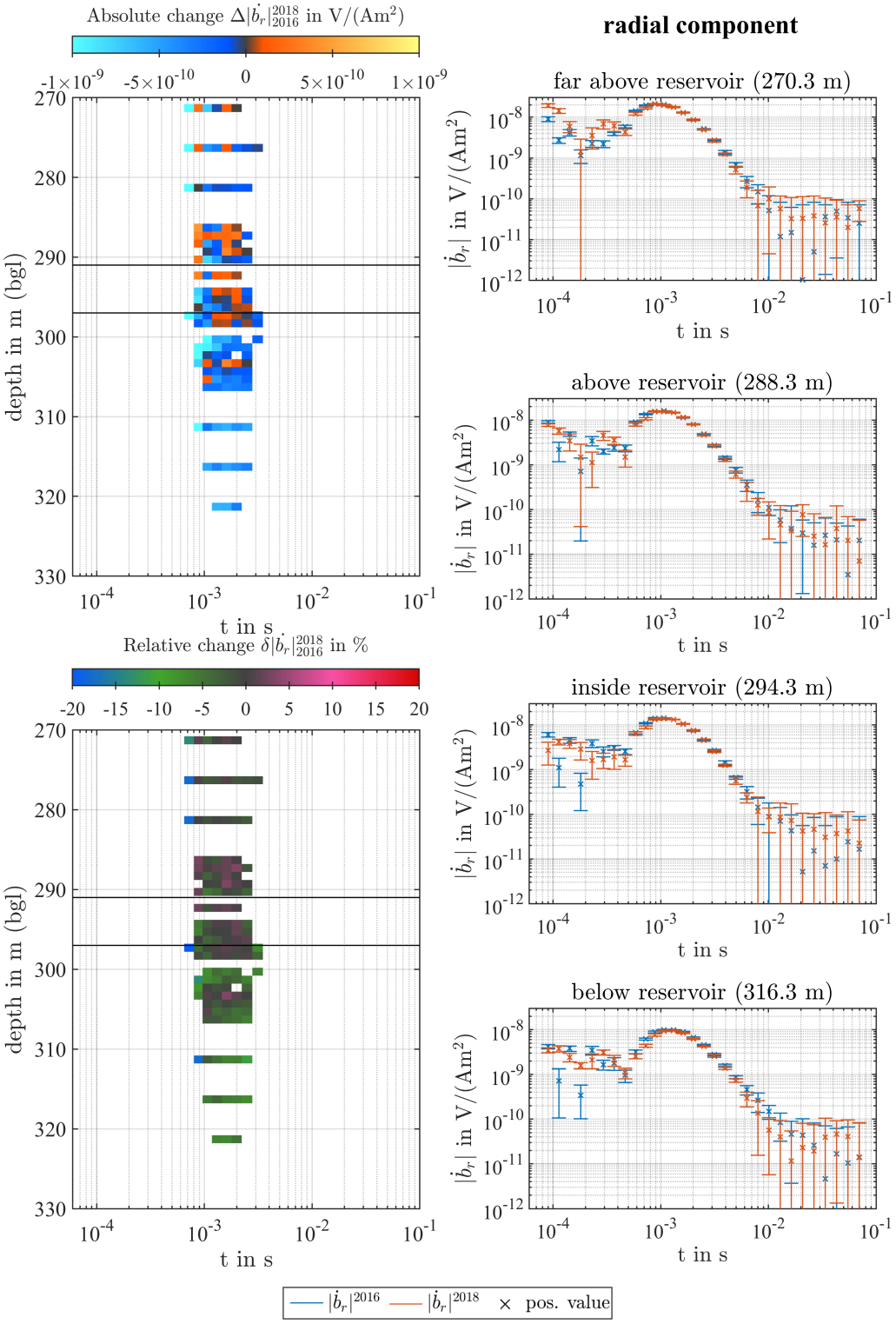


**Fig. C.3.:** (Left) Absolute differences $\Delta|\dot{b}_r|^{2018}_{2016}$ (top) and relative differences $\delta|\dot{b}_r|^{2018}_{2016}$ (bottom) between the absolute values of the vertical TEM responses of field surveys in 2016 and 2018 for the TEM57 transmitter setup limited to coefficients of variation $\leq$5 %. Black lines indicate identified reservoir limits. (Right) TEM responses $|\dot{b}_r|$ below, inside, above and far above the reservoir.

# C.5. Clustering results of TEM measurements for TEM67 transmitter setup

## C.5.1. Vertical component

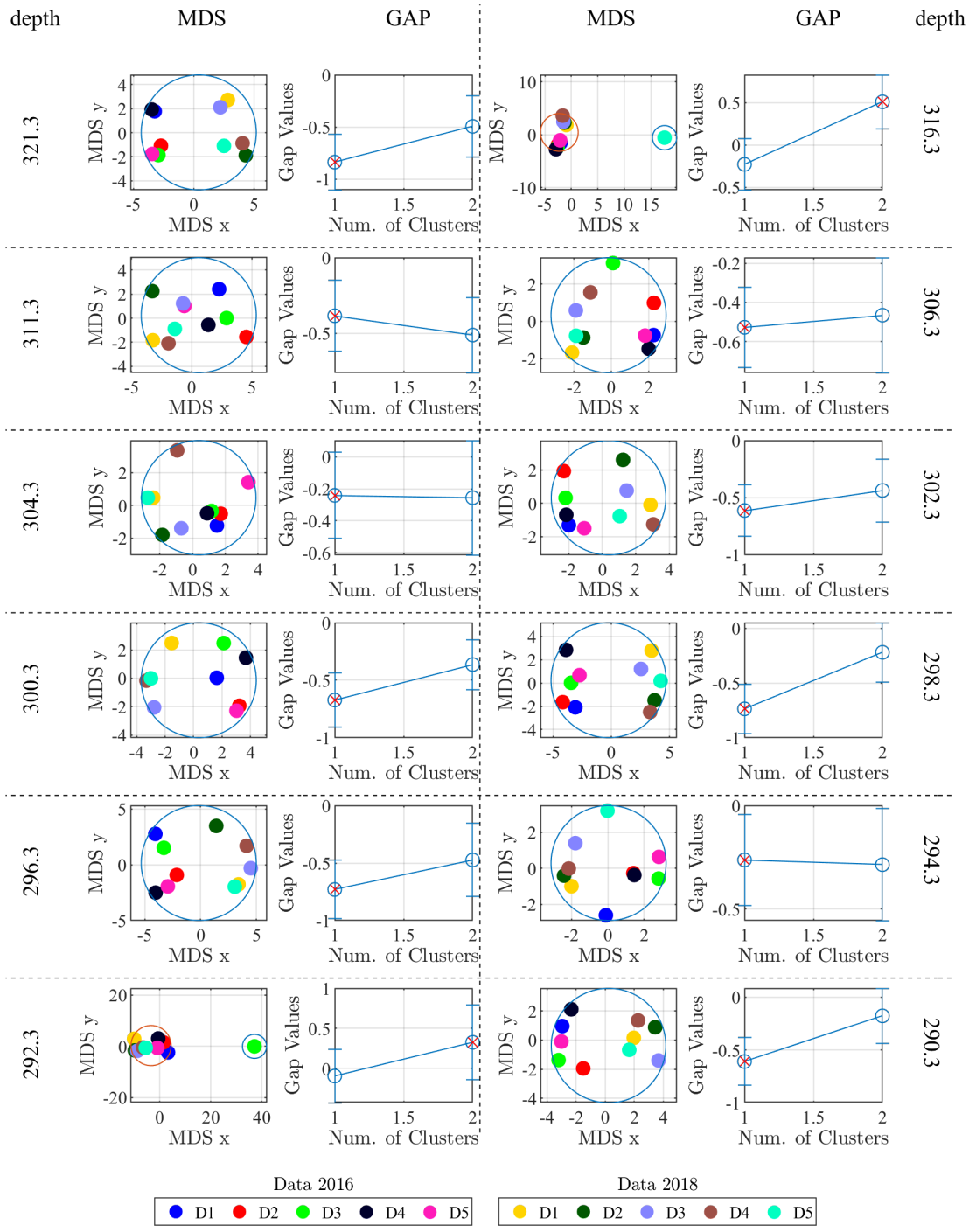


**Fig. C.4.:** Clustering results based on the DTW distance metric of the five consecutive measurement of the vertical transient response $\dot{b}_z$ in 2016 and 2018 for each observation depth along the observation borehole #2 at the FRS for the TEM67 transmitter setup. Clusters are represented by circles of different colors in the MDS representation. The optimal number of clusters is determined by applying the gap statistic.

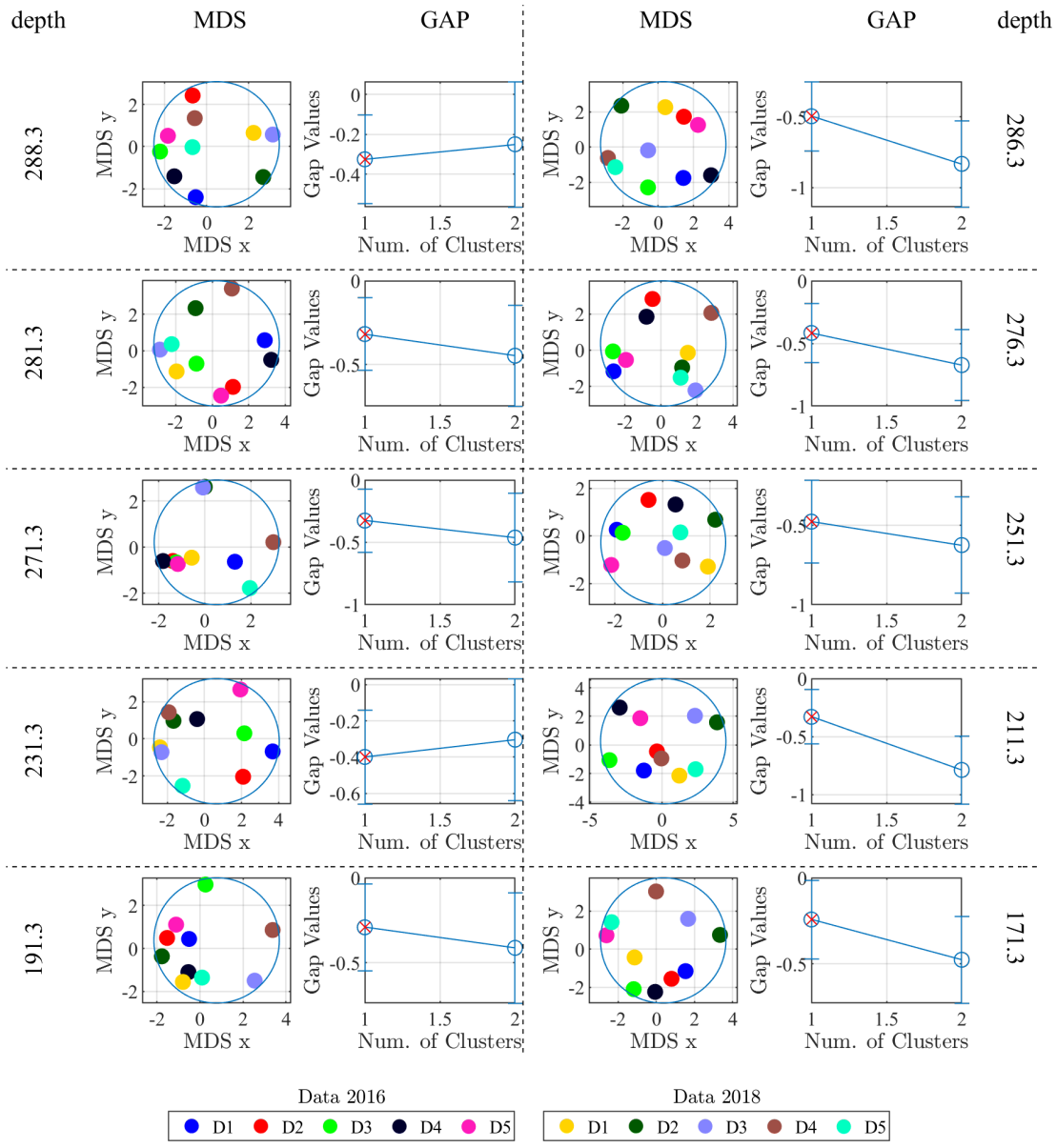


**Fig. C.5.:** Clustering results based on the DTW distance metric of the five consecutive measurement of the vertical transient response $\dot{b}_z$ in 2016 and 2018 for each observation depth along the observation borehole #2 at the FRS for the TEM67 transmitter setup. Clusters are represented by circles of different colors in the MDS representation. The optimal number of clusters is determined by applying the gap statistic (continued).

## C.5.2. Radial component

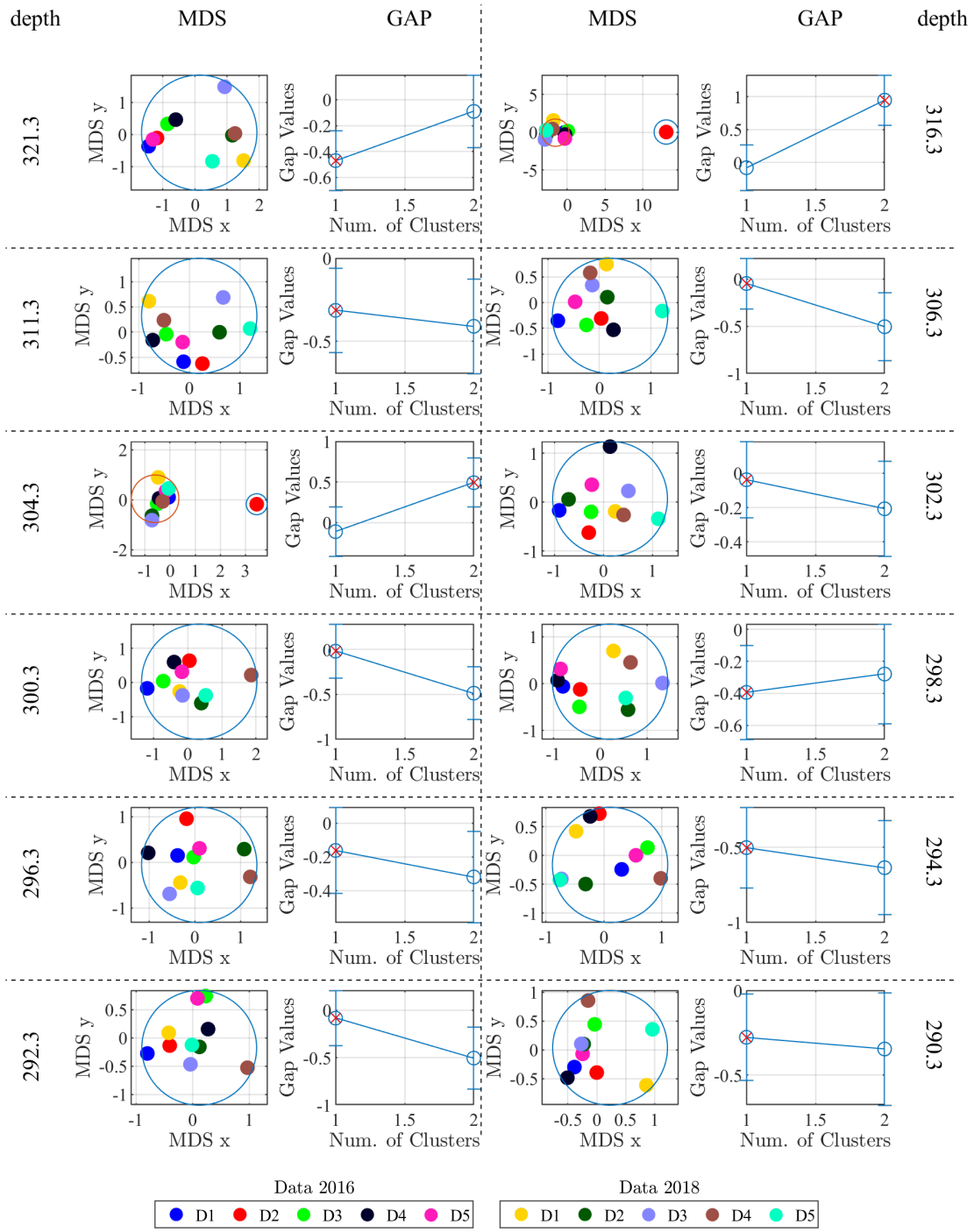


**Fig. C.6.:** Clustering results based on the DTW distance metric of the five consecutive measurement of the radial transient response $\dot{b}_r$ in 2016 and 2018 for each observation depth along the observation borehole #2 at the FRS for the TEM67 transmitter setup. Clusters are represented by circles of different colors in the MDS representation. The optimal number of clusters is determined by applying the gap statistic.

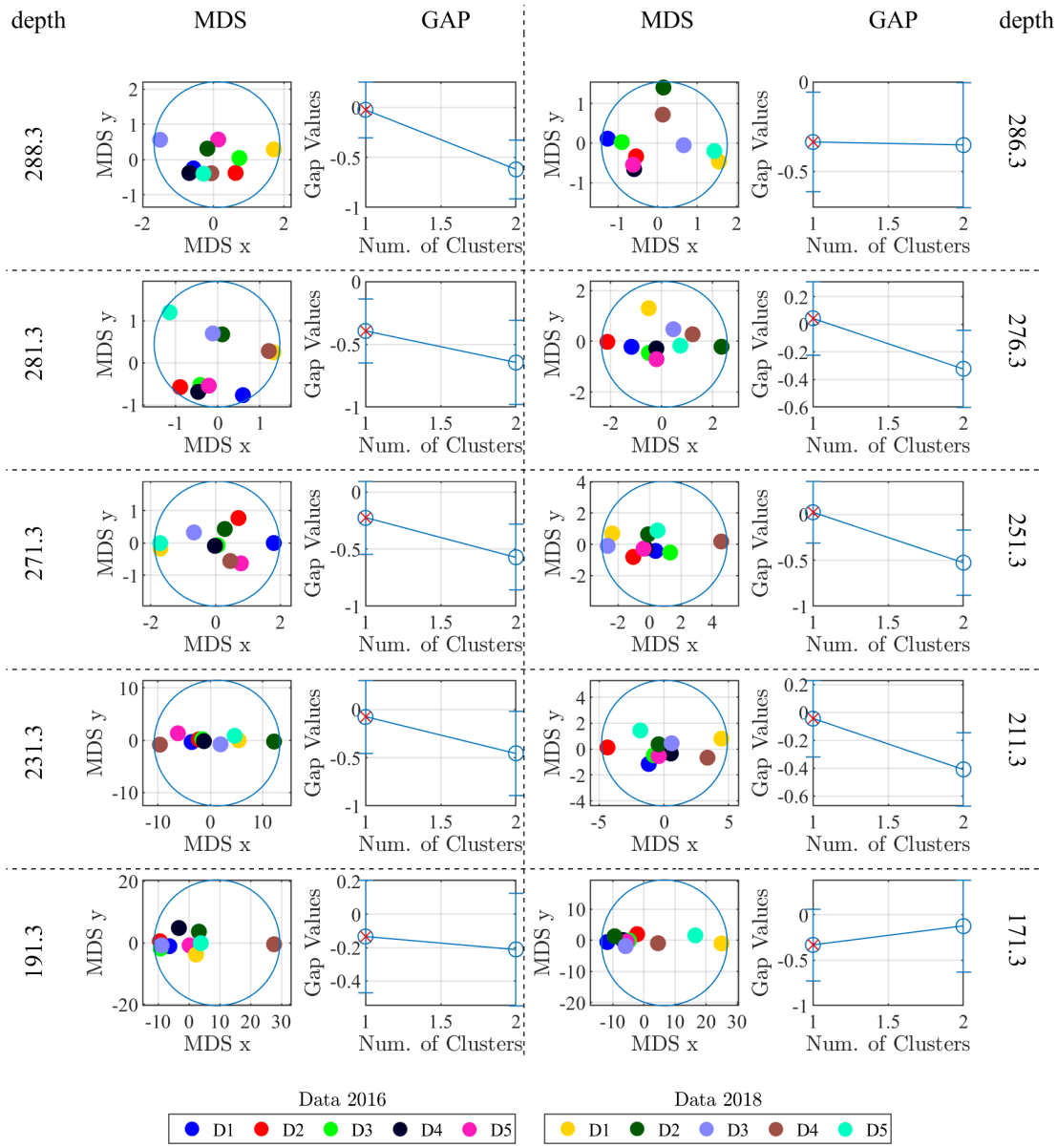


**Fig. C.7.:** Clustering results based on the DTW distance metric of the five consecutive measurement of the radial transient response $\dot{b}_r$ in 2016 and 2018 for each observation depth along the observation borehole #2 at the FRS for the TEM67 transmitter setup. Clusters are represented by circles of different colors in the MDS representation. The optimal number of clusters is determined by applying the gap statistic (continued).

# C.6. Clustering results of TEM measurements for TEM57 transmitter setup

## C.6.1. Vertical component

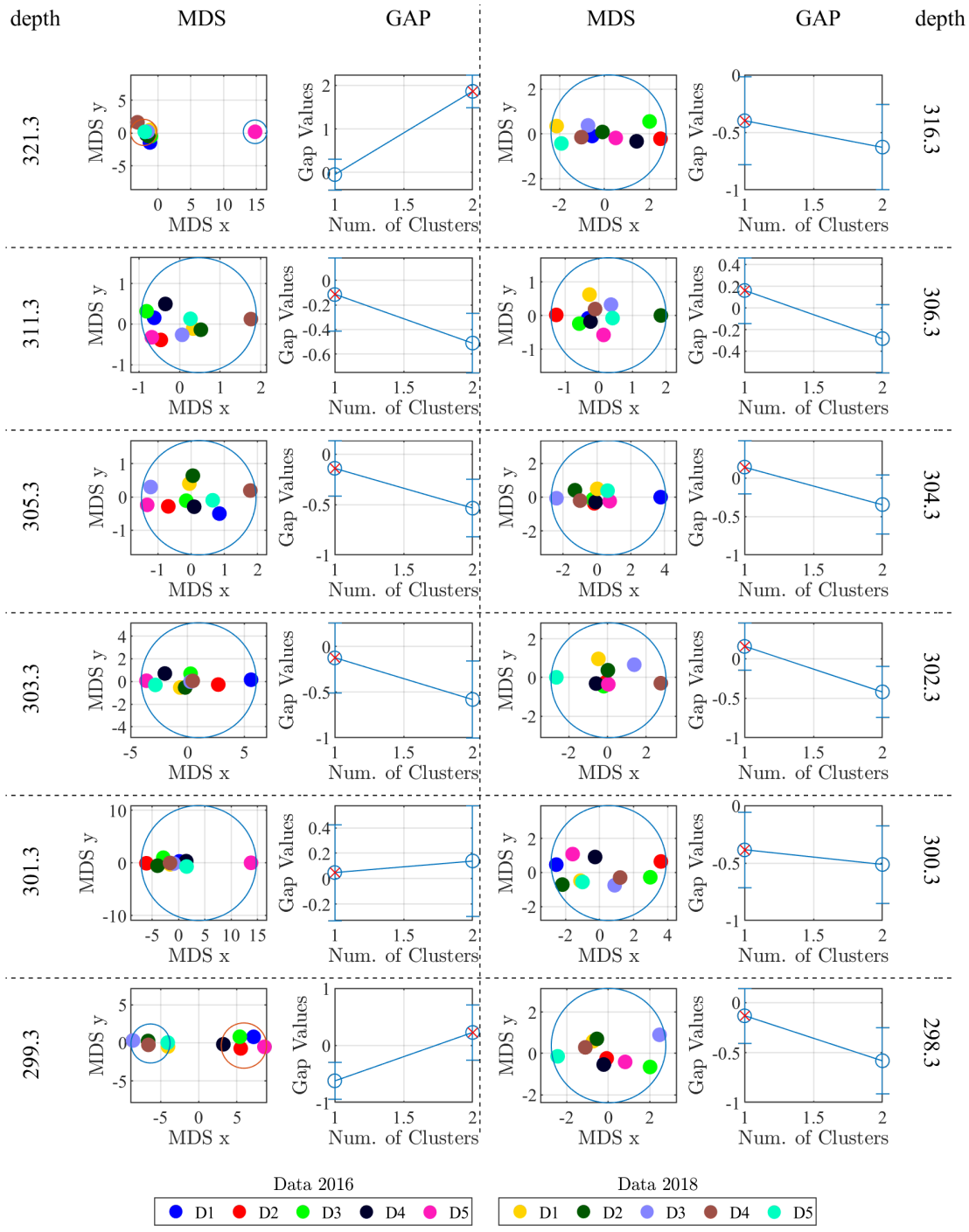


**Fig. C.8.:** Clustering results based on the DTW distance metric of the five consecutive measurement of the vertical transient response $\dot{b}_z$ in 2016 and 2018 for each observation depth along the observation borehole #2 at the FRS for the TEM57 transmitter setup. Clusters are represented by circles of different colors in the MDS representation. The optimal number of clusters is determined by applying the gap statistic.

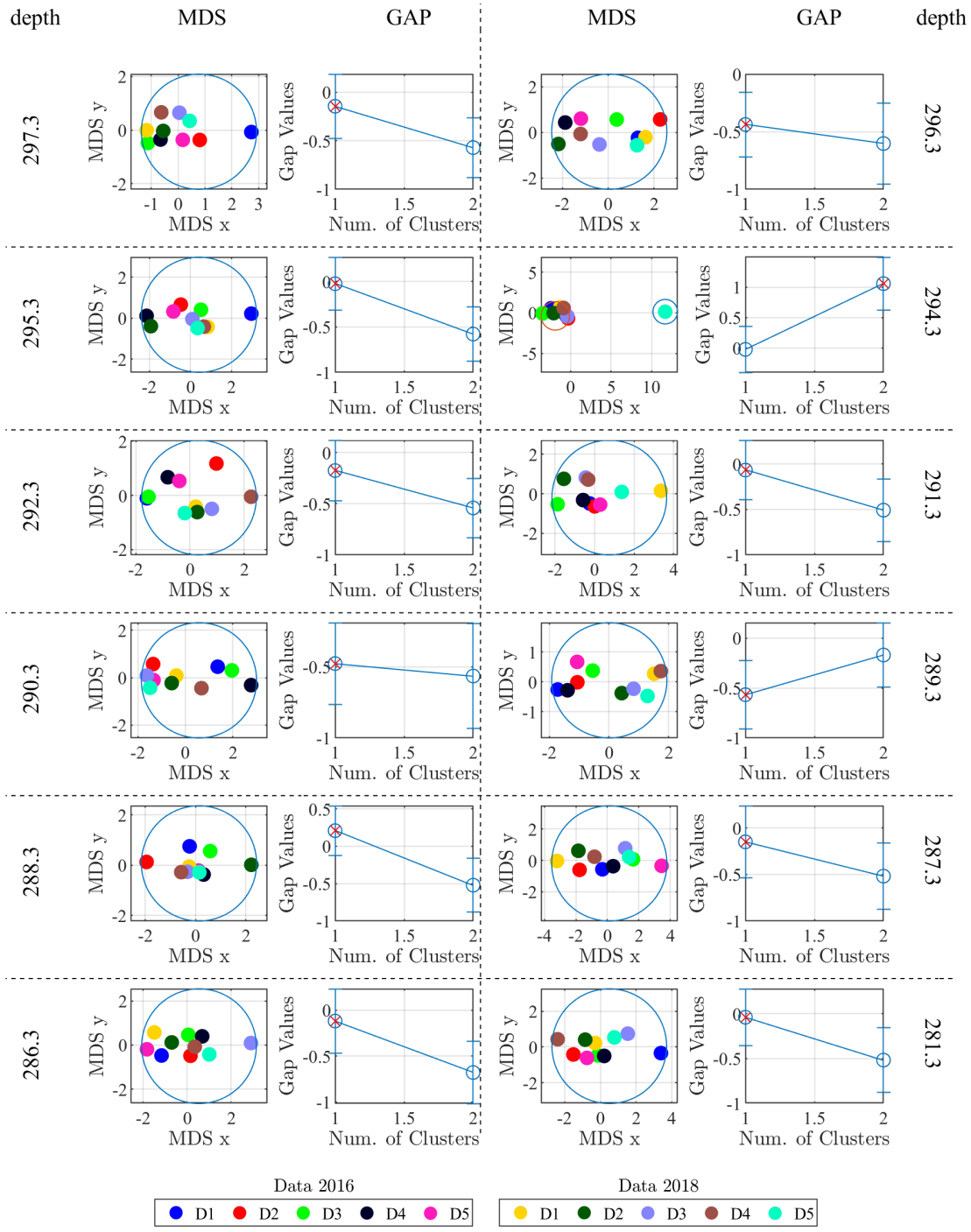


**Fig. C.9.:** Clustering results based on the DTW distance metric of the five consecutive measurement of the vertical transient response $\dot{b}_z$ in 2016 and 2018 for each observation depth along the observation borehole #2 at the FRS for the TEM57 transmitter setup. Clusters are represented by circles of different colors in the MDS representation. The optimal number of clusters is determined by applying the gap statistic (continued).

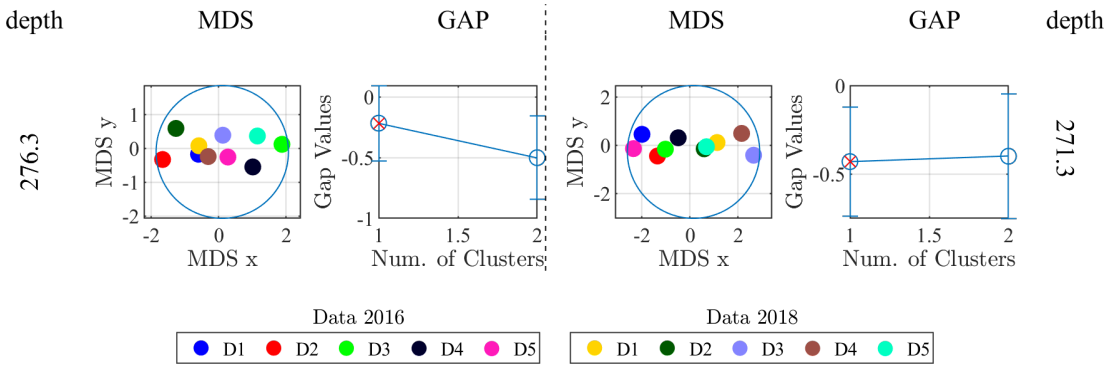


**Fig. C.10.:** Clustering results based on the DTW distance metric of the five consecutive measurement of the vertical transient response $\dot{b}_z$ in 2016 and 2018 for each observation depth along the observation borehole #2 at the FRS for the TEM57 transmitter setup. Clusters are represented by circles of different colors in the MDS representation. The optimal number of clusters is determined by applying the gap statistic (continued).

## C.6.2. Radial component

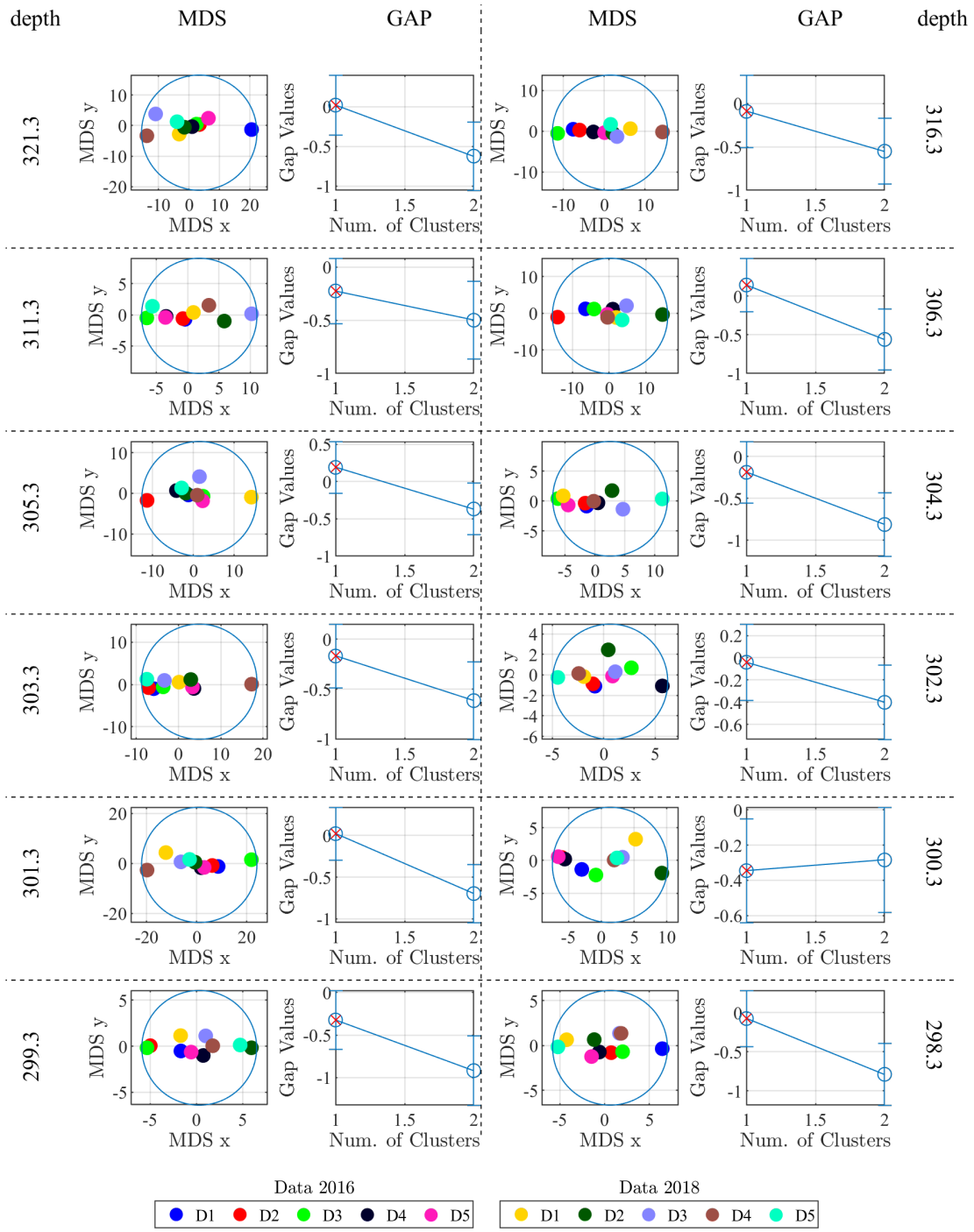


**Fig. C.11.:** Clustering results based on the DTW distance metric of the five consecutive measurement of the radial transient response $\dot{b}_r$ in 2016 and 2018 for each observation depth along the observation borehole #2 at the FRS for the TEM57 transmitter setup. Clusters are represented by circles of different colors in the MDS representation. The optimal number of clusters is determined by applying the gap statistic.

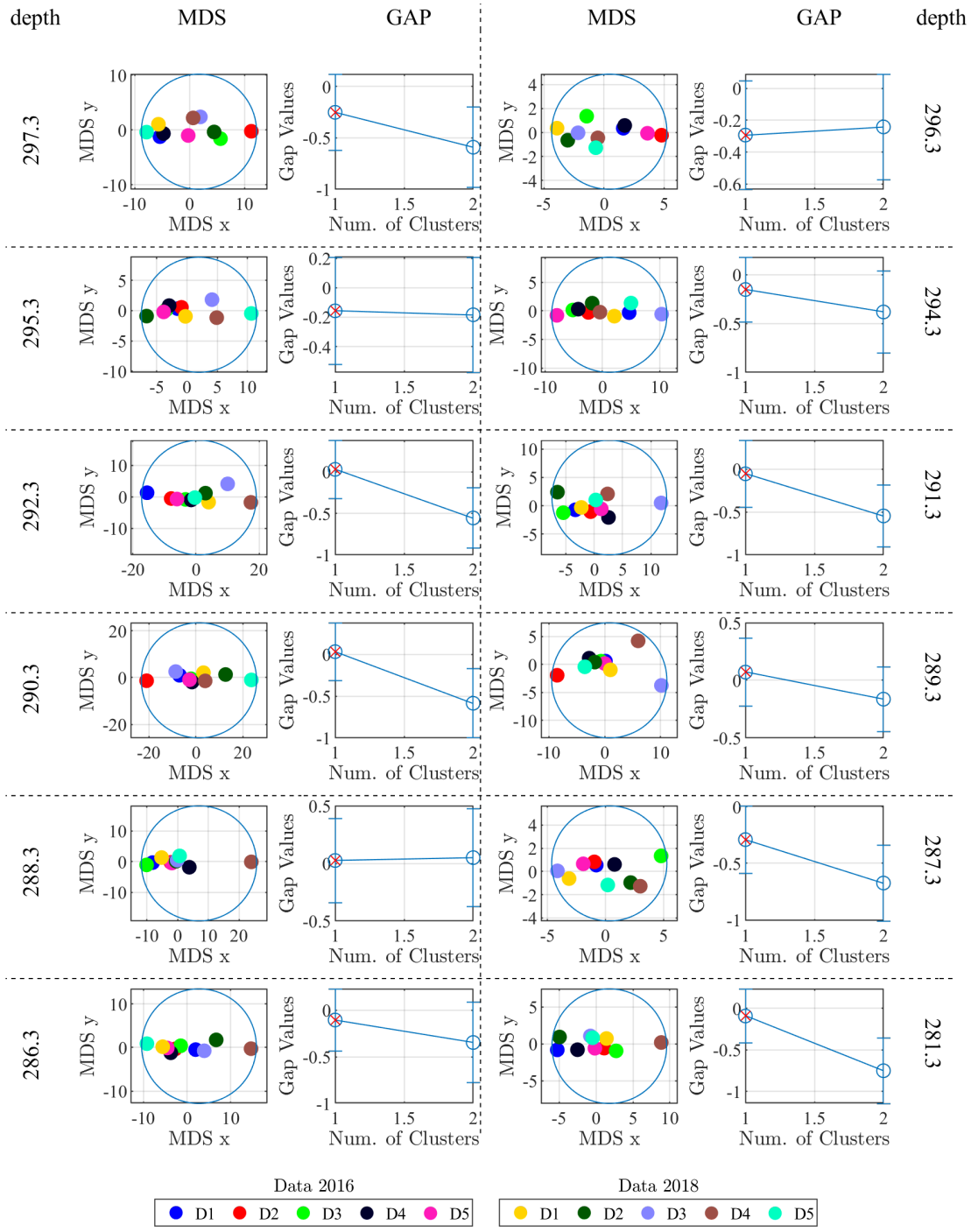


**Fig. C.12.:** Clustering results based on the DTW distance metric of the five consecutive measurement of the radial transient response $\dot{b}_r$ in 2016 and 2018 for each observation depth along the observation borehole #2 at the FRS for the TEM57 transmitter setup. Clusters are represented by circles of different colors in the MDS representation. The optimal number of clusters is determined by applying the gap statistic (continued).

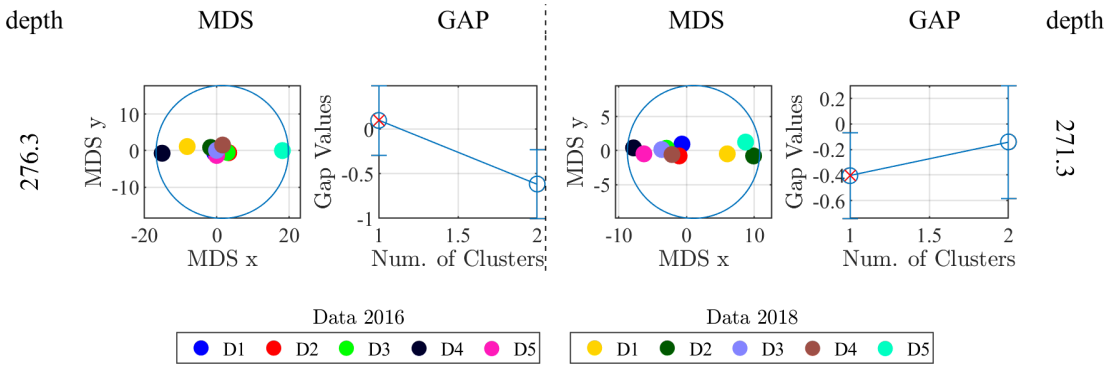


**Fig. C.13.:** Clustering results based on the DTW distance metric of the five consecutive measurements of the radial transient response $\dot{b}_r$ in 2016 and 2018 for each observation depth along the observation borehole #2 at the FRS for the TEM57 transmitter setup. Clusters are represented by circles of different colors in the MDS representation. The optimal number of clusters is determined by applying the gap statistic (continued).

# Bibliography

**Archie, G.E., 1942**. The electrical resistivity log as an aid in determining some reservoir characteristics. Trans. Americ. Inst. Mineral. Met. 146: pp. 54–62.

**Babu, G.P. and Murty, M.N., 1993**. A near-optimal initial seed value selection in K-means algorithm using a genetic algorithm. Pattern Recognition Letters 14: pp. 763 – 769.

**Barringer, A., 1962**. New approach to exploration- The INPUT airborne electrical pulse prospecting system. Min. Congr. J. 48: pp. 49–52.

**Berndt, Donald, J. and Clifford, J., 1994**. Using Dynamic Time Warping to find patterns in time series. Tech. rep., AAAI Technical Report WS-94-03.

**Bland, J.M. and Altman, D., 1986**. Statistical methods for assessing agreement between two methods of clinical measurement. The Lancet 327: pp. 307 – 310. Originally published as Volume 1, Issue 8476.

**Borg, I. and Groenen, P.J.F., 1997**. Modern multidimensional scaling: theory and applications. Springer series in statistics, Springer, New York.

**Börner, J.H.; Herdegen, V.; Repke, J.U. and Spitzer, K., 2013**. The impact of $CO_2$ on the electrical properties of water bearing porous media - laboratory experiments with respect to carbon capture and storage. Geophysical Prospecting 61: pp. 446 – 460.

**Börner, J.H.; Herdegen, V.; Repke, J.U. and Spitzer, K., 2015**. The electrical conductivity of $CO_2$-bearing pore waters at elevated pressure and temperature: a laboratory study and its implications in $CO_2$ storage monitoring and leakage detection. Geophysical Journal International 203: pp. 1072–1084.

**Börner, R.U., 2019**. A MATLAB implementation of a 1-D TEM inversion algorithm. 28. Schmucker-Weidelt-Kolloquium .

**Börner, R.U.; Ernst, O.G. and Güttel, S., 2015**. Three-dimensional transient electromagnetic modelling using Rational Krylov methods. Geophysical Journal International 202: pp. 2025–2043.

**Box, G.E.P.; Jenkins, G.M. and Reinsel, G.C., 2008**. Time series analysis: forecasting and control. 4th edn. Wiley series in probability and statistics, Wiley, Hoboken, NJ.

**Brockwell, P.J. and Davis, R.A., 1991**. Time Series: Theory and Methods. Springer-Verlag.

**Bustin, R., 1991**. Organic maturity in the western Canada sedimentary basin. International Journal of Coal Geology 19: pp. 319 – 358.

**Camargos, R.C.; Nietto, P.R. and do Carmo Nicoletti, M., 2016**. Agglomerative and divisive approaches to unsupervised learning in gestalt clusters. In International Conference on Intelligent Systems Design and Applications. Springer, pp. 35–44.

**Cassisi, C.; Montalto, P.; Aliotta, M.; Cannata, A. and Pulvirenti, A., 2012**. Similarity Measures and Dimensionality Reduction Techniques for Time Series Data Mining. Advances in Data Mining Knowledge Discovery and Applications : pp. 71–96.

**Christensen, N.B., 1990**. Optimized fast Hankel transform filters 1. Geophysical Prospecting 38: pp. 545–568.

**Christiansen, A.V.; Auken, E. and Sørensen, K., 2006**. The transient electromagnetic method. In Groundwater geophysics. Springer, pp. 179–225.

**Cole, K.S. and Cole, R.H., 1941**. Dispersion and Absorption in Dielectrics I. Alternating Current Characteristics. The Journal of Chemical Physics 9: pp. 341–351.

**Corduas, M., 2000**. La metrica autoregressiva tra modelli ARIMA: una procedura in linguaggio GAUSS. Quaderni di Statistica 2.

**Corduas, M. and Piccolo, D., 2008**. Time series clustering and classification by the autoregressive metric. Computational Statistics & Data Analysis 52: pp. 1860–1872.

**Crameik, T.D. and Massey, J.A., 1972**. Carbon Dioxide Injection Project Sacroc Unit, Scurry County, Texas. American Petroleum Institute, API-72-D001, API .

**Cuevas, A.; Febrero-Bande, M. and Fraiman, R., 2004**. An ANOVA test for functional data. Computational Statistics & Data Analysis 47: pp. 111–122.

**Department of Defense - United States of Amaerika, 2008**. GLOBAL POSITIONING SYSTEM and STANDARD POSITIONING SERVICE PERFORMANCE STANDARD. website. URL `https://www.gps.gov`. Visited on 30.09.2020.

**D'Gis Group, 2019**. GeoActivity Maps - searchable maps on well licenses and spuds covering Alberta, Saskatchewan, British Columbia and Manitoba URL `https://www.geoactivity.ca`. Visited 2019-04-03.

**Dickey, D.A. and Fuller, W.A., 1979**. Distribution of the Estimators for Autoregressive Time Series with a Unit Root. Journal of the American Statistical Association 74: pp. 427–431.

**Dongas, J.M. and Lawton, D.C., 2015**. Development of a geostatic model for a geoscience field research site in Alberta. GeoConvention 2015 4-8 May.

**Dongas, J.M. and Lawton, D.C., 2016**. Static characterization and dynamic simulated scenarios for monitoring a shallow $CO_2$ injection target. GeoConvention 2016 7-9 March.

**Dongas, J.M.; Lawton, D.C. and Pedersen, P.K., 2014**. Petrophysical analysis and interpretation for the development of a geostatic model for the initial investigation and characterization of a shallow target in the geoscience field research station (GFRS) area for $CO_2$ sequestration. University of Calgary, Department of Geosciences .

**Durbin, J., 1960**. The fitting of Time Series Models. Review of the International Statistical Institute : pp. 233–243.

**EASAC, 2013**. EASAC policy report 20 - Carbon capture and storage in Europe.

**EMIT, 2020**. Smartem24 receiver system manual URL `https://www.electromag.com.au/`. Visited on 15.02.20205.

**European Union**, **2009**. Directive 2009/31/EC of the European Parliament and of the Council - On the geological storage of carbon dioxide and amending Council Directive 85/337/EEC, European Parliament and Council Directives 2000/60/EC, 2001/80/EC, 2004/35/EC, 2006/12/EC, 2008/1/EC and Regulation (EC) No 1013/2006. OJ L 140 : pp. 114–135.

**Foged, N.; Auken, E.; Christiansen, A.V. and Sørensen, K.I.**, **2013**. Test-site calibration and validation of airborne and ground-based TEM systems. Geophysics 78: pp. E95–E106.

**Fuller, W.A.**, **1995**. Introduction to Statistical Time Series. 2nd edn. John Wiley & Sons, Inc.

**Genoics Limited**, **2006**. Geonics Protem-47D operating manual 3.0.

**GeoSN**, **2020**. Staatsbetrieb Geobasisinformation und Vermessung Sachsen GeoSN. 01099 Dresden .

**Hamann, C.H. and Vielstich, W.**, **1998**. Elektrochemie. Wiley-VCH.

**Hamblin, A.P.**, **1997**. Stratigraphic architecture of the Oldman Formation, Belly River Group, surface and subsurface of southern Alberta. Bulletin of Canadian Petroleum Geology 45: pp. 155–177.

**Hamblin, A.P.**, **1998**. Detailed core measured section of the Bearpaw/Horseshoe Canyon formations, C.P.O.G. Strathmore 7-12-25-25W4, east of Calgary, southern Alberta. Geological Survey of Canada, Open File 3589 .

**Harris, R.**, **2013**. Protem system response. Personal Communication with Geonics Ltd., e-mail.

**Hastie, T.; Tibshirani, R. and Friedman, J.H.**, **2009**. The Elements of Statistical Learning: Data Mining, Inference, and Prediction. 2nd edn. Springer Series in Statistics, Springer New York, New York, NY.

**Hawley, P.F.**, **1938**. Transients in electrical prospecting. GEOPHYSICS 3: pp. 247–257.

**Helwig, S. and Kozhevnikov, N.**, **2003**. Schwingungen in TEM Sendesignalen zu frühen Zeiten. 20. Kolloquium Elektromagnetische Tiefenforschung .

**Hering, E.; Martin, R. and Stohrer, M.**, **2004**. Physik für Ingenieure. Springer.

**Herzog, H.**, **1999**. An introduction to $CO_2$ separation and capture technologies. Energy Laboratory Working Paper .

**Hong, J. and MathWorks Technical Support Department**, **2020**. Why are negative GAP statistic values, provided by evalclusters, allowed as solution? (personal communication, April 27, 2020) .

**Hyndman, R.; Athanasopoulos, G.; Bergmeir, C.; Caceres, G.; Chhay, L.; O'Hara-Wild, M.; Petropoulos, F.; Razbash, S.; Wang, E. and Yasmeen, F.**, **2019**. forecast: Forecasting functions for time series and linear models. URL `http://pkg.robjhyndman.com/forecast`. R package version 8.10.

**IPCC**, **2005**. IPCC Special Report on Carbon Dioxide Capture and Storage. Prepared by Working Group III of the Intergovernmental Panel on Climate Change [Metz, B., O. Davidson, H. C. de Coninck, M. Loos, and L. A. Meyer (eds.)]. Cambridge University Press.

**Itakura, F., 1975**. Minimum prediction residual principle applied to speech recognition. IEEE Transactions on Acoustics, Speech, and Signal Processing 23: pp. 67–72.

**JafarGandomi, A. and Curtis, A., 2011**. Detectability of petrophysical properties of subsurface $CO_2$-saturated aquifer reservoirs using surface geophysical methods. The Leading Edge 30: pp. 1112–1121.

**Kardiyen, F. and Güney, H., 2015**. A Study on Time Series Clustering. Gazi University Journal of Science 28: pp. 331–347.

**Kaufman, L. and Rousseeuw, P.J., 1990**. Finding Groups in Data: An Introduction to Cluster Analysis. Wiley series in probability and mathematical statistics, Wiley, New York u.a.

**Kaufmann, L. and Rousseeuw, P., 1987**. Clustering by means of medoids. Data Analysis based on the L1-Norm and Related Methods : pp. 405–416.

**Keogh, E. and Ratanamahatana, C.A., 2005**. Exact indexing of dynamic time warping. Knowledge and Information Systems 7: pp. 358–386.

**Kertz, W., 1969**. Einführung in die Geophysik, vol. 1. BI-Wiss.-Verlag.

**Knödel, K. and Krummel, H., 2005**. Geophysik, vol. 3 of *Handbuch zur Erkundung des Untergrundes von Deponien und Altlasten*. 2nd edn. Springer.

**Kragh, E. and Christie, P., 2002**. Seismic repeatability, normalized rms, and predictability. Leading Edge (Tulsa, OK) 21: pp. 640+642–647.

**Kwiatkowski, D.; Phillips, P.C.; Schmidt, P. and Shin, Y., 1992**. Testing the null hypothesis of stationarity against the alternative of a unit root: How sure are we that economic time series have a unit root? Journal of Econometrics 54: pp. 159 – 178.

**Lawton, D.C.; Osadetz, K.G. and Saeedfar, A., 2017**. Monitoring technology innovation at the CaMI Field Research Station, Brooks, Alberta. GeoConvention 2017 15-19 March.

**Levy, G.M. and McNeil, J.D., 1984**. Technical Note TN-15 - Transient electromagnetic borehole logging. Tech. rep., Geonics Limited - 1745 Meyerside Dr. Mississauga, Ontario.

**Ley, H.A., 1935**. Geology of Natural Gas. American Association of Petroleum Geologists.

**Life Energy Motion, 2015**. Current transducer CKSR series. URL `www.lem.com`. Visited on 10.01.2020.

**Ljung, G.M. and Box, G.E.P., 1978**. On a measure of lack of fit in time series models. Biometrika 65: pp. 297–303.

**Lumley, D., 2010**. 4D seismic monitoring of $CO_2$ sequestration. The Leading Edge 29: pp. 150–155.

**Lumley, D.; Adams, D.; Wright, R.; Cole, S.; Markus, D. et al., 2008**. Seismic monitoring of $CO_2$ geo-sequestration: realistic capabilities and limitations. In 2008 SEG Annual Meeting. Society of Exploration Geophysicists.

**Macquet, M.; Lawton, D.C.; and Saeedfar, A., 2018**. Reservoir simulation and feasibility study for seismic monitoring at CaMI.FRS, Newell County, Alberta. GeoConvention 2018 7-11 May.

**Maharaj, E.A.**, **1996**. A significance test for classifying arma models. Journal of Statistical Computation and Simulation 54: pp. 305–331.

**Maharaj, E.A.; D'Urso, P. and Caiado, J.**, **2019**. Time series clustering and classification. Chapman & Hall/CRC computer science and data analysis series, CRC Press, Taylor & Francis Group, Boca Raton.

**Malecki, S.**, **2017**. Ein Verfahren zur absoluten räumlichen Poitionierung unter Tage mittels transienter elektromagnetischer Felder. Ph.D. thesis. Technische Universität Bergakademie Freiberg.

**Martin, R.**, **2009**. Development and application of 2d and 3d transient electromagnetic inverse solutions based on adjoint green functions: A feasibility study for the spatial reconstruction of conductivity distributions by means of sensitivities. Ph.D. thesis, Universität zu Köln, Institut für Geophysik und Meteorologie .

**Merziger, G. and Wirth, T.**, **2006**. Repetitorium der Höheren Mathematik. 5th edn.

**Müller, M.**, **2007**. Information retrieval for music and motion. Springer, Berlin.

**Munkholm, M. and Auken, E.**, **1996**. Electromagnetic Noise Contamination on Transient Electromagnetic Soundings in Culturally Disturbed Environments. Journal of Environmental and Engineering Geophysics 1.

**Myers, C.; Rabiner, L. and Rosenberg, A.**, **1980**. Performance tradeoffs in dynamic time warping algorithms for isolated word recognition. IEEE Transactions on Acoustics, Speech, and Signal Processing 28: pp. 623–635.

**Myung, I.J.**, **2003**. Tutorial on maximum likelihood estimation. Journal of Mathematical Psychology 47: pp. 90 – 100.

**Nabighian, M.** (ed.), **1989**. Electromagnetic Methods in Applied Geophysics - Theory, vol. 1 of *Investigations in Geophysics*. Society of Exploration Geophysicists.

**Nelson, M.T.; Biltz, G.R. and Dengel, D.R.**, **2015**. Repeatability of respiratory exchange ratio time series analysis. The Journal of Strength & Conditioning Research 29: pp. 2550–2558.

**Neusser, K.**, **2016**. Estimation of ARMA Models. Springer International Publishing, pp. 87–108.

**NIST/SEMATECH**, **2003**. e-handbook of statistical methods. National Institute of Standards and Technology, Gaithersburg MD, 20899. URL `http://www.itl.nist.gov/div898/handbook/`. Visited on 20.02.2019.

**Oates, T.; Firoiu, L. and Cohen, P.R.**, **2001**. Using Dynamic Time Warping to Bootstrap HMM-Based Clustering of Time Series. Springer Berlin Heidelberg, pp. 35–52.

**Oelschlägel, T.**, **2015**. Untersuchung der Stromfunktion in der Sendespule der Transientelektromagnetik-Apparatur Geonics TEM57 Mk2. unpuplished Master Thesis, Technische Universität Bergakademie Freiberg.

**Osadetz, K.G.; Lawton, D.; Saeedfar, A. and Rock, L.**, **2017**. CMC Research Inc.'s Field Resesch Station and Shell Quest. Tech. rep., Containment and Monitoring Institute and Shell.

**Pak, N.M.; Rempillo, O.; Norman, A.L. and Layzell, D.B.**, **2016**. Early atmospheric detection of carbon dioxide from carbon capture and storage sites. Journal of the Air & Waste Management Association 66: pp. 739–747.

**Peikert, T.; Kreth, A.; Garbe, H. and Potthast, S.**, **2014**. Die Schutzwirkung von IT-Schaltnetzteilen gegenüber leitungsgeführten Störungen auf der Netzspannung. emv : Internationale Fachmesse und Kongress für Elektromagnetische Verträglichkeit. Berlin. VDE-Verlag : pp. 723–730.

**Pelton, W.H.; Ward, S.H.; Hallof, P.G.; Sill, W.R. and Nelson, P.H.**, **1978**. Mineral discrimination and removal of inductive coupling with multifrequency ip. Geophysics 43: pp. 588–609.

**Peng, D.Y. and Robinson, D.B.**, **1976**. A New Two-Constant Equation of State. Industrial & Engineering Chemistry Fundamentals 15: pp. 59–64.

**Piccolo, D.**, **1990**. A distance measure for classifying arima models. Journal of Time Series Analysis 11: pp. 153–164.

**R Core Team**, **2020**. R: A Language and Environment for Statistical Computing. R Foundation for Statistical Computing, Vienna, Austria. URL `https://www.R-project.org`.

**Ramsay, J.O. and Silverman, B.W.**, **1997**. Functional data analysis. Springer series in statistics, Springer, New York. Literaturverz. S. [293] - 302.

**Ramsey, M.**, **2020**. Schlumberger Oilfield Glossary - Drilling Module. Texas Drilling Associates .

**Romanak, K.D.; Bennett, P.C.; Yang, C. and Hovorka, S.D.**, **2012**. Process-based approach to $CO_2$ leakage detection by vadose zone gas monitoring at geologic $CO_2$ storage sites. Geophysical Research Letters 39.

**Rousseeuw, P.**, **1987**. Silhouettes: A Graphical Aid to the Interpretation and Validation of Cluster Analysis. Journal of Computational and Applied Mathematics 20: pp. 53–65.

**Sakoe, H. and Chiba, S.**, **1978**. Dynamic programming algorithm optimization for spoken word recognition. IEEE Transactions on Acoustics, Speech, and Signal Processing 26: pp. 43–49.

**Schlumberger Limited**, **2016**. Borehole log 1F1-10-22-017-16W4 and 1F2-10-22-017-16W4. Personal Communication with CMC Reasearch Institutes, e-mail.

**Schön, J.**, **1996**. Physical Properties of Rocks - Fundamentals and Principles of Petrophysics, vol. 18 of *Handbook of Geophysical Exploration*. 1st edn. Pergamon.

**Sembiring, R.W.; Mohamad Zain, J. and Abdullah, E.**, **2011**. A Comparative Agglomerative Hierarchical Clustering Method to Cluster Implemented Course. Journal of Computing 2.

**Spitzer, K. and Wurmstich, B.**, **1999**. 11. Speed and Accuracy in 3-D Resistivity Modeling. pp. 161–176.

**Statham, L.**, **1936**. Electric earth transients in geophysical prospecting. GEOPHYSICS 1: pp. 271–277.

**Taylor, B.N. and Kuyatt, C.E., 2001**. Guidelines for Evaluating and Expressing the Uncertainty of NIST Measurement Results. National Institute of Standards and Technology, Gaithersburg MD, 20899. URL `http://physics.nist.gov/TN1297`. Visited on 20.02.2019.

**Tello, C.; Moraes, C.G.V.D.; Prata, T.S.; Derr, P.; Patel, J.; Siegfried, J.; Liebmann, J.M. and Ritch, R., 2010**. Repeatability of short-duration transient visual evoked potentials in normal subjects. Doc Ophthalmol 120: pp. 219–228.

**Tezkan, B., 1999**. A Review Of Environmental Applications Of Quasi-Stationary Electromagnetic Techniques. Surveys in Geophysics 20: pp. 279–308.

**Tibshirani, R.; Walther, G. and Hastie, T., 2001**. Estimating the Number of Clusters in a Data Set Via the Gap Statistic. Journal of the Royal Statistical Society Series B 63: pp. 411–423.

**Tsay, R.S., 2010**. Analysis of Financial Time Series. John Wiley & Sons, Ltd.

**Umberto, T., 2004**. A note on distance and parallelism between two ARIMA processes. Quaderni di Statistica 6: pp. 21–29.

**Ward, S.H. and Hohmann, G.W., 1988**. Electromagnetic theory for geophysical applications. In Electromagnetic Methods in Applied Geophysics: Voume 1, Theory. Society of Exploration Geophysicists, pp. 130–311.

**Werthmüller, D., 2017**. An open-source full 3D electromagnetic modeler for 1D VTI media in Python: empymod. Geophysics 82: pp. WB9–WB19.

**WorleyParsonsKomex, 2008**. Regional Groundwater Resource Assessment for the County of Newell No. 4. Tech. rep., County of Newell and AAFC-PFRA.

**Yogeshwar, P., 2014**. A resistivity-depth model of the central Azraq basin area, Jordan: 2D forward and inverse modeling of time domain electromagnetic data. Ph.D. thesis. Universität zu Köln.

**Zhdanov, M.S., 2009**. Geophysical electromagnetic theory and methods. Elsevier.

**Ziolkowski, A.; Parr, R.; Wright, D.; Nockles, V.; Limond, C.; Morris, E. and Linfoot, J., 2010**. Multi-transient electromagnetic repeatability experiment over the North Sea Harding field. Geophysical Prospecting 58: pp. 1159–1176.

**Zonge International, 2020**. NanoTEM fast-turnoff transceiver manual URL `http://zonge.com`. Visited on 15.02.20205.